

AN ISOTOPIC, TRACE ELEMENT, AND VOLATILE INVESTIGATION OF
LARGE-VOLUME RHYOLITE GENERATION AT THE PICABO VOLCANIC
FIELD OF THE YELLOWSTONE HOTSPOT TRACK

by

DANA LAUREN DREW

A THESIS

Presented to the Department of Geological Sciences
and the Graduate School of the University of Oregon
in partial fulfillment of the requirements
for the degree of
Master of Science

December 2013

THESIS APPROVAL PAGE

Student: Dana Lauren Drew

Title: An Isotopic, Trace Element, and Volatile Investigation of Large-Volume Rhyolite Generation at the Picabo Volcanic Field of the Yellowstone Hotspot Track

This thesis has been accepted and approved in partial fulfillment of the requirements for the Master of Science degree in the Department of Geological Sciences by:

Ilya Bindeman	Chairperson
Paul Wallace	Member
James Watkins	Member

and

Kimberly Andrews Espy	Vice President for Research and Innovation; Dean of the Graduate School
-----------------------	--

Original approval signatures are on file with the University of Oregon Graduate School.

Degree awarded December 2013

© 2013 Dana Lauren Drew

THESIS ABSTRACT

Dana Lauren Drew

Master of Science

Department of Geological Sciences

December 2013

Title: An Isotopic, Trace Element, and Volatile Investigation of Large-Volume Rhyolite Generation at the Picabo Volcanic Field of the Yellowstone Hotspot Track

Rhyolites of the Picabo volcanic field (10.4-6.6 Ma) of the Yellowstone hotspot in eastern Idaho are preserved as thick ignimbrites and lavas along the margins of the Snake River Plain. This study presents new O and Hf isotope data and U-Pb geochronology from individual zircons, O isotope data from major phenocrysts, whole rock Sr and Nd isotope data, whole rock geochemistry, and trace element and volatile analyses of quartz-hosted melt inclusions, which were used to characterize the evolution of rhyolite generation through the eruptive sequence. The chemical composition of the first eruption of the caldera complex, the Tuff of Arbon Valley, suggests rhyolite generation through repeated magma injection into the crust, remelting, crystallization, mixing, and crustal assimilation. Subsequent eruptions have diverse and low $\delta^{18}\text{O}$ signatures indicating rhyolite generation through the remelting of variably hydrothermally altered volcanics, followed by rapid batch assembly.

This thesis includes co-authored material previously published.

CURRICULUM VITAE

NAME OF AUTHOR: Dana Lauren Drew

GRADUATE AND UNDERGRADUATE SCHOOLS ATTENDED:

University of Oregon, Eugene
Pennsylvania State University, University Park

DEGREES AWARDED:

Master of Science, Geological Science, 2013, University of Oregon
Bachelor of Science, Geoscience, 2011, Pennsylvania State University

AREAS OF SPECIAL INTEREST:

Volcanology
Geochemistry

GRANTS, AWARDS, AND HONORS:

Staples Award, University of Oregon, 2013

Travel Grant, University of Oregon, 2013

Travel Grant, Geochemical Society, 2013

Library Literacy Award, Undergraduate Research Symposium, Pennsylvania State University, 2011

Miller Bruce Scholarship, Pennsylvania State University Geosciences Department, 2010

Dachille Memorial Award in Geochemistry, Pennsylvania State University Geosciences Department, 2010

Alumni Student Discovery Grant, Pennsylvania State University, 2010

Miller Bruce Scholarship, Pennsylvania State University Geosciences Department, 2009

Wilson Matthew J Scholarship, Pennsylvania State University Geosciences
Department, 2009

Drake Edwin Scholarship, Pennsylvania State University Geosciences
Department, 2009

Teas and Hedberg Scholarship, Pennsylvania State University Geosciences
Department, 2008

Kappmeyer-Isaacs Field Camp Award, Pennsylvania State University
Geosciences Department, 2008

Wilson Matthew J Honors Scholarship, Pennsylvania State University
Geosciences Department, 2007

PUBLICATIONS:

Drew, D.L., Bindeman, I.N., Watts, K.E., Schmitt, A.K., Fu, B., McCurry, M., 2013.
Crustal-scale recycling in caldera complexes and rift zones along the Yellowstone
hotspot track: O and Hf isotopic evidence in diverse zircons from voluminous
rhyolites of the Picabo volcanic field, Idaho. *Earth and Planetary Science Letters*
281, 63-77.

ACKNOWLEDGMENTS

I wish to express sincere appreciation to my advisor, Ilya Bindeman, for his guidance and encouragement, I would not have been able to accomplish everything I strived to if it was not for his support and enthusiasm for new data. I thank my committee members James Watkins and Paul Wallace for all their willingness to help and their feedback as well. I would like to also thank Jim Palandri for all his help in preparing and running samples on the laser fluorination line. His positive outlook kept even the longest days of running on the laser fluorination line enjoyable. I thank Ben Ellis, Frank Ramos, John Donovan, Julie Chouinard, and Adam Kent for their analytical help, and coauthors Kathryn Watts, Axel Schmitt, Bin Fu and Mike McCurry for their feedback, contributions, and editorial assistance.

I would also like to thank Dylan Colon for fieldwork assistance and laboratory help. I thank the melt inclusion laboratory group, James Rea, Robin Tuohy, Kristina Walowski, and especially Madison Myers, for all of their help when I was learning to doubly polish melt inclusions and analyze samples on the FTIR. I thank Angela Seligman, my officemate, colleague, and friend, for all her support and help throughout my time here, as well as Molly O'Neill. I wish to also thank Shari Douglas, Dave Stemple, and Vicki Arbeiter for their support, great conversations, and for making me feel like family. All the advice and encouragement from other graduate students and faculty members have also helped me to grow as a scientist and continually progress in my research. This work was supported by NSF grant EAR/CAREER-844772, and the ion microprobe facility at UCLA utilized during this study is partly supported by a grant from the Instrumentation and Facilities Program, Division of Earth Sciences, National Science Foundation. I wish to thank the

University of Oregon Department of Geological Sciences for the travel grants and scholarship I received. Lastly, I also thank my family, specifically my parents and my sister, for all their love and support over the years.

For my sister, Kelly Drew who taught me “the uglier a laugh looks from the outside, the more beautiful the soul of the contorted clown.”

TABLE OF CONTENTS

Chapter	Page
<p>I. CRUSTAL-SCALE RECYCLING IN CALDERA COMPLEXES AND RIFT ZONES ALONG THE YELLOWSTONE HOTSPOT TRACK: O AND HF ISOTOPIC EVIDENCE IN DIVERSE ZIRCONS FROM VOLUMINOUS RHYOLITES OF THE PICABO VOLCANIC FIELD, IDAHO</p>	1
Introduction.....	1
Volcanism of the Snake River Plain	1
Research Implications and Purpose	2
Background.....	7
Yellowstone Plume	7
Oxygen Isotopes and Hydrothermal Alteration	8
Defining the Picabo Volcanic Field.....	9
Local Tectonic Framework.....	10
Rhyolites That Define the Picabo Volcanic Field.....	14
Nonhotspot-Related Volcanism in and Surrounding the Snake River Plain ...	15
Quaternary Volcanics and Craters of the Moon Volcanics	15
Great Basin Rhyolites	16
Zircons as Robust Geochemical Recorders	16
Methods.....	18
Oxygen Isotopes.....	18
Whole Rock Geochemistry and Sr-Nd Isotopes	19
Zircon U-Pb Dating and O Isotopes.....	19
Hf Isotope Analyses of Zircon.....	20

Chapter	Page
Results.....	21
Geochronology of Picabo Ignimbrites and Lavas.....	21
Isotopic and Compositional Evolution: $\delta^{18}\text{O}$, $^{87}\text{Sr}/^{86}\text{Sr}$, $^{143}\text{Nd}/^{144}\text{Nd}$ and $^{176}\text{Hf}/^{177}\text{Hf}$	22
Heterogeneous $\delta^{18}\text{O}$ in Zircons.....	30
Discussion.....	31
Defining the Existence of Unexposed Calderas at Picabo.....	32
Petrogenetic Implications of the Geochemical and Isotopic Data.....	32
Mechanisms of Generating Low- $\delta^{18}\text{O}$ Rhyolites at the Picabo Volcanic Field.....	33
Significance of Zircon $\delta^{18}\text{O}$ Diversity and Hf Homogeneity in Voluminous Tuffs.....	39
Origin of Silicic Volcanism at the Picabo Volcanic Field and in the SRP.....	40
Conclusions.....	41
 II. CHEMICAL AND VOLATILE CONSTRAINTS ON THE GENESIS AND STORAGE OF RHYOLITE IN THE SNAKE RIVER PLAIN: INSIGHTS FROM QUARTZ-HOSTED MELT INCLUSIONS IN THE TUFF OF ARBON VALLEY. 43	
Summary.....	43
Introduction.....	44
Snake River Plain Silicic Volcanism and Caldera Cycles.....	44
Early Rhyolites in Caldera Cycles and the TAV.....	44
Goals of the Present Study.....	45
Methods.....	46
Results.....	47
Stratigraphy of the Studied Section and Sampling.....	47

Chapter	Page
Melt Inclusion Compositions.....	48
CL Zoning Patterns and Ti in Host Quartz.....	52
Discussion.....	56
Volatile and Chemical Variations.....	56
Comparison With Other Rhyolites From Different Tectonic Settings.....	59
Comparison With Topaz Rhyolites.....	63
Ti Variations in Quartz Across the Eruptive Stratigraphy.....	64
Mass Balance of the Volatile Budget With Isotopic and Chemical Constraints.....	67
Implications for the Initiation of Caldera Complexes in the SRP.....	71
Conclusions.....	72
APPENDICES.....	76
A. ADDITIONAL BACKGROUND INFORMATION.....	76
B. DETAILED SAMPLE DESCRIPTIONS AND LOCATIONS.....	78
C. LASER FLUORINATION LINE INSTRUCTIONS.....	83
D. QUARTZ AND ZIRCON MOUNT MAPS.....	85
E. ADDITIONAL GEOCHRONOLOGY TABLES.....	89
F. ADDITIONAL GEOCHEMICAL DATA, FIGURES, AND ANALYSIS.....	94
G. MIXING CALCULATION.....	115
H. ADDITIONAL MELT INCLUSION BACKGROUND INFORMATION.....	117
I. DETAILED METHODS, RAW FTIR MEASUREMENTS, AND PHOTOMICROGRAPHS.....	124
J. CATHODE LUMINESCENCE IMAGES.....	143

Chapter	Page
K. TI IN QUARTZ MEASUREMENTS, BACKSCATTER IMAGES OF SPOT LOCATIONS OF TI IN QUARTZ MEASUREMENTS	155
L. ADDITIONAL GEOCHEMICAL FIGURES AND TABLES.....	162
REFERENCES CITED.....	169

LIST OF FIGURES

Figure	Page
CHAPTER I	
1. Map of the Snake River Plain volcanic fields and crustal features of the western United States.	3
2. Map showing the Picabo volcanic field in the SRP and sampling localities of this study.	11
3. Generalized stratigraphic section of the Picabo rhyolites analyzed.....	12
4. Whole rock geochemistry plots of Picabo rhyolites, surrounding volcanic center rhyolites: Bruneau-Jarbidge, Twin Falls, Heise and Yellowstone, INEL-1 borehole rhyolites, Jim Sage and Cotterel Mountain rhyolites, Hawkins Basin volcanics, and Challis intrusives.....	24
5. a-b. Strontium variation with SiO ₂ of Picabo rhyolites and discriminant diagram of Rb versus Nb+Y.	25
6. a-c. Binary mixing model of ⁸⁷ Sr/ ⁸⁶ Sr _i versus ¹⁴³ Nd/ ¹⁴⁴ Nd of Picabo rhyolites, ⁸⁷ Sr/ ⁸⁶ Sr through time, and ¹⁴³ Nd/ ¹⁴⁴ Nd versus 1/Nd for Picabo rhyolites.....	26
7. δ ¹⁸ O compositions of major phenocryst phases: quartz, plagioclase and pyroxene, and calculated melt δ ¹⁸ O values versus U-Pb, Ar-Ar or K-Ar age	28
8. a-b. Compilation of δ ¹⁸ O compositions and U-Pb ages of individual zircons determined by ion microprobe and summary of δ ¹⁸ O zircon heterogeneity with average U-Pb age.	29
9. a-b. ε _{Hf} (t) versus U-Pb age of individual zircons from Picabo rhyolites with evolution lines of depleted mantle, CHUR (chondrite uniform reservoir) and average continental crust composition at various ages and ε _{Hf} (0) versus δ ¹⁸ O of individual zircons from Picabo rhyolites.	35
10. Summary of the petrogenetic mechanisms proposed for generating low-δ ¹⁸ O rhyolites at the Picabo volcanic field.	37
CHAPTER II	
1. Map of the Yellowstone hotspot volcanic fields and inset map of sampling localities of the Tuff of Arbon Valley at the Picabo volcanic field.	48

Figure	Page
2. Major element variations with SiO ₂ in comparison to other SRP volcanic fields, Challis volcanics, Topaz rhyolites and granites, Bishop Tuff quartz-hosted melt inclusions, and Yellowstone MFT quartz-hosted melt inclusions	50
3. TAV melt inclusion CO ₂ and H ₂ O determined by Fourier Transform Infrared Spectroscopy in comparison to the Bishop Tuff.....	51
4. Rare earth element diagram of Picabo TAV melt inclusions, Topaz rhyolites, Yellowstone and Bishop Tuff rhyolites.	51
5. Spider plot of Picabo TAV melt inclusions in comparison to Bishop Tuff and Mesa Falls Tuff (MFT) melt inclusions.....	52
6. Nb versus Rb of TAV melt inclusions in comparison to Picabo rhyolites, SRP rhyolites, Topaz rhyolites and granite, Bishop Tuff melt inclusions, Challis volcanics and intrusives, and Archean crust.....	53
7. Nb/Ce versus Rb/Ce of TAV melt inclusions in comparison to Picabo rhyolites, SRP rhyolites, Topaz rhyolites and granite, Bishop Tuff melt inclusions, Challis volcanics and intrusives, and Archean crust.....	54
8. U versus Th of TAV melt inclusions in comparison to Picabo rhyolites, SRP rhyolites (Heise, Twin Falls, and Bruneau Jarbidge), Topaz rhyolites and granite, Bishop Tuff melt inclusions, Challis volcanics and intrusives, and Archean crust	55
9. Annotated cathodoluminescence images highlighting zoning patterns and Ti concentrations in host quartz phenocrysts	56
10. Quartz (Qz), albite (Ab), and orthoclase (Or) ternary diagram of Tuff of Arbon Valley melt inclusion glass compositions in comparison to cotectic lines of H ₂ O-saturated minima and eutectics in haplogranitic melts as a function of pressure	60
11. Sr/Rb variations with Ba/Rb of Picabo rhyolites, SRP rhyolites, Challis volcanics and intrusives, Topaz rhyolites and granites, Bishop Tuff quartz-hosted melt inclusions, and Mesa Falls Tuff quartz-hosted melt inclusions	62
12. F versus Cl concentration of melt inclusions in comparison to olivine-hosted melt inclusions from Yellowstone, quartz-hosted melt inclusions from the Mesa Falls Tuff of Yellowstone, Bishop Tuff quartz-hosted melt inclusions, rehomogenized topaz granite inclusions, rehomogenized quartz-hosted melt inclusions from high-F rhyolites of Australia and plagioclase-hosted melt inclusions from Crater Lake.....	66

Figure	Page
13. Ti and Al trace element variations in quartz from the Picabo volcanic center in comparison to the Bishop Tuff.	67
14. The change in fluorine concentration with melt fraction at various partition coefficients, assuming an initial concentration of 557 ppm (upper crustal conditions).....	68
15. Generation of the stratified TAV magma body through multiple episodes of remelting or distillation.....	73
16. a-b. Generation of the TAV in comparison to subsequent volcanism at the Picabo volcanic field.....	74
 APPENDIX A	
A1. Seismic tomography cross section through the Yellowstone caldera.	76
A2. Cross sectional schematic of the interaction between the subducting slab and plume head.	77
 APPENDIX B	
B1. Photomicrograph of the Tuff of Arbon Valley in plane polarized light.	78
B2. a-b. Photographs of the Tuff of Arbon Valley at the Cove sampling site in Idaho.	79
B3. Photograph of fiamme-like structures in the West Pocatello rhyolite taken an outcrop off of Trail Creek Road near the town of Pocatello, ID.	80
B4. Photomicrograph of the West Pocatello rhyolite in cross polarized light.....	80
 APPENDIX D	
D1. Cathodoluminescence image of zircon mount used for geochronology and oxygen isotope measurements..	85
D2. Mount of doubly polished quartz-hosted melt inclusions.....	86
D3. Mount of ~1 to 3 mm quartz phenocrysts used for Ti measurements in quartz....	87
D4. Mount of <1 mm quartz phenocrysts used for Ti measurements in quartz.	88

Figure	Page
APPENDIX E	
E1. Probability distributions of U-Pb ages for zircon data of the Tuff of Arbon Valley, INEL 3686', West Pocatello rhyolite, Tuff of American Falls, Tuff of Lost River Sinks, Stevens Peak 2 rhyolite and Steven's Peak rhyolite.	89
APPENDIX F	
F1. Temperature of Picabo rhyolites calculated from rhyolite MELTS liquidus temperatures, and zircon saturation temperatures.....	98
F2. Trace element concentrations of Picabo rhyolites, bulk continental crust, primitive mantle, Big Southern Butte and East Butte, OIB and topaz rhyolites. ...	99
F3. a-k. K ₂ O versus SiO ₂ , Zr/Y versus Ba/Sr, Ba/La versus Th, Rb/Zr versus Ba/Sr, Y/Nb versus Ce/Nb, Ba/La versus SiO ₂ , U versus Th, La/Nb versus SiO ₂ , Sc versus Rb, and Sr versus Rb of Picabo rhyolites ..	100
F4. $\epsilon_{\text{Hf}}(t)$ versus U-Pb age for Picabo zircons.....	111
APPENDIX H	
H1. Distribution of topaz rhyolites in the western U.S. (Christiansen et al., 2007). ...	120
H2. Distribution of fluorspar deposits in the western U.S. (Van Alstine, 1976).....	122
H3. The effects of fluorine on the glass transition temperature of rhyolite and albite.....	123
APPENDIX I	
I1. a-d. Compilation of photomicrographs of singly polished melt inclusions.....	138
I2. Compilation of photomicrographs of doubly polished melt inclusions.....	142
APPENDIX J	
J1. a-d. CL images taken on the scanning electron microscope of melt inclusion host quartz phenocrysts.....	143
J2. Cathodoluminescence images of quartz phenocrysts from the West Pocatello rhyolite	147

Figure	Page
J3. a-e. Cathodoluminescence image of quartz phenocrysts from the upper TAV.....	148
J4. a-c. Cathodoluminescence image of quartz phenocrysts from the lower TAV.....	153
 APPENDIX L	
L1. a-d. K ₂ O variations with CO ₂ , TiO ₂ variations with CO ₂ , F variations with CO ₂ , and TiO ₂ variations with SiO ₂ of TAV melt inclusions.....	162
L2. a-d. Li variations with Rb, Li variations with H ₂ O, H ₂ O variations with Rb, and melt inclusion area with variations in H ₂ O of TAV melt inclusions	166

LIST OF TABLES

Table	Page
CHAPTER I	
1. Ages and compositions of Picabo ignimbrites and lavas in this study.	4
CHAPTER II	
1. Fourier Transform Infrared Spectroscopic data for TAV quartz-hosted melt inclusions	49
APPENDIX B	
B1. Sample Localities of the main rhyolites that we use to define the Picabo volcanic field.....	82
APPENDIX E	
E1. a-c. U/Pb ages, $\delta^{18}\text{O}$, $\epsilon_{\text{Hf}}(0)$, and $\epsilon_{\text{Hf}}(t)$ for individual zircon spots.....	90
APPENDIX F	
F1. Whole rock geochemistry analyzed by XRF at Washington State University. Major elements are normalized and trace elements are un-normalized.....	94
F2. Summary of the age and $\delta^{18}\text{O}$ of various Snake River Plain units between 10.4 and 6.6 Ma	96
F3. Petrographic summary of Picabo rhyolites, with volume percent phenocrysts, absence or presence of glomerocrysts, and order of abundance.....	96
F4. Summary of temperature estimates for Picabo rhyolites.	97
F5. Summary of whole rock $\delta^{18}\text{O}$ of Challis intrusive samples.....	97
F6. Whole rock ϵ_{Hf} measurements of select Picabo rhyolites.....	98
APPENDIX I	
I1. FTIR measurements of the OH^- , $\text{H}_2\text{O}_{\text{total}}$, molecular H_2O and bound OH^- absorbance peaks, and micrometer and reflectance thicknesses of melt inclusion wafers	127

Table	Page
I2. Ratios of total water to hydroxyl and molecular water to hydroxyl for individual FTIR analyses.....	132
I3. Normalized major elements and unnormalized total of rhyolitic TAV quartz-hosted melt inclusions.....	135
I4. Trace element concentrations (in ppm) of quartz-hosted rhyolitic melt inclusions of the TAV. Concentrations were corrected according to the individual SiO ₂ content of each inclusion.....	136
 APPENDIX K	
K1. Blank corrected trace element Ti, Fe, and Al concentrations (in ppm) in quartz samples analyzed for melt inclusions	155
K2. Blank and aggregate corrected Ti and Al trace element concentrations (in ppm) in quartz samples.....	158
 APPENDIX L	
L1. Maximum, average, and the detection limit Ti concentrations (ppm) in quartz and corresponding temperatures at various activities and a pressure of 2 kbars ...	162

CHAPTER I

CRUSTAL-SCALE RECYCLING IN CALDERA COMPLEXES AND RIFT ZONES ALONG THE YELLOWSTONE HOTSPOT TRACK: O AND HF ISOTOPIC EVIDENCE IN DIVERSE ZIRCONS FROM VOLUMINOUS RHYOLITES OF THE PICABO VOLCANIC FIELD, IDAHO

This chapter was published in *Earth and Planetary Science Letters* in 2013, volume 381, pages 63-77 (Drew et al., 2013). Coauthors, Ilya Bindeman and Axel Schmitt provided funding, assisted with data acquisition, and provided editorial assistance. Kathryn Watts and Bin Fu also assisted with data acquisition and provided editorial assistance. Michael McCurry and Ilya Bindeman assisted with sample collection.

Introduction

Volcanism of the Snake River Plain

Large-volume rhyolitic volcanism in the Snake River Plain (SRP) began at ~16 Ma and swept from Oregon to Nevada and through Idaho as the North American plate migrated southwest over the Yellowstone hotspot (Fig. 1; Pierce and Morgan, 1992; Schmandt et al., 2012). High heat fluxes and basalt input from the Yellowstone plume have facilitated large-scale melting of the crust and the formation of unique “SRP-type” rhyolites that are characterized by exceptionally large eruptive volumes, high magmatic temperatures, and anhydrous mineralogies (Nash et al., 2006; Branney et al., 2008; Christiansen and McCurry, 2008). The chemical and isotopic characteristics of SRP rhyolites have been experimentally and numerically modeled to be consistent with mid-crustal generation (≤ 10 km; Almeev et al., 2012; Rodgers and McCurry, 2009) and shallow-level (1-5 km) storage, assembly, and differentiation (Simakin and Bindeman, 2012).

Greater than 10,000 km³ of rhyolite with low- $\delta^{18}\text{O}$ values and diverse $\delta^{18}\text{O}$ zircon populations have erupted across the SRP over the past 16 Ma (Bindeman & Valley, 2001; Bindeman et al., 2007; Cathey et al., 2008; Watts et al., 2011, 2012). However, the

distribution and volume of low- $\delta^{18}\text{O}$ rhyolites is not homogeneous across the SRP. It appears that less focused magmatism and more frequent silicic eruptions with uniformly low- $\delta^{18}\text{O}$ values characterize the older Bruneau-Jarvis (BJ) and Twin Falls (TF) eruptive centers in the central SRP (CSRP) (Ellis et al., 2010; Bonnicksen et al., 2008; Boroughs et al., 2005; Cathey et al., 2008; Cathey and Nash, 2004), in contrast to the younger Heise and Yellowstone centers in the eastern SRP, which are characterized by fewer and larger individual caldera-forming eruptions that create nested caldera complexes with temporal decreases in $\delta^{18}\text{O}$ (Bindeman et al., 2007, 2008; Watts et al., 2011, 2012).

This thesis describes the Picabo eruptive center, which precedes Heise and Yellowstone and postdates BJ-TF in the spatiotemporal progression of the Yellowstone hotspot track (Fig. 1). Picabo produced at least three, but likely six major caldera-forming eruptions from 10.4-6.6 Ma (Table 1). Here I combine detailed isotopic, geochronologic, and geochemical studies using microanalytical methods to elucidate the mechanisms by which Picabo rhyolites were formed, and compare these mechanisms to those proposed for various large-volume rhyolites in the eastern and central SRP.

Research implications and purpose

“Supervolcanic” eruptions in geologic history have produced many of the most prolific igneous provinces on Earth, including the Yellowstone Plateau of the SRP. These caldera-forming eruptions can release 1,000s of cubic kilometers of magma, are orders of magnitude larger than any eruptions witnessed in historical time, and affect human populations, the climate, and the environment (Robock, 2010; Jones et al., 2007). Understanding how such immense volumes of silicic magma are generated, stored, and assembled in the crust is crucial to understanding potential geologic hazards. The SRP preserves a comprehensive history of explosive silicic volcanism and each caldera cluster comprising the Yellowstone hotspot track plays an integral role in reconstructing the eruptive framework, and aids in elucidating the petrogenetic history of rhyolite genesis through time. The Picabo volcanic field is the third youngest caldera cluster, and I use micro-analytical analyses of ignimbrites and lavas to relate crystal-scale isotopic

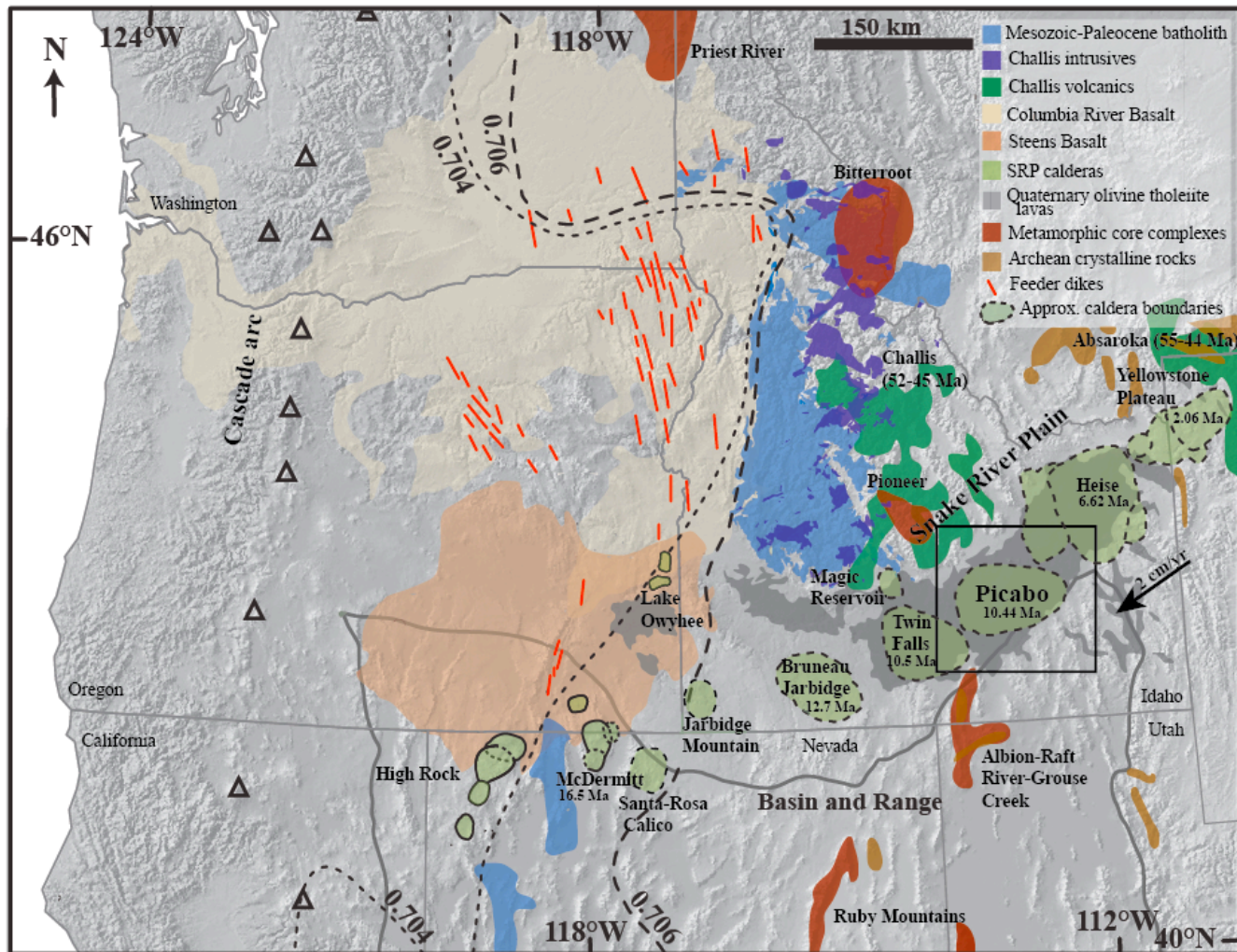


Fig. 1. Map of the Snake River Plain volcanic fields and crustal features in the western United States (adopted from the literature, see Appendix 2). The $^{87}\text{Sr}/^{86}\text{Sr}=0.706$ defines the transition from Mesozoic-Paleozoic accreted oceanic terranes to Precambrian craton (Farmer and Depaolo, 1983; Fleck and Criss, 1985).

Table 1.

Ages and compositions of Picabo ignimbrites and lavas in this study. The $^{206}\text{Pb}/^{238}\text{U}$ concordia ages have been disequilibrium corrected and are shown with 95% confidence intervals. Ar-Ar and K-Ar (italicized) ages are included for comparison. The zircon $\delta^{18}\text{O}$ range of individual zircon core measurements is presented with a one-sigma standard deviation (see the supplementary material for individual zircon data). The $\delta^{18}\text{O}_{\text{melt}}$ composition was calculated from the quartz and plagioclase phenocryst $\delta^{18}\text{O}$ measured compositions and from known fractionation factors between the mineral and melt for the average temperature of 850°C (Bindeman and Valley, 2003). Liquidus temperatures represent the first appearance of feldspar or quartz, and were calculated using rhyolite MELTS at a pressure of 1.5 kilobars, 3-wt% H_2O (using a water content of 1.5 wt. % would shift temperatures upwards by ~50°C), and QFM oxygen fugacity. Zircon saturation temperatures were calculated from whole rock compositions, specifically major elements and zirconium (Miller et al., 2003; Hanchar and Watson, 2003). $\varepsilon_{\text{Hf}}(0)$ is the current ε_{Hf} ($t=0$) (see Appendix for $\varepsilon_{\text{Hf}}(t)$ of the ε_{Hf} at the time of formation).

Unit	Sample	Abbr.	K/Ar-Ar age	U-Pb age	$\delta^{18}\text{O}$ (‰)				$\delta^{18}\text{O}_{\text{melt}}$	Temp (°C)	
			(Ma)	(Ma)	Qtz	Plag	Pyrx	Zrc Range	(‰)	Zrc Sat	Liq
*Tuff of Arbon Valley (upper)	PC-14	TAV _U	10.2 ^a	10.44±0.27	8.41	7.80	-	5.43-6.80	7.9	835	877
*Tuff of Arbon valley (lower)	PC-12	TAV _L	-	-	8.83	7.86	-	-	8.3	754	842
*Tuff of Little Chokecherry Canyon	PC-71	CC	9.34 ^a	9.70±0.12	-	4.20	3.47	0.98-2.00	4.8	860	832
Two and a Half Mile Rhyolite	PC-20	TFM	9.1 ^b	-	8.08	-	-	-	7.7	765	827
*INEL 3686'	INEL-1	INEL	-	8.31±0.22, 8.27±0.27 ^c	4.73	1.61	-	0.01-2.51	2.1	861	856
*West Pocatello rhyolite	PC-01	PR	7.9 ^c	8.25±0.26	-	2.79	2.35	0.97-2.75	3.3	877	833
Tuff of American Falls	PC-34	TAF	7.53 ^a	7.91±0.16	5.81	3.74	2.62	0.83-4.77	4.1	888	916
Hawley Spring	PC-76	HS	7.2 ^d	-	7.61	-	-	4.30-5.90	7.1	806	842
Tuff of Lost River Sinks	PC25	TLSR	8.81 ^a	7.05±0.13	-	6.22	-	4.08-5.73	6.8	837	816
Rhyolite of Steven's Peak 2	PC-19	SP2	-	6.86±0.19	-	4.14	-	1.30-6.44	4.7	862	859
Rhyolite of Steven's Peak	PC-16	SP	9.8 ^b	6.62±0.12 9.46±0.09-9.44	-	5.37	-	2.73-5.32	5.9	813	816
Lower Jim Sage	PC-62	JS	-	±0.10 ^f	-	2.27	-	-	2.8	856	853
Upper Jim Sage	PC-63	JS	-	8.21 ± 0.15 ^f	-	3.47	-	-	4.0	874	834
Idavada	PC-69	ID	-	-	-	7.15	-	-	6.6	782	933

^a Denotes Ar-Ar age from Anders et al. (2009).

^b Denotes K-Ar age from Kellogg et al. (1994).

^c Denotes K-Ar age from Kellogg et al. (1988).

^d Denotes K-Ar age from Morgan et al. (1984).

^e Denotes U-Pb age and data from McCurry and Rodgers (2009).

^f Denotes U-Pb age from Konstantinou et al. (2012).

* Denotes the major caldera-derived ignimbrites

Table 1 continued

Unit	$^{87}\text{Sr}/^{86}\text{Sr}_i$	$^{87}\text{Sr}/^{86}\text{Sr}$	$^{143}\text{Nd}/^{144}\text{Nd}$	$\epsilon_{\text{Nd}}(0)$	$\epsilon_{\text{Hf}}(0)$
*Tuff of Arbon Valley (upper)	0.72520	0.71507	0.51171	-18.0	-28
*Tuff of Arbon valley (lower)	0.71488	0.73443	0.51173	-17.7	-
*Tuff of Little Chokecherry Canyon	-	-	0.512334	-5.9	-7.7
Two and a Half Mile Rhyolite	0.71948	0.72078	0.51145	-23.2	-
*INEL 3686'	0.71234	<i>0.71234^c</i>	<i>0.51231^c</i>	-6.2	-
*West Pocatello rhyolite	0.71169	0.71231	0.5123	-6.5	-5.5
Tuff of American Falls	0.71197	0.71218	0.51229	-6.9	-5.7
Hawley Spring	-	-	0.51161	-20.1	-31.5
Tuff of Lost River Sinks	0.71204	0.71276	0.51211	-10.3	-11.8
Rhyolite of Steven's Peak 2	0.71052	0.71094	0.51224	-7.8	-9.7
Rhyolite of Steven's Peak	0.70994	0.71200	0.51225	-7.6	-9.5
Lower Jim Sage	-	-	-	-	-
Upper Jim Sage	-	-	-	-	-
Idavada			0.51190	-14.5	

variations to caldera-wide processes. Specifically I use O, Hf, Sr, and Nd isotopes to constrain how rhyolites obtain low- $\delta^{18}\text{O}$ signatures in tandem with how rhyolite genesis is impacted by repeated caldera formation and the modified crustal architecture created by Basin and Range extension. This research contributes to constraining: 1) the interconnection of meteoric water, extensional tectonics, and voluminous magma bodies in the shallow crust; 2) how magma bodies on the order of hundreds to thousands of cubic kilometers are assembled, and how these mechanisms contribute to triggering cataclysmic eruptions; and 3) changes in rhyolite production over the past 16 million years, which has direct implications on our understanding of the current magmatic system of Yellowstone Plateau.

The pervasive low- $\delta^{18}\text{O}$ signature of Snake River Plain rhyolites is a fingerprint of meteoric water, and demonstrates the inherent link between surface and subsurface processes in caldera complexes, specifically the remelting of hydrothermally altered source rock. The mechanism of generating a low- $\delta^{18}\text{O}$ signature in the Snake River Plain is highly debated with different mechanisms and source rocks proposed for various eruptive centers (Bindeman and Valley, 2001, Bindeman et al., 2008, Watts et al., 2011; Wolff et al., 2009, 2011; Hildreth et al., 1984). The Picabo eruptive center is located directly between centers where different models of low- $\delta^{18}\text{O}$ magma genesis are proposed. My research contributes to reconciling this contentious debate, suggesting that remelting of hydrothermally altered intracaldera tuffs as well as pre-existing low- $\delta^{18}\text{O}$ source rocks produced during Basin and Range extension contributes to low- $\delta^{18}\text{O}$ rhyolite genesis.

O and Hf isotopic signatures in zircon not only act as geochemical tracers, but also enable me to constrain how the magma was assembled prior to and/or during caldera collapse. The diverse isotopic signatures I observe in Picabo rhyolites, and which are observed in rhyolites of the adjacent volcanic centers, provide evidence for the coalescence of individual, shallow magma batches. This assembly process may itself be the trigger for caldera-forming eruptions. The coalescence of magma batches could occur in response to an increased supply of basalt to the base of a magma chamber, resulting in catastrophic magma assembly through density destabilization of the caldera roof

(Simakin and Bindeman, 2012). My rigorous multi-isotope study of the Picabo volcanic field contributes to our growing understanding of the chemical and physical processes that produce voluminous rhyolites and trigger caldera-forming eruptions in the Yellowstone hotspot track and worldwide.

Background

Yellowstone plume

The concept of mantle plumes has been controversial especially in regards to the Yellowstone hotspot track, however seismic tomography (Fig. A1 of Appendix A) and the comprehensive record of volcanism throughout the Snake River Plain provides strong evidence of a deep seated mantle plume (reaching depths of at least 500-600 km; Yuan and Dueker, 2005; Waite et al., 2006; Schmandt et al., 2012) driving volcanism. Although the plume has been imaged beneath Yellowstone, it has evolved in time and space changing shape through interactions with the lithosphere. The presence of the plume coupled with the movement of the North American plate creates a “conveyor-style” of volcanism with traces of plume interaction with the crust left in the form of caldera clusters across 700 km of the Snake River Plain (Morgan, 1972).

Within the first two to three million years of volcanism $\sim 234,000 \text{ km}^3$ of Columbia River and Steens basalt was erupted (Tolan et al., 1989; Carlson and Hart, 1988), with Camp and Ross (2004) advocating that the flood basalt phase was only 1.5 million years in duration. Silicic volcanism contemporaneous with the flood basalts produced approximately 3900 km^3 from volcanic centers High Rock, McDermitt, and Lake Owyhee (Coble and Mahood, 2012). This initial phase of silicic volcanism was dispersed over a $25,000 \text{ km}^2$ region, and this dispersal of volcanism has been associated with initial impingement of a $\sim 400 \text{ km}$ diameter plume head and spreading beneath the lithosphere (Coble and Mahood, 2012). The plume head is believed to have interacted with the Juan de Fuca slab, currently detected with seismic tomography (Liu and Stegman, 2011), an interaction that may have even increased the apparent rate of hotspot movement by the slab angle directing the plume to the surface (Pierce and Morgan, 2009). Interaction of the mantle plume with North American Plate motion, and the Juan

de Fuca slab led to a plume head to tail transition between 14 and 10 Ma (Fig. A2 of Appendix A; Pierce and Morgan, 2009). Volcanism induced by the plume tail was more focused and created individual caldera clusters throughout the eastern SRP.

Oxygen isotopes and hydrothermal alteration

A pervasive low- $\delta^{18}\text{O}$ signature of SRP rhyolites is observed in silicic volcanism throughout the SRP, and constrains the degree of hydrothermal alteration in the high temperature processes considered here. Not only is there an abundance of erupted low $\delta^{18}\text{O}$ ¹ rhyolites in the SRP, but Yellowstone also has a plethora of various hydrothermal features that have become characteristic of Yellowstone National Park. These features highlight the intimate association of meteoric water and magmatism. Specifically, Yellowstone National Park contains an abundance of hydrothermal features located in the 0.6 Ma Yellowstone caldera and Norris-Mammoth corridor, including geysers, fumaroles, mud pots and spring (Smith and Siegel, 2000) and an immense volatile flux (Werner and Brantley, 2000).

Groundwater and meteoric water interacts with country rock, and in regions of an elevated geotherm the water will flow down faults and fractures following the path of least resistance and will exchange oxygen with the surrounding rocks until a state of equilibrium is achieved. Hydrothermal convective cells will carry the water back towards the surface where in the Yellowstone region it is discharged at a rate of 3-4 m³/s (Fournier, 1989; Kharaka and Mariner, 2005) at one of ~10,000 various hydrothermal features in the form of water, vapor, and/or gases. During this process meteoric water, depleted in ¹⁸O, is exchanging with sedimentary or volcanic rocks enriched in ¹⁸O and thus the water is obtaining a higher $\delta^{18}\text{O}$ signature while the crustal rocks are obtaining lower $\delta^{18}\text{O}$ signatures. These hydrothermal features are surface manifestations of the interaction of heat provided by underlying magmatic intrusions, meteoric water, and cracks, fissures and faults. Meteoric water has also been previously shown to interact

¹ $\delta^{18}\text{O}$ values below a mantle value of 5.6 ‰ are considered low, due to either assimilation of rocks or fluids altered by meteoric waters.

with shallow plutonic bodies and caldera complexes (Friedman et al., 1974; Hildreth et al., 1984; Criss and Taylor, 1986; Gilliam and Valley, 1997).

The prevalence of hydrothermal features coupled with the comprehensive record of low $\delta^{18}\text{O}$ volcanism emphasizes the importance of understanding the role of hydrothermal alteration in rhyolite genesis. Oxygen isotopes provide a means of assessing shallow crustal process of caldera “cannibalization”, or remelting of previously erupted rhyolites that have been lowered in ^{18}O due to the interaction with hydrothermal meteoric waters (Taylor, 1986, Bindeman and Valley, 2001).

Defining the Picabo volcanic field

The Yellowstone hotspot track is defined by a spatiotemporal progression of large-volume volcanic fields, and the SRP is considered to be floored by overlapping calderas across its length and width (Fig. 1; Pierce and Morgan, 1992). However, a thick (~750 m to 2 km) veneer of Quaternary basalt blankets the Picabo, TF, and BJ volcanic fields (Doherty et al., 1979; Kuntz et al., 1992; Whitehead, 1992), concealing potential caldera ring fractures. The location of the Picabo volcanic field has been approximated on the basis of the outflow distribution of one prevalent unit, the Tuff of Arbon Valley (TAV), shown on Fig. 2, and isostatic gravity, Bouger, and aeromagnetic anomalies (Pierce and Morgan, 1992). Since volcanism has been previously associated with the TAV, the existence of the Picabo volcanic field has been speculative, because the eruption of the TAV was ~150 km east of where the hypothesized locus of the active hotspot is modeled to have been at ~10.5 Ma (Nash et al., 2006). This “early” eruption of the TAV was crystal-rich, biotite bearing, and possessed a strong Archean upper crustal isotopic signature (Table 1). The TAV is therefore markedly different than crystal poor SRP rhyolites with anhydrous mineralogies and muted upper crustal signatures (Nash et al., 2006; McCurry and Rodgers, 2009; Christiansen and McCurry, 2008). Since the TAV was the only rhyolite previously associated with Picabo, other than those recorded in the airfall record (Anders et al., 2009), the nature, history, and composition of the Picabo eruptive field was poorly constrained and its existence questioned (Nash and Perkins, 2012).

We have now assigned eight lava flows and voluminous ignimbrites of eastern Idaho (Figs. 2, 3) with the Picabo volcanic field based on our new and compiled geochronology and proximity to the hypothesized caldera boundary; these include the TAV, Two-and-a-Half-Mile rhyolite, Tuff of Hawley Springs, Tuff of Little Chokecherry Canyon, West Pocatello rhyolite, Tuff of American Falls, Stevens Peak, and Stevens Peak 2 rhyolites. In addition, there are a number of tuffs and lavas preserved in two deep geothermal boreholes: the 3.2 km Idaho National Laboratory borehole (INEL-1) and ~1.52 km WO-2 borehole (Doherty et al., 1979; McCurry and Rodgers, 2009; Anders et al., 2009; Shervais et al., 2006). The INEL-1 borehole consists of an upper 650 m of basaltic lava interbedded with alluvium and sediments underlain by 84 m of tuffaceous silt and clay and a series of devitrified and propylitically-altered rhyolite tuffs 2.5 km thick (Doherty et al., 1979). Zircons from these rhyolites yielded analytically indistinguishable U-Pb ages of 8.27 ± 0.27 , 8.04 ± 0.10 , and 8.35 ± 0.24 Ma (with increasing stratigraphic depth; McCurry and Rodgers, 2009). Based on thickness and lithology the rhyolites are presumed to be intracaldera fill (McCurry and Rodgers, 2009). We used the borehole INEL-1 to make isotopic and chemical correlations between intracaldera fill and outflow sheets, in order to further confirm the presence of buried calderas. The WO-2 borehole (5 km southeast of INEL-1) similarly intersected 1.15 km of basalt and 1.23 km of rhyolite (Shervais et al., 2006; McCurry and Rodgers, 2009). However, the rhyolite units (dated at 6.12 Ma and 6.38 Ma; Anders et al., 1997) are in the age range of the Blacktail Tuff of the Heise volcanic field (Morgan et al., 1984; Morgan and McIntosh, 2005), and therefore are not likely derived from Picabo magmatism. Since this borehole did not intersect Picabo rhyolites, we use the location of the borehole to help infer the northern caldera wall boundary (Fig. 2).

Local tectonic framework

The SRP is located in the northern Basin and Range province, a region now characterized by east-west extension (Miller et al., 1999; Stockli, 1999). Even prior to extension this region experienced a prolonged history of magmatism and regional folding, from the late Cretaceous through the early Cenozoic (Armstrong, 1978, 1991).

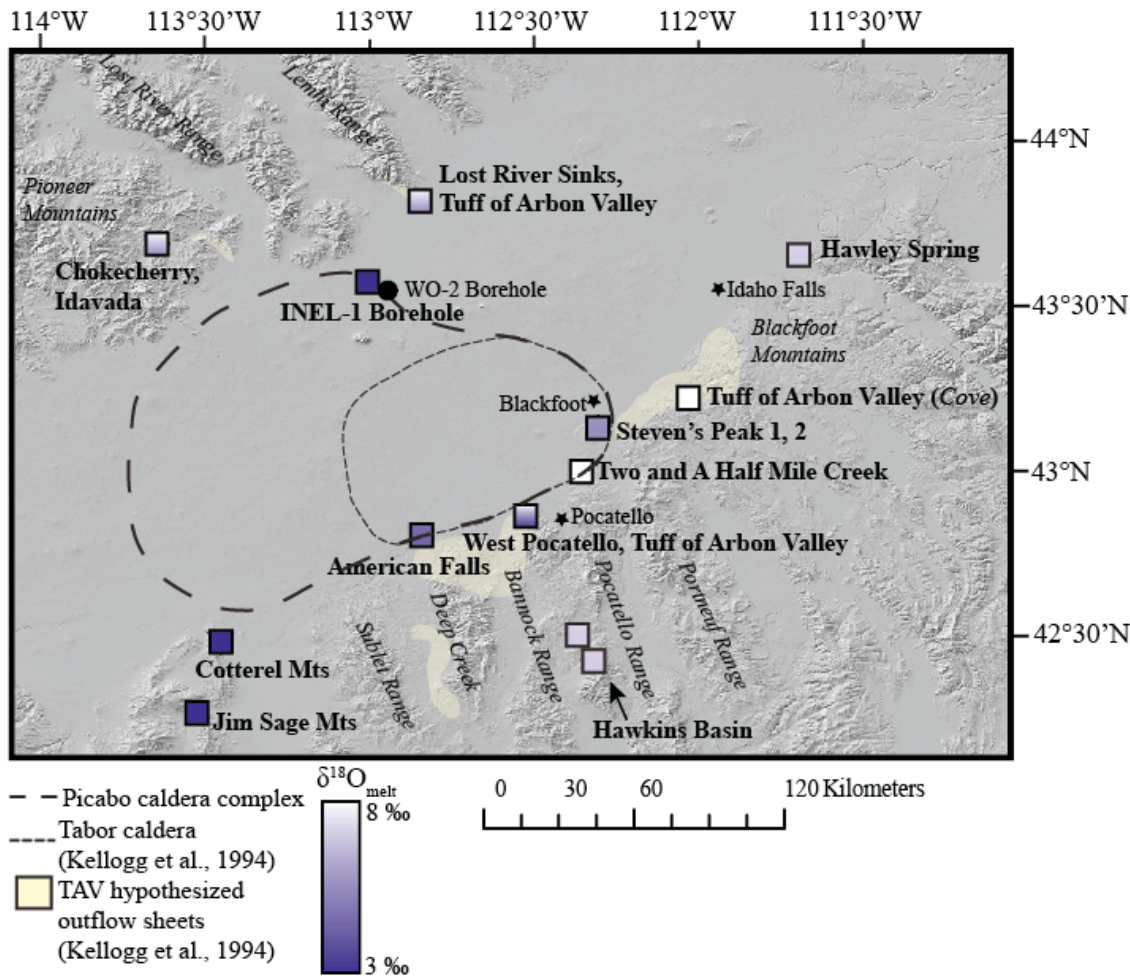


Fig. 2. Map showing the Picabo volcanic field in the SRP and the sampling localities of this study. The approximate boundary of the Tabor caldera, the source of the Tuff of Arbon Valley (TAV), is shown as well as approximate locations of TAV outflow sheets in yellow (Kellogg et al., 1994). The various sampling localities are square symbols with the color of the symbol corresponding to the $\delta^{18}\text{O}_{\text{melt}}$. Where more than one sample is present at a given locality, a gradient is used to depict the range of $\delta^{18}\text{O}_{\text{melt}}$.

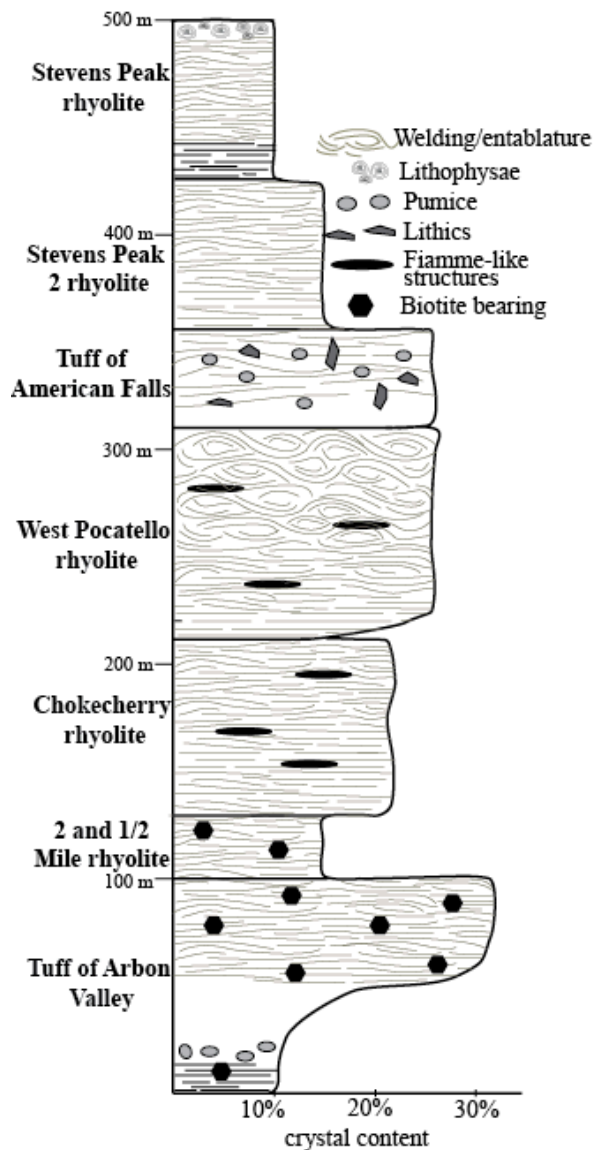


Fig. 3. Generalized stratigraphic section of the Picabo rhyolites analyzed in this study, highlighting the order of eruptions, defining field characteristics, volume percentage of crystals, and approximate thickness. Since the rhyolites are not exposed in the same locations the stratigraphic order is inferred from U-Pb zircon dating, and Ar-Ar and K-Ar ages.

The regional tectonic history modified the crustal architecture prior to hotspot track-related volcanism, affecting the crustal structure and strength (Bonnichsen et al., 2008).

The Idaho batholith is one of four batholiths, including the Sierra Nevada batholith, Coastal Plutonic complex, and Peninsular Ranges batholith, that formed in western North American during the Mesozoic to early Tertiary (Hamilton, 1978;

Hyndman, 1983). The main Idaho and Bitterroot batholith is composed of Cretaceous (~80-70 Ma; Foster et al., 2001) to Eocene, peraluminous two-mica granodiorite to granite plutons emplaced at 10 to 25 km (Hyndman, 1981, 1983; Hyndman and Foster 1988; Toth, 1987) with smaller bodies of quartz diorite and tonalite from the late Cretaceous (Chase et al., 1978; Bickford et al., 1981). During late stages of crystallization the plutons were intruded by basaltic-andesite to dacite dikes and small diorite stocks at shallower levels (Hyndman and Foster, 1988). The emplacement of the Bitterroot metamorphic core complex from ~80 to 53 Ma involved large-scale magma emplacement and partial melting of the middle crust (Armstrong and Ward, 1991), which led to crustal weakening evident in the change to an extensional tectonic regime ~50 Ma (Wernicke, 1992).

Extensional tectonics since ~15-10 Ma (Wells et al. 2000), have formed extensional basins and detachment systems, and exhumed metamorphic core complexes throughout the western U.S. (Coney, 1980; Foster and Fanning, 1997; Foster et al., 2007, 2010). The dominant phase of core complex exposure was between 54-52 Ma (Foster et al., 2001) and continued to 40 Ma (Foster and Raza, 2002). This was a time of regional transtension (Hyndman, 1980; Foster and Fanning, 1997; Foster et al., 2001; Breitsprecher et al., 2003) and 1 to 3 million years after the end of thrusting in the Cordilleran foreland fold and thrust belt at 55 Ma. The Albion-Raft River-Grouse Creek complex is a metamorphic core complex we consider to be of utmost relevance to this study, because it is located on the southern margin of the SRP, in close proximity to the Picabo volcanic field (Fig. 1). This core complex has also been recently shown to be exhumed beginning at 14 Ma and with faulting continuing to after 8.2 Ma (Konstantinou et al., 2012), both predating and occurring coevally with the development of the Picabo volcanic field. Magmatism accompanying extension includes the Challis-Absaroka and Great Basin volcanics (Armstrong and Ward, 1991; Best and Christiansen, 1991; Christiansen and Yeats, 1992; Gans, 1987). Volcanism of the Challis-Absaroka province (Fig. 1) initiated at 51 Ma and continued for ~5 to 10 million years, originally covering over half the state of Idaho with eruptive products (Orr and Orr, 1996). A series of granitoids associated with Eocene Challis volcanism (50-46 Ma; Armstrong et al., 1977; Criss and Fleck, 1987; House et al., 1993) was also emplaced throughout and adjacent to

the Idaho-Bitterroot batholith (Hyndman, 1983; Criss and Fleck, 1987; Toth 1987; Hyndman and Myers, 1988).

Basin and Range extension terminated just north of the current SRP and is thought to have been concentrated south of the SRP during the time of plume-related magmatism (Colgan and Henry, 2009). However, more evidence has surmounted suggesting that extension both predated and was coeval with plume-drive magmatism in the CSRP (Stockli, 1999; Konstantinou et al., 2012), creating conditions for faulting, hydrothermal alteration, and $\delta^{18}\text{O}$ preconditioning of the crust prior to SRP volcanism.

The Picabo volcanic center is located east of the major lithospheric boundary defined by the $^{87}\text{Sr}/^{86}\text{Sr}=0.706$ (Armstrong et al., 1977), representing the transition from accreted Mesozoic-Paleozoic oceanic terranes to Precambrian craton (Farmer and Depaolo, 1983; Fleck et al., 1985). Archean age crustal rocks appear as xenoliths in Neogene to Holocene mafic lavas (Leeman et al., 1985), exposures surrounding the SRP, inherited zircon grains in intrusive rocks, and detrital zircons derived from the Albion Mountains (Link et al., 2005). The Archean aged crustal rocks range in age from 2.5 to >3.5 Ga (Wolff et al., 2005) and range from granulite to mafic compositions.

Rhyolites that define the Picabo volcanic field

The rhyolites that constitute the Picabo volcanic field (see Figs. 2, 3 and Table 1) are found ~100 km apart on the northern and southern margins of the SRP as nonwelded and welded ignimbrites, lava flows, airfall, and reworked deposits (unit descriptions in the Appendix; Table B1 of Appendix B). We consider the TAV and West Pocatello rhyolite to be two major caldera-forming eruptions due to their extensive exposures on the surface and/or in the borehole. The other studied rhyolites are more localized due to limited preservation as a result of the highly dissected terrain, and therefore we are unable to locally trace the outflow-sheets or correlate rhyolites between locations. Due to this limited preservation and up to 2 km thick basaltic cover, we place an emphasis on the geochemical and isotopic evolution of the package of outflow deposits rather than field observations and distribution of the individual ignimbrites.

The TAV consists of a lower poorly-welded crystal-poor (~5%) airfall tuff with pumice, lithics and accretionary lapilli and an upper moderately welded crystal rich (>35%) tuff (Fig. B1 of Appendix B; Kellogg et al., 1994). We examined the type locality of the TAV, the Cove (Figs. 2 and B2), where >100 m of exposed section of both the upper and lower tuff is preserved (Kellogg et al., 1994). Anders et al. (2009) hypothesized that this unit represents two closely spaced eruptions, $^{40}\text{Ar}/^{39}\text{Ar}$ dated at 10.34 ± 0.01 and 10.16 ± 0.01 Ma, but our sampling locality at the Cove exhibited no cooling breaks. The source of the TAV is thought to be the Tabor caldera (Fig. 2; Kellogg et al., 1994), due the thickness and presence of full stratigraphic sections at the southern margin of the plain (McCurry, 2009) and observations that the ignimbrites thin to the south from the proposed caldera boundary. The Two-and-a-Half Mile rhyolite is geochemically and petrographically similar to the TAV, located along the eastern margin of the Tabor caldera. Picabo's subsequent eruptions (Table 1) produced more densely welded, crystal poor (5-25%) rhyolites similar to classic "SRP type" ignimbrites (Branney et al., 2008). For example, the voluminous West Pocatello rhyolite is a densely welded ignimbrite (25 vol. % phenocrysts) that is laterally extensive, capping mountains south of Pocatello (Figs. B3 and B4 of Appendix B).

Nonhotspot-related volcanism in and surrounding the Snake River Plain

The western United States has produced a wide variety of silicic volcanic products, including the subduction-related Great Basin volcanics, the Quaternary SRP bimodal volcanism derived by fractional crystallization (Craters of the Moon), and the topaz rhyolites related to continental extension (Topaz rhyolites). These rhyolites serve as endmember scenarios to compare hotspot-related SRP rhyolites.

Quaternary volcanics and Craters of the Moon volcanics

A large portion of the SRP is covered by Quaternary basalt that ranges in age from 16 Ma to 2 ka, and was erupted largely through vents located along the axial volcanic zone (McCurry et al., 2007). These basalt flows thin towards the northern and southern margins of the plain overlying rhyolites and/or sediment horizons capping

rhyolites. In the eastern SRP there are also a series of post hotspot Quaternary cryptodomes, domes and flows of high silica rhyolite. Many of these rhyolites have been estimated to have undergone ~77% fractional crystallization from a basaltic trachyandesite parent (McCurry et al., 2007) with very limited amounts of assimilation of Archean crust (less than 7%), as is suggested by Sr and Nd isotopes (McCurry et al., 2007). Therefore these magmas were produced by assimilation, recharge, mixing and fractional melting, with fractional crystallization as the dominant process.

Great Basin rhyolites

Great basin dacites and rhyolites are associated with subduction and melting of the mantle wedge. These magmas are calc-alkaline, magnesian, oxidized, wet, cool, Sr and Al rich, and Fe poor (Christiansen and McCurry, 2008; Best and Christiansen, 1991; Best et al., 1989). The main processes contributing to generation of this volcanic suite are magma mixing, crustal assimilation, and polybaric crystal fractionation (Christiansen and McCurry, 2008). The typical mineral assemblage is plagioclase, hornblende, biotite, quartz, magnetite, ilmenite, apatite and zircon (\pm titanite, pyroxene or sanidine). The Great Basin volcanics were emplaced during the Oligocene and were sourced from two large caldera complexes, the Indian Peak and the Central Nevada caldera complex in Utah and Nevada, which are associated with the ignimbrite flare up (Christiansen and McCurry, 2008).

Zircons as robust geochemical recorders

Zircon, zirconium orthosilicate, is a highly resistant accessory mineral found in intermediate to Si-saturated igneous systems that can host a series of geochemically significant trace elements. By analyzing the trace element composition of zircon the magmatic history, as well as the thermal history, of a volcanic system can be reconstructed. The crystallization of zircon is largely dependent on zircon saturation and temperature and to a lesser extent on the chemistry of the magma (Hoskin and Schaltegger, 2003). As with many minerals, crystallization is triggered by a decrease in temperature, which can result from magma cooling or degassing (Peytcheva et al., 2008).

More specifically, growth and dissolution of zircon is a function of the diffusion of zirconium through the melt and saturation or undersaturation of zircon in the melt, emphasizing that the balance between zircon saturation and temperature changes in the melt is fundamental to preserving inherited zircons in late stage eruptions. For example Bindeman et al. (2008) suggests that 40 ppm undersaturation and $\sim 8^\circ\text{C}$ of overheating characterizes the recycling of intracaldera rhyolites and preserves residual zircons.

Although zircons are present in low abundances they impact trace element partitioning and magma chemistry, and are becoming increasingly important due to their chemical resistance and low elemental diffusivities (Cherniak et al., 1997; Cherniak and Watson, 2003). Zircons are particularly useful in that they incorporate a series of trace elements including Hf, rare earth elements (REE), P, U and Th, through simple or coupled substitution (Hoskin and Schaltegger, 2003). The incorporation of U makes zircons ideal for U-Pb dating coupled with O and Hf isotope analyses. Zircons are able to effectively preserve magmatic $\delta^{18}\text{O}$ because there are slow diffusion rates of oxygen through zircon (Valley et al., 1994; Watson and Cherniak, 1997; Peck et al., 2003) and zircons have high closure temperatures. (Watson and Cherniak, 1997; Peck et al., 2003 and Valley, 2003). Due to their refractory nature, zircons are also resistant to secondary hydrothermal alteration of $\delta^{18}\text{O}$ (Gilliam and Valley, 1997) and typically survive melting episodes (Watson, 1996).

Zircon is specifically ideal for $^{176}\text{Hf}/^{177}\text{Hf}$ measurements because zircons concentrate Hf and contain less than 0.0005 $^{176}\text{Lu}/^{177}\text{Hf}$, which can be considered a negligible amount. Therefore zircons effectively preserve the original $^{176}\text{Hf}/^{177}\text{Hf}$ in which they formed. Zircons have also been shown to be Lu-Hf closed systems, and other than the addition of rims the original core $^{176}\text{Hf}/^{177}\text{Hf}$ is typically unaffected by metamorphism (Kinney et al., 2003). Since the systematics of Sm/Nd is very similar to that of Hf/Lu these systems are typically used in conjunction, however Hf has been found to be an even more sensitive indicator because Hf and Lu are found in higher abundances and are more chemically different than Sm and Nd (Valley et al., 2010). Bulk sample $^{176}\text{Hf}/^{177}\text{Hf}$ is a traditional and widely used technique for tracing magma signatures

however the pioneering study by Patchett et al. (1981) has led to the analysis of $^{176}\text{Hf}/^{177}\text{Hf}$ in zircons becoming more widely used.

Methods

76 samples were collected during two-weeks of field work in eastern Idaho on the northern and southern margins of the SRP. Samples were targeted based on previous U-Pb and Ar-Ar dating, which emphasized a preliminary link to the Picabo volcanic center. All samples were analyzed for $\delta^{18}\text{O}$ of major phenocrysts (plagioclase, quartz, and pyroxene) and select samples were analyzed for major and trace elements, Sr and Nd isotopes, and O and Hf isotopes and U-Pb ages of zircon. Basal vitrophyres were analyzed preferentially over tuffs during chemical analyses because the crystal-rich nature facilitated mineral extraction.

Oxygen isotopes

Oxygen isotope ratios of quartz and plagioclase were measured by laser fluorination of 1 to 8 grains (1.1 to 1.8 mg) at the University of Oregon Stable Isotope Laboratory (protocols from Bindeman, 2008). Grains were loaded in a plug and reacted with reagent, BrF_5 , in order to activate and mobilize the oxygen present in each sample. The oxygen was mobilized in the form of O_2 , and traveled through a series of cryogenic traps to remove all reagent and contaminating gases. These traps were held at liquid nitrogen temperatures. Once the gas passed through the traps and a mercury diffusion pump removed final traces of F_2 the remaining O_2 was converted to CO_2 by reacting with a platinum-graphite converter. The CO_2 was then analyzed with a MAT 253 mass spectrometer. Unknowns were analyzed with the Gore Mt. Standard ($\delta^{18}\text{O} = 5.75\text{‰}$), and variability in the four to six standards run during each analytical session were used to correct the $\delta^{18}\text{O}$ of unknowns. Whole-rock Challis intrusives (provided by Richard Gaschnig) were also analyzed for $\delta^{18}\text{O}$ by laser fluorination using a sample chamber designed for highly reactive samples that isolates samples during lasing (see Appendix C for laser fluorination instructions).

Whole rock geochemistry and Sr-Nd isotopes

In preparation for bulk rock XRF and Sr-Nd analyses, whole rock samples were crushed using both a ceramic and corundum mortar and pestle. Major and trace elements were analyzed by X-ray fluorescence (XRF) at the GeoAnalytical Laboratory at Washington State University on a ThermoARL Advant'XP+ sequential X-ray fluorescence spectrometer. Sr and Nd isotope analysis was conducted on a sector 54 Thermal Ionization Mass Spectrometer (TIMS) at the University of New Mexico. For $^{87}\text{Sr}/^{86}\text{Sr}$ analyses the standard NBS987 was used (standard measurements were 0.710294 ± 0.000011 , 0.710271 ± 0.000011) and the blank contained 96 pg of Sr. For $^{143}\text{Nd}/^{144}\text{Nd}$ the standard JNdi-1 was used (standard measurements were 0.512098 ± 0.000013 , 0.512097 ± 0.000009) and the blank contained 120 pg of Nd. Initial $^{87}\text{Sr}/^{86}\text{Sr}$ was calculated using the U-Pb zircon ages and Rb and Sr trace element corrected concentrations. Two additional samples were analyzed for $^{176}\text{Hf}/^{177}\text{Hf}$ and $^{143}\text{Nd}/^{144}\text{Nd}$ at Washington State University on a ThermoFinnigan Neptune MC-ICPMS (see Table F1 of Appendix F).

Zircon U-Pb dating and O isotopes

Individual zircon cores (and a few additional rims) were analyzed for $\delta^{18}\text{O}$ and U-Pb dated using the CAMECA ims 1270 ion microprobe at the University of California, Los Angeles. Zircons were extracted from eight different whole rock samples by dissolving 80 to 180 g of powdered whole rock (sieved remnants of samples through the jawcrusher). Out of the zircons extracted 12 to 20 individual crystals per sample were handpicked, mounted, and polished to approximately 75% of their initial size. The polished zircons were mapped using reflected light, backscatter, and cathode luminescence imaging to reveal zoning patterns in individual zircons (Fig. D1 of Appendix D). For U-Pb dating, a ^{16}O primary beam was used, and the standard AS3 (1099.1 Ma; Paces and Miller, 1993) was used for calibrations of U, Th, and Pb sensitivities. External reproducibility of AS3 $^{206}\text{Pb}/^{238}\text{U}$ ages was 1.6% for the analytical session (1 standard deviation; $n = 52$). Ion intensities were measured over 12 to 15 cycles

with a ~15 nA beam and 25 to 30 μm lateral resolution (depth resolution $<1 \mu\text{m}$). Common-Pb and disequilibrium corrections follow procedures outlined in Schmitt et al. (2003). The mount was repolished to remove all traces of the U-Pb analysis crater, and the same lateral domains used on each zircon were targeted for oxygen isotopic analysis using a Cs^+ beam. Standards KIM-5 ($\delta^{18}\text{O} = 5.09\text{‰}$; Valley, 2003) and AS3 (5.34‰; Trail et al, 2007) were used to correct for instrumental mass fractionation. Analytical reproducibility was estimated from the standard deviation (s.d.) of replicate analyses of KIM-5 and AS3 zircons mounted on the same mount in close spatial proximity to the unknowns. In three analytical sessions, these values were 0.38‰ (n = 54), 0.27‰ (n = 12), 0.14‰ (n = 31), and yielded a weighted average of 0.29. Accuracy was checked through intercalibration of KIM-5 and AS3, and the averages were found to agree within 0.2‰ of their nominal values (see Tables E1. A through C of Appendix E for raw geochronology and $\delta^{18}\text{O}$ data).

Hf isotope analyses of zircon

Zircon spots analyzed on the ion microprobe were later analyzed for $^{176}\text{Hf}/^{177}\text{Hf}$ at the Australian National University, Canberra on a 193 nm excimer laser-based HELEX ablation system with a Neptune multiple-collector ICPMS as described by Eggins et al. (2005). The laser spot sizes were 37 μm and the ablation time was 60 seconds for each analysis (protocols from Woodhead et al., 2004). The standard zircons used were 91500, FC-1, Mud Tank, QGNG, Temora-2, and Plesovice (Slama et al., 2008; Woodhead et al., 2005; Wiedenbeck et al., 1995), and the spot to spot reproducibility was typically better than 0.00004 (2 standard deviations) as shown below (standard: average \pm 2 SD).

91500: 0.282305 \pm 0.00047 (2sd, n=46);

FC-1: 0.282173 \pm 0.00039 (n=10);

Mud Tank: 0.282501 \pm 0.000023 (n=10);

Plesovice: 0.282480 \pm 0.000027 (n=90);

QGNG: 0.281613 \pm 0.000039 (n=10);

Temora-2: 0.282661 \pm 0.000040 (n=25).

The isobaric interference protocols of ^{176}Lu and ^{176}Yb on ^{176}Hf were used for measurement corrections and are described by Woodhead et al. (2004). The Yb and Hf mass biases were determined by directly measuring $^{173}\text{Yb}/^{171}\text{Yb}$ and $^{179}\text{Hf}/^{177}\text{Hf}$ during the run, and the ratio of $^{176}\text{Yb}/^{177}\text{Hf}$ was calculated using the natural $^{176}\text{Yb}/^{173}\text{Yb}$ ratio. By assuming that the mass bias behavior of Lu is analogous to that of Yb, the ratio $^{176}\text{Lu}/^{177}\text{Hf}$ was calculated using $^{175}\text{Lu}/^{176}\text{Lu}=0.02656$ and measured ^{175}Lu . $^{176}\text{Hf}/^{177}\text{Hf}$ data was reduced offline using the software package Iolite (e.g., Paton et al., 2011). Two samples were analyzed for $^{176}\text{Hf}/^{177}\text{Hf}$ at Washington State University on a Finnigan Neptune MC-ICPMS. For these analyses the spot size was 40 μm and the ablation time was 42 to 56 seconds. The data was corrected (correction factor = 1.00015225) using the standard zircon, Plesovice, which was analyzed in the same analytical session as the unknowns (see Table E1.A of Appendix E for raw Hf isotope data).

Results

Geochronology of Picabo ignimbrites and lavas

Our U-Pb dating of zircon cores from six ignimbrites (Table 1) establishes that the duration of volcanism at the Picabo volcanic field is 10.44-6.62 Ma (Fig. E1 of Appendix E). Comparison of the U/Th disequilibria-corrected U-Pb ages with published Ar-Ar and K-Ar ages (Anders et al., 2009; Kellogg et al., 1988, 1994) indicate that the majority of Picabo zircon populations are within uncertainty of the Ar-Ar age for samples where eruption ages are available (TAV, West Pocatello rhyolite and Tuff of American Falls). Notable exceptions are the Tuff of Lost River Sinks and the rhyolite of Stevens Peak, which have significantly older Ar-Ar/K-Ar ages that do not overlap our determined U-Pb ages. The K-Ar age of the Stevens Peak rhyolite was likely inaccurate and an updated Ar-Ar age would be expected to be in agreement with the reported U-Pb age. The Tuff of Lost River Sinks we sampled was likely the Blacktail Creek Tuff and therefore demonstrates agreement with an Ar-Ar age of $6.63\pm 0.03\text{Ma}$ (Morgan and McIntosh, 2005).

We also studied the following newly identified units (Table 1, Table F2 of Appendix F): Idavada biotite-bearing trachydacites ($>9.34\text{ Ma}$; Ar-Ar dated by Anders et

al., 2009), Jim Sage and Cotterel Mountain rhyolites (9.5-8.2 Ma; U-Pb dated by Konstantinou et al., 2012), and the Hawkins Basin volcanics (6.63-6.09 Ma; U-Pb dated by Pope, 2002).

Isotopic and compositional evolution: $\delta^{18}\text{O}$, $^{87}\text{Sr}/^{86}\text{Sr}$, $^{143}\text{Nd}/^{144}\text{Nd}$ and $^{176}\text{Hf}/^{177}\text{Hf}$

In order to assess the petrogenetic mechanisms of assembling large volumes of high silica rhyolites into isotopically distinct supervolcanic magma chambers, $\delta^{18}\text{O}$, $^{87}\text{Sr}/^{86}\text{Sr}_i$, $^{143}\text{Nd}/^{144}\text{Nd}$ and ϵ_{Hf} were used to fingerprint crustal scale processes. Sr and Nd isotopes of whole rock samples and Hf isotopes of zircons provide a proxy for crustal assimilation. During coupled assimilation and fractional crystallization in a magma chamber, continual heating and melting of the surrounding country rock results in a magma body becoming progressively higher in $^{87}\text{Sr}/^{86}\text{Sr}_i$ and lower in $^{143}\text{Nd}/^{144}\text{Nd}$. This process would be facilitated by repeated basalt injections from the Yellowstone plume, thought to be the main driver of crustal anatexis in the SRP.

Studied Picabo samples are largely metaluminous low- to high-silica (74-77% SiO_2) rhyolites (Table F1 of Appendix F) with a range in crystal content of <5 to 35 volume % phenocrysts and liquidus temperatures of 850°C on average (estimated using rhyoliteMELTS) (Tables F3 and F4 and Fig. F1 of Appendix F). The mineral assemblage is dominated by plagioclase, alkali feldspar, clinopyroxene, orthopyroxene, Fe-Ti oxides, \pm quartz, \pm biotite/hornblende, and \pm accessory zircon (Table F3 of Appendix F). Variations in major and trace element whole rock geochemistry between individual rhyolites is largely governed by fractionation of this mineral assemblage (Fig. 4, 5a), and demonstrates a general enrichment in high field strength elements and an A-type granite signature (Fig. 5b; Fig. F2 and F3.A through K of Appendix F). Rhyolites also demonstrate a range in $^{87}\text{Sr}/^{86}\text{Sr}$ from 0.71094 to 0.73443 (Fig. 6a,b). Picabo rhyolites span a $\delta^{18}\text{O}_{\text{melt}}$ range from 8.3 to 2.1‰ and a $\delta^{18}\text{O}_{\text{zircon}}$ range of 6.80 to 0.01‰ (Fig. 7, 8). Major phases of quartz and plagioclase display small ranges in $\delta^{18}\text{O}$ within samples,

suggesting equilibrium at magmatic temperatures and therefore magmatic $\Delta^{18}\text{O}_{\text{melt-plag}}$ and $\Delta^{18}\text{O}_{\text{melt-quartz}}$ (Fig. 7), which were used to calculate $\delta^{18}\text{O}_{\text{melt}}$.²

Volcanism initiated with the normal- $\delta^{18}\text{O}$ ($\delta^{18}\text{O}_{\text{melt}}=7.9\text{‰}$) TAV (10.44 Ma), which exhibits upper crustal characteristics in that it has an extremely low- $\epsilon_{\text{Nd}}(0)$ (-17.7) and $-\epsilon_{\text{Hf}}(0)$ (-28) (Table 1). The TAV possesses large vertical zonation from high-silica rhyolite at the base to low-silica rhyolite at the top. This transition in SiO_2 is coupled with significant zoning in $^{87}\text{Sr}/^{86}\text{Sr}_i$ from 0.72520 in the Sr-poor lower tuff to 0.71488 in the upper tuff, demonstrating dramatic compositional changes within a single eruption (Fig. 6a,b). However, there is $<0.4\text{‰}$ difference in the average $\delta^{18}\text{O}_{\text{melt}}$ between the base and top of the section, which is $<1\text{‰}$ variation observed within the individual samples of the TAV. Similarly, we observed only a small difference in $\epsilon_{\text{Nd}}(0)$ from the base (-17.7) to the top (-18) of the tuff (Fig. 6c), suggesting negligible zoning in $\delta^{18}\text{O}$ and $\epsilon_{\text{Nd}}(0)$ in our analyzed samples. However, Nash et al. (2006) reports an $\epsilon_{\text{Nd}}(0)$ of -19, which suggests the presence of minor zoning in ϵ_{Nd} (~ -17.7 to 19) of the TAV. Both the ~ 9.1 Ma Two-and-a-Half Mile rhyolite and Tuff of Hawley Spring are similarly normal- $\delta^{18}\text{O}$ rhyolites ($\delta^{18}\text{O}_{\text{melt}}=7.7\text{‰}$, 7.1‰ accordingly) with extremely low- $\epsilon_{\text{Nd}}(0)$ (-23, -30.9 accordingly). Due to the similarities in the TAV, Two-and-a-Half-Mile rhyolite, and Tuff of Hawley Spring, we consider the Two-and-a-Half-Mile rhyolite to be a post-TAV lava flow derived from the proposed caldera ring fracture, and the Tuff of Hawley Spring to be a TAV outflow deposit.

On the northern side of the plain the oldest Idavada units (1 through 3) underlying the Tuff of Little Chokecherry Canyon (9.3 Ma), but overlying Eocene Challis volcanics, also have normal $\delta^{18}\text{O}_{\text{melt}}$ values of 7.0‰ , 6.9‰ and 6.6‰ , respectively. We propose that these rhyolites are related to the TAV due to the presence of biotite. The overlying 9.3 Ma Tuff of Little Chokecherry Canyon rhyolite has a lower $\delta^{18}\text{O}_{\text{melt}}$ value of 4.8‰ and a primitive $\epsilon_{\text{Hf}}(0)$ of -7.7.

² The fractionation factor between individual quartz phenocrysts and melt is derived from a linear correlation with temperature (Bindeman and Valley, 2003; Bindeman et al., 2003), while the plagioclase fractionation factor is dependent on a linear correlation with SiO_2 (Valley et al., 2003). In samples where quartz was the dominant phenocryst phase, TAV and Two and a Half Mile rhyolite, a $\Delta(\text{quartz-melt})$ of 0.5‰ was used, corresponding to a temperature of $\sim 800^\circ\text{C}$. For all other samples where plagioclase was the dominant phenocryst, a $\Delta(\text{plagioclase-melt})$ was calculated and was $\sim -0.57\text{‰}$ for 73-77% SiO_2 .

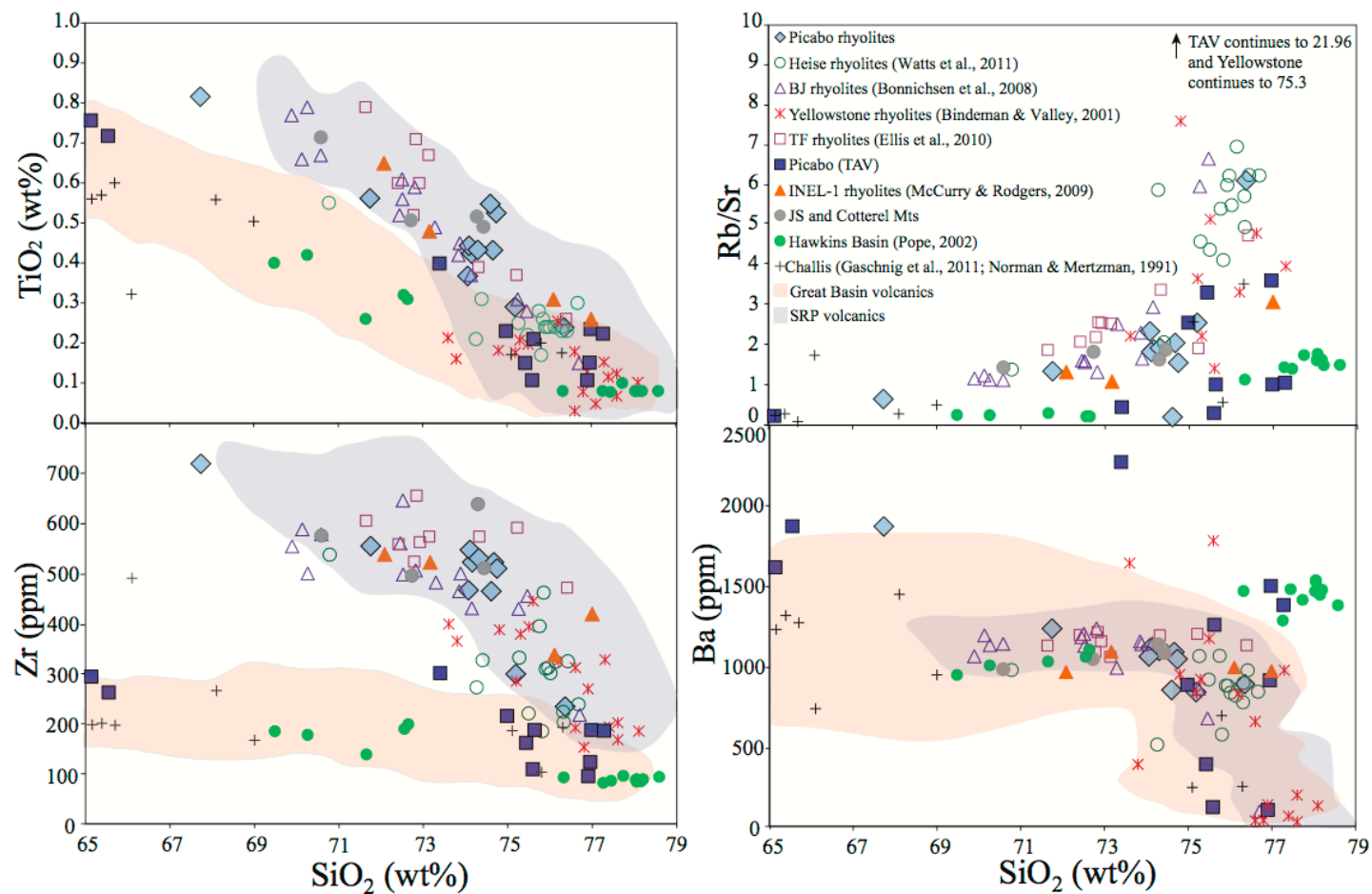


Fig. 4. Whole rock geochemistry plots of Picabo rhyolites, surrounding volcanic center rhyolites: Bruneau-Jarbidge, Twin Falls, Heise and Yellowstone, INEL-1 borehole rhyolites, Jim Sage and Cotterel Mountain rhyolites, Hawkins Basin volcanics, and Challis intrusives. Fields of the Oligocene Great Basin volcanics and range of Snake River Plain compositions are shown for comparison. The Great Basin-Challis volcanics are wet, oxidizing and are derived from subduction processes (Christiansen and McCurry, 2008), which greatly contrasts with the dry and reducing conditions of Snake River Plain rhyolites.

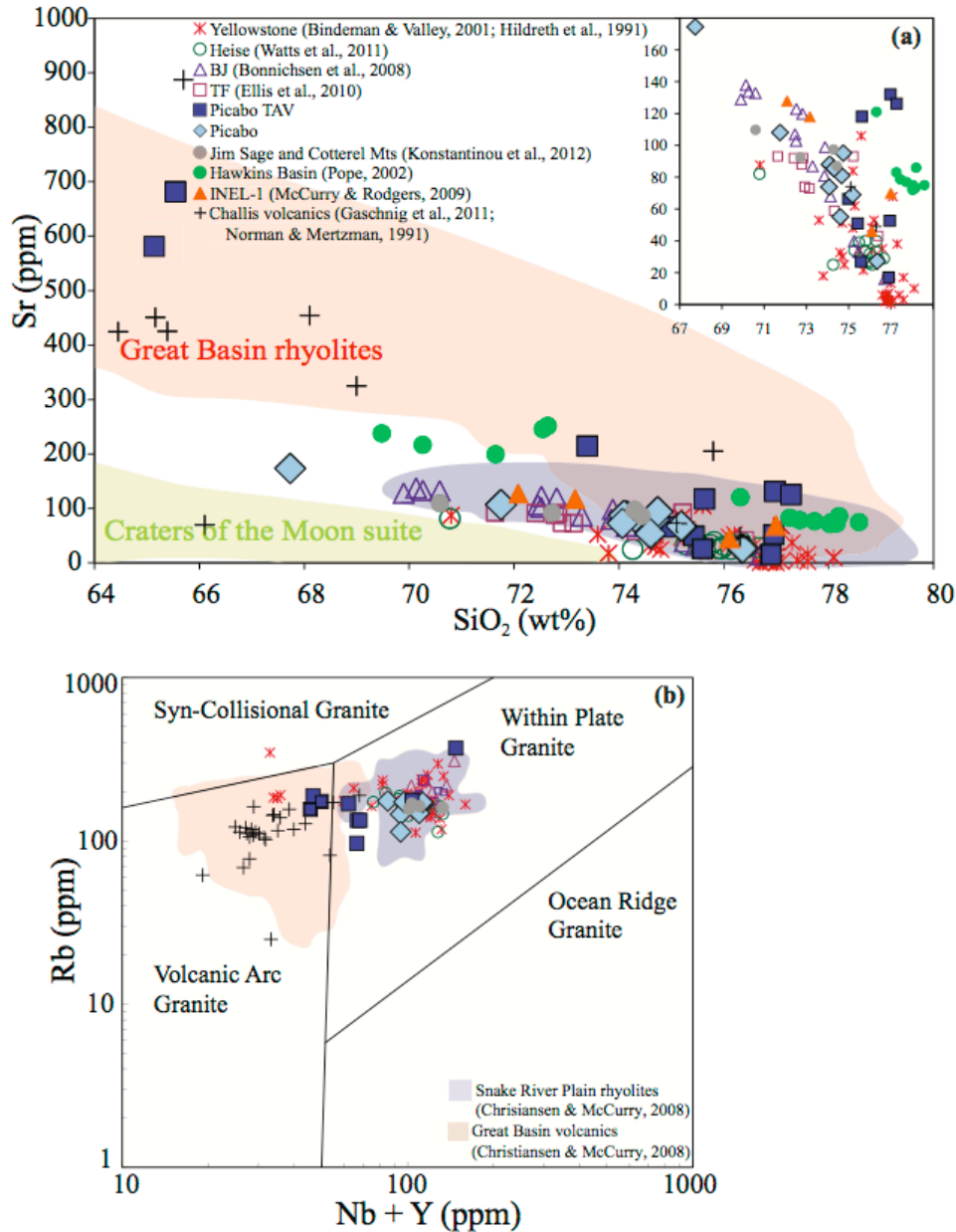


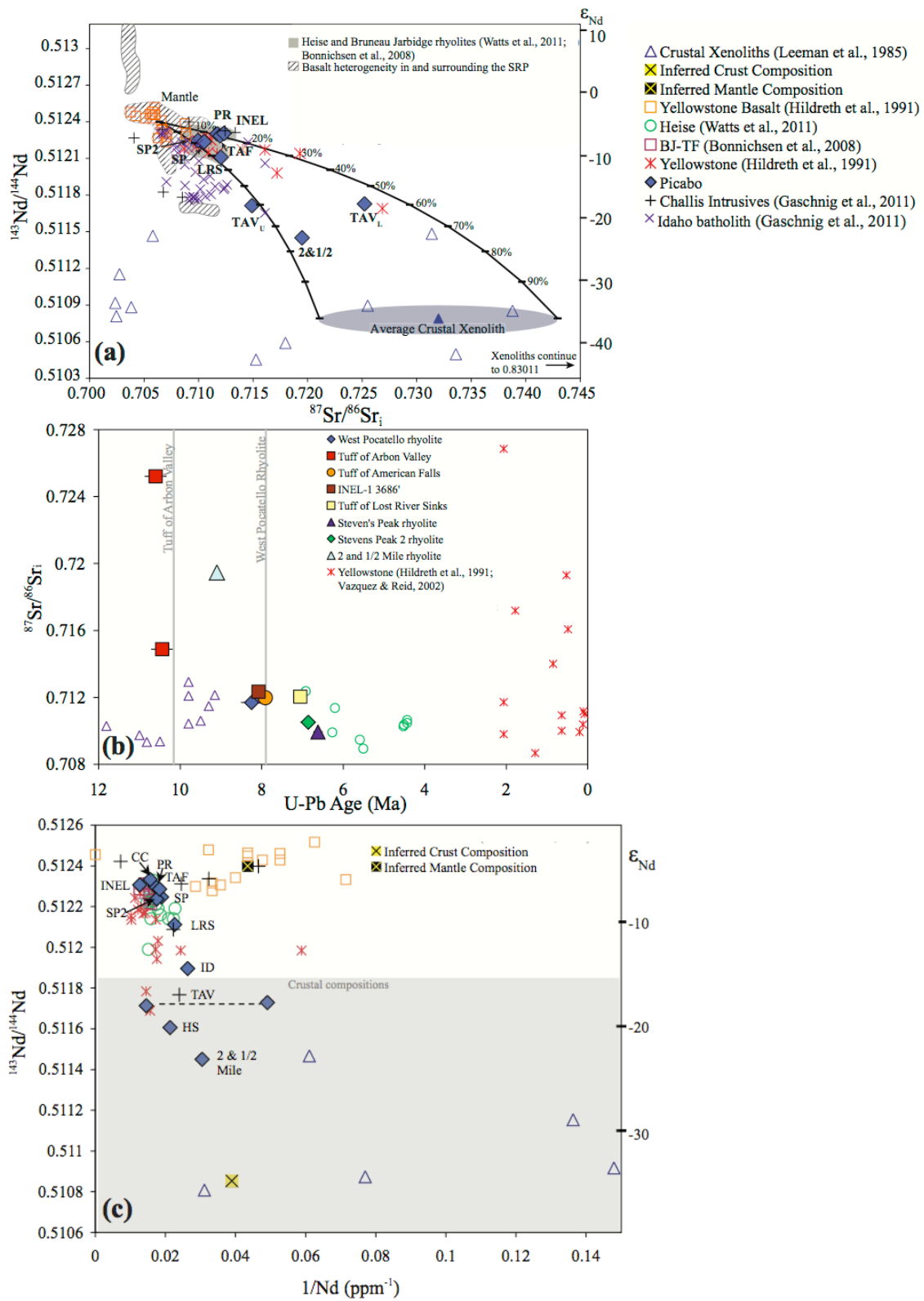
Fig. 5. a. Strontium variation with SiO₂ for Picabo rhyolites, Jim Sage and Cotterel Mt. rhyolites, Hawkins Basin volcanics, and Challis volcanic and intrusives, in comparison to typical Snake River Plain rhyolites and western U.S. volcanics: Quaternary Craters of the Moon volcanic suite and Oligocene Great Basin rhyolites (modified from Christiansen and McCurry, 2008). The Sr-rich nature of the Great Basin volcanics is a result of wet conditions suppressing plagioclase crystallization. **b.** Discriminant diagram of Rb versus Nb+Y for different fields of granite to demonstrate how Snake River Plain rhyolites consistently have a within plate geochemical signature contrasting to the subduction-related signature of the Great Basin volcanics and Challis intrusives and volcanics (discriminant diagram of Pearce et al. (1984); modified from Christiansen and McCurry (2008)).

The sequence of eruptions that followed includes the voluminous 8.25 Ma West Pocatello rhyolite and the 7.91 Ma Tuff of American Falls. The West Pocatello rhyolite possesses the lowest $\delta^{18}\text{O}_{\text{melt}}$ value (3.3‰) and highest $\epsilon_{\text{Nd}}(0)$ (-6.5) and $\epsilon_{\text{Hf}}(0)$ (-5.5) found at the Picabo volcanic field (Fig. 6c). We correlate the West Pocatello rhyolite to a rhyolite of the INEL-1 borehole based on nearly identical $\epsilon_{\text{Nd}}(0)$ (-6.5 and -6.2) and zircon U-Pb ages (8.25 ± 0.26 , 8.27 ± 0.27 , respectively).³ We consider these units to be coeval extracaldera and intracaldera parts of the same voluminous low- $\delta^{18}\text{O}$ eruption. The dacitic Tuff of American Falls is comparable to the West Pocatello rhyolite (within U-Pb dating error) in that it has low- $\delta^{18}\text{O}_{\text{melt}}$ (4.1‰), and primitive $\epsilon_{\text{Nd}}(0)$ (-6.87) and $\epsilon_{\text{Hf}}(0)$ (-5.7) (Figs. 6, 7, 8, 9).

The three youngest Picabo units (7.05-6.62 Ma; Table 1), the Tuff of Lost River Sinks, Stevens Peak rhyolite, and a newly identified unit, Stevens Peak 2, have moderately low and distinct $\delta^{18}\text{O}_{\text{melt}}$ values (5.0‰, 5.9‰, and 4.7‰, respectively), which are higher than the West Pocatello rhyolite (Figs. 7, 8a,b). Each of these three units has

Fig. 6. a. (next page) Binary mixing model of $^{87}\text{Sr}/^{86}\text{Sr}_i$ versus $^{143}\text{Nd}/^{144}\text{Nd}$ of Picabo rhyolites, surrounding eruptive centers (Heise, Yellowstone and Bruneau-Jarbidge), Challis intrusives ($^{87}\text{Sr}/^{86}\text{Sr}_{t=9 \text{ Ma}}$), Idaho batholith ($^{87}\text{Sr}/^{86}\text{Sr}_{t=9 \text{ Ma}}$) and crustal xenoliths. $^{87}\text{Sr}/^{86}\text{Sr}$, $^{143}\text{Nd}/^{144}\text{Nd}$, Sr, and Nd crustal xenolith data from Leeman et al. (1985) was averaged and one standard error in $^{87}\text{Sr}/^{86}\text{Sr}$ was used for the crustal end-members for the binary mixing lines. The average composition of $^{87}\text{Sr}/^{86}\text{Sr}$, $^{143}\text{Nd}/^{144}\text{Nd}$, Sr, and Nd is 0.73199 ± 0.01091 , 0.51079 ± 0.000113 , 347.16, and 18.22 accordingly. The Sr and Nd data of Yellowstone basalts (Hildreth et al., 1991) was averaged and a composition of 0.7063, 0.5124, 300 ppm, and 23 ppm accordingly, was used to represent the primitive SRP end-member. The basalt field demonstrates the variability in basalt throughout the Snake River Plain (includes data from Camp and Hanan, 2008; Hughes and McCurry, 2004; Graham et al., 2009). **b.** $^{87}\text{Sr}/^{86}\text{Sr}$ of Picabo, Heise, and Bruneau-Jarbidge/Twin Falls rhyolites through time. Grey lines are Ar-Ar ages (Anders et al., 2009; Kellogg et al., 1994) of the Tuff of Arbon Valley, Pocatello Rhyolite and Tuff of American Falls. The two points for the Tuff of Arbon Valley are representative of the lower and upper tuff and demonstrate the large vertical isotopic zoning. U-Pb age error bars are one standard error. **c.** $^{143}\text{Nd}/^{144}\text{Nd}$ versus $1/\text{Nd}$ of Picabo and surrounding volcanic centers in comparison to Yellowstone basalts, Archean crustal xenoliths, and Challis intrusives. The gray field represents the approximate range of Archean crust in $^{143}\text{Nd}/^{144}\text{Nd}$ (McCurry and Rodgers, 2009).

³ Although INEL-1 3686⁷ and the West Pocatello rhyolite are isotopically similar there are differences in the whole rock geochemistry (MgO, MnO, CaO, Na₂O and K₂O), which we attribute to intracaldera hydrothermal alteration and re-crystallization inside the INEL-1 samples.



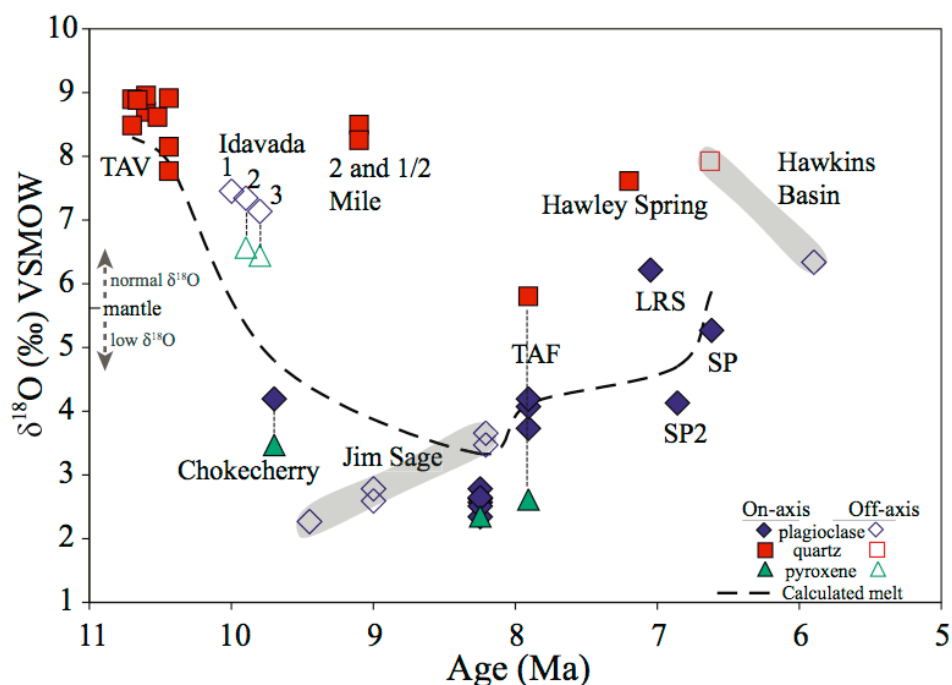


Fig. 7. $\delta^{18}\text{O}$ compositions of major phenocryst phases: quartz, plagioclase and pyroxene, and calculated melt $\delta^{18}\text{O}$ values versus U-Pb, Ar-Ar or K-Ar age. Filled symbols correspond to the main rhyolites used to define the Picabo volcanic field while open symbols represent samples of approximate Picabo age, but whose association with the Picabo volcanic field is poorly constrained, these include: Hawkins Basin (Pope, 2002), Jim Sage (Konstantinou et al., 2012), and Idavada volcanics. The Two-and-a-Half-Mile rhyolite and Hawley Springs rhyolite are plotted against K-Ar dates (Kellogg et al., 1988 and Morgan et al., 1984 respectively). The Idavada volcanics and middle Jim Sage member ages are approximated based on stratigraphic succession. The $\delta^{18}\text{O}_{\text{melt}}$ curve is calculated from the TAV quartz $\delta^{18}\text{O}$ and the West Pocatello rhyolite, Tuff of American Falls, Stevens Peak and Stevens Peak 2 plagioclase $\delta^{18}\text{O}$.

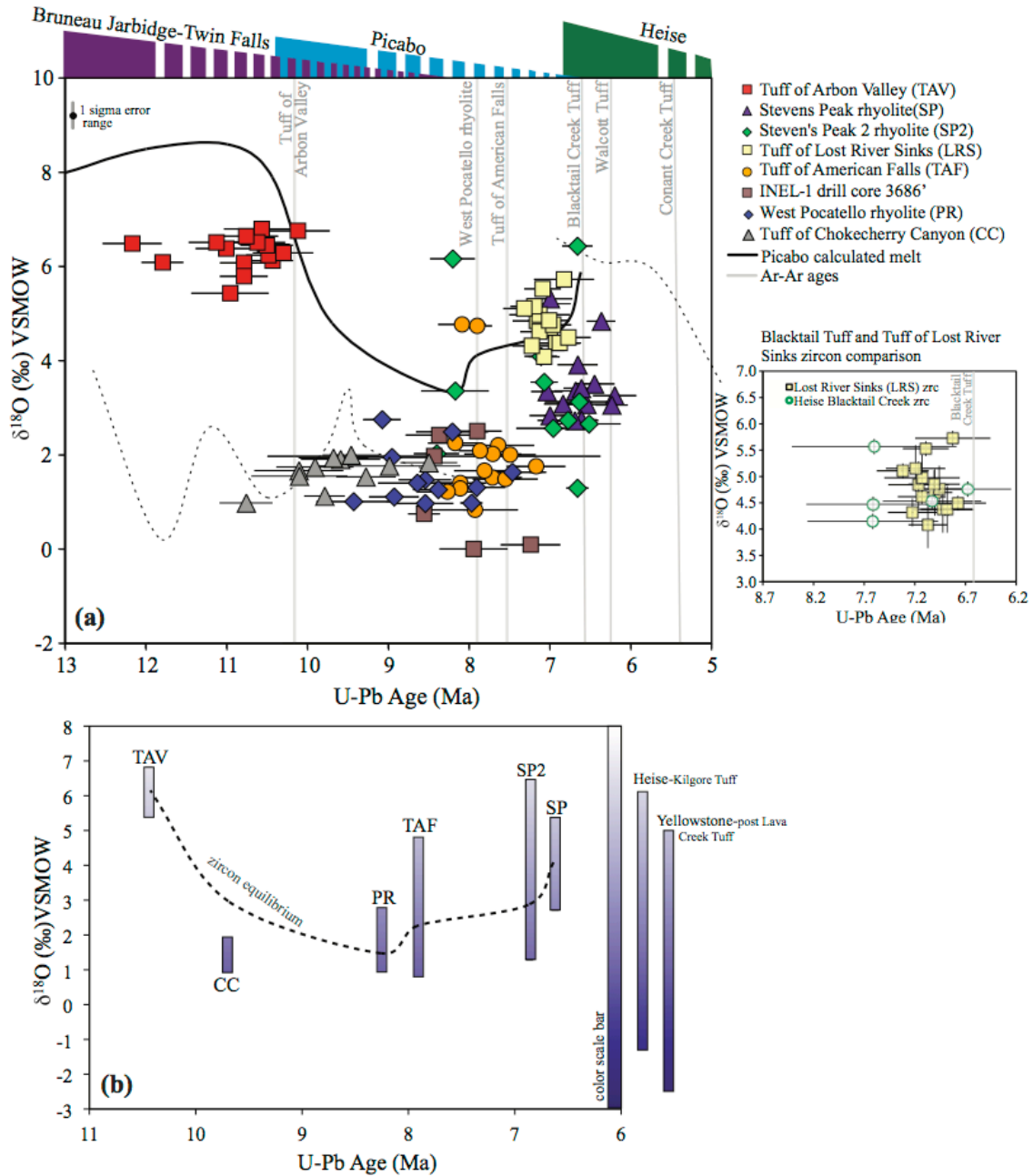
subtle differences in $\delta^{18}\text{O}$ and U-Pb age of zircons, and critical differences in whole rock chemistry, mineralogy and Sr-Nd-Hf isotopic values (Table 1) that provides evidence that these samples represent distinct eruptions (Table A3.1, A3.2). Stevens Peak 2 and Stevens Peak rhyolites have relatively primitive $\epsilon_{\text{Nd}}(0)$ signatures of -7.8 and -7.6, respectively as well as primitive $\epsilon_{\text{Hf}}(0)$ of -9.7 and -9.5, respectively.

We found that the 7.05 Ma Tuff of Lost River Sinks displays striking similarities to the Blacktail Creek Tuff of the younger Heise volcanic center in zircon U-Pb ages, normal- $\delta^{18}\text{O}$ melt and zircon compositions (Fig. 8a), whole rock geochemistry, $^{87}\text{Sr}/^{86}\text{Sr}_i$ (0.00034 difference), and ϵ_{Nd} (0.55 difference). We do observe minor mineral abundance

differences on the order of 5%; however, the phenocryst identities and morphologies are very similar. Due to the isotopic and chemical similarities in the Blacktail Creek Tuff of the Heise volcanic center and the Tuff of Lost River Sinks we consider these units to be related, and therefore we do not associate the Lost River Sinks rhyolite with Picabo volcanism. The Tuff of Lost River Sinks also underlies the Blacktail Creek Tuff at the sampling locality, further supporting that these rhyolites are related.

The thick (~1 km) suite of rhyolitic lavas and a thin capping ignimbrite exposed in the Jim Sage and Cotterel Mountains (Fig. 2) (Konstantinou et al., 2012; Covarrington, 1983; Pierce et al., 1983) were found to have low- $\delta^{18}\text{O}_{\text{melt}}$ values (Jim Sage melt: 2.8 to 4.0‰; Cotterel Mt: 3.0‰). We also note that the trace and major element characteristics of the Jim Sage and Cotterel Mt. volcanics fall within the SRP rhyolite range (Fig. 4). On the southeast side of the proposed Picabo caldera we found the Hawkins Basin rhyolites (6.09-6.63 Ma; Pope, 2002) to have normal $\delta^{18}\text{O}_{\text{melt}}$ values (7.4 to 6.8‰). These rhyolites demonstrated significantly different trends in Zr, Ba, Rb/Sr, and K_2O with SiO_2 than the majority of compiled Picabo, Heise, BJ, TF and Yellowstone samples indicating contrasting fractionation trends (Fig. 4; Fig. F3. a through k of Appendix F). We do not consider the Hawkins Basin volcanics to be related to Picabo volcanism.

Fig. 8. a. (next page) Compilation of $\delta^{18}\text{O}$ compositions and U-Pb ages of individual zircons determined by ion microprobe. Calculated melt values are shown by the solid (Picabo) and dashed (Heise and Bruneau Jarbidge-Twin Falls) lines. Bruneau-Jarbidge/Twin Falls and Heise melt compositions are from Bonnicksen et al. (2008) and Watts et al. (2011), accordingly. Heise Ar-Ar ages are from Morgan and McIntosh (2005) and Picabo Ar-Ar ages (and K-Ar ages) are from Anders et al. (2009) and Kellogg et al. (1988, 1994), and are all shown by solid vertical grey lines. U-Pb age error bars are drawn at 1 standard error, and the $\delta^{18}\text{O}$ error bar reflects the weighted average of the standard errors (0.29 for 97 analyses). The colored bars at the top of the figure signify the approximate eruption duration of the three volcanic centers: Twin Falls, Picabo, and Heise, highlighting the presence of contemporaneous eruptions from different volcanic centers. The $\delta^{18}\text{O}$ melt curve is calculated from the $\delta^{18}\text{O}$ of major phenocrysts, plagioclase and quartz (same as Fig. 7). **b.** Summary of $\delta^{18}\text{O}$ zircon heterogeneity with average U-Pb age. Each bar corresponds to the range of $\delta^{18}\text{O}_{\text{zircon}}$ measured for each sample. The dotted line is the calculated zircon equilibrium $\delta^{18}\text{O}$, 1.8‰ less than the calculated melt $\delta^{18}\text{O}$, emphasizing the presence of disequilibrium zircons in the erupted rhyolites. Ranges of $\delta^{18}\text{O}_{\text{zircon}}$ for Heise and Yellowstone are derived from Watts et al. (2011) and Bindeman et al. (2008), respectively.



Heterogeneous $\delta^{18}\text{O}$ in zircons

High-resolution $\delta^{18}\text{O}$ analyses of zircon cores were compared within individual samples, between samples, and to major phenocryst $\delta^{18}\text{O}$ compositions. As previously mentioned, major phenocrysts (quartz and plagioclase) display homogenous $\delta^{18}\text{O}$ and are in equilibrium with the melt, however the TAV is one exception in that

quartz $\delta^{18}\text{O}$ values were found to be variable up to $\sim 1\text{‰}$ (within an individual TAV sample). Zircons on the other hand display appreciable heterogeneity within individual samples indicating magmatic disequilibrium (Fig. 8b).

As shown in Fig. 8a, the most significant trends in $\delta^{18}\text{O}_{\text{melt}}$ are the lowering from the 8.3‰ TAV to the 3.3‰ West Pocatello rhyolite, with a subtle recovery in $\delta^{18}\text{O}$ in the waning stages. The initial decrease and later recovery in $\delta^{18}\text{O}$ through time also corresponds to an increase in $\delta^{18}\text{O}_{\text{zircon}}$ heterogeneity from $\sim 1\text{‰}$ variation in the TAV up to 5‰ in the lower $\delta^{18}\text{O}$ units. The two xenocrystic zircons that are 1.3 million years older than the main zircon population have the same normal- $\delta^{18}\text{O}_{\text{zirc}}$ composition. The other five Picabo rhyolites have larger $\delta^{18}\text{O}_{\text{zirc}}$ ranges of $1.6\text{--}5.1\text{‰}$ within individual samples, which is well outside the 2σ -reproducibility for a homogeneous zircon standard ($\sim 0.5\text{‰}$). Stevens Peak 2 has the greatest variability in $\delta^{18}\text{O}_{\text{zirc}}$ (1.3 to 6.4‰), with the majority of zircons from 2.4 to 4.4‰ . The two inherited zircons are 1.42 million years older, but are within the same normal $\delta^{18}\text{O}$ range as the primary magmatic zircon population.

Discussion

Defining the existence of unexposed calderas at Picabo

We use the following lines of evidence to support the existence of nested calderas in the Picabo volcanic field, which allows us to interpret and characterize the geochemical evolution of the series of eight ignimbrites and lavas we have associated with Picabo (Table 1):

- 1) Several thick (10^3 's to >100 m) ignimbrite outflow-sheets with great spatial extent at the northern and southern margins of the plain, with ages between 10.4 and 6.6 Ma.
- 2) Geochemical and geochronological correlation of one 8.25 Ma Picabo ignimbrite, the West Pocatello rhyolite, with a 1000 m thick intracaldera fill from the INEL-1 borehole.

- 3) Unique geochemical and isotopic compositions of dated Picabo rhyolites in comparison to contemporaneous eruptions from surrounding volcanic fields to the west (BJ-TF) and east (Heise).

Petrogenetic implications of the geochemical and isotopic data

In order to assess the petrogenesis of large-volume, isotopically-distinct magmas erupted from the Picabo volcanic field of the eastern SRP, we use a suite of stable and radiogenic isotopic data to quantify the proportions of the mantle, upper Archean crust and hydrothermally-altered crust in Picabo rhyolites. Volcanism began at the Picabo volcanic field with the eruption of the normal- $\delta^{18}\text{O}$ TAV, with extremely radiogenic Sr and less radiogenic Nd and Hf isotope ratios (Figs. 6a-c, 9a), supporting derivation from melting of significant portions (~50-60%) of upper continental crust (Fig. 6a; calculation is outlined in Appendix G). This upper crustal contribution to the TAV is ~20-30% greater than is estimated for the majority of other Picabo units, as well as BJ-TF and Heise rhyolites (Fig. 6a,b). Given the highly radiogenic $^{87}\text{Sr}/^{86}\text{Sr}$ of the TAV and the Two-and-a-Half-Mile rhyolite, and the strong contrast in Sr isotopes between the lower and upper TAV, variable proportions as well as variable end-member compositions of isotopically diverse upper Archean crust are required. The presence of biotite also suggests that the TAV had a lower magmatic temperature, and amphibole geobarometry indicates that crystallization occurred at ~300 MPa corresponding to a depth of ~10km (McCurry, 2009). Owing to its extreme crustal signature, we speculate that the TAV was either generated prior to the direct passage of the plume, leading to a lower magma flux, which would enable crustal assimilation to greatly overpower the isotopic composition of SRP basalt and/or that the magma reservoir was isolated (and perhaps partially or fully crystalline) from later Picabo eruptions.

The majority of eruptions following the TAV were low- $\delta^{18}\text{O}$, and all possess more primitive radiogenic isotopic signatures, requiring a greater proportion of lower to mid crust and basaltic magma. Christiansen and McCurry (2008) demonstrated that partial melting of gabbro rather than upper crustal rocks or lower crustal granulite can better reproduce trace element signatures (Rb, Th, U, and Pb) of most SRP rhyolites.

However, the moderately elevated $^{87}\text{Sr}/^{86}\text{Sr}_i$ of all Picabo rhyolites also suggests these magmas sampled a greater portion of Archean crust than surrounding centers (Fig. 6b). The 9.7 Ma Tuff of Little Chokecherry Canyon and 9.44 Ma Jim Sage rhyolite (Konstantinou et al., 2012) are low- $\delta^{18}\text{O}$, and there is evidence for low- $\delta^{18}\text{O}$ zircons of 9.43 ± 0.36 Ma (Fig. 8a) indicating that low- $\delta^{18}\text{O}$ volcanism started between 9.7 and 9.4 Ma, ≤ 1 million years after the eruption of the TAV.

The West Pocatello rhyolite and Tuff of American Falls were sourced from a magma reservoir containing entrained xenocrystic zircons (1035 and 580 Ma) and zircons derived from pure crustal melts with extreme $\epsilon_{\text{Hf}}(0)$ as low as -38 (Fig. 9; Fig. F4 of Appendix F), further corroborating evidence that the later Picabo rhyolites received upper crustal input, although the isotopic signature reflects an overwhelming basaltic component. The later eruptions, Stevens Peak and Stevens Peak 2 rhyolites, were also relatively isotopically primitive, and possess $\delta^{18}\text{O}$ higher than the West Pocatello rhyolite, suggesting that observed isotopic trends are not uniform throughout the eruptive sequence and after the initial lowering of $\delta^{18}\text{O}$ there is recovery to more elevated $\delta^{18}\text{O}$ and lower $\epsilon_{\text{Hf}}(0)$.

Mechanisms of generating low- $\delta^{18}\text{O}$ rhyolites at the Picabo volcanic field

With the discovery of abundant low- $\delta^{18}\text{O}$ rhyolites at Picabo, it now appears that the presence of voluminous low- $\delta^{18}\text{O}$ rhyolites characterizes nearly all caldera complexes in the SRP. Bindeman et al. (2008) and Watts et al. (2011) proposed that the process for generating Yellowstone and Heise low- $\delta^{18}\text{O}$ rhyolites is nested caldera collapse, with repeated caldera formation (at least two nested calderas) creating conditions for hydrothermal alteration and subsequent remelting of buried intracaldera tuffs. This mechanism of bulk cannibalization of erupted pyroclastic rocks leads to the formation of voluminous low- $\delta^{18}\text{O}$ rhyolites at the end of caldera cluster evolution in the eastern SRP. In the CSRP, persistently low- $\delta^{18}\text{O}$ volcanism from the exposed inception of volcanic activity has led Boroughs et al. (2005, 2012) to advocate that the low- $\delta^{18}\text{O}$ signatures in the CSRP predate volcanism and are derived from hydrothermally altered crustal material

from the Idaho batholith. However, the vast majority of the Idaho batholith and Archean crustal rocks in the SRP are high- $\delta^{18}\text{O}$ (King and Valley, 2001; Criss and Fleck, 1987), and thus are an unlikely source of voluminous low- $\delta^{18}\text{O}$ magmatism. The Idaho batholith is also located to the west of the Picabo volcanic field (Fig. 1) and therefore spatially makes an unlikely source.

There is compelling geologic evidence (i.e., spatial distribution) that both the TAV, Chokecherry Canyon rhyolite, and West Pocatello rhyolite were formed as a result of caldera collapse in the SRP. However, whether a caldera formed between the TAV and the Tuff of Little Chokecherry Canyon remains unknown. The presence of older normal- $\delta^{18}\text{O}$ units followed by low- $\delta^{18}\text{O}$ units at Picabo seemingly supports the genesis of low- $\delta^{18}\text{O}$ magmas at Picabo by the nested caldera model proposed for Heise and Yellowstone. In this scenario, hydrothermally altered intracaldera TAV is the source of later low- $\delta^{18}\text{O}$ melts. However, the “upper crustal” geochemical characteristics of the TAV would require at least 50% dilution by SRP basalt to justify the more primitive radiogenic isotopic signature of later erupted, low- $\delta^{18}\text{O}$ units (Fig. 6a). In addition, the lack of intermediate $\delta^{18}\text{O}$ values between the TAV and Chokecherry Canyon-West Pocatello rhyolites presents mass balance challenges because it is unknown whether intracaldera TAV reached sufficient depths to be remelted at the time of the first low- $\delta^{18}\text{O}$ magma genesis. While this is not inconceivable, an alternative explanation is that the voluminous 9-7 Ma low- $\delta^{18}\text{O}$ volcanism at the Picabo volcanic field shares some similarities with the “persistent” low- $\delta^{18}\text{O}$ volcanism at the BJ-TF centers to the west (Fig. 8a) (Cathey and Nash, 2009; Seligman, 2012).

Without definitive evidence that caldera clusters existed during eruption of the first low- $\delta^{18}\text{O}$ rhyolite at Picabo, we search for alternative source rocks (other than buried and hydrothermally altered TAV) to be melted, and mechanisms (other than caldera collapse) to expedite hydrothermal alteration and melting. The possible source rocks include: 1) “Picabo” age intracaldera tuffs of 10.4-9.0 Ma that have not been identified near the surface, or in the INEL-1 borehole; 2) far-traveled ignimbrite units derived from the west, TF in particular, which preceded or were coeval with early Picabo volcanism; and 3) Eocene Challis volcanics.

These potential source rocks could be hydrothermally altered by low- $\delta^{18}\text{O}$ meteoric waters syneruption, during uplift and SRP plume-crust interaction, or during TAV caldera collapse. We include Challis as a potential source because Challis intrusives

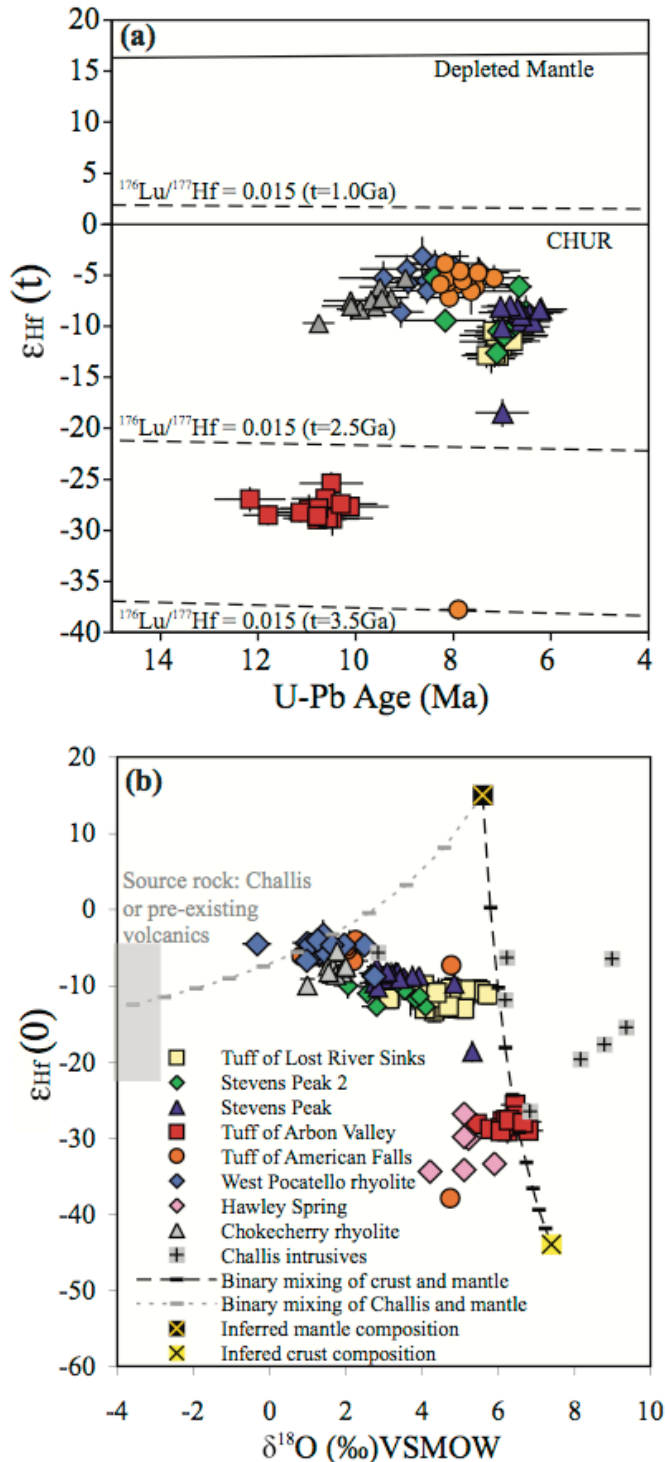


Fig. 9. a. $\epsilon_{\text{Hf}}(t)$ versus U-Pb age of individual zircons from Picabo rhyolites with evolution lines of depleted mantle, CHUR (chondrite uniform reservoir) and average continental crust composition at various ages. One-sigma error bars are shown for the age and two-sigma error bars for $\epsilon_{\text{Hf}}(0)$. **b.** $\epsilon_{\text{Hf}}(0)$ versus $\delta^{18}\text{O}$ of individual zircons from Picabo rhyolites. The inferred crust composition is the average $\delta^{18}\text{O}$ of SRP xenoliths from Watts et al. (2010) and the average ϵ_{Hf} of Archean crust worldwide (Vervoort and Patchett, 1996). The Challis field is approximated from whole rock $\delta^{18}\text{O}$ of Challis volcanics (Criss et al. 1991) and whole rock ϵ_{Hf} of Challis intrusives (Gaschnig et al. 2011). The low $\delta^{18}\text{O}$ Challis deposits range from 1.6 to -8.8‰, and although these values are not representative of the entire Challis deposit they serve as an end-member for low $\delta^{18}\text{O}$ Challis volcanics. The dotted lines are individual binary mixing models between the Challis and mantle (grey-dotted) and Archean crust and mantle (black-dashed) with individual tick marks corresponding to 10% increments.

and volcanics: 1) are regionally abundant and exposed proximal to the Picabo volcanic field (Fig. 1); 2) are already low- $\delta^{18}\text{O}$ in certain regions of Idaho due to syneruptive water-rock interaction (locally down to -8.8‰ ; Criss et al., 1991), however hydrothermal alteration is heterogeneous and sporadic; and 3) possess more primitive isotopic compositions (-3.5 to $-19.7 \epsilon_{\text{Hf}}(0)$; Gaschnig et al., 2011) than the Archean crust or TAV (Fig. 6a, 9b). Thus, melting of the Challis volcanics inside of the collapsed TAV block (Fig. 10) would generate low- $\delta^{18}\text{O}$ Picabo volcanics without greatly impacting the Sr-Nd-Hf isotopic signature.

The proposed source rocks have the potential to constitute stratigraphically lower portions of the collapsed block and therefore would be closer to the heat source than intracaldera TAV for melting and generation of the first low- $\delta^{18}\text{O}$ magmas <1 million years after the TAV eruption. In this scenario, the purpose of the TAV caldera collapse is to create conditions for burial, further hydrothermal alteration, and melting without contributing mass. It is also likely that the 10.4 Ma TAV plutonic residuum was already fully crystalline by the time of voluminous low- $\delta^{18}\text{O}$ Picabo volcanism at ~ 9.7 Ma, and could therefore be crosscut by the invading basalts to melt proposed sources in the intracaldera block.

An additional mechanism (other than caldera collapse) that would facilitate hydrothermal alteration and the juxtaposition of the proposed source rocks and heat source (required for melting) is Basin and Range extension (Fig. 10). We suggest that pre-modification of the crust due to Basin and Range extension, as well as SRP-plume driven extension would have allowed for hydrothermal alteration prior to caldera collapse. During Basin and Range extension, the formation of normal and detachment faults would down-drop the altered source units and provide additional heating and fracturing necessary to further elevate water-rock ratios, facilitating hydrothermal alteration in the upper crust.

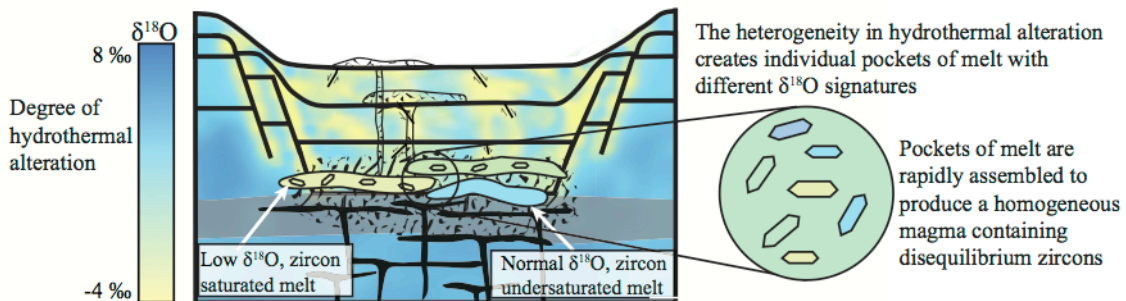
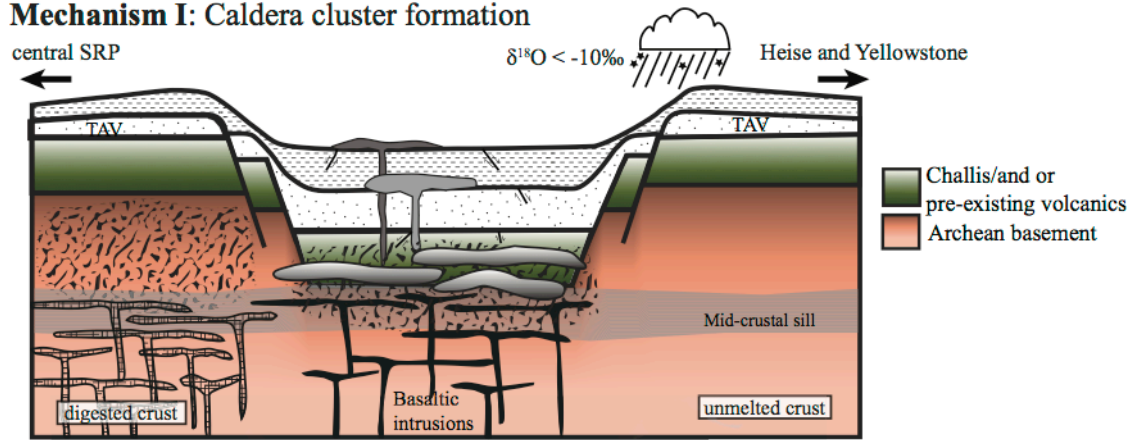
We advocate that the exhumation of metamorphic core complexes is one mechanism by which Basin and Range extension can facilitate hydrothermal alteration and production of low- $\delta^{18}\text{O}$ rhyolites. For example, exhumation of metamorphic core complexes has been specifically proposed for the Jim Sage Mts (Konstantinou et al., 2012), on the southern margin of the SRP between the Pocatello and TF volcanic fields

(Fig. 1). Konstantinou (2011) describes the Jim Sage volcanics as being erupted from small eruptive centers along the Raft River Detachment-Albion Fault system, which exhumed the local metamorphic core complex, and proposed that associated faulting could have facilitated deep magma migration from the SRP. Konstantinou (2011) also allows for the possibility that the Jim Sage volcanics are associated with SRP volcanism. Although Basin and Range extension coeval with Picabo magmatism is not required to produce the rhyolites observed (e.g., caldera collapse on Fig. 10 is sufficient), it would further facilitate the process and demonstrate the intertwined history of local tectonics and plume-driven magmatism in the SRP.

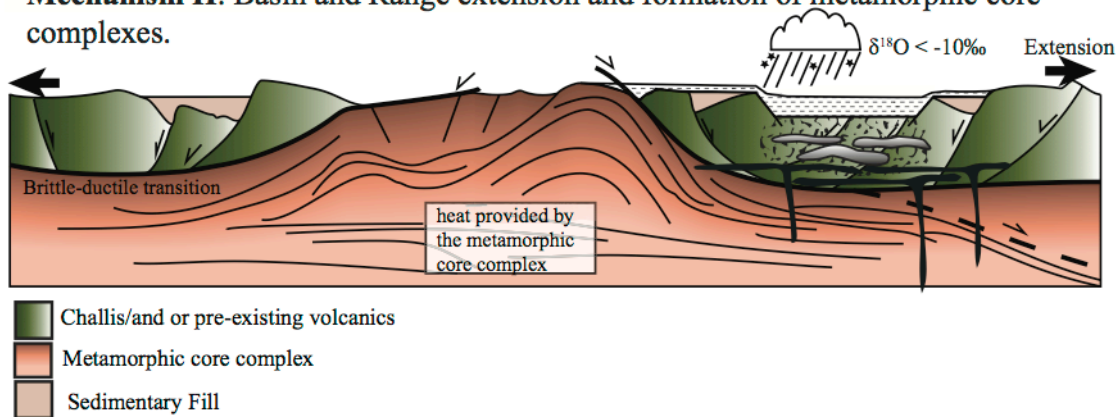
This model which we propose for “pre-modification” of the crust with respect to $\delta^{18}\text{O}$ applies to the CSRP (BJ-TF) and Picabo center where an overabundance of low $\delta^{18}\text{O}$ rhyolites are observed. However, caldera collapse is still an important pre-requisite to bring “pre-altered” source rocks closer to underlying heat sources, thus requiring the magma storage be shallow (Almeev et al., 2012). Our model has critical differences from the model proposed by Leeman et al. (2008), because we suggest that it is unlikely that: 1) water will travel up the temperature gradient; 2) water will remain isotopically

Fig. 10. (next page) Summary of the petrogenetic mechanisms proposed for generating low- $\delta^{18}\text{O}$ rhyolites at the Picabo volcanic field. The general features applicable to both mechanisms are a mid-crustal sill developing near the brittle-ductile transition of the crust, individual pockets of rhyolite melt forming from remelting gabbro with heat input from the pervasive basalt supply, alteration by low- $\delta^{18}\text{O}$ meteoric water, and generation of variable $\delta^{18}\text{O}$ signatures. Mechanism I demonstrates how repeated caldera formation results in the formation of a caldera cluster, and the progressive lowering of intracaldera rhyolite, bringing these units closer to basaltic intrusions (Bindeman and Valley, 2001; Watts et al., 2011). Hydrothermal alteration of buried deposits is shown by the blue to yellow gradient, emphasizing the heterogeneity of alteration we propose to be present. We also illustrate smaller lava flows between caldera forming eruptions that sample pockets of rhyolite melt with variable $\delta^{18}\text{O}$ compositions. As the North American plate migrates over the mantle plume, the crust, modified by basaltic intrusions, is progressively digested. Mechanism II demonstrates one example of how extensional tectonics of the Basin and Range can modify the crust and facilitate hydrothermal alteration. The exhumation of a metamorphic core complex is shown (modified from Rey et al., 2009), which facilitates hydrothermal alteration by extensive faulting coupled with the heat input from the intruded igneous and metamorphic rocks. The exhumation of this core complex causes a pre-modification of the crust with respect to $\delta^{18}\text{O}$.

Mechanism I: Caldera cluster formation



Mechanism II: Basin and Range extension and formation of metamorphic core complexes.



unaffected on the descent to mid-crustal depths of 500-700°C at 15 km; and 3) such great depths will have the necessary porosities for effective water-rock interaction. We postulate that in order to imprint significant low- $\delta^{18}\text{O}$ signatures on tens of thousands of cubic kilometers of source rocks (thousands of which are required to be melted to generate low- $\delta^{18}\text{O}$ SRP magmas), a fundamental two-stage process is required. First, shallow interaction between heated meteoric waters and source rocks with large porosities at high water-rock ratios; second, melting of these source rocks at depth following burial. A plume-derived heat source can induce shallow hydrothermal

alteration and melting, which can be further facilitated by the heat supplied during exhumation of metamorphic core complexes. Therefore rift burial during Basin and Range extension and burial during caldera collapse can create conditions suitable for remelting of the surface-altered rocks.⁴

Significance of zircon $\delta^{18}\text{O}$ diversity and Hf homogeneity in voluminous tuffs

The zircon heterogeneity, which we now observe at Picabo, suggests that isolated pockets of melt with unique $\delta^{18}\text{O}$ signatures were derived from variably altered volcanic predecessors and rapidly assembled prior to eruption. These individual pockets of melt were of variable temperature and zircon saturation, and therefore not all pockets of melt crystallized zircons. In order to preserve the observed O isotope diversity on a cm-scale these pockets of melt had to be thoroughly mixed prior to eruption. By retaining heterogeneous $\delta^{18}\text{O}$ signatures, many of the zircons are erupted in disequilibrium with the host melt. The lack of inherited zircons also implies that zircons dissolved and re-precipitated from these pockets of diverse $\delta^{18}\text{O}$ melt. In contrast to the heterogeneous zircon $\delta^{18}\text{O}$, we observe homogeneous zircon Hf isotope signatures for all analyzed Picabo rhyolites. The presence of zircons diverse in $\delta^{18}\text{O}$ and homogeneous in ϵ_{Hf} (Fig. 9b) suggests that the zircons crystallized after remelting variably hydrothermally-altered tuffs (affecting $\delta^{18}\text{O}$, but not Hf), which themselves were already homogenized in whole rock ϵ_{Hf} isotopic composition during earlier magmatism and convection. The occasional low- $\epsilon_{\text{Hf}}(0)$ zircon xenocrysts indicate that Archean crust was added to the low- $\delta^{18}\text{O}$ magma chambers as well, but in small proportions (Fig. 9a).

These diverse zircons and their host batches were assembled in a single reservoir and erupted without delay to prevent annealing by diffusion and solution-reprecipitation.

⁴ The model presented supports a detachment fault model creating an asymmetric geometry of exhumed metamorphic core complexes, which relies on a simple shear mode of extension as opposed to a pure shear model involving gneiss doming (Gans and Konstantinou). However the interaction of the plume with existing detachment (or low angle) faults has the potential to interact with the faults present and later create a more gneiss doming model as a result of the buoyancy of the plume. The presence of metamorphic core complexes existing throughout the western United States (Fig. 1) suggests inherent qualities of the regional continental crust. The variables that affect extensional settings include the thermal state of the lithosphere, crustal thickness, mantle dynamics, crustal anisotropy, amount and rate of extension, and the presence of magmatism (Friedmann and Burbank, 1995).

We speculate that the process of rapid coalescence of individual (diverse in $\delta^{18}\text{O}$) shallow magma batches may be the trigger for the caldera-forming eruptions, and could have occurred in response to an increased supply of basalt at the base of the magma chamber (e.g. Simakin and Bindeman, 2012). This increased supply of basalt could result in catastrophic magma assembly by merging individual magma batches, density destabilization of the caldera roof, and a caldera-forming eruption of low- $\delta^{18}\text{O}$ tuffs with diverse zircons.

Origin of silicic volcanism at the Picabo volcanic field and in the SRP

With the discovery of new rhyolites with diverse $\delta^{18}\text{O}$ compositions at the Picabo volcanic field it is now evident that nearly all SRP caldera clusters for the past ~16 Ma have produced voluminous low- $\delta^{18}\text{O}$ rhyolites, either at the end of caldera cluster evolution (Yellowstone, Heise), or throughout the eruptive sequence (CSRP). Picabo shares key similarities with Heise and Yellowstone, having produced initially normal- $\delta^{18}\text{O}$ magmas followed by voluminous low- $\delta^{18}\text{O}$ rhyolites in the later stages of caldera complex evolution. Like the voluminous low- $\delta^{18}\text{O}$ Kilgore Tuff of the Heise volcanic field (Watts et al., 2011), Picabo's low- $\delta^{18}\text{O}$ rhyolites (West Pocatello rhyolite, Tuff of Little Chokecherry Canyon, Tuff of American Falls, Stevens Peak, and Stevens Peak 2) possess diverse zircon populations. This transition from normal- to voluminous low- $\delta^{18}\text{O}$ rhyolites happens at all three centers after a ~2 Ma time delay from the onset of the first voluminous normal- $\delta^{18}\text{O}$ rhyolitic tuff eruption. At Picabo, <1 Ma separates eruption of the normal- $\delta^{18}\text{O}$ TAV from the low- $\delta^{18}\text{O}$ Tuff of Chokecherry Canyon. At Heise and Yellowstone, it appears that two to three nested caldera collapses are required to produce ~1000 km³ of low- $\delta^{18}\text{O}$ rhyolites, therefore the predominance of low- $\delta^{18}\text{O}$ rhyolites at Picabo suggests that it shares similarities with the western eruptive centers, BJ-TF, whose exposed sections display overabundant low- $\delta^{18}\text{O}$ rhyolites with diverse zircons throughout the eruptive sequence. As we discussed above, these similarities suggest that a pre-modification of the crust was made possible in Basin and Range rift zones, and accelerated the process of low- $\delta^{18}\text{O}$ magma genesis at Picabo and volcanic fields to the west.

Another important result from our study is that there is significant spatiotemporal overlap between volcanism at TF-BJ, Picabo and Heise, indicating that eruptions at these various volcanic fields are contemporaneous during the transition between eruptive centers (Fig. 8a). However, the waning cycle of low- $\delta^{18}\text{O}$ volcanism in the BJ-TF centers, represented mostly by lavas (10.5-8 Ma), display universally low- $\delta^{18}\text{O}$ signatures (Bonnichsen et al., 2008; Boroughs et al., 2005; Ellis et al., 2010; Seligman, 2012), while the contemporaneous and newly developing Picabo center started with large-volume normal- $\delta^{18}\text{O}$ ignimbrite eruptions at 10.44 Ma. Likewise, the latest stages of volcanism at Picabo from 8.25-6.62 Ma were characterized by low- $\delta^{18}\text{O}$ values and diverse zircons, while the contemporaneous eruptions at Heise began with the normal- $\delta^{18}\text{O}$ Blacktail Creek Tuff with more homogenous zircons (newly determined; Fig. 8a. inset). Late-stage low- $\delta^{18}\text{O}$ Picabo eruptions reached a maximum $\delta^{18}\text{O}_{\text{melt}}$ of 5.9‰, a close yet distinguishable $\delta^{18}\text{O}$ difference between the contemporaneous Heise and Picabo rhyolites.

Our new zircon U-Pb geochronology data also reveal a decreasing lifespan of each caldera complex across the Yellowstone hotspot track. Large-volume ignimbrite volcanism in the BJ-TF complexes spans ~12.8-10.5 Ma, followed by lavas as young as 6Ma (Bonnichsen et al., 2008), thus BJ-TF has a lifespan of ~4-6 million years. Picabo volcanism spans ~3.8 million years (this study), Heise spans ~2.6 million years (Watts et al., 2011) and Yellowstone spans ~2 million years (Christiansen, 2001). Coupled with the decreasing lifespan is a decrease in the number of caldera-forming eruptions: BJ-TF (abundant, ~10-12), Picabo (~3-6), Heise (4) and Yellowstone (3). We interpret these spatiotemporal trends in eruption frequency and volcanism duration as reflecting a combination of the following: increasing thickness of the lithosphere from 40 km beneath TF to 47km beneath Yellowstone (Yuan et al., 2010), and/or decreasing potency of the Yellowstone plume (Bonnichsen et al., 2008).

Conclusions

The Picabo eruptive center produced a series of voluminous rhyolites from 10.4-6.6 Ma that become progressively lower in magmatic $\delta^{18}\text{O}$ and more heterogeneous in

zircon $\delta^{18}\text{O}$ through the eruptive sequence. These trends are similar to what has been observed at Heise and Yellowstone, underscoring the importance of recycling hydrothermally altered intracaldera rhyolites at the end of caldera cluster evolution. In addition, similarities to BJ-TF suggest that coeval rifting, extension, and metamorphic core complex formation may further promote hydrothermal alteration and production of low- $\delta^{18}\text{O}$ source rocks. It now appears that at Picabo, Heise, and Yellowstone the eruption of $\sim 1000 \text{ km}^3$ of low- $\delta^{18}\text{O}$ rhyolites with diverse zircon crystal cargoes heralds the end of caldera cluster evolution, and after volcanism initiates at a new location with normal $\delta^{18}\text{O}$ values and homogeneous zircon populations. The heterogeneous zircon population in late-stage low- $\delta^{18}\text{O}$ magmas supports our petrogenetic model that previously erupted tuffs and their subvolcanic roots were variably altered and lowered in $\delta^{18}\text{O}$, and subsequently re-melted or “cannibalized” at the crustal-scale, causing the silicic crust to become more refractory and mafic. Our work also demonstrates the importance of large-scale batch assembly occurring on timescales more rapid than O isotope re-equilibration of zircons, but long enough to chemically homogenize the melt and $\delta^{18}\text{O}$ composition of phenocrysts. Picabo, is the third youngest volcanic field of the Yellowstone hotspot track, and the isotopic evolution of the suite of rhyolites we have studied contributes to our growing understanding of past and future magmatic activity at Yellowstone.

CHAPTER II

CHEMICAL AND VOLATILE CONSTRAINTS ON THE GENESIS AND STORAGE OF RHYOLITE IN THE SNAKE RIVER PLAIN: INSIGHTS FROM QUARTZ-HOSTED RHYOLITIC MELT INCLUSIONS IN THE TUFF OF ARBON VALLEY

Summary

The Yellowstone hotspot track has produced an abundance of silicic products over the course of a series of volcanic cycles that characterize the Snake River Plain (SRP). We report analyses of quartz-hosted rhyolitic melt inclusions from pumice clasts in the Tuff of Arbon Valley (TAV). These data provide the first reliable volatile constraints on the genesis of the rare, lower temperature rhyolites in the SRP. The TAV, a voluminous, caldera-forming rhyolite, represents the commencement of volcanism (10.44 Ma) at the Picabo volcanic field of the Yellowstone hotspot track. Distinct features of our data include high F concentrations up to 1.38 wt.%, homogenous Cl concentrations of on average 0.08 wt.%, H₂O contents ranging from 2.3 to 6.4 wt.%, CO₂ contents ranging from 79 to 410 ppm, and enrichment of incompatible elements compared to subsequent Picabo rhyolite whole rock data, Bishop Tuff melt inclusions, and Mesa Falls melt inclusions. We couple melt inclusion data with Ti measurements and cathodoluminescence (CL) imaging of the host quartz phenocrysts to further elucidate the petrogenetic evolution of the TAV. Specifically, we observe a variety of CL zoning patterns, the most critical being the presence of bright CL cores (higher Ti), occasional bright CL rims (higher Ti) and truncated oscillatory zoning. With this new volatile and chemical data coupled with Sr-Nd-Hf-O isotopic constraints we will investigate how the TAV is generated and how this mechanism differs from other rhyolites of the SRP (Drew et al., 2013). We interpret the high H₂O and F, and incompatible trace element enrichments in the context of a model involving repeated fractional crystallization, melt extraction, and rejuvenation. We refer to this as a distillation model, because a one stage crystallization event would require >90% crystallization, precluding melt extraction in significant quantities. The distillation model is further supported by the complex zoning

patterns in quartz phenocrysts, which support influx of magma into a zoned magma chamber. First order similarities to the first caldera forming eruption of other caldera clusters in the SRP (Yellowstone, Heise and Bruneau Jarbidge) suggests that the lower temperature, more hydrous rhyolites of the SRP are fundamental to the initiation of a caldera cluster. Specifically, the initial eruptions prime the crust for subsequent magmatism and have a tendency to produce large batholith-like magma bodies.

Introduction

Snake River Plain silicic volcanism and caldera cycles

The Snake River Plain (SRP) has recorded a comprehensive 16 million year history of voluminous silicic volcanism and preserved a series of caldera clusters throughout the Yellowstone hotspot track. An abundance of hot, dry, and densely welded eruptions have been produced and are now considered characteristic of rhyolite genesis in the Yellowstone hotspot track (Branney et al., 2008). However, there are less common rhyolites that have been interpreted to be more H₂O rich and with lower pre-eruptive temperatures (Nash et al., 2006). Rhyolitic volcanism in the eastern SRP and extending into the western SRP is predominantly cyclic, with calderas forming repeatedly at each location. These eruptive cycles are manifested in low $\delta^{18}\text{O}$ (<5.6‰) and diverse $\delta^{18}\text{O}$ zircons of rhyolites of the eastern SRP (Heise, Yellowstone, and Picabo) due to the progressive recycling of volcanic products affected by hydrothermal alteration (Watts et al., 2011; Bindeman et al., 2008, 2001; Drew et al., 2013). This transition to recycling of volcanic roots implies that the early eruptions, specifically the first eruption at each caldera cluster, involves a greater component of pre-existing crustal rocks compared to subsequent eruptions, when the recycling process becomes more important.

Early rhyolites in caldera cycles and the TAV

In the SRP, many of the first or early rhyolites that represent the commencement of volcanism at various volcanic centers show heightened levels of crustal assimilation, and are the most crystal-rich tuffs of their corresponding volcanic sequences (Watts et al.,

2011; Hildreth et al., 1991; Bindeman and Valley, 2001; Nash et al., 2006; Drew et al., 2013). These rhyolites include the Tuff of Arbon Valley of the Picabo volcanic field (Fig. 1), the Huckleberry Ridge Tuff-Member C of Yellowstone, the Blacktail Creek Tuff of Heise, and the Jarbidge rhyolite of Bruneau Jarbidge.

The 10.44 Ma Tuff of Arbon Valley (TAV) has distinct isotopic and chemical characteristics compared to what is considered typical for SRP rhyolites (Nash et al., 2006; Kellogg et al., 1994). The TAV is biotite bearing, poorly-welded, and chemically and isotopically zoned. More specifically, the distinct isotopic characteristics of the TAV include normal $\delta^{18}\text{O}_{\text{melt}}$ (7.9-8.3 ‰), extremely radiogenic and zoned $^{87}\text{Sr}/^{86}\text{Sr}_i$ ratios (ranging from 0.72520 to 0.71488), and low ϵ_{Nd} and ϵ_{Hf} ratios (-18 and -28, respectively, in the upper tuff) (Drew et al., 2013). These characteristics suggest that ~50% by mass of the TAV was derived by melting of Archean upper crust. Although these characteristics are considered atypical of SRP rhyolites, they are similar to many metaluminous rhyolites and A-type granites found worldwide (e.g. Bishop Tuff; Roberge et al., 2013; Wallace et al., 1999; Hildreth and Wilson, 2007).

The more “crustal” radiogenic isotopic signatures, normal to high- $\delta^{18}\text{O}$, and chemical signatures of the first rhyolites erupted indicate these rhyolites are distinct from typical low- $\delta^{18}\text{O}$ SRP rhyolites yet still generic A-type granites. The Jarbidge rhyolite of the Bruneau Jarbidge volcanic center has isotopic similarities to the Tuff of Arbon Valley ($\delta^{18}\text{O} = 8.8$, $\epsilon_{\text{Nd}} = -23$), as well as the Blacktail Creek Tuff of Heise and Huckleberry Ridge Tuff Member C of Yellowstone but to a lesser extent, demonstrating that the process producing these atypical characteristics is not an isolated occurrence at the Picabo volcanic field (Hildreth et al., 1991; Watts et al., 2011; Calliccoat and Bruesecke, 2009).

Goals of the present study

This study tests how the first large-magma body of a caldera cluster is generated and assembled in the crust (prior to being crystallized and recycled in a caldera cluster) (Fig. 1). The chemical and isotopic features of the TAV coupled with the preservation of quartz-hosted melt inclusions in rapidly quenched pumice fragments enables us to assess

the pre-eruptive magma composition, and specifically, the source and mechanism of generating F, H₂O and incompatible element enrichments (see Appendix H for a more extensive introduction).

This study addresses the following questions:

- 1) How is the first rhyolite of a caldera cluster generated? How does this generation mechanism differ from subsequent volcanism?
- 2) More specifically, how can the initiation of volcanism at a new caldera cluster produce rhyolite with a more enriched incompatible element signature in comparison to typical low $\delta^{18}\text{O}$ rhyolites in the SRP?
- 3) Do high volatile contents in SRP rhyolites, specifically F, result from formation processes that concentrate volatiles or from source rocks with unusually high volatile contents?
- 4) How can incompatible-element-enriched rhyolites (Rb/Sr ratios >5000) be generated and extracted in a magma?

Methods

We present pre-eruptive volatile and major and trace element data from quartz-hosted rhyolitic melt inclusions from the rapidly-quenched airfall pumice of the TAV (whole rock SiO₂ = 76.9 wt.%). Quartz phenocrysts were extracted from individual pumice clasts, and the melt inclusions that we analyzed were glassy, fully enclosed in the phenocryst host, and only rarely contained vapor bubbles (Figs. I1. A through D, and I2 of Appendix I). Eighteen melt inclusions, twelve of which contained reliable volatile data, were doubly intersected and analyzed for H₂O and CO₂ contents by Fourier Transform Infrared (FTIR) Spectroscopy at the University of Oregon on a Thermo-Nicolet Nexus 670 FT-IR spectrometer coupled with a Continuum IR microscope. When H₂O contents were too high to quantify using the fundamental OH stretching vibration at 3570 cm⁻¹, the 4520 cm⁻¹ and 5230 cm⁻¹ peaks and the total water calculation by Zhang et al. (1997) were used (Table I1 of Appendix I). Analyses were excluded based on the quality of spectra data that was characterized by the agreement of the ratios of total water

to hydroxyl and molecular water to hydroxyl between spectra for individual melt inclusions (Table I2 of Appendix I).

Major element compositions, as well as F, S and Cl concentrations, in the melt inclusions were analyzed on the Cameca SX100 electron microprobe at the University of Oregon MicroAnalytical Facility (Table I3 of Appendix I). Using the FEI Quanta 200 Environmental Scanning Electron Microscope (ESEM) at the University of Oregon, cathodoluminescence (CL) images were acquired to investigate zoning patterns in the host quartz grains. CL images of quartz phenocrysts from the lower airfall and upper welded tuff of the TAV were taken in addition to images of the inclusion-bearing crystals to constrain systematic relationships, because only portions of the quartz are preserved through the melt inclusion preparation process (Figs. J1. a through d, J2, J3. a through d and J4. a through c of Appendix J). Trace elements Ti, Fe, K, Na, and Al in the host quartz phenocrysts were also determined on the Cameca SX100 electron microprobe at a beam energy of 15 keV, a beam diameter of 10 microns and a beam current of 100 nA (Tables K1 and K2 of Appendix K). The detection limit for Ti is 30 ppm and therefore no trends in quartz Ti concentrations were interpreted for measurements less than 30 ppm. Trace elements of individual melt inclusions were analyzed at Oregon State University in the W. M. Keck Collaboratory for Plasma Mass Spectrometry with a VG PQ ExCell quadrupole ICP-MS and NewWave DUV 193 nm ArF Excimer laser system. A 50-micron spot sized was used, and standards were NIST-612 and BCR-2G. Trace element concentrations were calculated based on ratios of the element of interest to Si coupled with the measured SiO₂ contents of inclusions by the electron microprobe (Table I4 of Appendix I).

Results

Stratigraphy of the studied section and sampling

Pumice clasts for this study were collected from near the base of the stratigraphy at the type locality of the TAV, the Cove, where >100 m of exposed section of both the upper and lower tuff is preserved (Kellogg et al., 1994). Anders et al. (2009) report ⁴⁰Ar/³⁹Ar dates for the TAV of 10.34±0.01 and 10.16±0.01 Ma, however since no cooling breaks were observed at the Cove locality, we consider our sampling locality to represent

a single eruption. The studied stratigraphic section of the TAV at the Cove consists of a glassy, well-sorted, crystal-poor (~5%) tuff with lapilli, overlain by a strongly stratified lapilli tuff that grades into a massive upper welded, crystal-rich (>35%) tuff (Fig. 1) (U-Pb dated to be 10.44 ± 0.27 Ma; Drew et al., 2013). Another important difference between the upper and lower tuff is quartz size: quartz phenocrysts from the lower tuff do not exceed 1 mm in length whereas phenocrysts from the upper tuff are at least 1 to 2 mm in length.

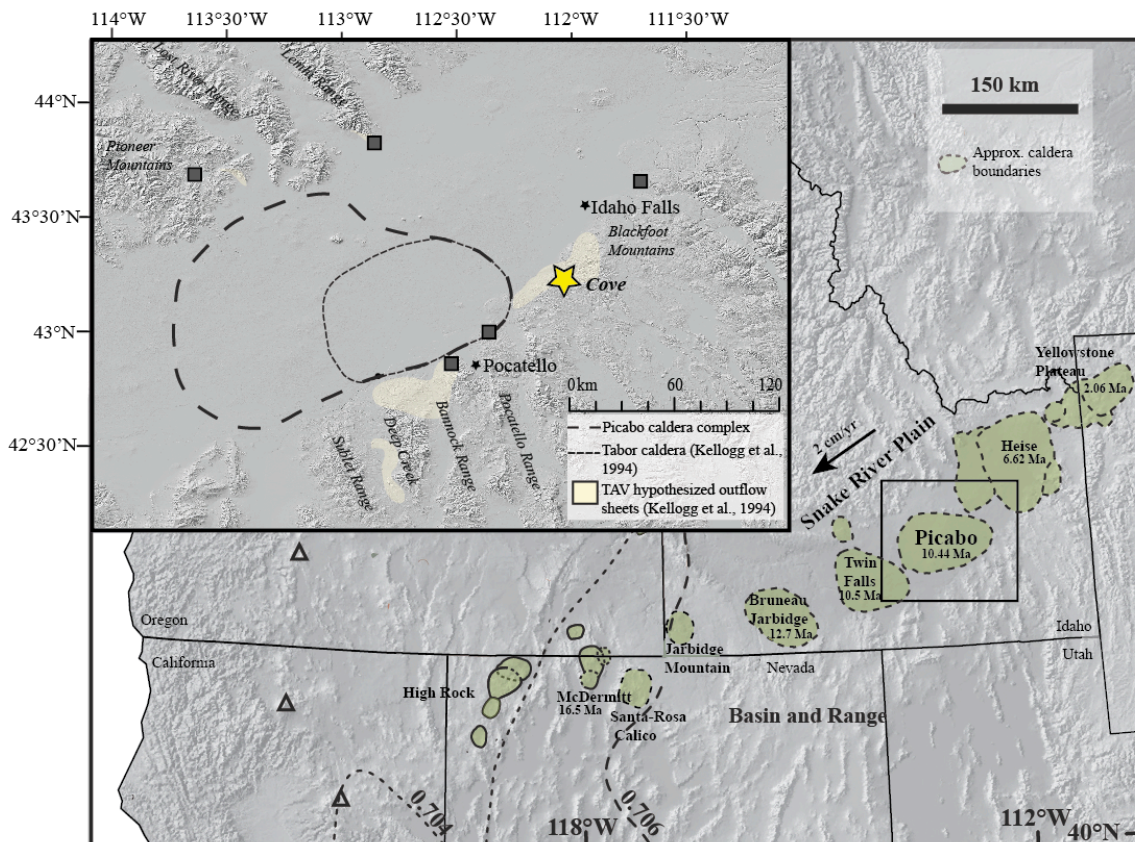


Fig. 1. Map of the Yellowstone hotspot volcanic fields and inset map of sampling localities of the Tuff of Arbon Valley of the Picabo volcanic field (modified from Drew et al., 2013). The yellow star is where the samples for melt inclusion analyses were collected.

Melt inclusion compositions

TAV melt inclusions are high-SiO₂ rhyolites (75.54 to 78.80 wt. %) and contain high Al₂O₃ (12.43-13.10 wt. %) and low TiO₂ (≤ 0.06 wt. %) and MgO (≤ 0.03 wt. %) (Fig. 2). The majority of inclusions are also peraluminous to slightly metaluminous, and

the major and trace element composition of the melt inclusions is largely homogeneous. H₂O contents range from 2.4 to 6.4 wt.%, and CO₂ contents range from 79 to 410 ppm (Table 1), corresponding to a maximum vapor saturation pressure of ~2 kbar (Fig. 3). There are no significant trends between SiO₂, K₂O, MgO, or F with CO₂. An important feature of the TAV rhyolitic melt inclusions is the presence of high F, up to 1.38 wt. %, in comparison to Cl, which does not exceed 0.09 wt. %. Trace element characteristics include depletions in P, Sr, Zr, Ti and LREEs (Fig. 4, 5) and enrichments in Li, B, Rb, Nb, Y, Sn, Th, and U, in comparison to rhyolitic quartz-hosted melt inclusions of the Mesa Falls Tuff (MFT) of Yellowstone and the Bishop Tuff.

Five inclusions contain higher K₂O (8.4 to 9.1 wt. %) and lower Na₂O, SiO₂, and Li, and sporadic concentrations of P, although they are within the range of H₂O and CO₂ concentrations of the main population of TAV melt inclusions. All of these inclusions also have irregular boundaries or are located near cracks. Possible interpretations are that these quartz are xenocrystic, or the inclusions were re-entrants initially and only sealed later, and therefore contain modified compositions. Since these inclusions do not appear to be xenocrystic, based on CL imaging, we support that they are re-entrants. Three different inclusions also contain high CO₂, two of which are located in the same host crystal and have high MgO and FeO, low F, and very different trace element concentrations. The difference between these two inclusions and the average composition of the TAV melt inclusions include, but is not limited to, higher LREEs, Ti, Ba, and Th concentrations, and lower B and Rb concentrations (Figs. 4, 5, 6, 7, and 8).

Table 1.
Fourier Transform Infrared Spectroscopic data for TAV quartz-hosted melt inclusions.

Sample	H ₂ O (wt. %)	std. error	CO ₂ (ppm)	std. error
PC-P1.2 MI 2	4.94	0.22	196	10.1
PC-P1.4	4.69	0.04	179	3.1
PC-P2.6	3.45	0.07	270	10.6
PC-P3.1 MI 1	4.59	0.25	103	5.7
PC-P3.1 MI 2	6.43	0.27	145	3.4
PC-P3.2	5.33	0.41	410	33.3
PC-P3.3	2.27	0.19	120	4.1
PC-P4.1	3.49	0.49	190	48.0
PC-P5.1 MI 1	4.79	0.12	396	4.4
PC-P5.1 MI 2	3.93	0.78	393	5.2
PC-P6.3 MI 1	3.84	0.06	97	2.7
PC-P6.3 MI 2	4.83	0.14	79	1.1

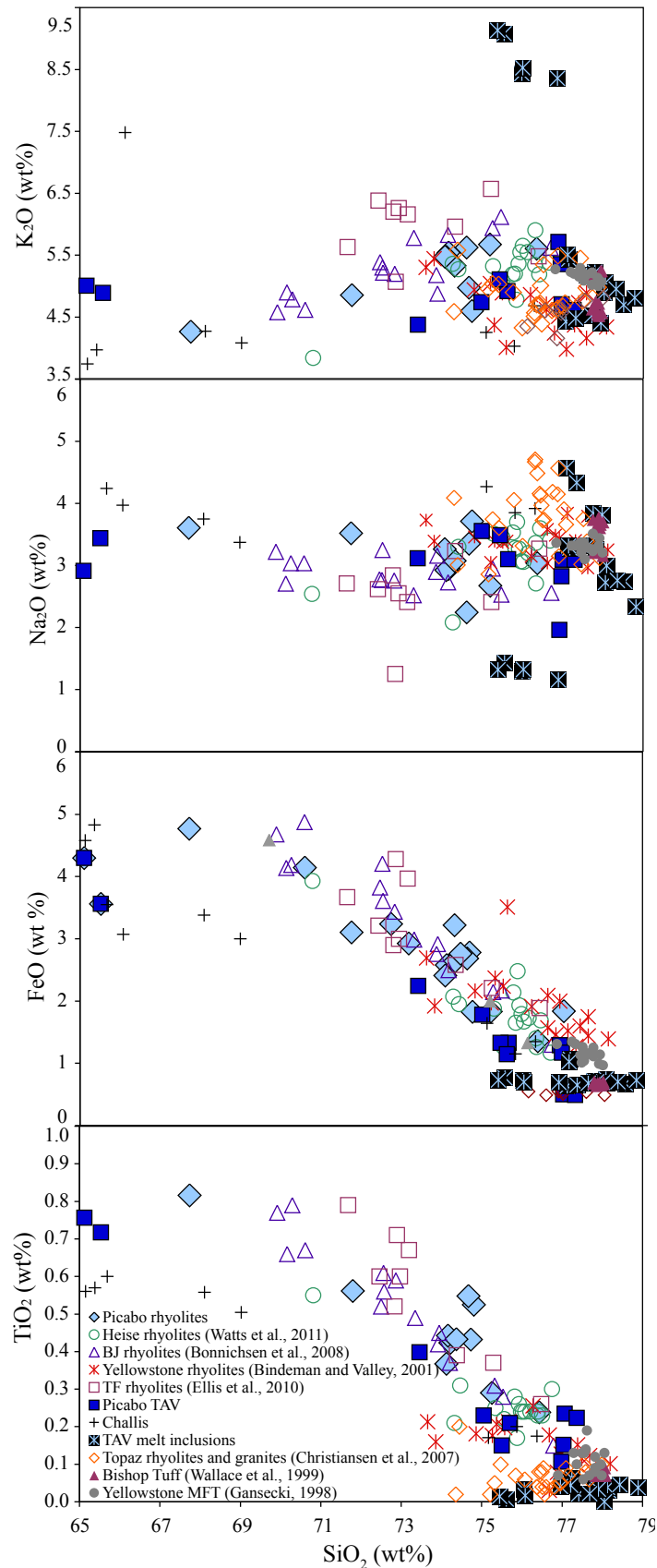


Fig. 2. Major element variations with SiO₂ in comparison to other SRP volcanic fields, Challis volcanics, Topaz rhyolites and granites, Bishop Tuff quartz-hosted melt inclusions, and Yellowstone MFT quartz-hosted melt inclusions.

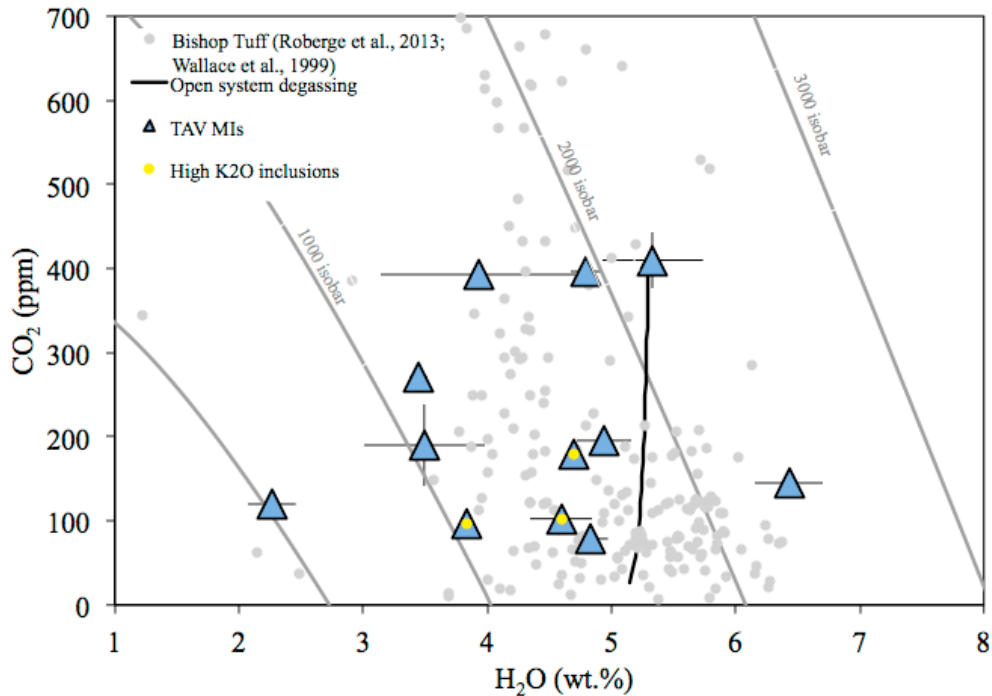


Fig. 3. TAV melt inclusion (MI) CO₂ and H₂O determined by Fourier Transform Infrared Spectroscopy in comparison to the Bishop Tuff. Isobars (at 800°C) and the open system degassing curve were calculated using VolatileCalc (Newman and Lowenstern, 2002).

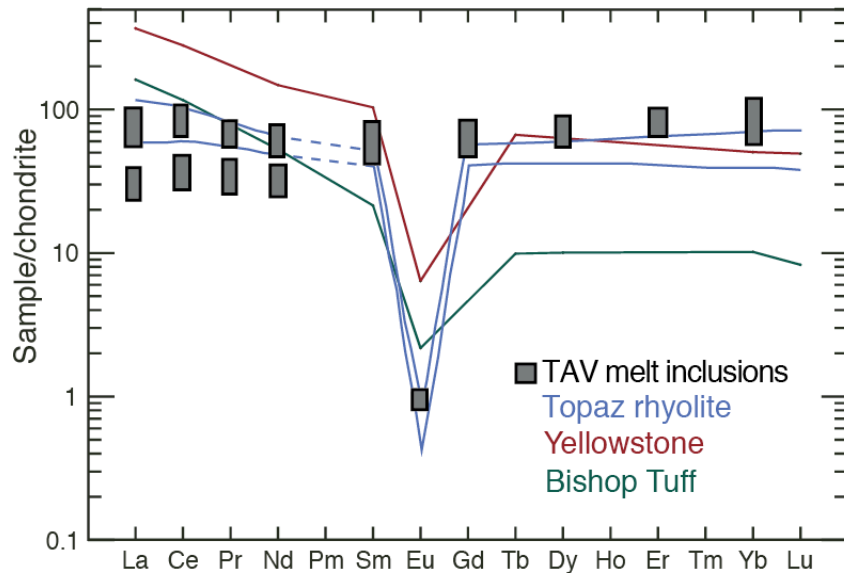


Fig. 4. Rare earth element diagram of Picabo TAV melt inclusions, Topaz rhyolites (Christiansen et al., 2007), Yellowstone and Bishop Tuff rhyolites (modified from Glazner et al., 2008). All trace elements are normalized to chondrite (Sun and McDonough, 1989). Grey bars correspond to the range spanned by the TAV melt inclusion data, on the left side where there is separation represents the compositional distinction between the two most primitive inclusions and the main population of melt inclusions.

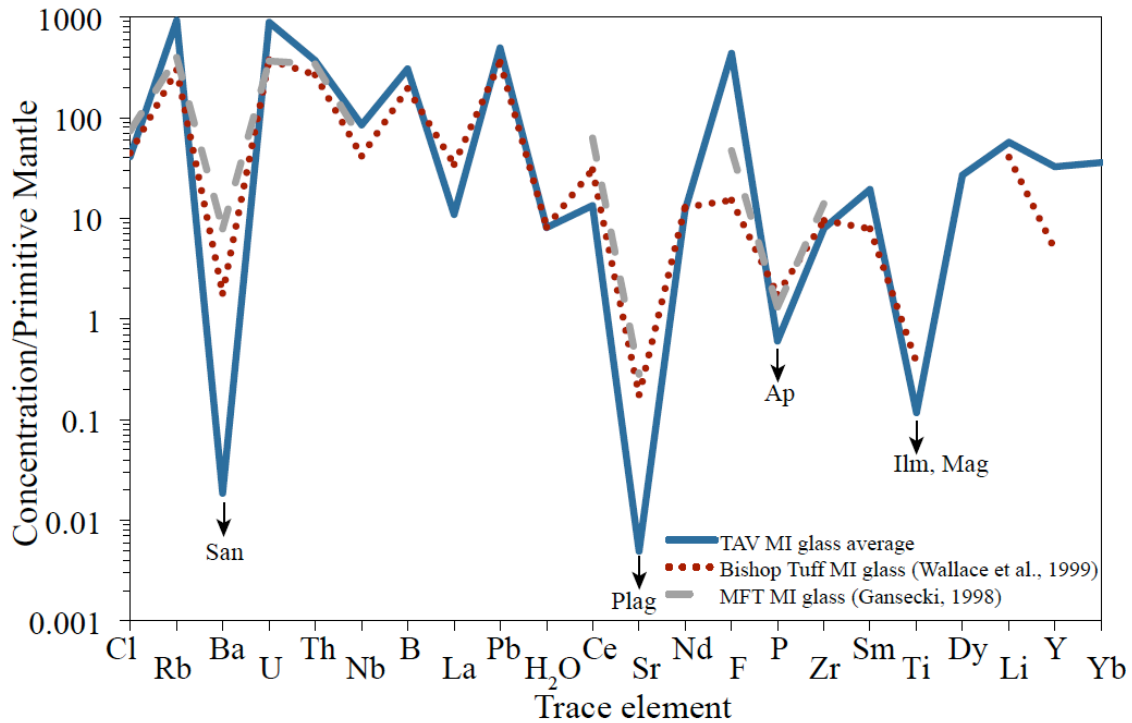


Fig. 5. Spider plot of Picabo TAV melt inclusions in comparison to Bishop Tuff and Mesa Falls Tuff (MFT) melt inclusions. Trace elements are normalized to the primitive mantle (McDonough and Sun, 1995).

CL zoning patterns and Ti in host quartz

Cathodoluminescence (CL) emission properties can provide petrologic insight into complex crystal growth histories and changes in crystallization conditions. CL intensity correlates to Ti content of quartz (Wark and Watson, 2006; Thomas et al., 2010), and the Ti content is a function of temperature, pressure, and TiO_2 activity in the melt. However, temperature, pressure, and TiO_2 activity can change throughout the life of a magmatic system, and other factors such as melt composition and growth rate can also affect Ti fluctuations in quartz (Wilson et al., 2012), precluding direct measurement of pressure or temperature changes with Ti variations.

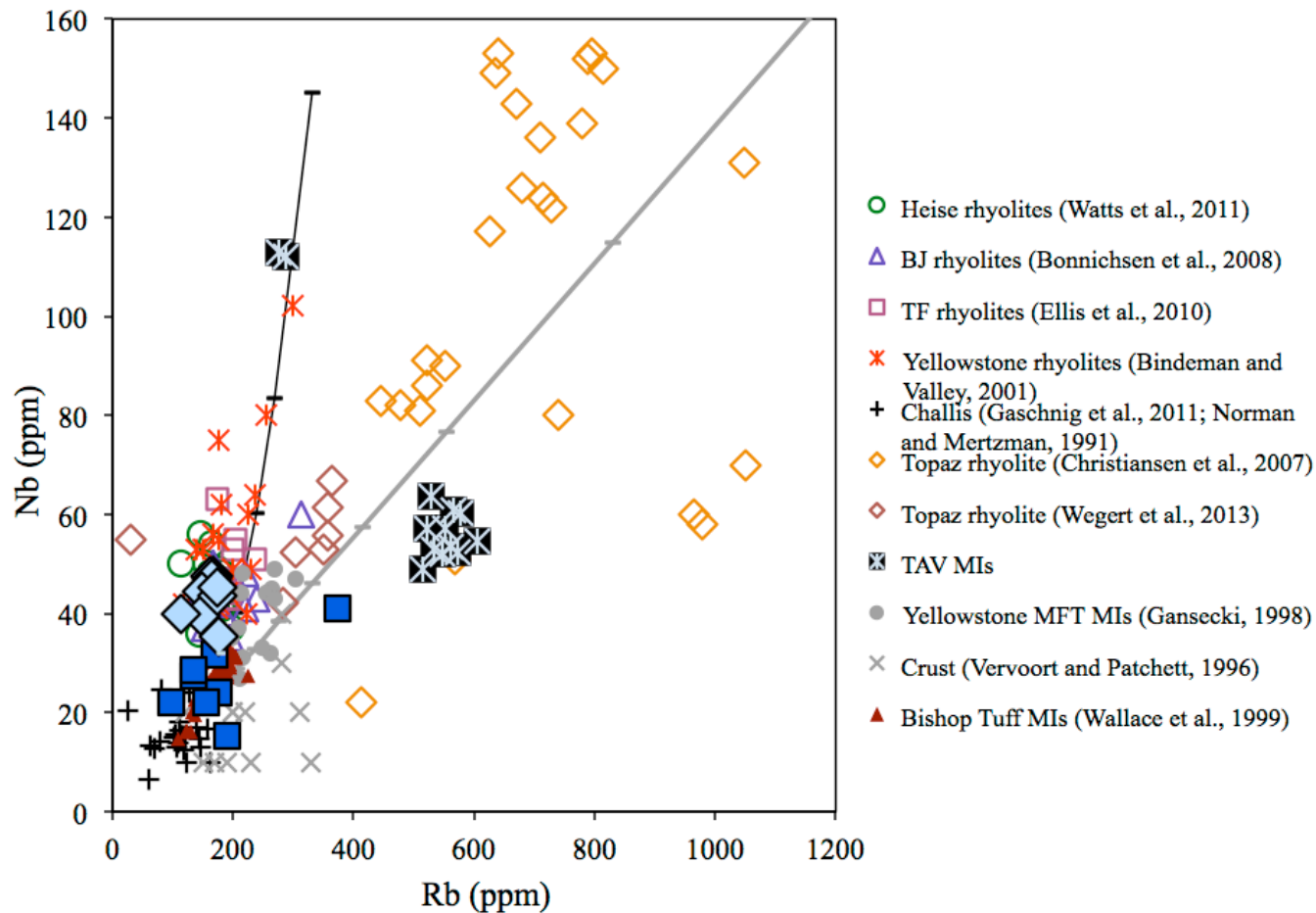


Fig. 6. Nb versus Rb of TAV melt inclusions in comparison to Picabo rhyolites, SRP rhyolites (Heise, Twin Falls, and Bruneau Jarbidge), Topaz rhyolites and granite, Bishop Tuff melt inclusions, Challis volcanics and intrusives, and Archean crust. The black and grey line represent fractional crystallization of 10 wt.% increments beginning at a low silica rhyolite composition. The black fractional crystallization curve assumes partition coefficients of 0.7 and 0.2 and initial concentrations of 166 and 23 for Rb and Nb, respectively. The grey fractional crystallization curve assumes partition coefficients of 0.

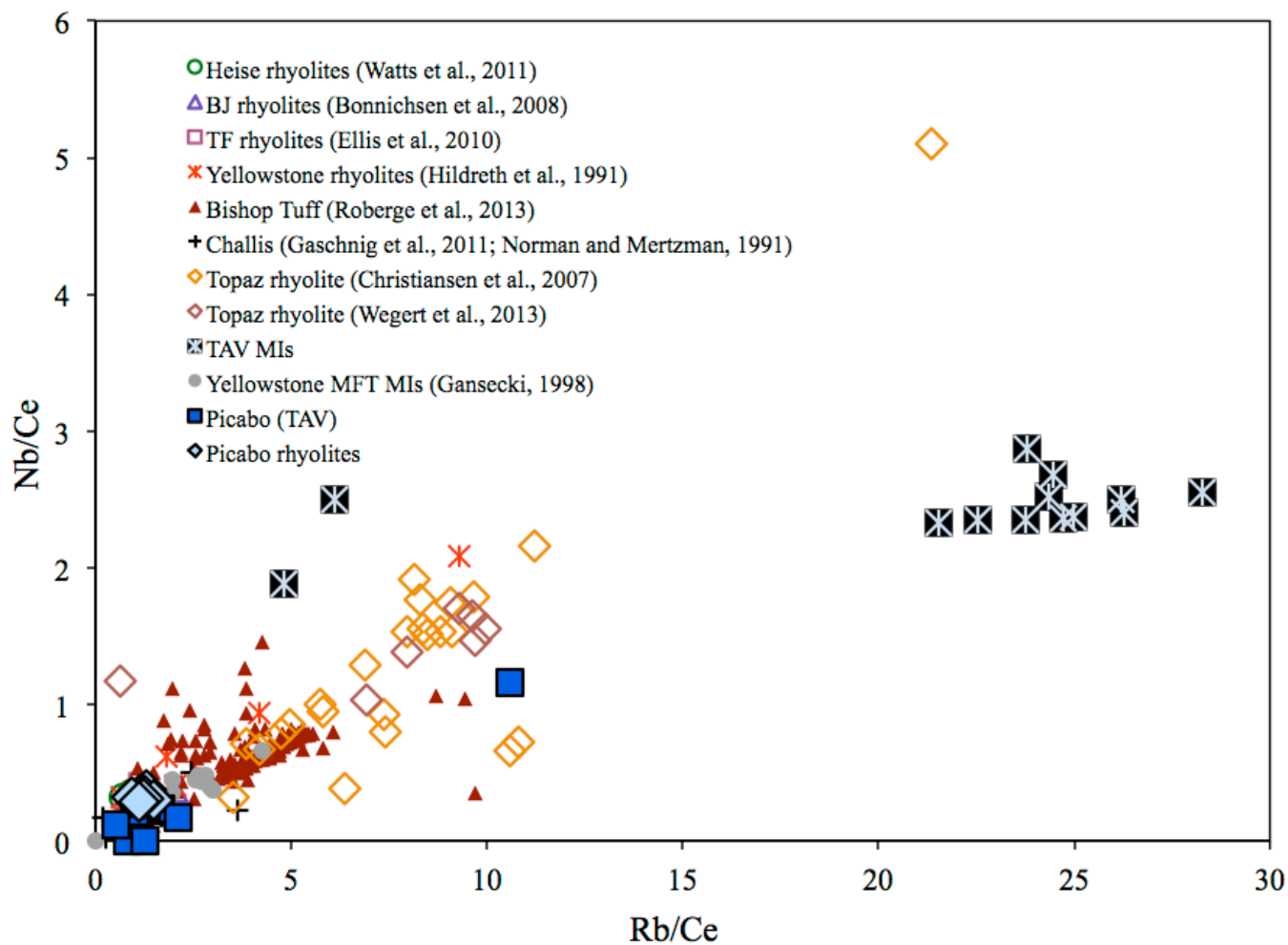


Fig. 7. Nb/Ce versus Rb/Ce of TAV melt inclusions in comparison to Picabo rhyolites, SRP rhyolites (Heise, Twin Falls, and Bruneau Jarbidge), Topaz rhyolites and granite, Bishop Tuff melt inclusions, Challis volcanics and intrusives, and Archean crust. Nb and Rb are normalized to Ce to remove the effects of refractory phase, apatite.

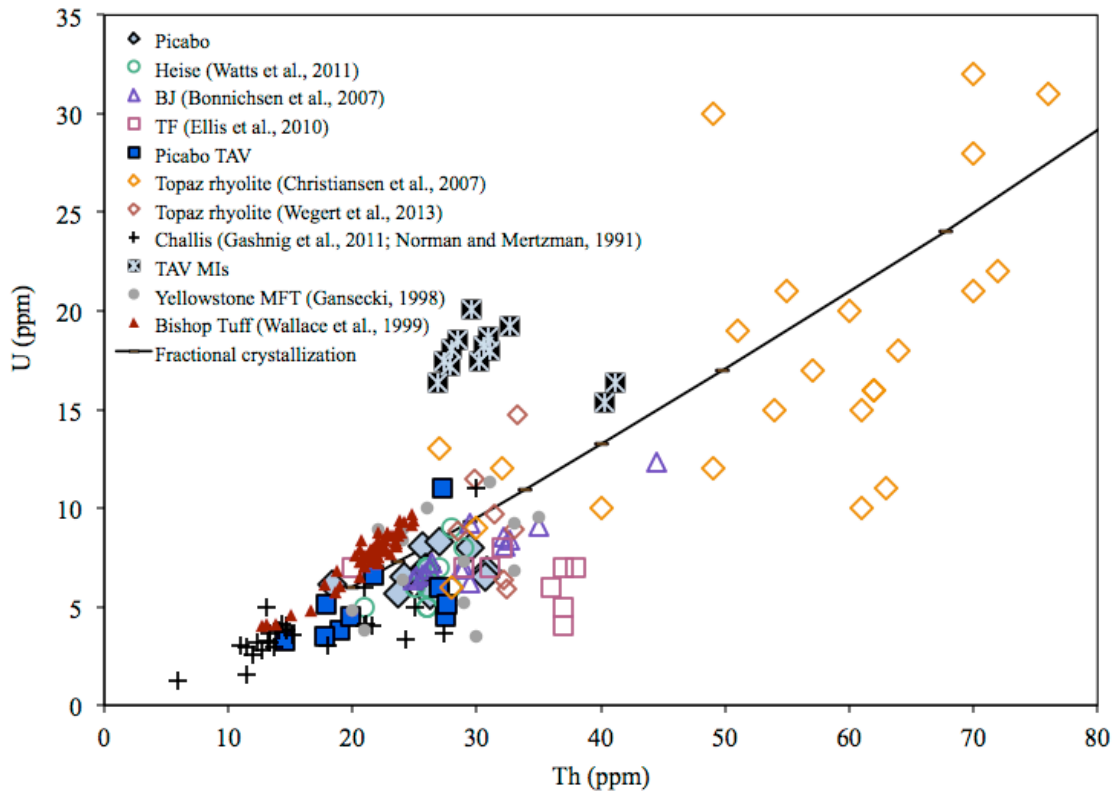


Fig. 8. U versus Th of TAV melt inclusions in comparison to Picabo rhyolites, SRP rhyolites (Heise, Twin Falls, and Bruneau Jarbidge), Topaz rhyolites and granite, Bishop Tuff melt inclusions, Challis volcanics and intrusives, and Archean crust. The black line represents fractional crystallization of 10% increments beginning at a low silica rhyolite composition. This fractional crystallization line assumes a mineralogy representative of typical Yellowstone hotspot rhyolites (Watts et al., 2011) and bulk partition coefficients of 0.137 and 0.154, and initial concentrations 6 and 10 ppm for U and Th, accordingly.

Distinct CL features of host quartz grains include the occasional presence of bright rims and cores (bright cores: 12.5% of grains, bright rims: 19% of grains), and prevalent truncated zones of oscillatory zoning (Fig. 9). The Ti variations do not encapsulate all the complexity in the CL images, which is likely due to small Ti variations due to growth rate or variations in other trace elements (Fe, Al, Li). Comparison of the CL images with whole quartz phenocrysts from the lower airfall and upper ignimbrite revealed that only phenocrysts from the lower airfall had similar patterns to the quartz hosts with analyzed melt inclusions. Bright cores were not observed in the few phenocrysts from the upper airfall imaged (Appendix J). Although the bright cores in the lower tuff do not have large Ti changes, the boundaries are extremely sharp. CL imaging of the upper tuff also revealed that the 1-2 mm grains analyzed are only

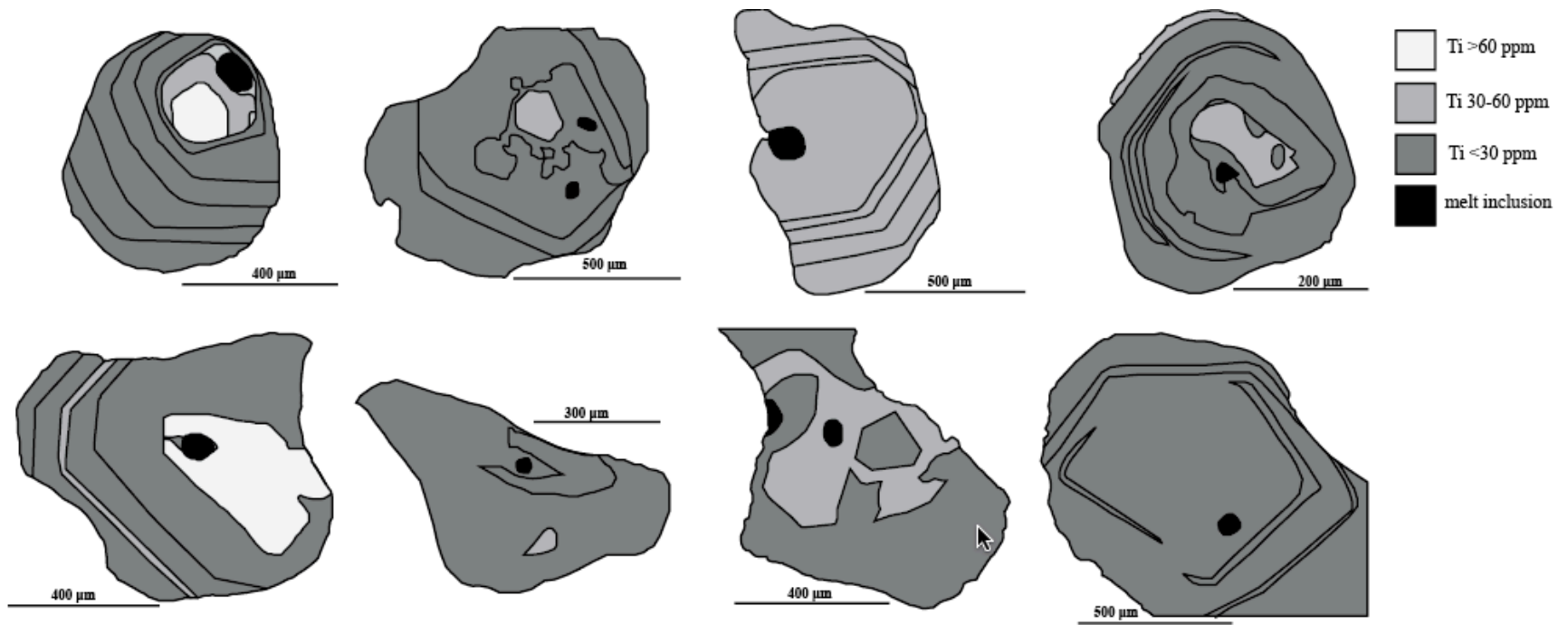
broken fragments of what were once much larger grains. It appears that thicker and more diffuse CL zones (up to 250 microns) are present in the quartz grains from the upper tuff, with little evidence for small-scale oscillatory zoning. The majority of Ti measurements of host quartz grains (of the lower airfall) were less than 60 ppm, with the occasional bright rims and cores reaching concentrations greater than 60 ppm, but not exceeding 82 ppm Ti. Quartz CL patterns and Ti measurements of the upper crystal-rich portion of the deposit yielded significantly higher Ti concentrations and a wider range of variation from <60 ppm to 196 ppm Ti (Appendix K).

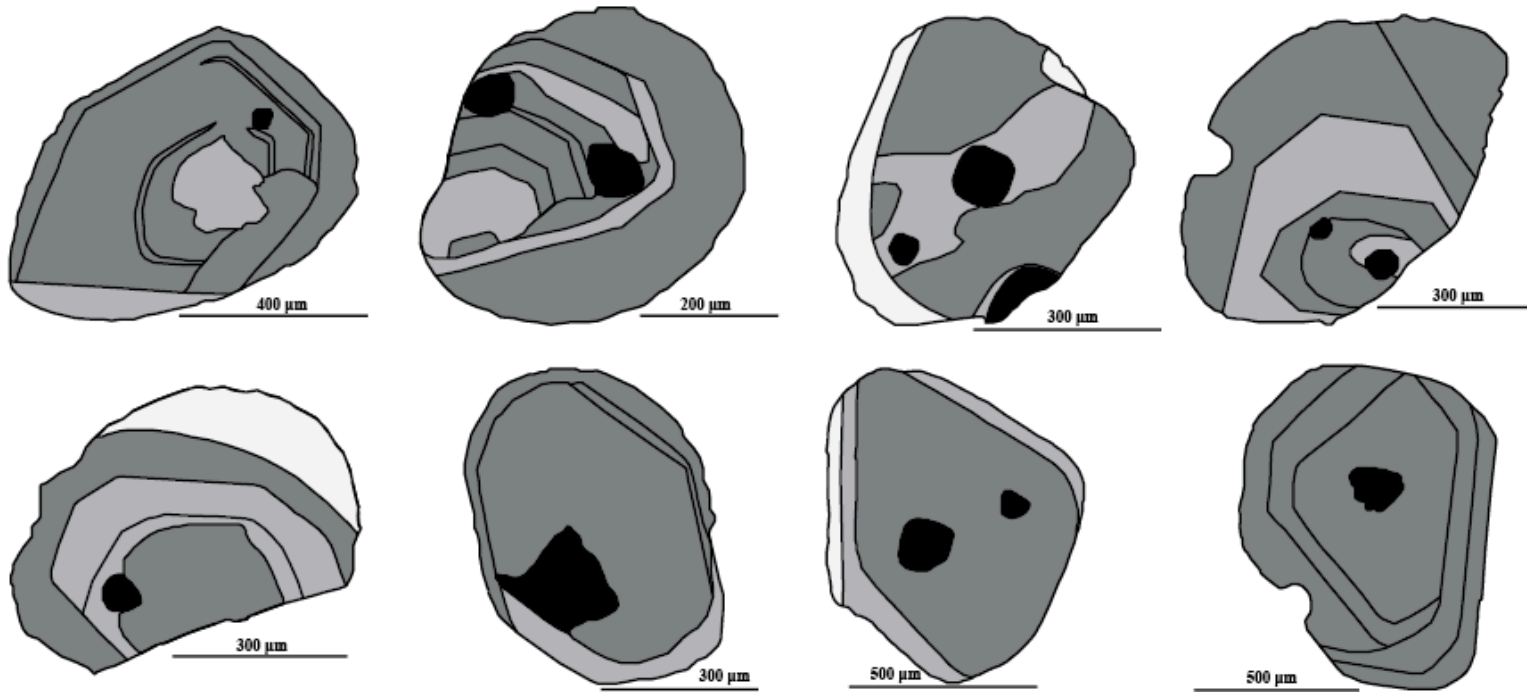
Discussion

Volatile and chemical variations

The variations in H₂O and CO₂ indicate a vapor saturation pressure of between ~1 and 2 kbar, equivalent to a maximum entrapment depth of ~7.6 km (Fig. 3). Although the majority of melt inclusions do not contain vapor bubbles a trend of increasing TiO₂ and CO₂ is observed, suggesting vapor saturation during crystallization (Fig. L1. b. of Appendix L). The maximum pressure is also consistent with the quartz-albite-orthoclase eutectic (Fig. 10). Although TiO₂ shows subtle variations with CO₂, no other major element variations are observed with changes in CO₂ and H₂O (Figs. L1. a through d of Appendix L). The variability in H₂O and CO₂ contents can be attributed to hydrogen loss, as well as fractional crystallization. Melt inclusions with lower H₂O contents, but CO₂ contents equivalent to the main population of melt inclusions, are interpreted to have experienced hydrogen diffusion. In order to further assess the impact of hydrogen diffusion on the composition of melt inclusions we have compared changes in Li and Rb to H₂O, since Li is a fast-diffusing element and Rb is a slow-diffusing element (Figs. L2. a through c of Appendix L). A large range in Li is observed with uniform Rb concentrations, and therefore ~5 inclusions likely lost Li by diffusion. Similarly there is a

Fig. 9. (next 2 pages) Annotated cathodoluminescence images, highlighting zoning patterns and Ti concentrations in host quartz phenocrysts. Please note that not all zones are as sharp as they appear above and please refer to the actual CL images to assess boundaries between zones. Melt inclusions are shown in black and Ti concentrations are shown in three groups, less than 30 ppm (below instrument detection limits), between 30 and 60 ppm, and greater than 60 ppm.





subtle trend of H₂O with melt inclusion size suggesting that smaller inclusions experienced diffusive loss of H and fast-diffusing elements (Fig. L2. d of Appendix L). However, since hydrogen loss only affected a few samples, we do not consider it to have affected the data set as a whole and we focus our analysis on elements that are slow diffusing.

The TAV melt inclusion major and trace element concentrations indicate extreme differentiation, with Sr/Rb and Ba/Rb ratios of < 0.002 and 0.009, respectively (Fig. 11). Trace element concentrations indicate crystallization of the mineral assemblage of quartz, plagioclase, sanidine, and biotite as well as apatite (due to low P₂O₅), zircon (low Zr), and allanite and chevkinite (low LREEs). Relative to other Picabo rhyolites (whole rock), the TAV melt inclusions show an enrichment in U relative to Th and enrichments in Rb relative to Nb (Figs. 6, 7 and 8). The two inclusions with the highest CO₂ have contrasting trace element concentrations, which appear to more closely resemble fractional or equilibrium crystallization of Bishop Tuff rhyolites (Roberge et al., 2013). The two populations of melt inclusions are a function of subtle changes in the mineral assemblage (specifically biotite) and the presence of refractory phases (allanite, chevkinite, apatite). The main population shows nearly equal incompatibility of Nb and Rb, and more incompatible U than Th, in contrast to the more primitive inclusions that demonstrate Nb is more incompatible than Rb, and U and Th have equal incompatibilities. The two more primitive inclusions have less differentiated compositions, and were likely entrapped in an intermediate horizon within the stratified magma chamber. Assuming these two inclusions represent a more primitive rhyolite, then the most incompatible elements (B, Rb, Th, Sn, and Li) demonstrate a ~2 to 3 fold enrichment in concentrations of the main population of inclusions.

Comparison with other rhyolites from different tectonic settings

We interpret the high volatile content (Table 1 and Fig. 3) and incompatible element enrichment of the majority of melt inclusions and location at the base of the stratigraphy to indicate that the melt inclusions were trapped in a high-silica cap of the magma reservoir. We interpret the chemical and isotopic differences between the base

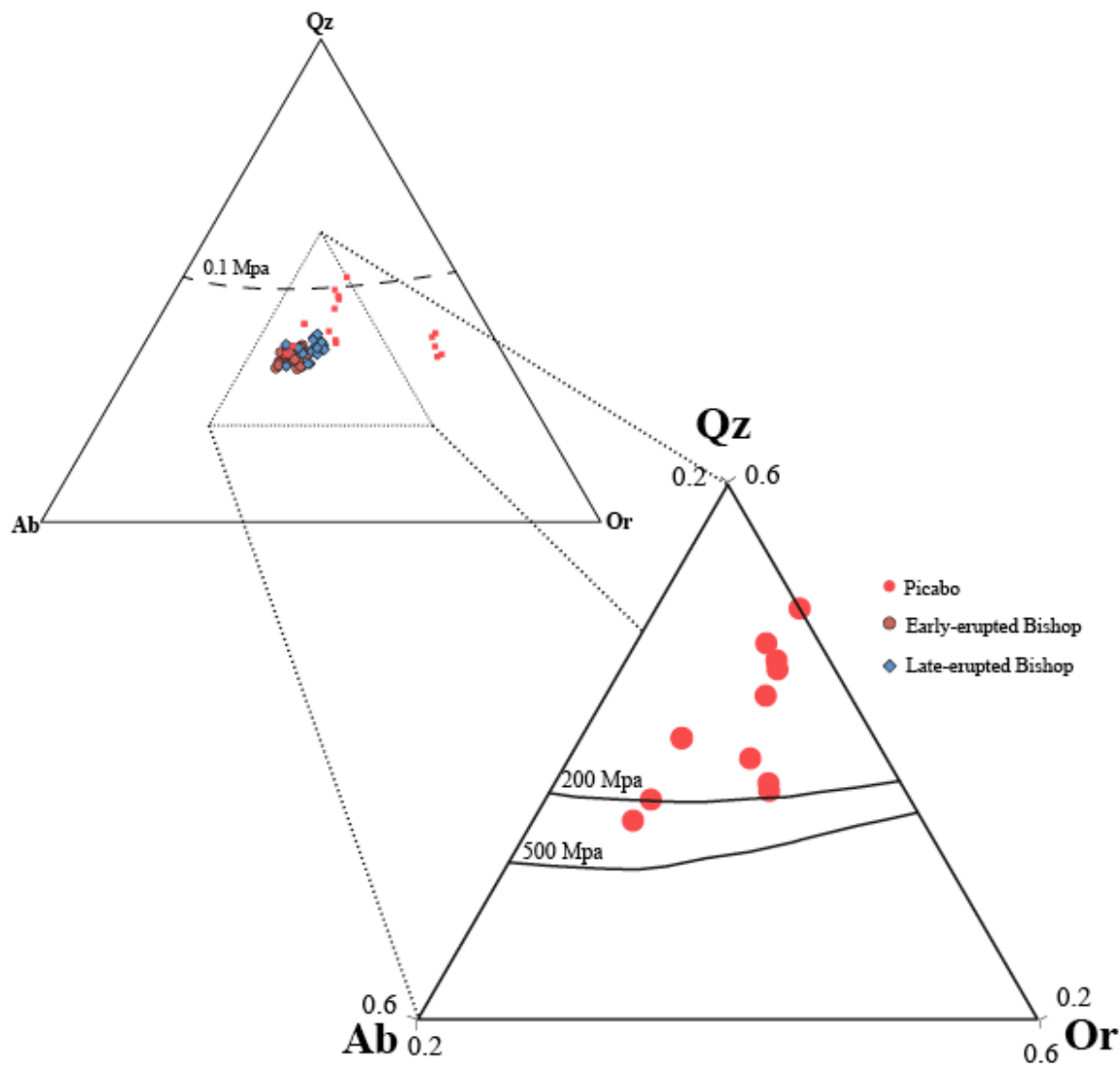


Fig. 10. Quartz (Qz), albite (Ab), and orthoclase (Or) ternary diagram of Tuff of Arbon Valley melt inclusion glass compositions in comparison to cotectic lines of H₂O-saturated minima and eutectics in haplogranitic melts as a function of pressure (Blundy and Cashman, 2001; Tuttle and Bowen, 1958; Luth et al., 1964; Ebadi and Johannes, 1991). Quartz, albite, and orthoclase compositions were calculated from major element compositions normalized with volatile components, using CIPW calculator (IqPet). 200 and 500 MPa boundaries are from Almeev et al. (2012) and 0.1 MPa line is from Brugger et al. (2003).

and top of the TAV stratigraphy to suggest at least two zones in a stratified magma chamber. However, a full chemical investigation of the entire stratigraphy is beyond the scope of this study, and we cannot deduce if the chamber was continuously zoned between these compositions or if they represent two distinct parts of the chamber. What we refer to herein as a zoned magma chamber refers to these two chemical and isotopic horizons.

In order to highlight the distinct chemical features of the TAV melt inclusions, we have compared the composition, including F and Cl concentrations, to that of the following contrasting silicic systems: 1) More proximal to the plate-margin: Bishop Tuff quartz-hosted rhyolitic melt inclusions (Wallace et al., 1999; Roberge et al., 2013, Anderson et al., 2000) and subduction related Crater Lake plagioclase-hosted melt inclusions (Bacon et al., 1992); and 2) Intraplate or A-type: Mesa Falls Tuff of Yellowstone (Gansecki, 1998), and rehomogenized topaz rhyolite inclusions from (Agangi et al., 2012). We only discuss slow diffusing elements from the rehomogenized inclusions (F, Cl, Rb, Nb, Ce) due to the possible effects of hydrogen diffusion during initial cooling and the rehomogenization process. Similarly, we only compare the TAV to the Mesa Falls Tuff because these inclusions were the only glassy and non-rehomogenized melt inclusions of Yellowstone (Gansecki, 1998). The Bishop Tuff has been regarded as a classical example of a stratified magma chamber (Hildreth, 1979; Wallace et al., 1999; Anderson et al., 2000; Roberge et al., 2013; Hildreth and Wilson, 2007) and therefore serves as a means to compare the chemical enrichments and depletions induced by zoned magma chambers. The TAV melt inclusions have similar major element compositions to the Mesa Falls and Bishop Tuff quartz-hosted melt inclusions, but extremely contrasting trace element trends. Most notably, the TAV melt inclusions have F concentrations that are an order of magnitude greater than that of both the Bishop Tuff and Crater Lake volcanics, and comparable to that of other high-F topaz rhyolites found worldwide (Christiansen et al., 2007, 1984; Burt et al., 1982).

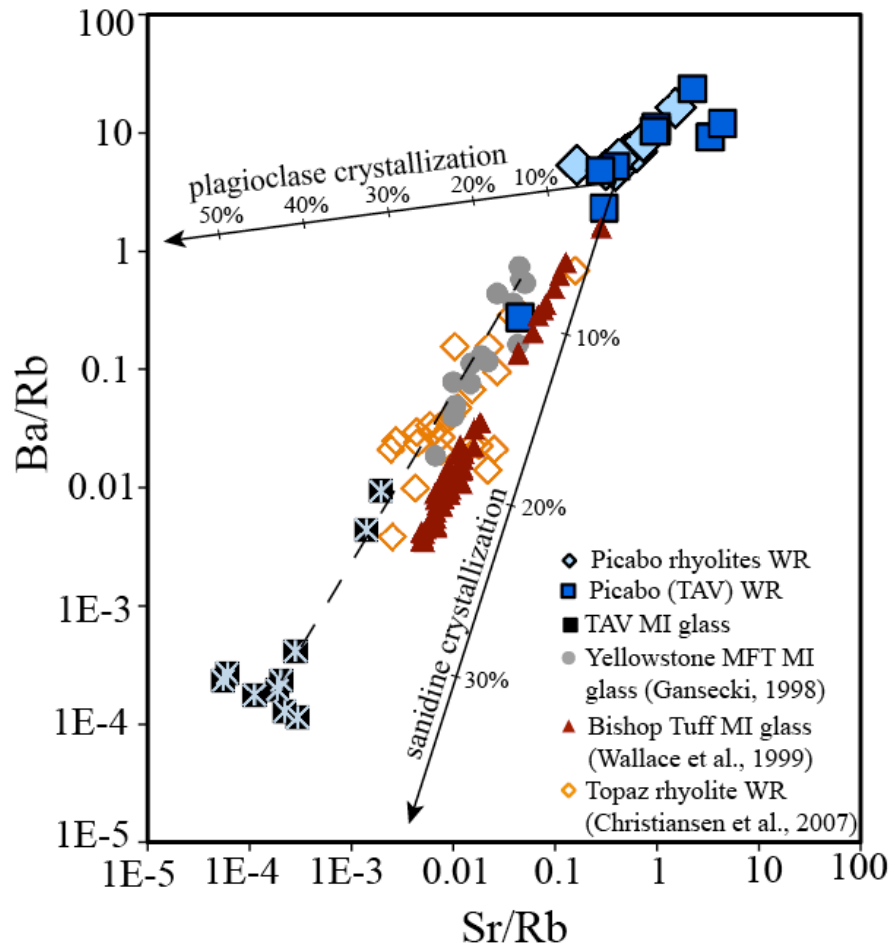


Fig. 11. Sr/Rb variations with Ba/Rb of Picabo rhyolites, SRP rhyolites, Challis volcanics and intrusives, Topaz rhyolites and granites, Bishop Tuff quartz-hosted melt inclusions, and Mesa Falls Tuff quartz-hosted melt inclusions. The solid lines represent fractional crystallization trends of plagioclase and potassium feldspar (Anderson et al., 2000). The dashed line emphasizes the correlation between the TAV melt inclusions and MFT melt inclusions.

Comparison with topaz rhyolites

At least 30 different volcanic centers have erupted topaz rhyolites in the western United States (with occurrences in Mexico as well) during the Late Cenozoic (Christiansen et al., 2007, 1983; Burt et al., 1982) (Fig. H2 and H3 of Appendix H). These rhyolites are named topaz rhyolites largely for their mineralogy and distinct chemical composition. Christiansen et al. (2007) identified their ancient plutonic counterparts to be Proterozoic rapakivi granites found in Finland (Haapala, 1977) and central Arizona (Kortemeier and Burt, 1988), and Mesoproterozoic high fluorine rhyolites have even been found in Southern Australia as well (Agangi et al., 2012). Characteristics typical of topaz rhyolites include high F concentrations in glass (0.2-2 wt. %), enriched lithophile elements, flat REE patterns with negative Eu anomalies, F/Cl ratios >3, high Fe/Mg, low fO_2 (near the QFM buffer), A-type granite chemical compositions, mineral assemblages including quartz, sanidine, and sodic plagioclase, and crystallization temperatures of ~650-700°C (Christiansen et al., 2007). Topaz rhyolites do not have a significant crustal affinity, and in topaz rhyolites from Wah Wah Mountains, Utah $^{87}\text{Sr}/^{86}\text{Sr}$ ratios range from 0.7053 to 0.710 and ϵ_{Nd} ranges from -4.4 to -11.4 (Christiansen et al., 2007). Christiansen et al. (2007) stresses the spatial and temporal association of topaz rhyolites with both extension and previous subduction-related calc-alkaline magmatism.⁵

The high F in the rhyolitic melt inclusions of the TAV suggests an inherent similarity to topaz rhyolites. Trimble and Carr (1976) also report topaz in the lower TAV in regions near the American Falls reservoir, which was likely the result of vapor phase crystallization. However, topaz was not observed in the samples analyzed in this study. The high $^{87}\text{Sr}/^{86}\text{Sr}$ ratios, high crystallinity (up to 35 vol. %), and trace element characteristics of the TAV melt inclusion glass and whole rock compositions demonstrate there are differences between topaz rhyolites and the TAV (Figs. 6, 7, 8, and 11). More specifically, comparison of the geochemistry of whole rock TAV samples, TAV melt

⁵ Topaz rhyolites have been associated with the northern segments of the Rio Grande Rift (Wegert et al., 2013), opening of the Nevada rift (Stewart et al., 1975; Zoback and Thompson, 1978; John et al., 2000), extension in the Great Basin (Zoback et al., 1981), detachment faulting in western Arizona (Suneson and Lucchitta, 1983), and back-arc graben formation (Armstrong, 1978).

inclusions, and topaz rhyolite show that the TAV melt inclusion glass composition resembles the topaz rhyolite composition, however the TAV whole rock data does not. This suggests that although the TAV was initially generated by similar mechanisms to the topaz rhyolite, magma mixing prior to eruption resulted in a different final magmatic composition. The lower Nb of the TAV whole rock data supports that this magma contained a significant crustal component.

Ti variations in quartz across the eruptive stratigraphy

The systematic difference in the Ti content of quartz in the lower TAV (PC-12) and the upper TAV (PC-14) has important implications for the genesis and storage of the erupted rhyolite. The Ti content of quartz in the lower TAV is extremely low with only occasional cores and rims reaching Ti concentrations greater than 60 ppm, in comparison to the upper TAV, which has Ti concentrations exceeding 100 ppm (Fig. 13). These Ti trace element variations suggest an innate difference in the pressure, temperature, and/or TiO₂ activity, and thus the magmatic conditions. More specifically, the upper TAV represents a magma with higher temperatures, lower pressures, and/or higher TiO₂ activity.

The CL zoning patterns (e.g., truncated oscillatory zones, bright cores, and bright rims) and changing Ti concentration of quartz suggest at least two resorption events, where phenocrysts were partially resorbed and began to recrystallize, however, the small variations in Ti suggest that the compositional, temperature and/or pressure changes were minor in the lower tuff and more significant in the upper tuff. This is what we would expect for a zoned magma chamber with magma influx to the base. In this scenario, the highest silica rhyolite would concentrate at the top of the chamber as a crystal-poor melt lens with the largest crystals settling to the base (Bachmann and Bergantz, 2008), a process enhanced by the reduced viscosity due to the presence of high F. Hotter magma injected at the base of the system would influence the temperature at the base of the chamber and only small temperature changes would translate upwards in the magma body. Similarly, there are pressure differences between the upper and lower tuff due to the locations within the magma body that also influence Ti concentrations of the crystallizing quartz.

The crystal-rich nature of the upper TAV further supports stratification because the high crystallinity would hamper complete convection and homogenization. The presence of large quartz fragments in the upper TAV supports magma mixing, rejuvenation, or recharge because a temperature increase greater than 50°C would provide the necessary overheating to fragment and possibly anneal quartz grains of the upper TAV (Bindeman, 2005), in addition to fragmentation during transport and deposition in the pyroclastic flow.

Although we do not use Ti measurements to constrain absolute pressures and temperatures, if we just consider the upper tuff and assume a constant approximate pressure and TiO_2 activity then the upper TAV zoning would span a temperature range of ~200°C. We are not advocating that such a large temperature gradient existed in the magma system, however this range of 200°C emphasizes that the quartz from the upper tuff experienced significant changes in magmatic conditions, changes more significant than those observed for the Bishop Tuff (Wark et al., 2007). As mentioned previously, this can be a result of crystal settling and influx of high temperature magma at the base. In the lower tuff (quartz bearing melt inclusions) if we assume TiO_2 activities of 0.9, 0.6, and 0.2 and using the Huang and Audetat (2012) calibration, the average Ti concentration of 32 ppm in quartz would yield temperatures of 615, 654, and 783°C accordingly (Table L1 of Appendix L). The presence of allanite (McCurry et al., 2009) suggests that the magma temperature did not exceed 765°C (Vazquez et al., 2004), bracketing the temperature between ~615 and 765°C for the lower tuff and emphasizing that this tuff crystallized at a lower temperature than typical Picabo rhyolites, which have liquidus temperatures of ~850°C (Drew et al., 2013). At these lower temperatures and high crystallinity in the upper tuff, the presence of high fluorine likely facilitated melt extraction since fluorine reduces the magma density and viscosity (Dingwell and Webb, 1992; Fig. H3 of Appendix H).

CL zoning of quartz from the Bishop Tuff shows evidence for high Ti rims, thickest in the late erupted units and thinner in the early units, and continuous oscillatory zoning (Peppard et al., 2001; Roberge et al., 2013). Patterns described by Peppard et al. (2001) include weakly zoned cores and bright CL rims, and crystals with no CL intensity differences and weakly zoned cores and dark rims. In comparison to the TAV, important

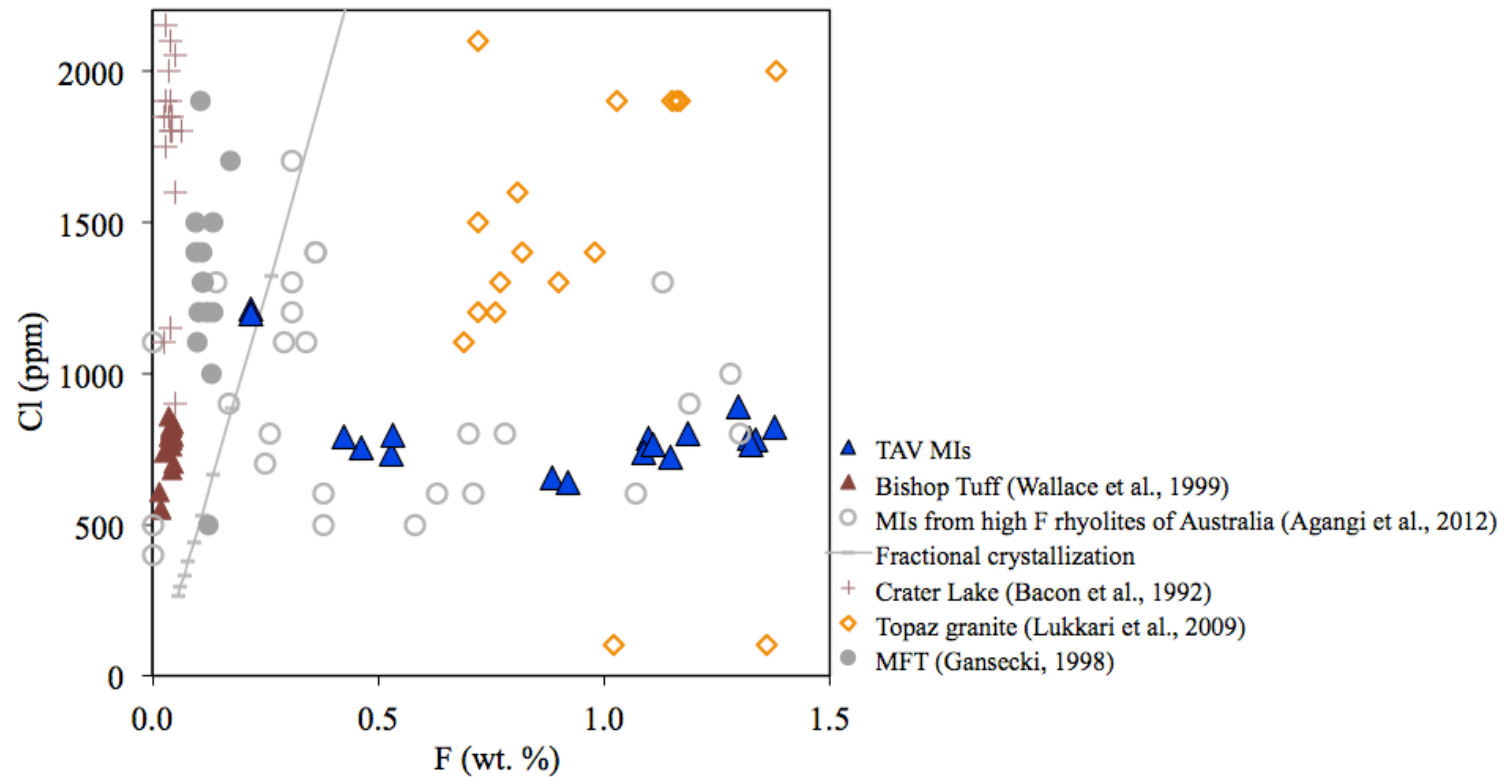


Fig. 12. F versus Cl concentration of melt inclusions in comparison to olivine-hosted melt inclusions from Yellowstone (Stefano et al., 2011), quartz-hosted melt inclusions from the Mesa Falls Tuff of Yellowstone (Gansecki, 1998), Bishop Tuff quartz-hosted melt inclusions (Wallace et al., 1999), rehomogenized topaz granite inclusions (Lukkari et al., 2009), rehomogenized quartz-hosted melt inclusions from high-F rhyolites of Australia (Agangi et al., 2012) and plagioclase-hosted melt inclusions from Crater Lake (Bacon et al., 1992). The solid line represents a fractional crystallization curve with tick marks at increments of 10%. The grey crystallization curve assumes partition coefficients of 0.044 and 0.004 for F and Cl, respectively, and initial concentrations of 0.056 wt. % F and 226 ppm Cl.

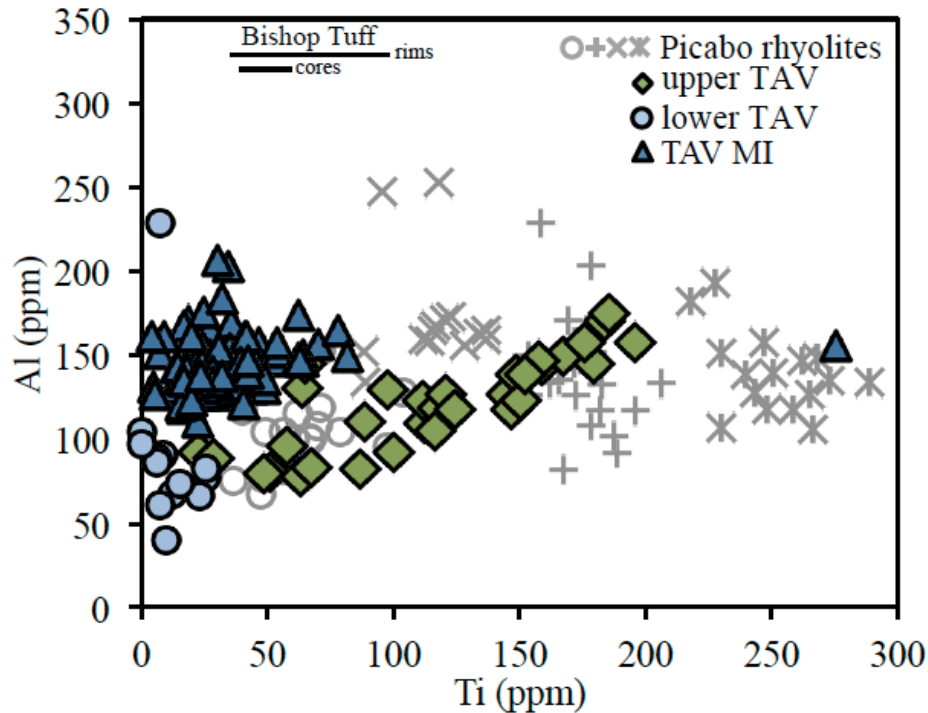


Fig. 13. Ti and Al trace element variations in quartz from the Picabo volcanic center in comparison to the Bishop Tuff. The Bishop Tuff spans 44.3 to 57.2 ppm in the cores and 39.8 to 98.2 ppm in the rims (Wark et al., 2007).

distinctions include that there are fewer episodes of rejuvenation and mixing, and no extremely distinct high Ti cores in the Bishop Tuff.

Mass balance of the volatile budget with isotopic and chemical constraints

The whole rock $^{87}\text{Sr}/^{86}\text{Sr}$ and $^{143}\text{Nd}/^{144}\text{Nd}$ isotopic data of Drew et al. (2013) coupled with melt inclusion H_2O , CO_2 , F, and trace element constraints from this study have enabled us to assess the source and mechanisms contributing to rhyolite generation. We first investigate the feasibility of generating rhyolites with incompatible element and F enrichments through more traditional mechanisms of crustal melting and fractional crystallization.

A previous Sr and Nd isotopic mass balance for the TAV by Drew et al. (2013) demonstrated that ~50% by mass of the TAV is derived from upper Archean crust. Rudnick and Gao (2003) report average upper crustal concentrations of F to be 557 ppm, middle crust to be 524 ppm and lower crust to be 570 ppm. Assuming complete

incompatibility ($D=0$), a 50% partial melt of any crust (to satisfy our isotopic constraints) would only double the F concentration (~ 1100 ppm). However, low degree partial melts can produce higher concentrations, for example 2% partial melting can scavenge the required ~ 2.8 wt. % F (Fig. 14). At more realistic higher degrees of partial melting, starting from greater than 5% the addition of crust essentially dilutes the melt in F. The inability to produce high F due to melting Archean crust suggests other sources or mechanisms are necessary to concentrate F in the rhyolite.

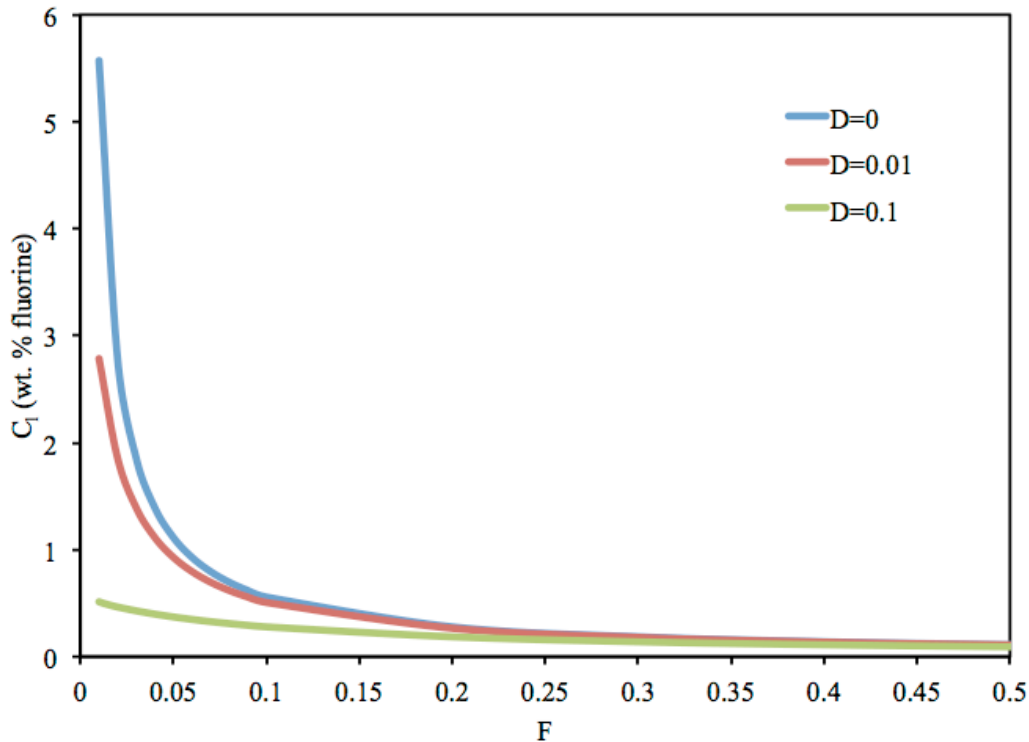


Fig. 14. The change in fluorine concentration with melt fraction at various partition coefficients, assuming an initial concentration of 557 ppm (these upper crustal conditions are from Rudnick and Gao, 2003).

Fractional crystallization of the magma assuming complete incompatible behavior of F and Cl ($D=0$), can only produce the F and Cl concentrations observed through 97-98% fractional crystallization with starting compositions of 210 and 20 ppm, respectively. To produce the Crater Lake and Bishop Tuff rhyolites F needs to be significantly more compatible (at least an order of magnitude increase in the partition coefficient) than Cl, and to produce the TAV and topaz rhyolites the opposite is needed, with extremely incompatible F (Fig. 12). The large variation in the TAV F concentrations also suggests preserved compositional heterogeneities.

Not only is the enrichment in F unusual, but the excess of F in comparison to Cl is a feature that is difficult to explain by crustal melting, for the TAV and even intraplate (A-type) rhyolites in general (Christiansen et al. 2007). Thus a critical aspect of understanding the genesis of the TAV involves the source of high F and low Cl or the fractionation and separation of F and Cl, and below we consider if these characteristics can be generated by differentiating basalt from a fertile or subduction pre-enriched mantle. Minor amounts of F can be stored in nominally halogen free mantle minerals, because F has experimental partition coefficients of 0.031 to 0.037 in orthopyroxene (0.0007 to 0.0033 in olivine; Beyer et al., 2012). More specifically, Beyer et al. (2012) demonstrated that depleted mid-ocean ridge basalt can have a concentration of 6 to 15 ppm of F and ocean island basalt can have 8 to 31 ppm (Beyer et al., 2012). Even in considering the effects of a previous episode of subduction beneath the region where the TAV formed, F is much less incompatible than Cl and therefore subduction pre-enrichment would produce the opposite effect (high Cl/F ratios). Other studies (John et al., 2011; Straub and Layne, 2003) have even suggested that 95% of subducted F is recycled back into the mantle, generating F-poor magmas.

We consider the possible sources of F and incompatible element enrichments to include:

- 1) Melting of a phlogopite-enriched mantle source. F substitution for OH⁻ increases the vapor absent melting temperature to between ~1354 and 1390°C and therefore this mechanism would require higher temperatures. Melting of phlogopite typically generates low-degree lamproitic melts rather than A-type granites (Peterson et al., 1991; Fritschle et al., 2013) and therefore could be a contributing factor, but only in small volumes. However, there is no evidence of coeval lamproites in the Picabo region.
- 2) Melting of an ore deposit or stock in the crust, related to previous hydrothermal alteration of the Challis volcanics. However, this does not reconcile the source of fluorine associated with many of these deposits, and the normal $\delta^{18}\text{O}$ of quartz in the TAV (Drew et al., 2013) provides evidence that hydrothermally altered (and thus likely low- $\delta^{18}\text{O}$, e.g. Taylor, 1974) source rocks did not contribute to the

petrogenesis of the TAV. This mechanism is also location dependent and assumes these intrusives exist without surface evidence.

- 3) Low degree or disequilibrium partial melting of a biotite rich lithology in the lower to middle crust and rapid melt segregation. However, generating the volumes necessary for the TAV coupled with melt extraction and accumulation in a stratified magma reservoir, makes this mechanism difficult to achieve.
- 4) Gas purging and vapor-phase metal transport during crystallization or second boiling (Huber et al., 2012) resulting in magma segregation and accumulation of F, H₂O, and complexed metals at the magma chamber roof. Closed system vapor saturated crystallization serves as a mechanism to concentrate exsolved volatiles, however the presence of high concentrations H₂O and CO₂ preclude the extensive degassing of the melt, which would be required to strongly deplete Cl.
- 5) Previous melting of the crust depleted the crust in Cl prior to TAV-related volcanism, creating greater potential to increase F concentrations relative to Cl during subsequent melting. Skjerlie and Johnston (1992) demonstrated that by biotite-dehydration melting, fluorine-rich melt (up to 0.13 wt. %) can be generated. We consider their experiment as a realistic upper limit for F concentration by single-stage partial melting. However, this does not reconcile the enrichment in incompatible elements in the erupted magma and still requires coupling with significant crystallization to further enrich the extracted melt in F.
- 6) We prefer a distillation model, which includes greater than two episodes of remelting and fractionation at depth in the crust leading to a progressive distillation of F (and other incompatible elements) in rhyolite coupled with fractional crystallization. This process would be facilitated by the input of basalt, which would release heat and volatiles to the overlying rhyolite and suffer from a density trap induced by the growing rhyolitic magma body. Unlike subsequent rhyolites in the Picabo area that are related to recycling of rocks in caldera

complexes and have low- $\delta^{18}\text{O}$ signatures, we envision that the formation of the TAV, and other rhyolites in the beginning of each caldera cluster (Fig.1), involves prolonged, mid-crustal, low-melt production intrusion/differentiation episodes lasting ~ 2 Ma.

The enrichment in F relative to Cl is a complex problem, however the topaz rhyolites and granites found worldwide emphasize that the generation mechanism and source are not unique to the TAV. The crust and mantle although solely cannot produce the necessary chemical compositions through single stage fractional crystallization or crustal melting, both have concentrations of F greater than Cl and therefore we propose a model for progressive distillation or sequestration to generate the TAV (Fig. 15). More specifically, repeated injection and rejuvenation of rhyolite emplaced in the crust (as required by isotopes) coupled with fractional crystallization would continually extract volatiles and incompatible elements. This process would be further facilitated by previous melting that increased the F/Cl ratio of the crust and a low degree partial melt of the mantle as the initial source. The end result of distillation is a zoned magma chamber at 7.6 km with a high silica rhyolite cap. This model requires heat influx throughout rhyolite generation and excessive stalling and differentiation in the crust, which is supported by low degree partial melts from the plume rather than full plume impingement later on (Fig. 16).

Implications for the initiation of caldera complexes in the SRP

Similarities to the TAV are also expressed in subtle chemical variations at other caldera clusters in the SRP. The Blacktail Creek Tuff of the Heise volcanic center has the highest $^{87}\text{Sr}/^{86}\text{Sr}_i$ ratio (0.71238) of all erupted Heise rhyolites and is the most crystal rich at 10-20 vol. % (Watts et al., 2011). Similarly, the 2.1 ka Huckleberry Ridge Tuff Member C of the Yellowstone Plateau has the highest $^{87}\text{Sr}/^{86}\text{Sr}_i$ (0.72685) of the Yellowstone rhyolites and 0.5‰ higher $\delta^{18}\text{O}$ of quartz and zircon than other normal $\delta^{18}\text{O}$ rhyolites of Yellowstone (Bindeman and Valley, 2001; Hildreth et al., 1991). Bindeman and Valley (2001) attribute these isotopic signatures in the Huckleberry Ridge Tuff to a zoned magma chamber, which further suggests parallels to the TAV system. The 16 Ma

Jarbidge rhyolite of the Bruneau Jarbidge eruptive center, also has $^{143}\text{Nd}/^{144}\text{Nd}$ ratios comparable to the TAV (0.511366; Nash et al., 2006) and high crystallinity of up to 25 to 35 vol. % (Calliccoat and Bruesecke, 2009). These first order similarities suggest that initial low degree melts of the plume and/or priming of the crust during the first eruption has a tendency to generate more crystal rich magmas with greater crustal contributions, and concentrations of incompatible trace elements. These signatures become diluted when full plume impingement occurs inducing large degree mantle melting. These crystal-rich and radiogenic rhyolites are thus critical tracers for the initiation of volcanism at a new location, have the potential to be used in locations where the volcanic record is not as well preserved and further reinforce the cyclical nature of volcanism in the SRP. Therefore, although researchers (Hildreth et al., 1991; Nash et al., 2006) have referred to many of these eruptions as chemically and/or spatially anomalous, due to their appearance ahead of direct plume impingement (Nash et al., 2006), these rhyolites represent initiation of a caldera cluster and are related to the evolution of the volcanic center. We therefore suggest that reference to on-axis plume volcanism should take into account spatial-temporal tectonic and magmatic processes and not only genetic geochemical similarities.

Conclusions

The Yellowstone hotspot track has produced an abundance of hot, dry, and densely welded silicic eruptions that have been used to characterize volcanic centers of the SRP, but minimal attention has been paid to the several pumiceous and rapidly quenched eruptive products. Pre-eruptive volatile and chemical data from quartz-hosted melt inclusions from the airfall of the TAV coupled with Sr, Nd, and O isotopic constraints elucidate the mechanism by which lower temperature, H_2O , F, and incompatible element rich rhyolites can be generated in the SRP, typically ahead of the passage of the plume. We present a model of a ramping up magmatic cycle that includes the production of lower degree mantle and crustal melts, which initially mix together forming isolated silicic pockets with enriched isotopic and elemental signatures in the middle crust.

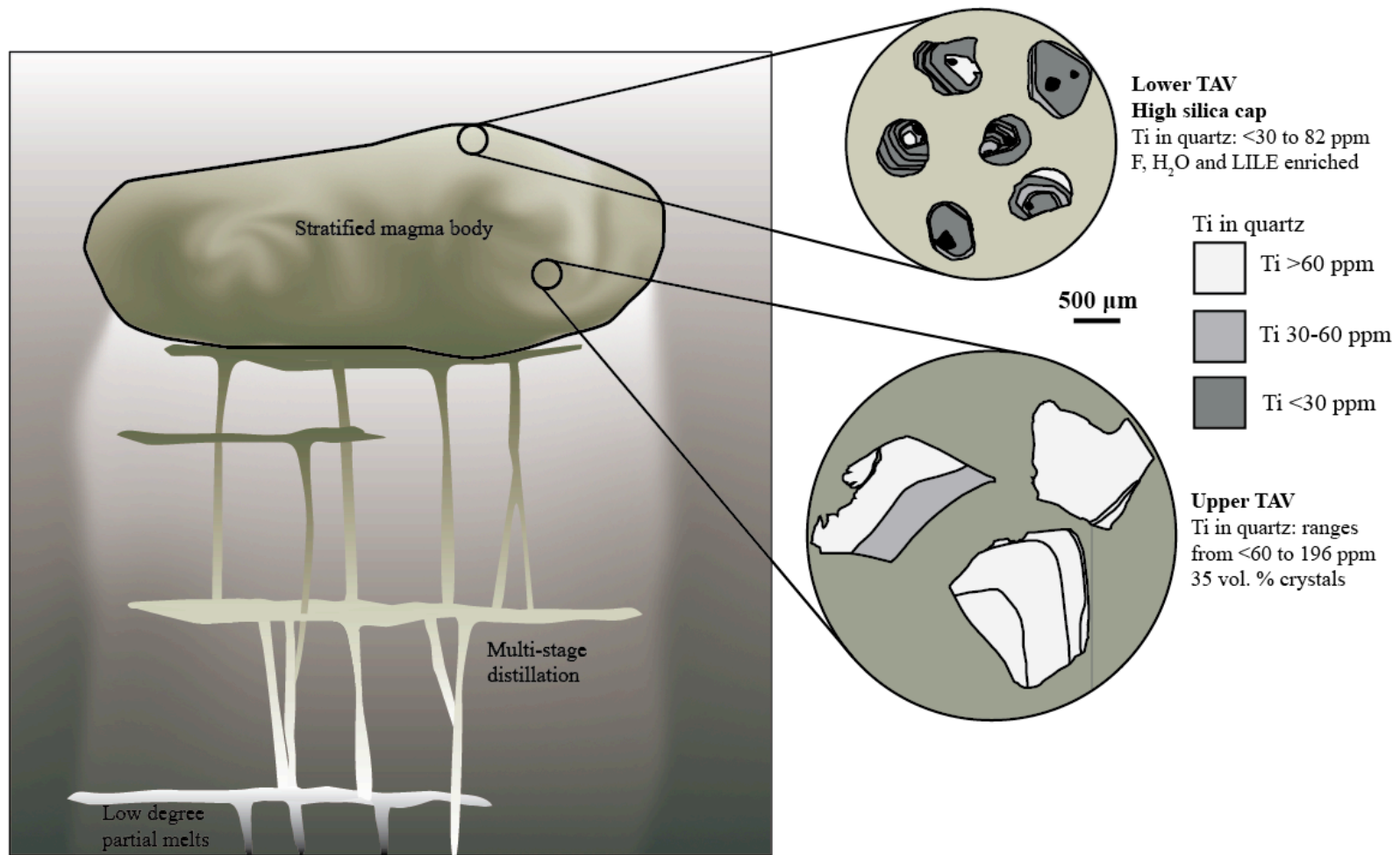
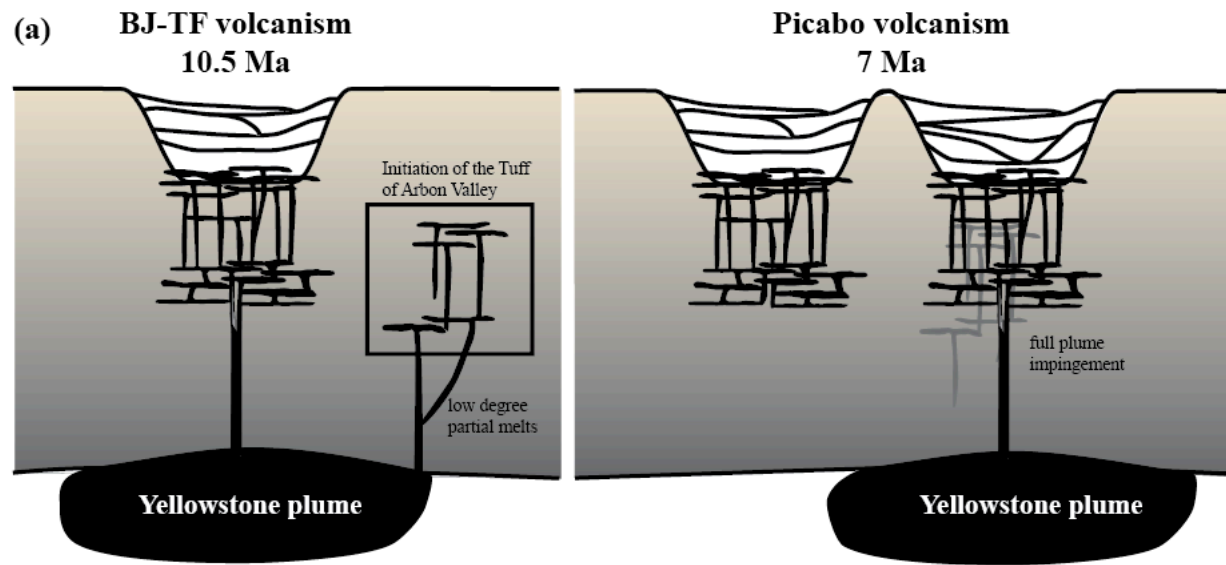


Fig. 15. Generation of the stratified TAV magma body through multiple episodes of magma injection, crystallization, and remelting or distillation. Quartz phenocrysts from the lower and upper tuff and corresponding CL zones of specified Ti concentrations are shown to scale to emphasize the change in size and Ti concentration.



(b) Multi-stage distillation model

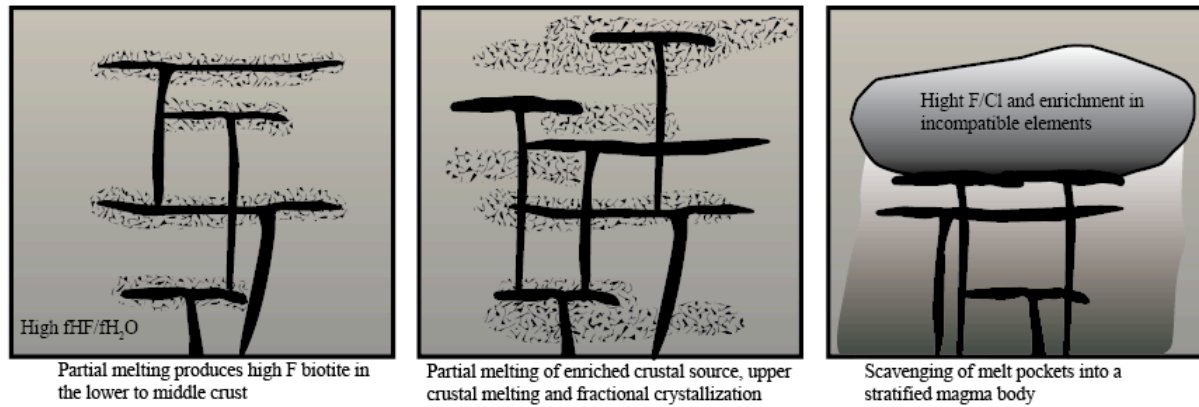


Fig. 16. a. Generation of the TAV in comparison to subsequent volcanism at the Picabo volcanic field, highlighting the importance of low degree partial melts versus full plume impingement. **b.** Three steps necessary for generation of the TAV.

Repeated injection and differentiation of basalt leads to multi-stage remelting/crystallization of already sequestered silicic pockets emplaced in the crust to produce a segregated and differentiating single magma body. This process is further facilitated by the concentration of volatiles in a high silica cap of the magma reservoir, low-degree partial melts derived from the Yellowstone plume, and previous melting of the Archean crust. The occasional bright cores and rims, and prevalent resorption and oscillatory zoning patterns in the cathodoluminescence images of the host quartz phenocrysts further support perturbed magma storage. This study emphasizes that the TAV and similar rhyolites in the SRP, such as the Jarbidge rhyolite, Huckleberry Ridge Tuff-Member C and Blacktail Tuff, are not as anomalous as previously considered and are instead the result of more extreme recycling, differentiation, mixing, and crustal melting in the middle to upper crust.

APPENDIX A

ADDITIONAL BACKGROUND INFORMATION

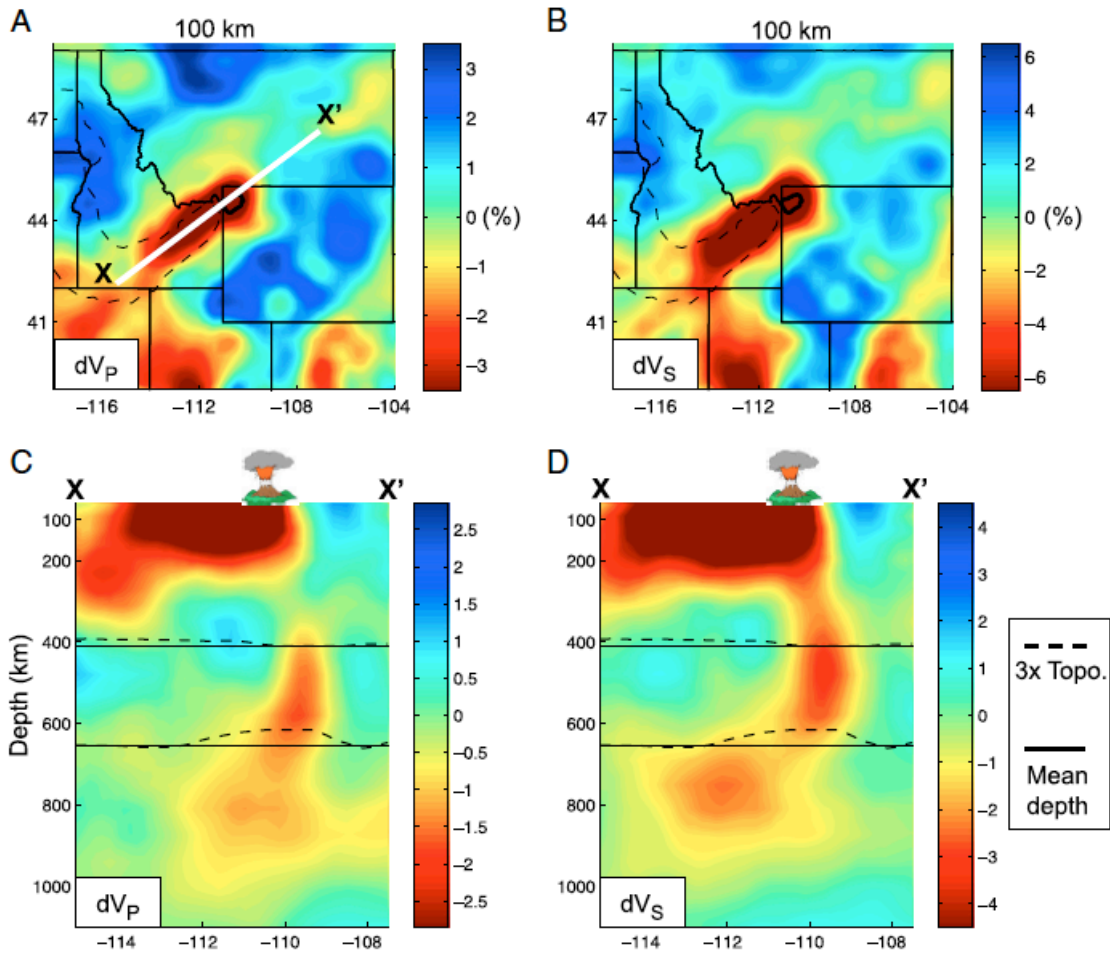


Fig. A1. Seismic tomography (V_p and V_s) cross-section through the Yellowstone caldera (Schmandt et al., 2012).

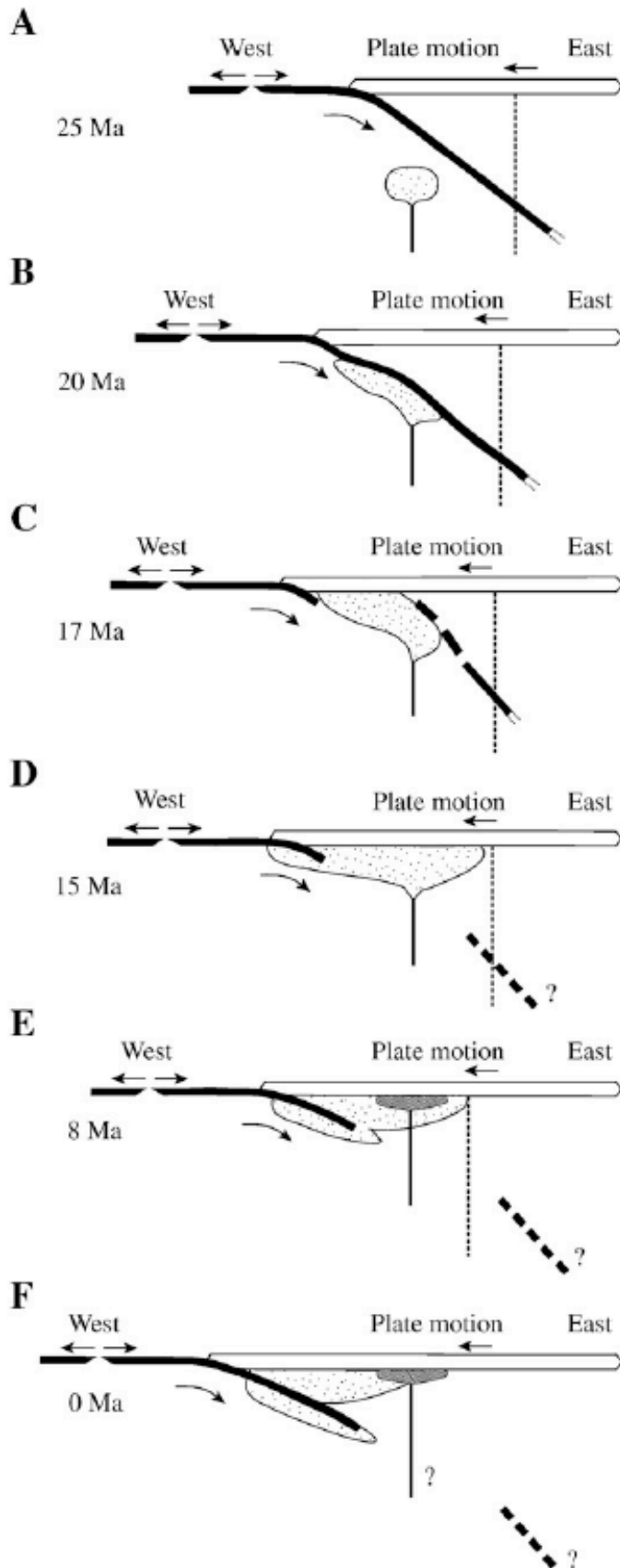


Fig. A2. Cross sectional schematic of the interaction between the subducting slab and the plume head through time. At 17 Ma the plume penetrates the slab and transition from the plume head to tail occurs at 8 Ma (white stippled: plume head and grey stippled: plume tail) (Pierce and Morgan, 2009).

APPENDIX B

DETAILED SAMPLE DESCRIPTIONS AND LOCATIONS

Lava-like ignimbrites can be difficult to distinguish from lavas in the SRP since these ignimbrites often lack pumice and lithic lapilli, and are densely welded and rheomorphic. In this study ignimbrites were identified primarily by field characteristics including: lateral traceability, low aspect ratio, presence of a basal vitrophyre, and fiamme.

Tuff of Arbon Valley (TAV): The TAV is the most regionally extensive unit found on both the northern and southern margins of the plain, and consists of two main parts: a lower poorly welded crystal poor (<5 to 10%) tuff with pumice, lithics and accretionary lapilli and an upper moderately welded crystal rich ($\geq 35\%$) tuff with planar bedding, interpreted to be an ash flow and surge deposit (Kellogg et al., 1994). This sequence contains biotite and amphibole, making it readily distinguishable from other SRP rhyolites. The type locality of the Tuff of Arbon Valley is the Cove, a site in the Blackfoot Mountains, where both the upper and lower tuff is present and the TAV reaches a thickness of ~ 100 m (Kellogg et al., 1994). At the Cove site no cooling breaks were observed between the lower and upper tuff, however it has been hypothesized that this unit represents two closely spaced eruptions (Anders et al., 2009). At the northern margin of the plain at least two outcrops of the TAV are present (Morgan and McIntosh, 2005) one that we sampled for this study at the edge of the Lemhi Range. These exposures suggest distal deposits and support a caldera source at the southern margin of the plain.

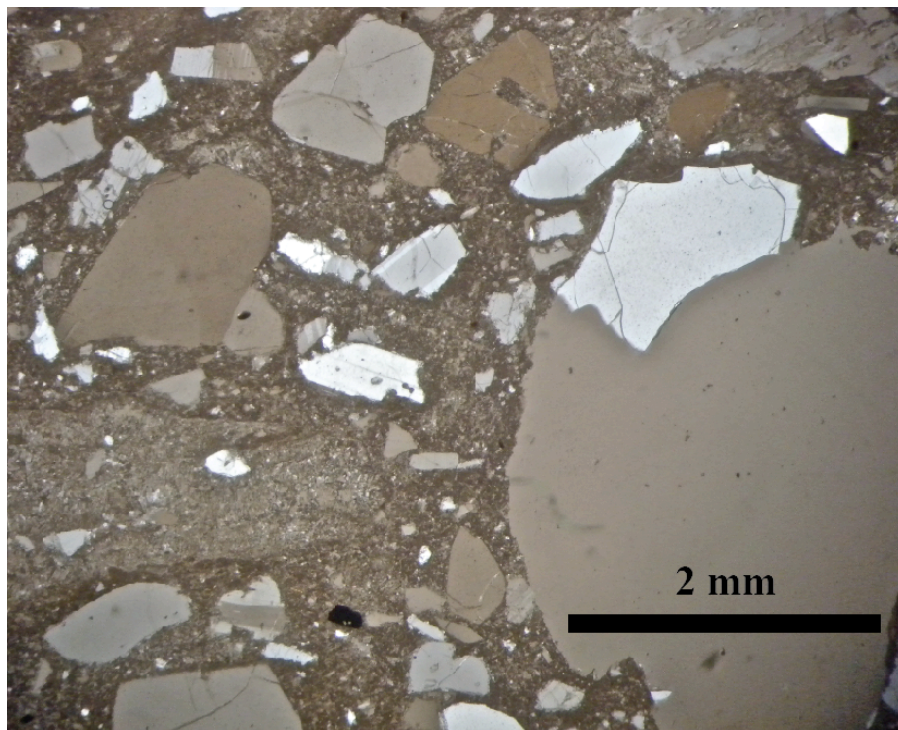


Fig. B1. Photomicrograph of the Tuff of Arbon Valley in plane polarized light.



Fig. B2. Photographs (taken by Ilya Bindeman) of the Tuff of Arbon Valley at the Cove sampling site in Idaho. Photograph a. captures the entire outcrop from the poorly welded base to the densely welded, crystal rich tuff at the top. The lower photograph, b., highlights stratification in the lower tuff.

Two-and-a-Half Mile rhyolite: A post-TAV biotite-bearing lava with a basal vitrophyre. It is located along the eastern margin of the Tabor cauldron and was likely a large volume lava sourced from the caldera ring fracture zone, similar to voluminous post-caldera lavas of the young and well-exposed Yellowstone caldera (Christiansen, 2001).

West Pocatello rhyolite: A densely welded lava-like ignimbrite (25 vol. % phenocrysts) that is laterally extensive with a low-aspect ratio, capping mountains south of Pocatello in the Bannock Range. This ignimbrite contains elongate fiamme-like structures up to 25

cm long as well as entablature jointing, and is found on the southern side of the plain. This unit is also found as a poorly-welded reworked deposit with laminar and trough cross-bedding.



Fig. B3. Photograph of fiamme-like structures in the West Pocatello rhyolite taken an outcrop off of Trail Creek Road near the town of Pocatello, ID.

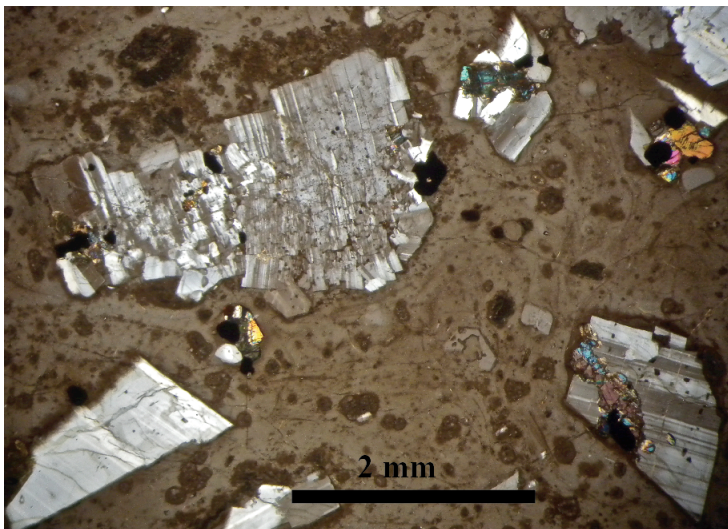


Fig. B4. Photomicrograph of the Tuff of West Pocatello rhyolite in cross polarized light.

Tuff of American Falls: A moderately welded and poorly sorted tuff containing abundant lithics and pumice up to a centimeter in size. Found solely on the southern side of the plain.

Stevens Peak and Stevens Peak 2 rhyolites: Stevens Peak rhyolite is a crystal poor (5-10 vol. % phenocrysts) lithophysae tuff with spherulites and a basal vitrophyre. The Stevens Peak 2 is also an ignimbrite found on an adjacent hilltop to the Stevens Peak rhyolite and is distinguishable by whole rock geochemistry and mineralogy (10-15 vol. % phenocrysts). Both are found solely on the southern side of the plain.

Tuff of Hawley Spring: A TAV-like rhyolite that was crystal rich (25 to 30 vol. % phenocrysts), biotite-bearing and highly altered. Found solely on the southern side of the plain.

Tuff of Lost River Sinks: A densely welded tuff with elongate weathered cavities and an associated basal vitrophyre. Specifically, the Tuff of Lost River Sinks is found at Howe Point, where it is underlying (or in continuation of) the Blacktail Creek Tuff, the first eruptive unit of the neighboring Heise volcanic field (Morgan and McIntosh, 2005). At this same location the poorly welded crystal poor section of the Tuff of Arbon Valley is found deposited in faulted paleovalleys adjacent to Miocene basalt.

Tuff of Little Chokecherry Canyon: A tuff with fiammé (up to 2 cm) and elongate glass shards, and is found on the northern side of the plain in the Pioneer Mountains.

INEL-1 borehole: The 3,159 m INEL-1 borehole penetrates 750 m of olivine tholeiite basalt interbedded with silt, sand and tuffaceous silt and approximately 2.5 km of rhyolites (Doherty et al., 1979). All samples except the shallowest are propylitically altered (McBroome, 1981) however much of this alteration appears to be isochemical except for sample 3686', which has a low major element total coupled with high K₂O/Na₂O and MgO (McCurry and Rodgers, 2008); this is common for propylitic alteration. Although these borehole samples are heavily altered some primary textures are preserved as well as phenocryst pseudomorphs and relics; based on these preserved petrographic features McCurry and Rodgers (2008) found samples 3686' and 10365' to contain 9% and 26% phenocrysts, respectively with plagioclase>>quartz, pyroxene, opaques±sanidine as well as accessory zircon and apatite. Sample 4686' (23% phenocrysts) contains sanidine>quartz>pyroxene, opaques and accessory zircon and apatite (McCurry and Rodgers, 2008).

Table B1.

Sample Localities of the main rhyolites that we use to define the Picabo volcanic field

Sample Name	Abbrev.	Location	Coordinates
West Pocatello rhyolite	PC-01	Trail Creek Road	N 42° 51.846, W 112° 30.848
Tuff of Arbon Valley	PC-14/12	The Cove	N 43° 14.493, W 112° 02.670
Two and a Half Mile rhyolite	PC-20	Blackfoot Mts	N 43° 00.722, W 112° 20.990
Tuff of Lost River Sinks	PC-25	Howe Point	N 43° 48.250, W 112° 50.894
Tuff of American Falls	PC-34	American Falls	N 42° 47.169, W 112° 50.270
Stevens Peak/Stevens Peak 2	PC-16/19	Stevens Peak	N 43° 8.167, W 112° 18*
Tuff of Chokecherry Canyon	PC-71	Antelope Creek Rd	N 43°41.543, W 113°38.429
Tuff of Hawley Spring	PC-76	Heise Cliffs	N 43°38.816, W 111°41.888°
2515', 3686', 4860', 10365'	INEL-1	-	
	Borehole		N 43.5802, W 112.996*

* Coordinates are from a different source, coordinates for the borehole are from Doherty et al. (1979) and coordinates for Stevens Peak are from Kellogg et al. (1988).

Literature used in data compilation for Fig. 1a:

- The base map and caldera boundaries not otherwise mentioned are modified from Coble and Mahood (2012).
- Heise caldera boundaries are from Morgan and McIntosh (2005) and Watts et al. (2011)
- Santa Rosa Calico, Jarbidge Mountain, Lake Owyhee boundaries are from Bruseke et al. (2008)

Major geologic units include:

- Columbia River Basalt province (Camp and Hanan, 2008)
- Steens Basalt (Coble and Mahood, 2012)
- Idaho batholith and Challis intrusives (Gaschnig et al., 2011)
- Challis and Absaroka volcanics (Konstantinou et al., 2012)
- Metamorphic core complexes (Konstantinou et al., 2012)
- Archean crystalline rocks (Nash et al., 2006)
- Quaternary olivine tholeiite lavas (Kuntz et al., 1992; Christiansen et al., 2002).

APPENDIX C

LASER FLUORINATION LINE INSTRUCTIONS

Main Reaction: $\text{SiO}_2 + \text{BrF}_5 \rightarrow \text{SiF}_4 + \text{O}_2$ and leftover reagent

CO_2 : reference gas

Main idea: O_2 doesn't freeze at liquid nitrogen temperatures so first few steps are to get rid of reagent and move the O_2 sample along. Then the carbon film converts sample to O_2 , which does freeze at liquid nitrogen temperatures.

- Always begin with adding reagent by turning the green handle below the surface for 5 seconds (for a sample ~1.4) while on the knobs around it are closed. Then freeze it in the left corner, closest to sample chamber.
- Then re-melt so it is trapped between the valves and sample chamber
- Laser the sample on the computer
 - Calibrate it when you first begin running
 - Always laser at 50% zoom
 - Hit fire and begin lasering and slowly increase until you begin seeing light
 - Slowly increase and never go above 28%
 - Garnet: Increase laser power to ~7% and then laser around edges to try to melt it into a ball (should react to form a white fluffy residue).
 - Plagioclase: Center beam on grains and slowly increase power
 - Quartz: Center beam on grains and slowly increase power to 16%, the sample will emit a lot of light, and you do not need to move the laser until the light emission begins to decrease. You should still increase the power at the end to make sure all sample has reacted. No residue should be left behind. If grains contain melt inclusions they may also jump so be careful in initial laser power increase.
- Freeze the left corner before opening any valves and freeze other three tubes by refilling the other three containers with liquid nitrogen
- Slowly open the first 3 valves one by one, waiting 5 seconds in between.
- Once it stops boiling you know most of the sample has moved
- Watch the gage (note what the baseline is) it will increase to ~1000 (if less than 1000, you will most likely have to use the cold finger) and then return to baseline and increase a tiny a bit.
- Turnoff the heater and close the valves to the left. Move the trap around the corner.
- Sample frozen so melt the U tube and glass tube and proceed to trap/freeze it in the corner
- Go to the computer and make sure you let out the previous sample (return bellow to 100) and wait for it to return to -3 on the mechanical pump (lower pump) before you turn on the diffusion pump
- Close valve and turn heaters on
- Look for kick, then turn heater off and freeze and move around the corner. Melt the tube with the carbon filter and the last U tube.

- Close valve and open front one to let it into the pin tube. When you open the valve look at the digital gage because this number divided by 10 is the approximate molar yield. If sample is below ~15 micromoles then you should use the cold finger. If samples is below 7 micromoles then there is a chance you will not be able to analyze this sample even with use of the cold finger and full compression of the bellow.

Computer

- When you begin in the morning do a peak center (don't touch until completed) and an auto focus (and pass to gas configuration).
- Left corner should always read Dual Inlet and CO₂
- When adjusting the bellows you always want the mv readings to be 50 mV of one another and pressure readings on the main screen to be of 0.8 (left should be 0.7 or 0.8 higher then left)
 - This is so there is not a pressure mismatch (balance between linearity and sensitivity).
- Before you can switch to the turbo pump make sure the reading is to the power of -3.

APPENDIX D
QUARTZ AND ZIRCON MOUNT MAPS

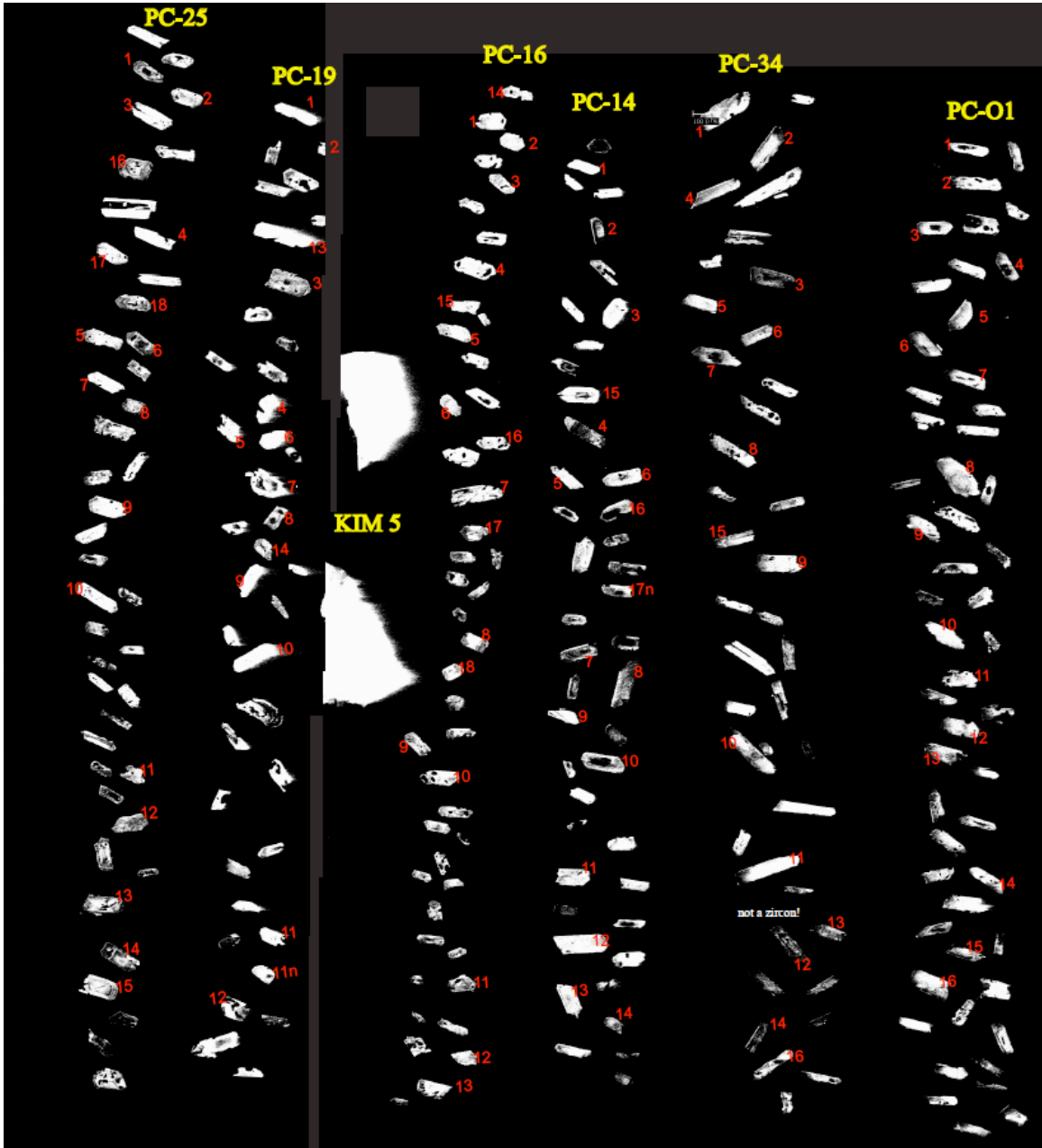


Fig. D1. Cathodoluminescence image of zircon mount used for geochronology and oxygen isotope measurements. Although not shown here, AS3 zircons are mounted to the left of sample PC-25 and were used as the U-Pb dating standard.

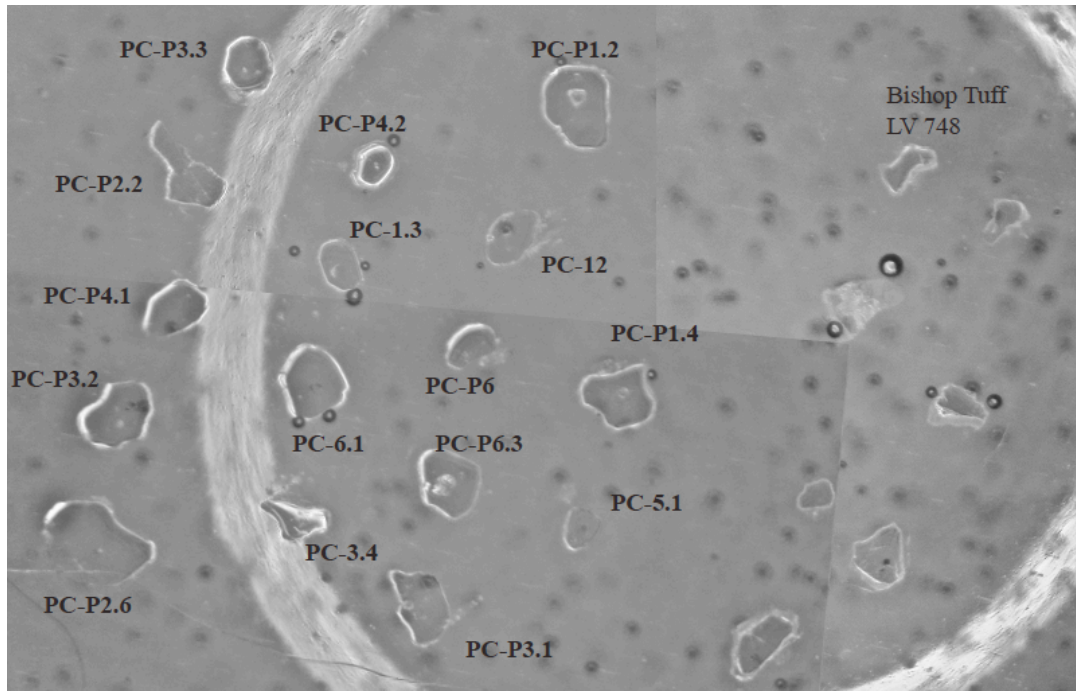


Fig. D2. Mount of doubly polished quartz-hosted melt inclusions. Bishop Tuff quartz phenocrysts are not doubly polished and are significantly thicker than the Picabo phenocrysts.

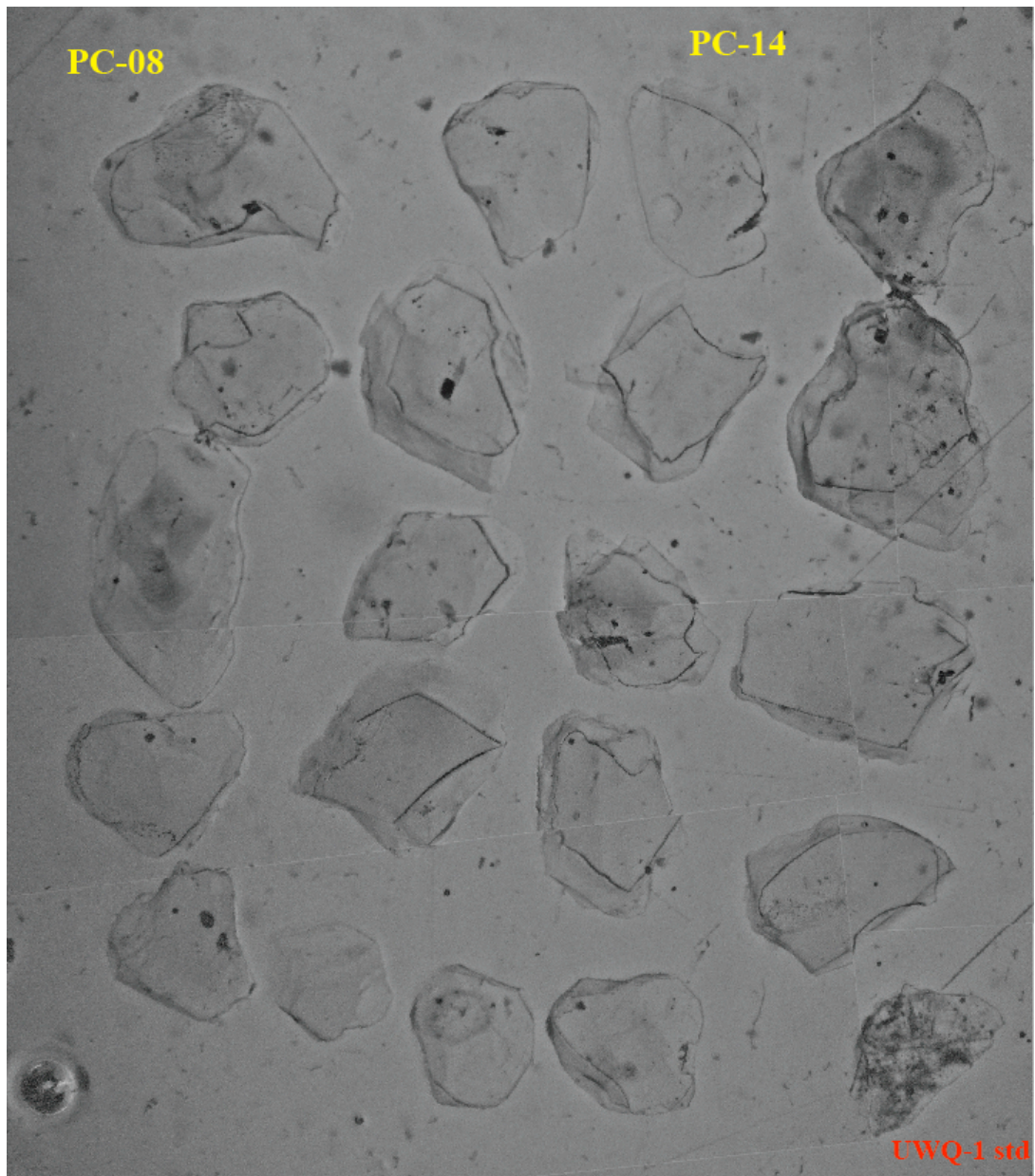


Fig. D3. Mount of ~1 to 3 mm quartz phenocrysts used for Ti measurements in quartz. This mount contains three fiducial marks that can be used to accurately reproduce the mount orientation used previously.

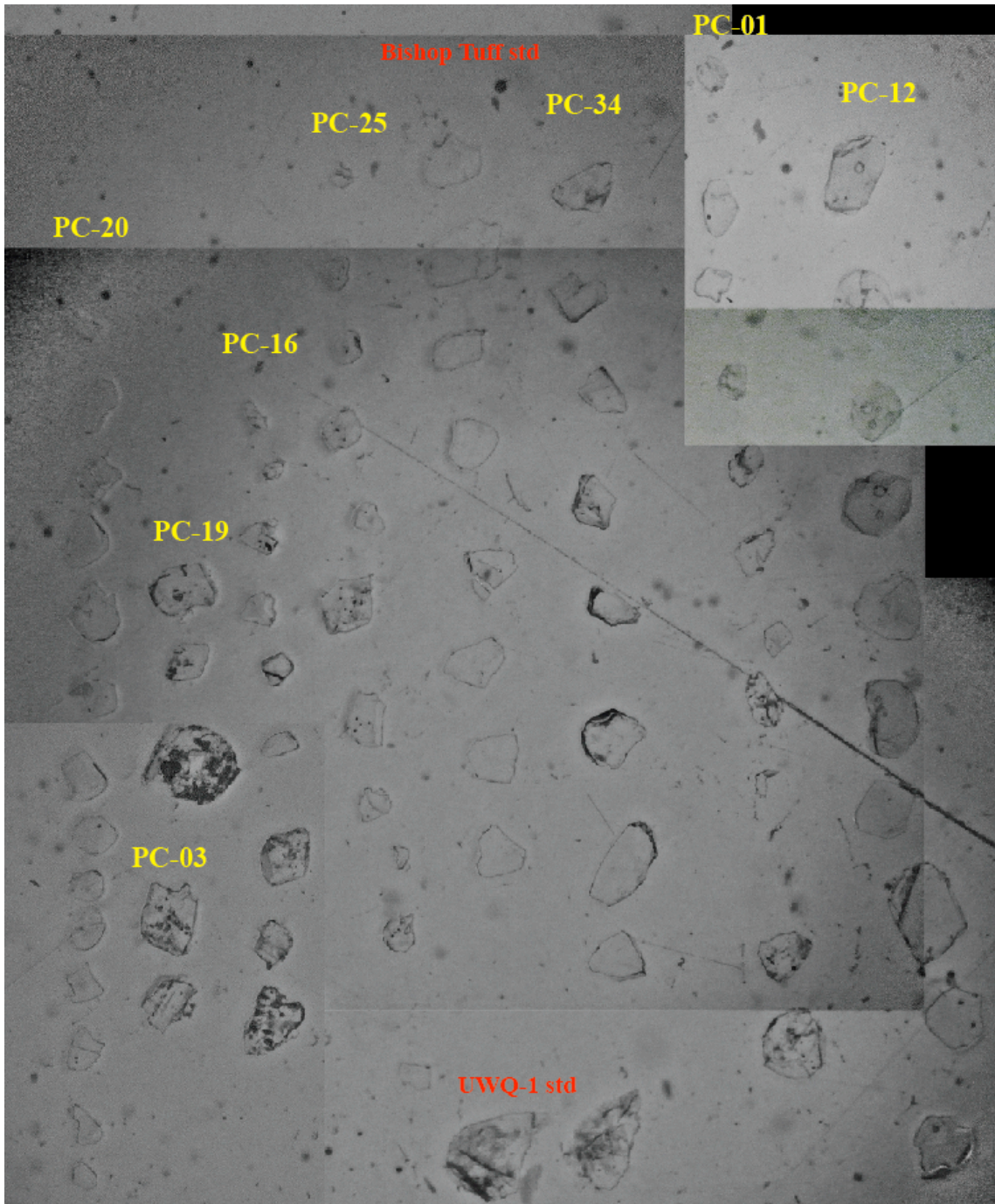


Fig. D4. Mount of <1 mm quartz phenocrysts used for Ti measurements in quartz. This mount contains three fiducial marks that can be used to accurately reproduce the mount orientation used previously.

APPENDIX E

ADDITIONAL GEOCHRONOLOGY TABLES

U-Pb zircon age probability distributions

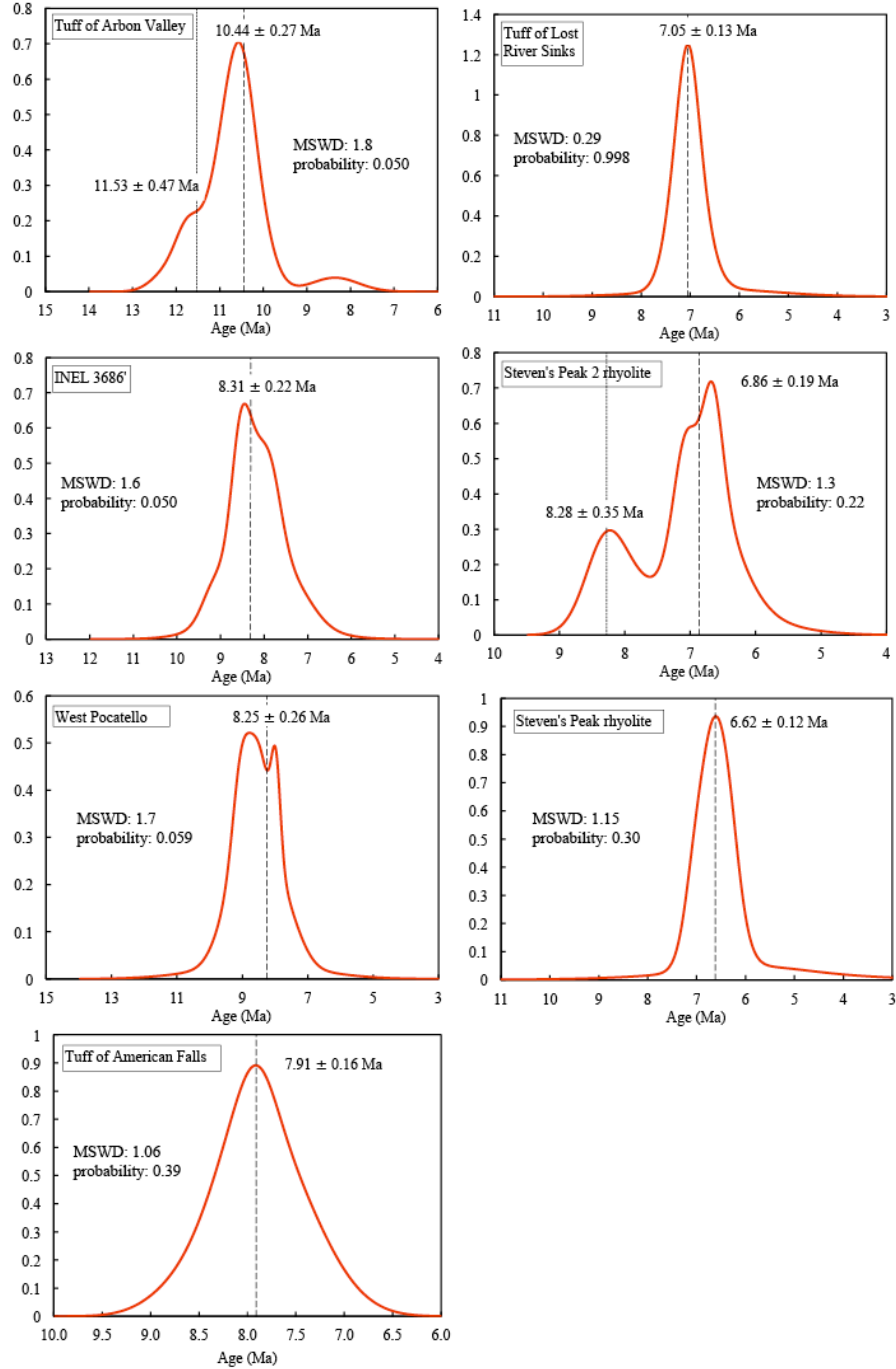


Fig. E1. Probability distributions of U-Pb ages for zircon data of the Tuff of Arbon Valley, INEL 3686', West Pocatello rhyolite, Tuff of American Falls, Tuff of Lost River Sinks, Stevens Peak 2 rhyolite and Steven's Peak rhyolite.

We use the U-Pb age to characterize the timing of volcanism and we do not interpret the variability to provide additional information on the residence time of zircon in the magma chamber. McCurry and Rodgers (2009) report U-Pb zircon ages for INEL-1 3686' and report a weighted mean of 8.27 ± 0.27 Ma (MSWD=1.8, probability=0.036) further supporting a correlation between the West Pocatello rhyolite and INEL-1 3686' rhyolite. Zircon ages and cumulative U-Pb age probabilities indicate recognizable inheritance only in the TAV (~11.5 Ma), West Pocatello rhyolite (2080 Ma and 335 Ma), and Stevens Peak 2 rhyolite (~8.26 Ma).

Table E1. a.

U/Pb ages, $\delta^{18}\text{O}$, $\epsilon_{\text{Hf}}(0)$, and $\epsilon_{\text{Hf}}(t)$ for individual zircon spots.

Sample_Spot location	ϵ_{Hf} (0)	ϵ_{Hf} (t)	2 s.e.	$^{206}\text{Pb}/^{238}\text{U}$ Age (Ma)	1 s.e.	$\delta^{18}\text{O}_{\text{SMOW}}$ (‰)	1 s.e.	U (ppm)
PC-25_1	-12.1	-11.9	0.9	7	0.17	4.7	0.38	1423
PC-25_2	-11.4	-11.2	1	6.92	0.29	4.38	0.38	517
PC-25_3	-10.8	-10.6	1.4	7.09	0.23	5.53	0.14	513
PC-25_16	-13.3	-13.2	1.4	7.22	0.24	4.32	0.27	469
PC-25_17	-11.7	-11.6	1.2	6.39	1.09	3.14	0.27	346
PC-25_4	-12.8	-12.7	1.3	7.16	0.3	4.84	0.38	218
PC-25_18	-11.8	-11.6	0.7	7.01	0.25	4.85	0.27	355
PC-25_5	-11.6	-11.5	0.9	7.13	0.37	4.97	0.38	204
PC-25_6	-13	-12.9	1.1	7.07	0.19	4.08	0.38	1008
PC-25_7	-11.1	-11	1.2	6.83	0.37	5.73	0.14	173
PC-25_8	-12.9	-12.7	1.2	7.13	0.24	4.62	0.14	315
PC-25_9	-10.6	-10.5	1.3	7.19	0.29	5.15	0.38	355
PC-25_10	-10.5	-10.3	1.4	6.96	0.22	4.76	0.38	480
PC-25_11	-13	-12.9	1.3	7.32	0.26	5.11	0.14	276
PC-25_12	-11.6	-11.5	0.7	6.77	0.28	4.49	0.14	451
PC-25_13	-12.8	-12.6	1.1	6.73	2.82	4.7	0.38	269
PC-25_14	-9.9	-9.8	0.9	6.61	1.57	4.05	0.38	248
PC-25_15	-10.9	-10.8	1.3	6.88	0.26	4.37	0.38	424
PC-19_1	-10.2	-10.1	1.4	6.78	0.38	2.73	0.38	123
PC-19_2	-10.6	-10.5	1.3	7.07	0.17	3.55	0.38	992
PC-19_13	-11	-10.9	1.3	6.96	0.45	2.57	0.27	82
PC-19_3	-12.8	-12.6	0.9	9.44	2.29	2.8	0.38	8298
PC-19_4	-10	-9.9	1.7	7.86	1.24	2.06	0.38	96
PC-19_5	-12.7	-12.6	1	7.11	0.2	4.1	0.38	875
PC-19_6	-11.8	-11.6	1.3	6.27	0.84	3.82	0.38	97
PC-19_8	-11.4	-11.2	1.1	6.55	1.56	3.93	0.38	1197
PC-19_14	-5.4	-5.3	1.2	8.4	0.28	2.03	0.14	893
PC-19_9	-9.6	-9.4	1.1	8.18	0.42	3.36	0.14	133
PC-19_10c	-6.3	-6.1	1.1	6.66	0.14	1.3	0.14	852
PC-19_10r	-	-	-	6.5	0.53	-	-	89
PC-19_11	-8.7	-8.5	1.6	6.52	0.39	2.66	0.14	114
PC-19_11n	-8.8	-8.6	1.2	6.64	0.42	3.13	0.14	89
PC19_12c	-	-	-	8.21	0.28	6.16	0.14	299
PC19_12r	-	-	-	7.8	0.38	-	-	131
PC19_7	-	-	-	6.66	0.19	6.44	0.14	432
PC-16_14	-8.2	-8	1.2	7.45	16.28	3.31	0.27	260
PC-16_1	-8.8	-8.7	1.5	6.68	0.26	3.36	0.38	268

PC-16_2	-8.9	-8.7	1	6.45	0.25	3.51	0.38	343
PC-16_3	-8.5	-8.4	1.2	6.2	0.27	3.26	0.38	382
PC-16_4	-9.1	-8.9	1	6.55	0.26	3.07	0.38	405
PC-16_15	-8.2	-8.1	1.1	7.04	0.19	3.35	0.27	385
PC-16_5	-8.7	-8.6	1	6.66	0.25	3.92	0.14	334
PC-16_6	-9.6	-9.5	1.1	6.61	0.19	2.75	0.38	595
PC-16_16	-8.8	-8.6	1.4	5.81	1.67	3.75	0.27	377
PC-16_7	-9.7	-9.6	1.4	6.37	0.18	4.84	0.14	557
PC-16_17	-8.5	-8.4	1.6	5.91	2.13	3.19	0.27	297
PC-16_8	-8.5	-8.3	1	6.24	0.2	3.06	0.14	295
PC-16_18	-7.6	-7.4	1.3	5.9	1.01	2.81	0.27	407
PC-16_9	-9.1	-8.9	1.2	6.61	0.22	3.42	0.38	404
PC-16_10	-8.4	-8.3	1.2	6.69	0.23	2.73	0.38	349
PC-16_11	-8.1	-8	0.9	6.84	0.23	3.08	0.38	348
PC-16_12	-10.3	-10.1	0.9	7	0.25	2.84	0.38	303
PC-16_13	-18.6	-18.5	1.4	7	0.27	5.32	0.14	382
PC-14_1	-28.2	-28	1.4	11	0.5	5.43	0.38	144
PC-14_2c	-27.7	-27.5	0.9	10.5	0.3	6.47	0.14	287
PC-14_2r	-	-	-	11.6	0.3	-	-	906
PC-14_3	-	-	-	11	0.4	6.38	0.38	335
PC-14_15	-28.8	-28.6	1	10.8	0.3	5.79	0.27	603
PC-14_4c	-27.8	-27.6	0.9	10.4	0.3	6.13	0.14	412
PC-14_4r	-	-	-	10.1	0.3	-	-	390
PC-14_5	-29.1	-28.9	1.7	10.5	0.3	6.24	0.38	250
PC-14_6	-27.9	-27.7	1	10.1	0.4	6.76	0.38	162
PC-14_16	-28.8	-28.6	1	11.8	0.3	6.09	0.27	7454
PC-14_17n	-27.2	-27	1.2	12.2	0.4	6.49	0.14	8531
PC-14_7	-25.6	-25.4	1.1	10.5	0.3	6.45	0.38	525
PC-14_8	-28.5	-28.3	1	11.1	0.3	6.51	0.14	214
PC-14_9	-27.7	-27.5	0.9	8.35	0.53	6.22	0.14	82
PC-14_10	-29.1	-28.9	1	10.8	0.3	6.08	0.38	2172
PC-14_11	-29	-28.8	0.8	10.6	0.5	6.8	0.38	301
PC-14_12	-27.1	-26.9	1.1	10.6	0.3	6.51	0.14	172
PC-14_13	-27.7	-27.4	1	10.3	0.4	6.29	0.38	196
PC-14_14	-28.1	-27.9	1.2	10.8	0.4	6.64	0.38	195
PC-34_1_1	-6.1	-5.9	1	7.93	0.53	0.83	0.14	73
PC-34_1_2	-6.6	-6.4	1.3	-	-	-	-	-
PC-34_2	-7.4	-7.2	1.1	8.09	0.3	4.77	0.14	217
PC-34_4	-5.5	-5.3	1.1	7.71	0.37	1.52	0.38	135
PC-34_3	-37.9	-37.8	1	7.9	0.18	4.74	0.14	1070
PC-34_5	-6.3	-6.1	1.1	7.55	0.4	1.49	0.38	108
PC-34_6	-6.8	-6.6	2.3	7.64	0.45	2.2	0.38	86
PC-34_7	-5.9	-5.7	1.8	8.11	0.33	1.4	0.38	170
PC-34_8	-5.4	-5.2	1.1	8.11	0.3	1.29	0.38	193
PC-34_15	-4.8	-4.6	2.1	7.87	0.26	2.09	0.14	215
PC-34_9	-5.4	-5.3	1.3	7.17	0.36	1.75	0.38	128
PC-34_10c	-6.1	-5.9	1.2	8.27	0.37	1.22	0.38	161
PC-34_10r	-	-	-	8.7	0.34	-	-	123
PC-34_11	-5.3	-5.2	1.3	7.71	0.35	2.02	0.38	108
PC-34_12	-38.1	-38.1	1.6	-	-	-	-	-
PC-34_13	-5.7	-5.5	1.1	7.81	0.37	1.66	0.38	195
PC-34_14	-4.9	-4.7	1.6	7.49	0.32	2	0.38	134
PC-34_16	-4	-3.9	1.1	8.17	0.34	2.25	0.27	144

PC-01_1	-6.9	-6.7	1.8	557	15	-	-	180
PC-01_2	-5.5	-5.3	1.7	9.43	0.46	1.01	0.38	106
PC-01_3c	-8.8	-8.6	1.5	9.08	0.23	2.75	0.14	780
PC-01_3r	-	-	-	9.05	0.5	-	-	113
PC-01_4	-4.5	-4.4	1.3	8.61	1.76	-0.33	0.38	429
PC-01_5	-5.8	-5.6	0.9	7.91	0.36	1.31	0.14	109
PC-01_6	-4.3	-4.2	1.1	7.97	0.14	0.98	0.38	681
PC-01_7	-5.9	-5.8	1.3	8.93	0.31	1.11	0.14	397
PC-01_8	-47.2	-1.5	1.1	2080	60	-	-	67
PC-01_9	-5.7	-5.6	1.1	8.55	0.33	1.48	0.38	193
PC-01_10	-4.6	-4.5	1.4	8.41	1.67	1.05	0.38	101
PC-01_11	-3.3	-3.2	1.9	8.64	0.48	1.4	0.38	99
PC-01_12	-4.7	-4.5	1.4	8.21	0.45	2.49	0.14	94
PC-01_13	-6.7	-6.5	1.3	8.55	0.35	0.97	0.38	130
PC-01_14	-4.6	-4.4	1.4	8.96	0.48	1.95	0.14	130
PC-01_15	-4	-3.9	1.3	8.38	0.31	1.26	0.38	169
PC-01_16	-4.7	-4.5	1.2	7.47	0.42	1.63	0.38	56
PC-71_1	-8.3	-8.1	1.0	9.59	0.49	1.90	0.15	197
PC-71_2	-7.4	-7.2	0.8	9.28	0.37	1.53	0.15	253
PC-71_3	-6.4	-6.1	0.7	9.51	0.43			255
PC-71_4	-7.7	-7.5	0.8	10.1	0.6	1.66	0.13	253
PC-71_5	-8.6	-8.4	0.8	9.91	0.48	1.74	0.13	397
PC-71_6	-7.7	-7.4	1.0	9.68	0.43	1.93	0.13	198
PC-71_7	-8.2	-8.0	1.4	10.1	0.6	1.55	0.13	127
PC-71_8	-5.5	-5.3	1.0	8.99	0.88	1.76	0.12	219
PC-71_9	-9.9	-9.7	0.8	10.8	0.3	0.98	0.12	5353
PC-71_10	-7.5	-7.3	0.8	9.46	0.35	2.00	0.12	292
PC71_11c	-	-	-	9.79	0.25	1.13	0.12	7383
PC71_11r	-	-	-	8.50	0.35	1.84	0.12	223
PC-76_1	-30.1	-29.9	0.9	6.33, 7.15	0.56, 0.78, 2.7,	5.21	0.15	1835, 1081, 317,
PC-76_2	-33.4	-33.2	1.1	15.9, 14.2	3.7	5.90	0.15	348
PC-76_3	-34.4	-34.2	1.0	9.4	0.3	4.20	0.15	9281
PC-76_4	-26.8	-26.6	1.1	-	-	-	-	-
PC-76_5	-34.3	-34	1.2	-	-	-	-	-
PC-76_6	-29.8	-29.6	0.9	-	-	-	-	-

Individual zircon analyses of oxygen isotopes, hafnium isotopes, and U-Pb ages. All analyses targeted zircon cores, however when both a core and rim measurement were possible and analyzed we have annotated the analysis with c for core and r for rim. Grey boxes indicate data that was excluded due to large errors. Since sample PC-76 geochronology is extremely variable, an age of 9.4 Ma was used for the initial ϵ_{Hf} calculation.

Table E1. b.

Additional geochronology and oxygen isotope data of individual zircons of the INEL-1 drillcore.

Sample	Spot location	$^{206}\text{Pb}/^{238}\text{U}$ Age (Ma)	Std error	$\delta^{18}\text{O}_{\text{SMOW}}$ ‰
INEL-1	3686_1c	8.56	0.20	0.75
INEL-1	3686_1r	-	-	0.42
INEL-1	3686_2r	8.44	0.37	1.97
INEL-1	3686_3c	7.24	0.42	0.09
INEL-1	3686_3r	7.94	0.41	0.01
INEL-1	3686_4c	8.37	0.30	2.42
INEL-1	3686_4r	7.90	0.36	2.51

Table E1. c.

Additional oxygen isotope data of individual zircons of the Blacktail Creek Tuff.

Blacktail Creek Tuff	$\delta^{18}\text{O}_{\text{SMOW}}$ ‰	Std error
95_2001a_z15_1	4.59	0.15
95_2001a_z15_2	4.36	0.15
95_2001_z20_1	4.15	0.15
95_2001_z27_1	4.75	0.15
95_2001_z27_2	4.77	0.15
95_2001_z28_1	4.57	0.15
95_2001_z28_2	4.49	0.15
95_2001_z30_1	5.49	0.15
95_2001_z30_2	5.64	0.15

APPENDIX F

ADDITIONAL GEOCHEMICAL DATA, FIGURES, AND ANALYSIS

Table F1.

Whole rock geochemistry analyzed by XRF at Washington State University. Major elements are normalized and trace elements are un-normalized.

	West Pocatello PC-01a	Lower TAV PC-12a	Upper TAV PC-14a	Stevens Peak PC-16a	Stevens Peak 2 PC-19a	2 and ½ Mile PC-20a	Lost River Sinks PC-25a	TAF PC-34a
SiO ₂	74.16	76.90	73.40	76.35	74.74	76.95	75.18	67.73
TiO ₂	0.42	0.11	0.40	0.24	0.53	0.15	0.29	0.82
Al ₂ O ₃	12.77	12.84	14.20	12.34	12.35	12.49	12.96	15.47
FeO*	2.57	1.29	2.25	1.36	1.83	1.17	1.84	4.77
MnO	0.05	0.09	0.02	0.04	0.08	0.02	0.03	0.08
MgO	0.20	0.41	0.16	0.21	0.31	0.11	0.33	0.63
CaO	1.28	0.68	1.99	0.76	1.78	0.89	0.98	2.46
Na ₂ O	2.95	1.96	3.12	3.04	3.71	2.83	2.67	3.61
K ₂ O	5.55	5.71	4.38	5.61	4.60	5.36	5.67	4.26
P ₂ O ₅	0.06	0.02	0.09	0.05	0.07	0.03	0.04	0.17
Tot _{unnorm}	95.32	90.65	96.64	94.78	97.31	95.55	94.79	94.69
Ni	4.6	4.5	5.5	1.6	1.6	1.9	4.8	6.8
Cr	3.9	12.3	6	4.2	4	3.4	5.6	11.4
Sc	4.1	10.3	6.8	2.8	5.6	3.1	2.5	7.4
V	7.5	10.7	21.6	8.5	8.1	2.9	6.8	32.1
Ba	1085.6	102.7	2269.4	888.2	1044	909.6	837.5	1869.6
Rb	165.4	373.3	97	167	149.1	190.2	176.7	114.2
Sr	87.2	17	214.8	27.3	95.2	52.6	69	174.5
Zr	523	95.2	301.3	234.7	510.4	124	299.6	719.8
Y	62.4	106.9	44.5	57.6	65.6	31.3	49.9	54.7
Nb	46.2	40.9	22.1	43.4	44.3	15.4	35.3	40
Ga	18.9	19.3	16.9	16.7	18.1	16.4	16.8	21
Cu	2.7	2.2	3.2	2.5	1.8	3.3	2.2	9.9
Zn	66.4	46.6	42.5	56.8	75.7	25.8	57.8	84.4
Pb	25.3	49.5	25.4	26.9	31	32.6	28.7	23
La	74.6	16.9	109.2	67.9	69.9	45.1	63.8	67.2
Ce	143.4	35.3	185.1	132.4	132.9	89.9	119.5	125.2
Th	25.6	27.2	14.5	27	24.2	27.6	29.4	18.4
Nd	59.2	20.4	69.1	53	57.2	32.9	44.3	54.6
U	8.1	11	3.3	8.3	6.5	5.1	8	6.1

*from McCurry and Rodgers (2009).

Table F1 continued

	PR reworked	HB (Tsr2)	CM	JS _L	JS _U	JS _M	ID 2	ID 3	CC	HS	Borehole INEL-1* INEL 3686'
	PC-37	PC-52	PC-61	PC-62	PC-63	PC-65	PC-68	PC-69	PC-71	PC-76	
SiO ₂	75.59	77.44	70.59	72.72	74.44	74.29	65.14	65.54	74.06	74.98	73.16
TiO ₂	0.107	0.077	0.714	0.507	0.490	0.516	0.756	0.718	0.368	0.230	0.48
Al ₂ O ₃	12.64	12.65	13.06	12.89	12.55	12.62	16.38	16.86	12.62	13.29	12.90
FeO*	1.14	1.00	4.15	3.24	2.76	3.22	4.30	3.56	2.41	1.78	2.93
MnO	0.047	0.028	0.070	0.057	0.048	0.028	0.072	0.061	0.043	0.013	0.14
MgO	0.42	0.05	0.69	0.40	0.29	0.30	1.47	1.04	0.23	0.25	0.84
CaO	0.82	0.83	2.08	1.66	1.44	1.01	3.70	3.65	1.28	0.97	3.46
Na ₂ O	3.35	3.57	3.61	3.40	2.93	3.15	2.92	3.44	3.26	3.55	1.90
K ₂ O	5.51	4.33	4.69	4.90	4.97	4.80	5.01	4.89	5.48	4.74	4.13
P ₂ O ₅	0.362	0.013	0.358	0.208	0.079	0.066	0.261	0.237	0.246	0.191	0.07
Tot _{unnorm}	94.71	97.8	97.24	97.30	96.97	98.17	96.26	97.82	96.89	96.78	94.58
Ni	0	0	5	3	3	4	8	12	3	4	-
Cr	12	3	13	6	5	4	20	27	5	4	-
Sc	7	2	7	6	6	7	8	8	5	2	-
V	7	1	29	16	11	11	72	69	10	16	-
Ba	121	1478	979	1044	1081	1135	1614	1870	1060	883	1090
Rb	177	111	158	170	164	160	175	156	174	170	129
Sr	27	79	110	92	87	97	582	682	74	66	118
Zr	109	86	576	496	511	639	295	263	468	216	523
Y	61	34	59	60	65	82	26	24	68	30	-
Nb	43.5	14.9	43.0	43.4	45.7	50.7	24.0	22.2	45.3	31.8	-
Ga	16	15	19	19	20	20	19	20	21	19	-
Cu	6	2	5	6	4	5	13	16	7	3	-
Zn	37	31	74	67	67	86	60	54	68	50	-
Pb	37	31	25	25	26	25	22	20	26	25	-
La	32	36	75	78	80	89	59	51	85	76	-
Ce	72	71	147	149	149	145	110	94	158	131	-
Th	26	21	24	28	28	26	22	18	31	28	32.3
Nd	34	25	59	60	63	75	45	38	64	47	79
U	7	6	7	7	7	7	7	5	7	5	5.3
Cs	2	0	5	4	1	1	10	4	2	2	-

Table F2.

Summary of the age and $\delta^{18}\text{O}$ of various Snake River Plain units between 10.4 and 6.6 Ma. The Ar-Ar and K-Ar ages are derived from a: Konstantinou et al. (2012); and b: Pope (2002). The $\delta^{18}\text{O}$ melt composition was calculated from the quartz and plagioclase phenocryst $\delta^{18}\text{O}$ measured compositions from known fractionation factors between the mineral and melt for the temperature range of 700 to 850°C (Bindeman et al., 2003; Bindeman and Valley, 2003).

Unit	Sample	Location	Abbrev.	Age (Ma)	$\delta^{18}\text{O}$ average (‰)		
					Qtz	Plag	Melt
Idavada 1	PC-67	Antelope Cr Rd	ID 1	-	-	7.46	7.0
Idavada 2	PC-68	Antelope Cr Rd	ID 2	-	-	7.35	6.9
Idavada 3	PC-69	Antelope Cr Rd	ID 3	-	-	7.14	6.6
Lower Jim Sage	PC-62	JS Mts	JS _L	9.46 ± 0.09 - 9.44 ± 0.10 ^a	-	2.27	2.8
Upper Jim Sage	PC-63	JS Mts	JS _U	8.21 ± 0.15 ^a	-	3.47	4.0
Cotterel Mountains	PC-61	Cotterel Mts	CM	-	-	2.49	3.0
Hawkins Basin (Tsr2)	PC-52	Bannock Range	HB 2	6.63±0.04 ^b	7.92	-	7.4
Hawkins Basin (Tsr3)	PC-56	Bannock Range	HB 3	-	-	6.34	6.8
Hawkins Basin (Tsr4)	PC-55	Bannock Range	HB 4	6.09±0.64 ^b	-	-	-

Table F3.

Petrographic summary of Picabo rhyolites, with volume percent phenocrysts, absence or presence of glomerocrysts, and order of abundance. Abundance abbreviations are Q: quartz, P: plagioclase, S: sanidine, C: clinopyroxene, O: orthopyroxene, F: Fe-oxide opaque minerals, B: biotite, H: hornblende, Ch: chevkinite, Al: allanite, Zr: zircon, and Ap: apatite. Samples annotated (a) were analyzed by McCurry (2009). It remains unknown whether chevkinite, allanite and apatite are present in samples other than the Tuff of Arbon Valley.

Unit	Sample	Abbrev	% Phenocrysts	Glomerocryst	Order of Abundance
Tuff of Arbon Valley (upper)	PC-08	TAV _U	35	N (very few)	-
Tuff of Arbon Valley (upper)	-	TAV ^a	-	-	S, Q, P, B-O, F (minor Ch, Al, Zr, Ap) ^a
Tuff of Arbon Valley (lower)	-	TAV ^a	-	-	S, Q, P, B, H, F (minor Ch, Zr, Ap) ^a
Two and a Half Mile Rhyolite	PC-20	TFM	10 to 15	Y	Q, P, S, B (minor Zr)
West Pocatello rhyolite	PC-01	PR	25	Y	P, Q, S, C, O, F (minor Zr)
Tuff of Lost River Sinks	PC25	TLRS	15 to 20	N	P, Q, S, C, F (minor Zr)
Rhyolite of Steven's Peak 2	PC-19	SP2	10 to 15	Y	P, S, C, O, F (minor Zr)
Rhyolite of Steven's Peak	PC-16	SP	5 to 10	N	P, S, C, O, F (minor Zr)

Table F4.

Summary of temperature estimates for Picabo rhyolites. Liquidus temperatures (liq.) were estimated using rhyolite MELTS. The liquidus temperatures at the NNO and QFM buffers reflect the first appearance of spinel. The liquidus temperatures reflecting the appearance of feldspar (fspar) or quartz were calculated at a QFM oxygen fugacity. All three fspar refers to the appearance of albite, anorthite, and sanidine. Liquidus temperatures were calculated at a pressure of 1.5 kilobars and 3-wt% H₂O (using a water content of 1.5 wt. % would shift temperatures upwards by ~50°C). Zircon saturation temperatures were calculated from whole rock compositions, specifically major elements and zirconium (Miller et al., 2003; Hanchar and Watson, 2003).

	Zrc. Sat.	Liq. (NNO)	Liq. (QFM)	Liq: app of fspar/quartz	Observation
*Tuff of Arbon Valley (upper)	835	919	906.84	877	all three fspar
*Tuff of Arbon valley (lower)	754	869	871.48	842	quartz
*Tuff of Little Chokecherry Canyon	860	942	929	832	all three fspar
Two and a Half Mile Rhyolite	765	832	828	827	quartz
*INEL 3686'	861	954	948	856	all three fspar
*West Pocatello rhyolite	877	953	940	833	all three fspar
Tuff of American Falls	888	1031	1018	916	all three fspar
Hawley Spring	806	884	872	842	all three fspar
Tuff of Lost River Sinks	837	908	895	816	all three fspar
Rhyolite of Steven's Peak 2	862	900	891	859	all three fspar
Rhyolite of Steven's Peak	813	862	851	816	all three fspar
Lower Jim Sage	856	978	965	853	all three fspar
Upper Jim Sage	874	957	944	834	all three fspar

Table F5.

Summary of whole rock $\delta^{18}\text{O}$ of Challis intrusive samples (samples provided by Richard Gaschnig).

Sample ID	$\delta^{18}\text{O}$ whole rock	s.d.
07RMG10	2.85	0.014
07RMG23	9.36	0.031
07RMG34	6.84	0.024
07RMG51	6.19	0.033
07RMG64	6.23	0.035
07RMG65	8.99	0.027
08AMT019	8.17	0.018
08RAB026	8.04	0.035
08RMG32	8.79	0.024
10RL894	6.30	0.023
10RL897	6.58	0.022

Table F6.Whole rock ϵ_{Hf} measurements of select Picabo rhyolites.

Sample	$^{176}\text{Hf}/^{177}\text{Hf}$	$\epsilon_{\text{Hf}}(0)$	2 SE
PC-76	0.281941	-29.9	0.2
PC-69	0.282045	-26.2	0.2
PC-71	0.282627	-5.6	0.2

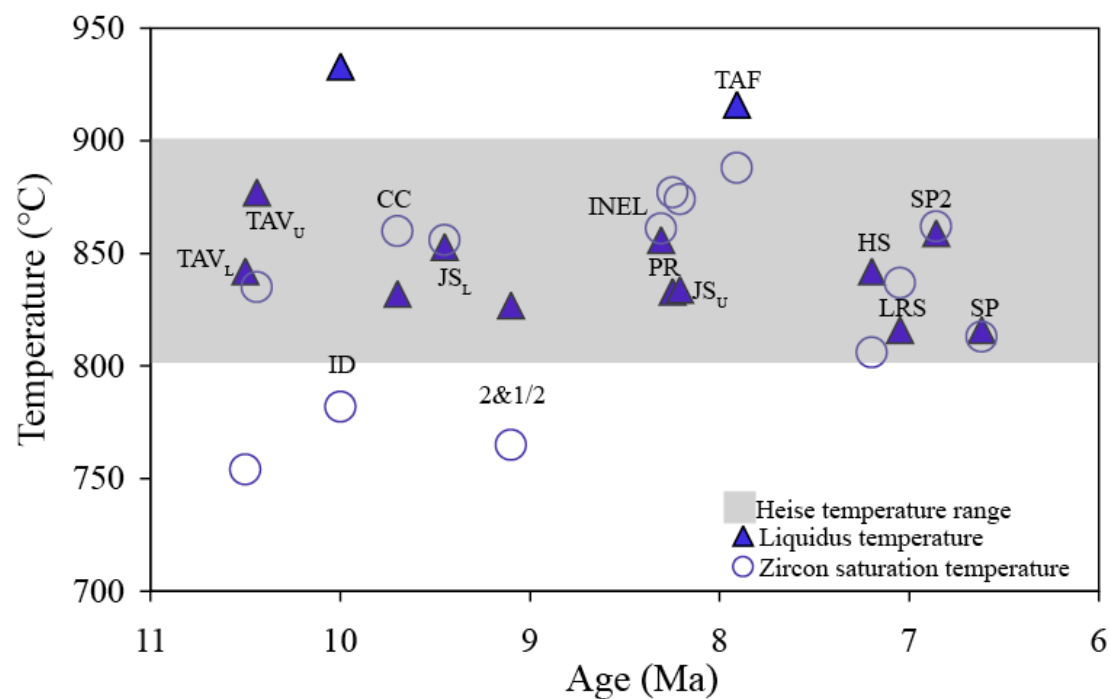


Fig. F1. Temperature of Picabo rhyolites calculated from rhyolite MELTS liquidus temperatures (represent the first appearance of feldspar or quartz, and were calculated at a pressure of 1.5 kilobars, 3-wt% H₂O, and QFM oxygen fugacity), zircon saturation temperatures.

Geothermometry for the Tuff of Arbon Valley was previously determined for feldspar and Fe-Ti oxide pairs from the basal airfall unit of the Tuff of Arbon Valley and indicated a temperature of $733 \pm 15^\circ\text{C}$ (Henshaw, 2002). However, ilmenite-magnetite thermometry and thermodynamic modeling by Henshaw (2002) yielded discordant results. Chemical disequilibrium between the Fe-Ti oxides as well as the low feldspar and Fe-Ti oxide temperatures, which deviate from liquidus, zircon saturation and Ti in quartz temperatures, indicate that many of the minerals present in the TAV are in disequilibrium.

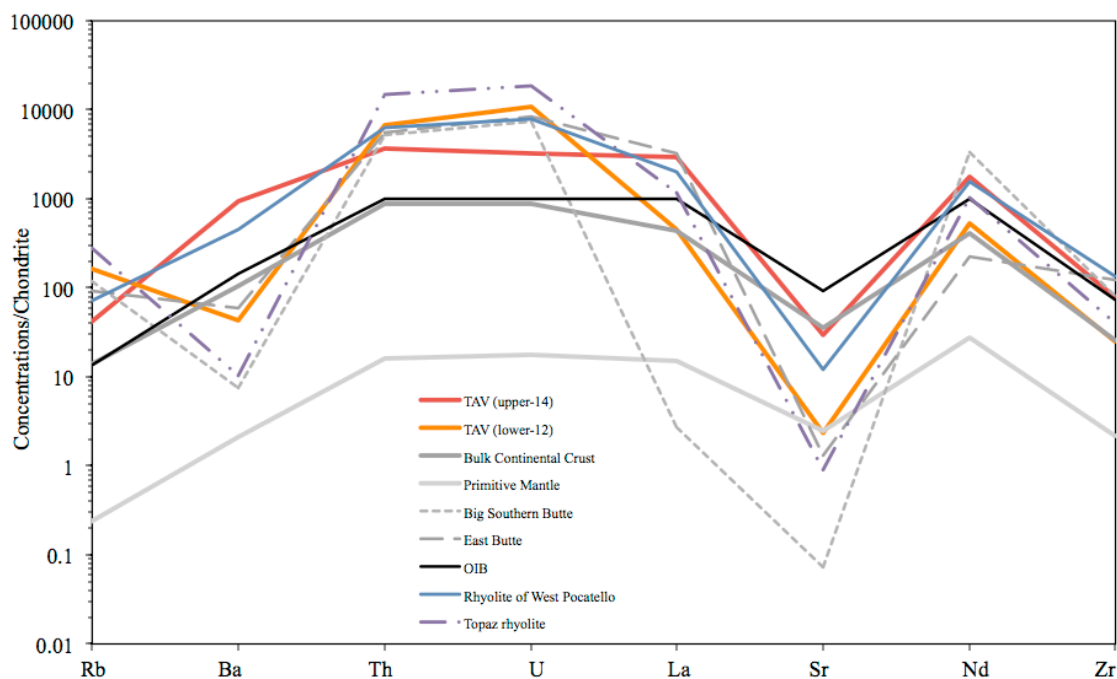


Fig. F2. Trace element concentrations of Picabo rhyolites, bulk continental crust (Taylor and McLennan, 1985), primitive mantle (Taylor and McLennan, 1985), Big Southern Butte and East Butte (McCurry et al., 2007), OIB (Taylor and McLennan, 1985) and topaz rhyolites (Christiansen et al., 2007). All concentrations are normalized to chondrite (Cl) (McDonough and Sun, 1995).

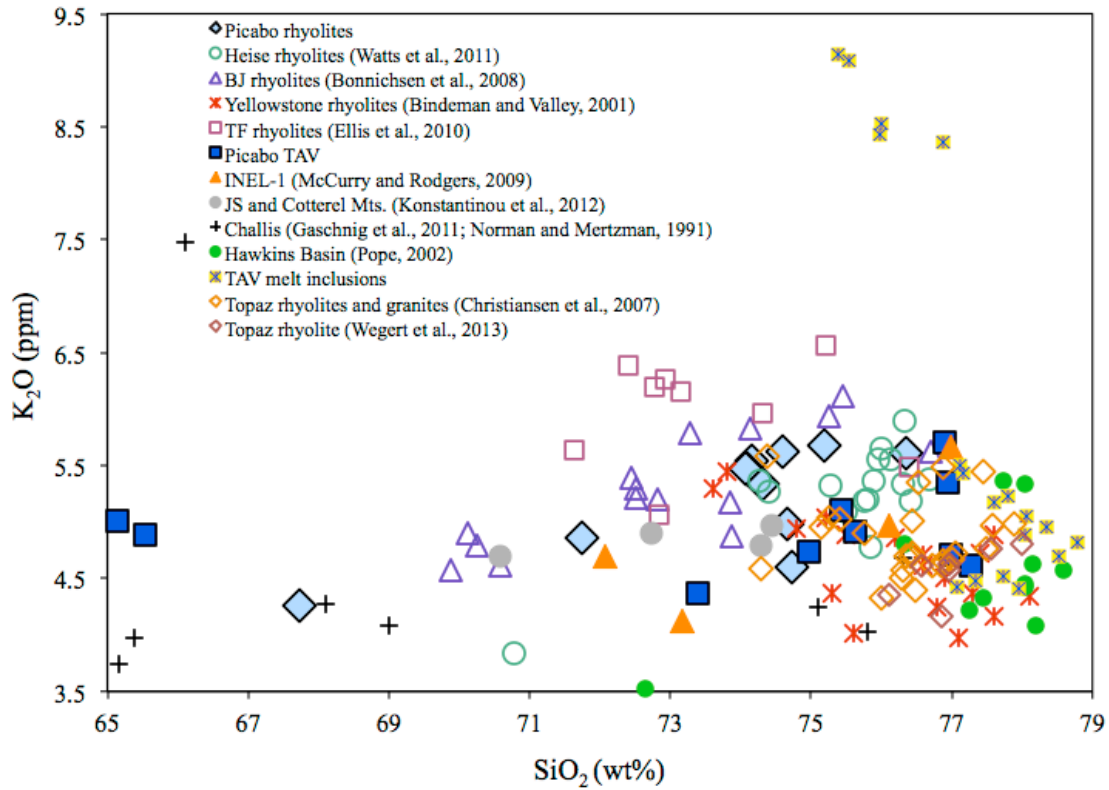


Fig. F3. a. K₂O versus SiO₂ for Picabo rhyolites in comparison to surrounding SRP volcanic centers, INEL-1 borehole samples, Jim Sage and Cotterel Mountain volcanics, Challis volcanics and intrusives, and Hawkins Basin volcanics.

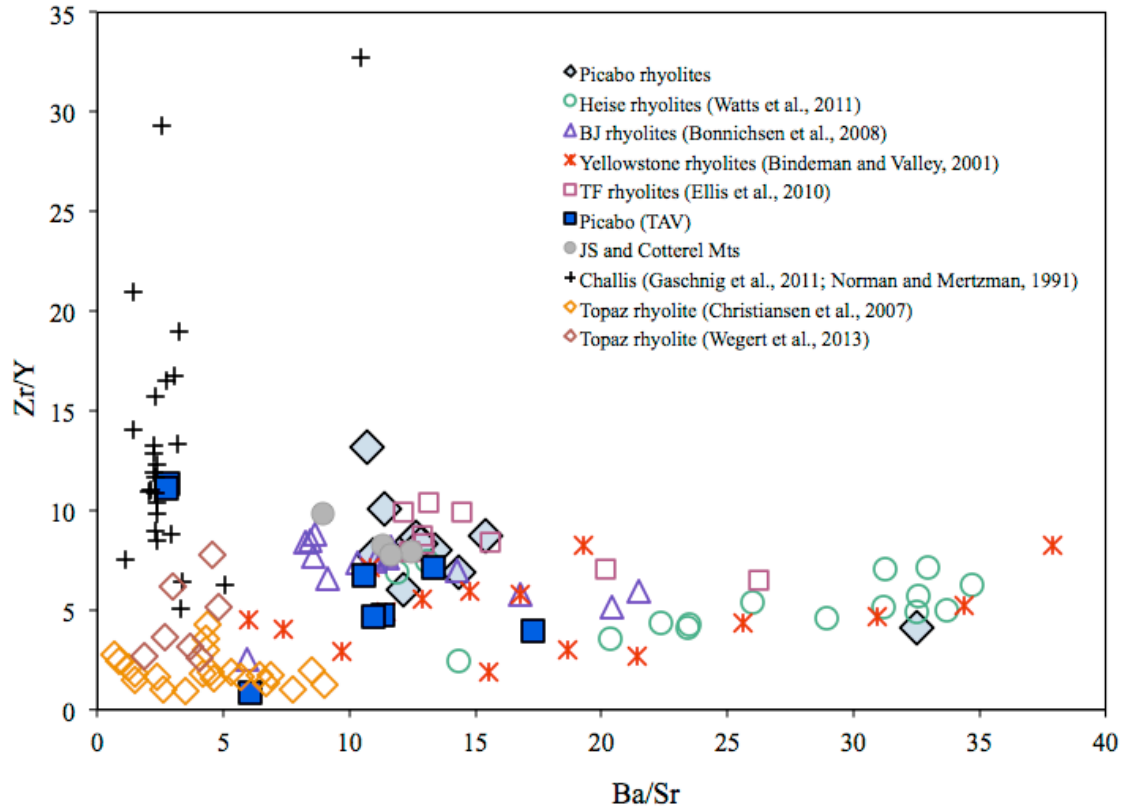


Fig. F3. b. Zr/Y versus Ba/Sr of Picabo rhyolites in comparison to surrounding SRP volcanic centers, Jim Sage and Cotterel Mountain volcanics, Challis volcanics and intrusives, Topaz rhyolites and granites, and Hawkins Basin volcanics.

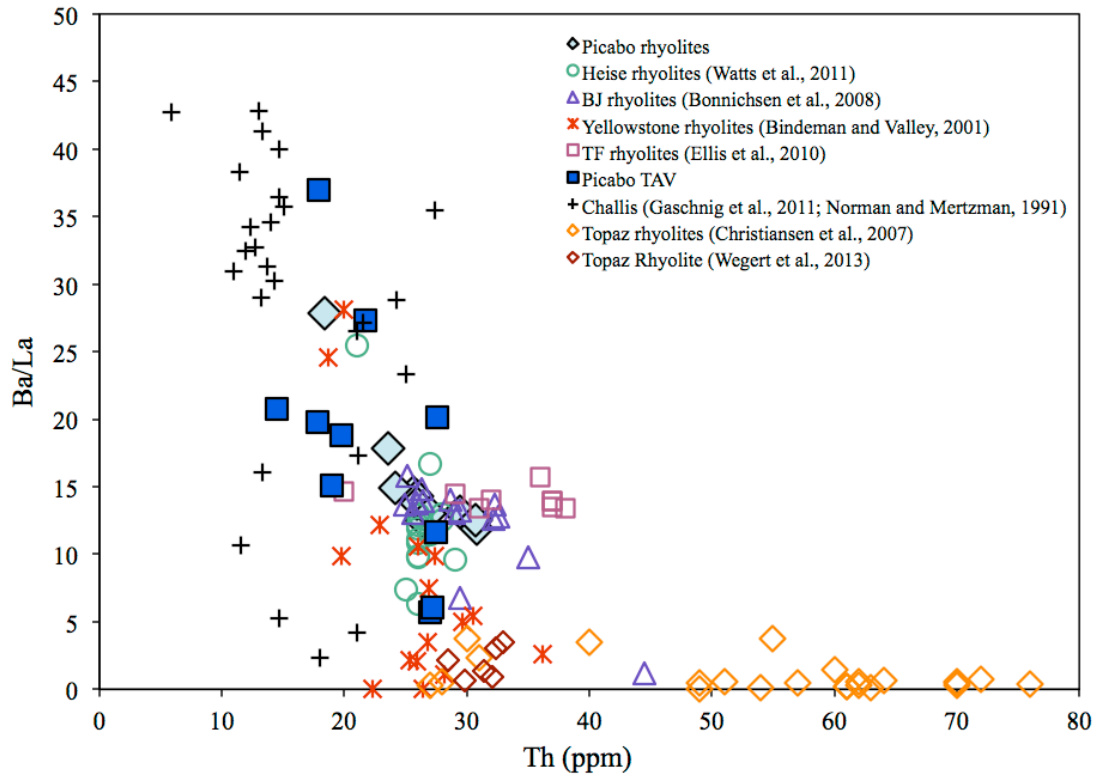


Fig. F3. c. Ba/La versus Th of Picabo rhyolites in comparison to surrounding SRP volcanic centers, Challis volcanics and intrusives, and Topaz rhyolites and granites.

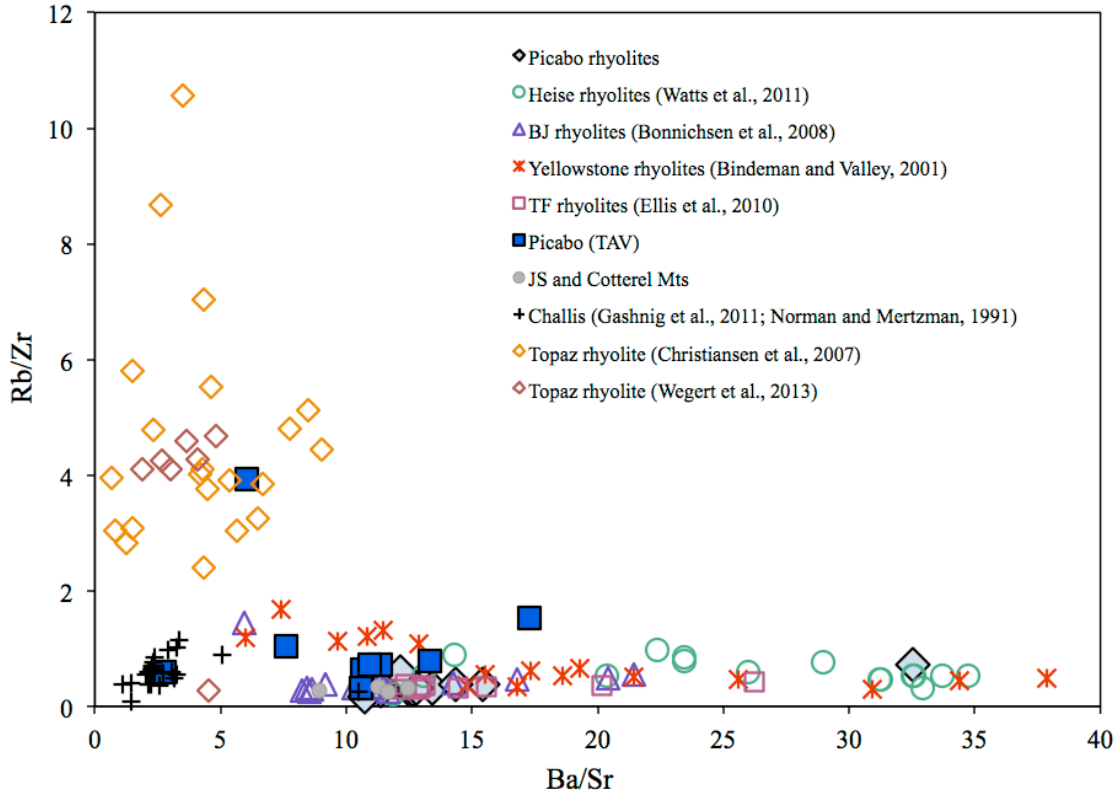


Fig. F3. d. Rb/Zr versus Ba/Sr of Picabo rhyolites in comparison to surrounding SRP volcanic centers, Jim Sage and Cotterel Mountain volcanics, Challis volcanics and intrusives, and Topaz rhyolites and granites.

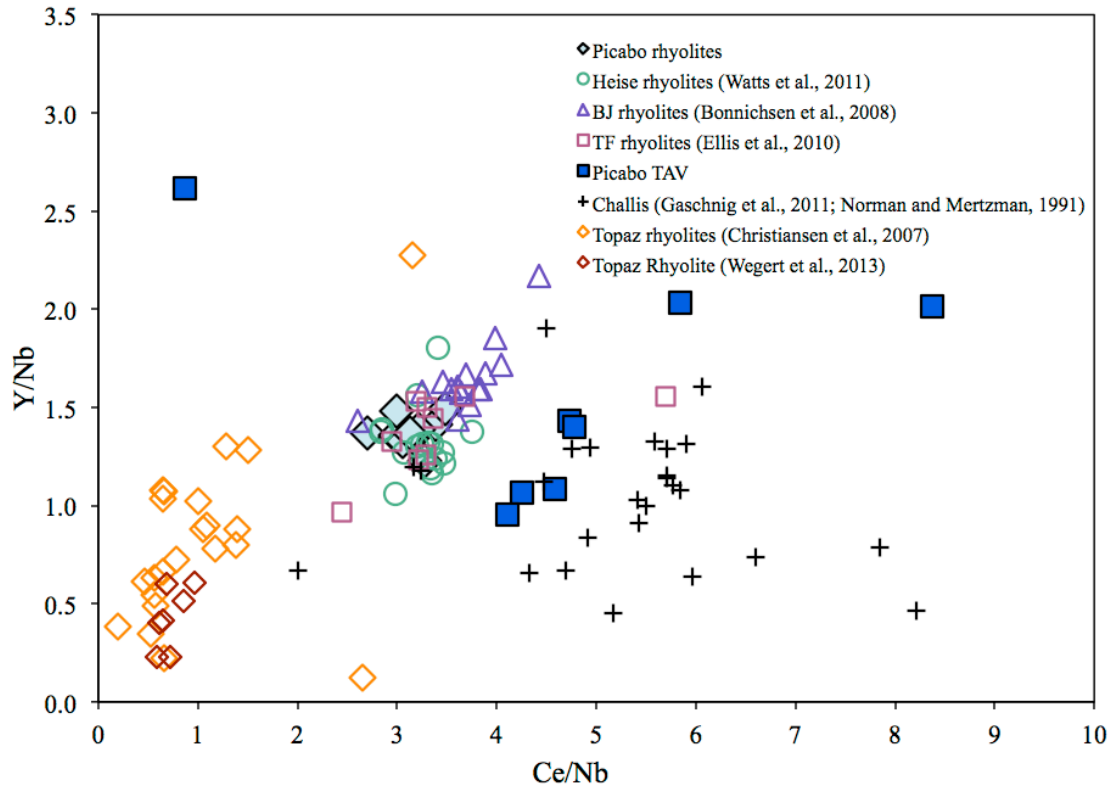


Fig. F3. e. Y/Nb versus Ce/Nb of Picabo rhyolites in comparison to surrounding SRP volcanic centers, Challis volcanics and intrusives, Topaz rhyolites and granites, and Hawkins Basin volcanics.

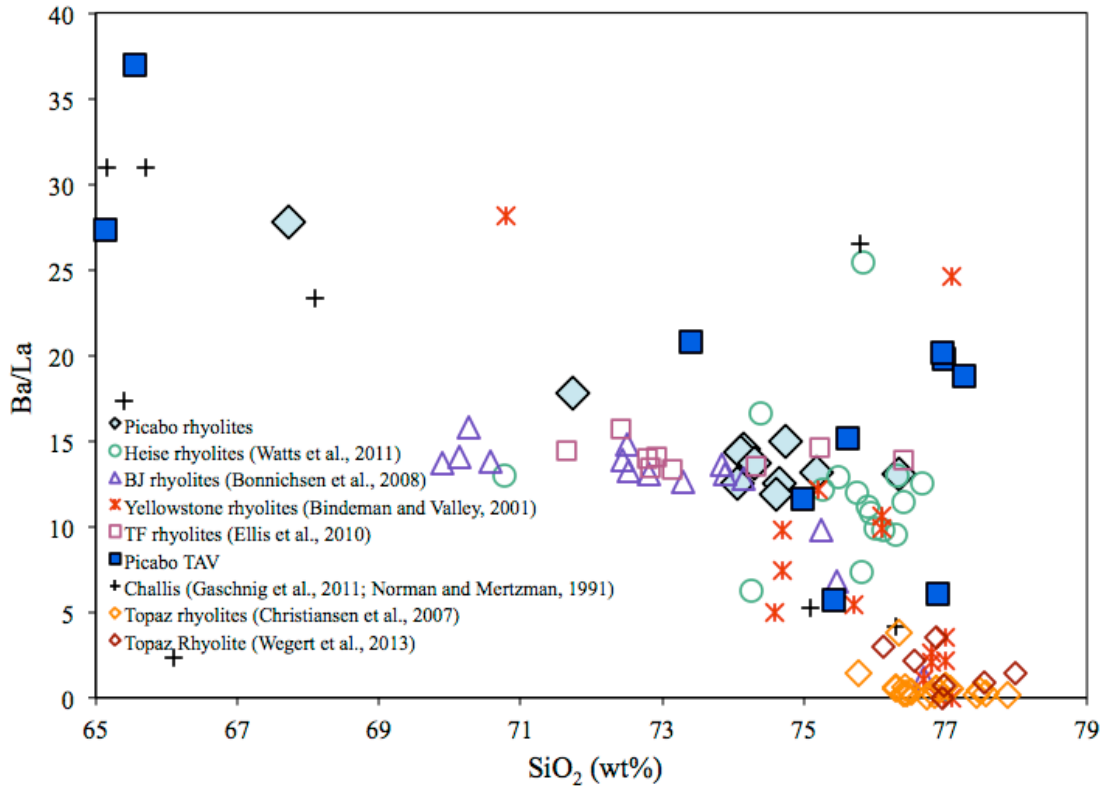


Fig. F3. f. Ba/La versus SiO₂ of Picabo rhyolites in comparison to surrounding SRP volcanic centers, Challis volcanics and intrusives, and Topaz rhyolites and granites.

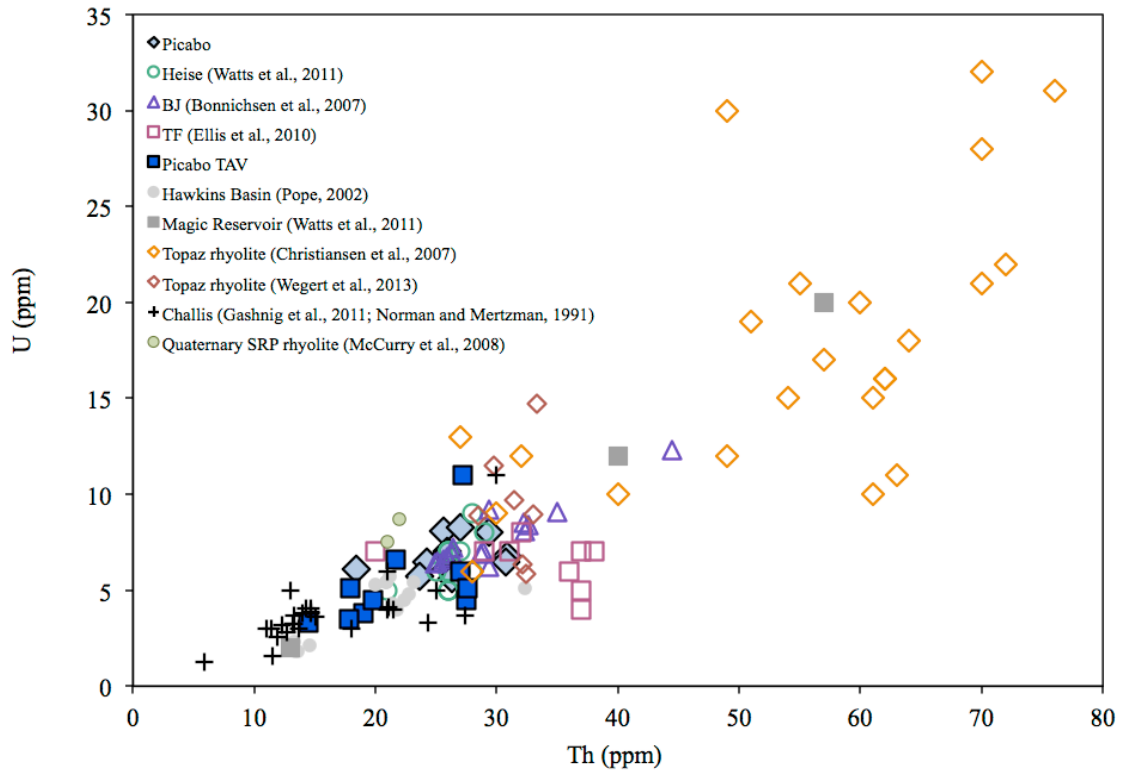


Fig. F3. g. U versus Th for Picabo rhyolites in comparison to surrounding SRP volcanic centers, Challis volcanics and intrusives, Magic Reservoir, Quaternary SRP volcanics, Topaz rhyolites and granites, and Hawkins Basin volcanics.

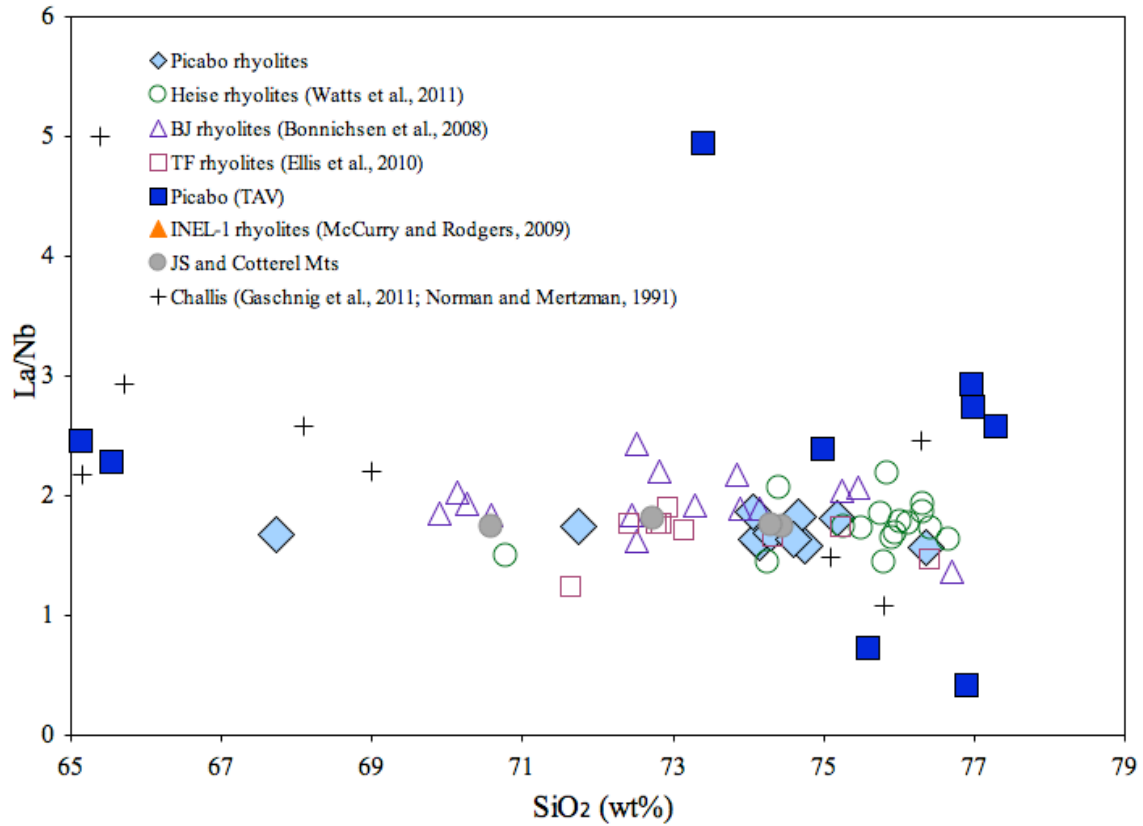


Fig. F3. h. La/Nb versus SiO₂ for Picabo rhyolites in comparison to surrounding SRP volcanic centers, INEL-1 borehole samples, Jim Sage and Cotterel Mountain volcanics, and Challis volcanics and intrusives.

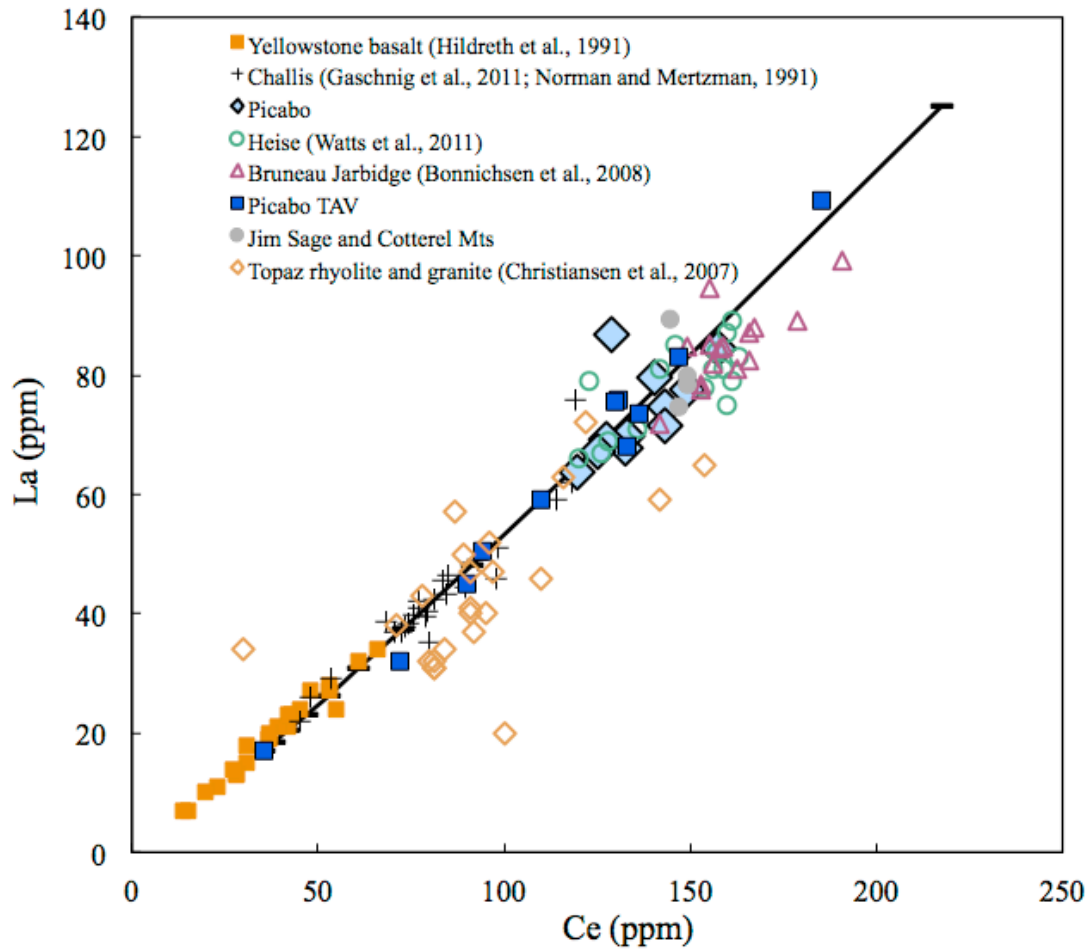


Fig. F3. i. La versus Ce for Picabo rhyolites in comparison to surrounding SRP volcanic centers, INEL-1 borehole samples, Jim Sage and Cotterel Mountain volcanics, Yellowstone basalt, and Challis volcanics and intrusives.

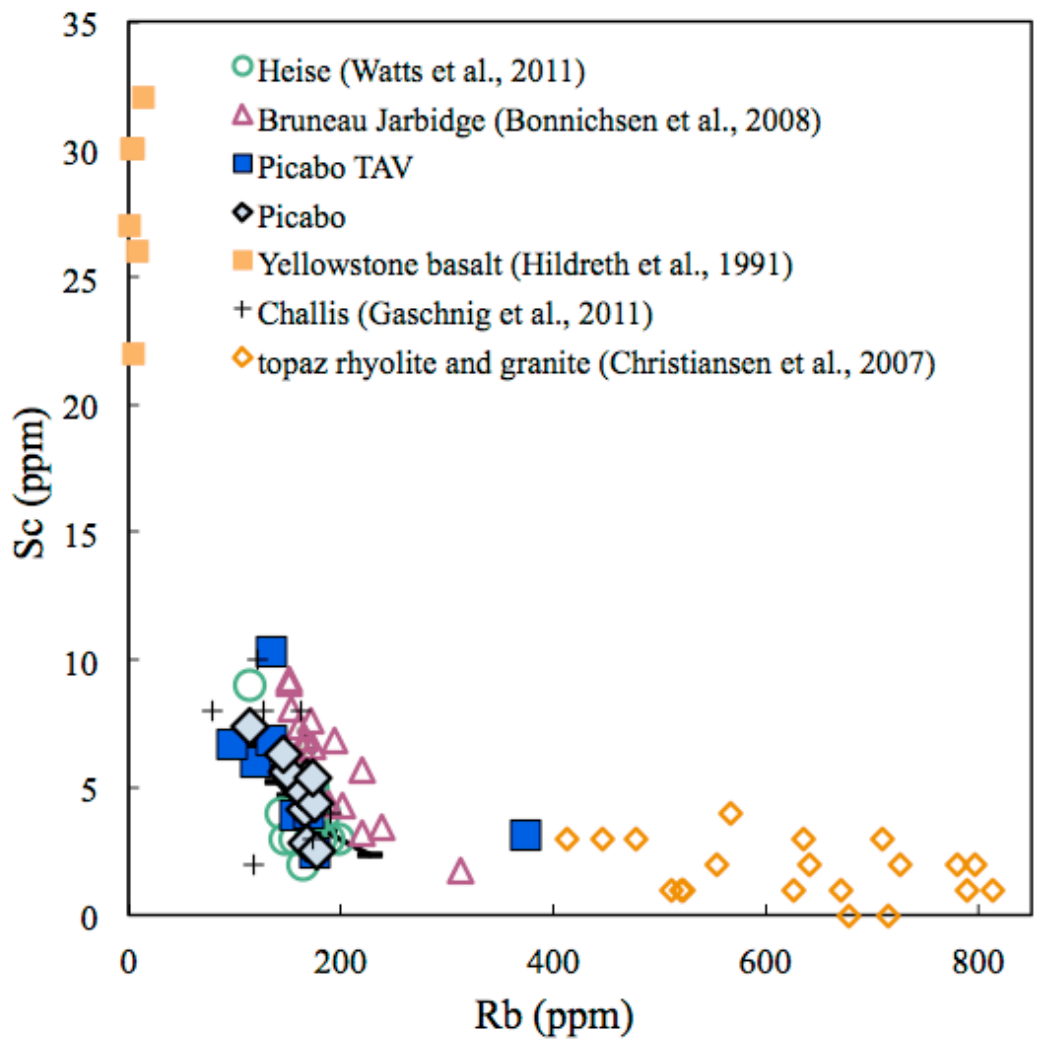


Fig. F3. j. Sc versus Rb for Picabo rhyolites in comparison to surrounding SRP volcanic centers, Yellowstone basalt, and Challis volcanics and intrusives.

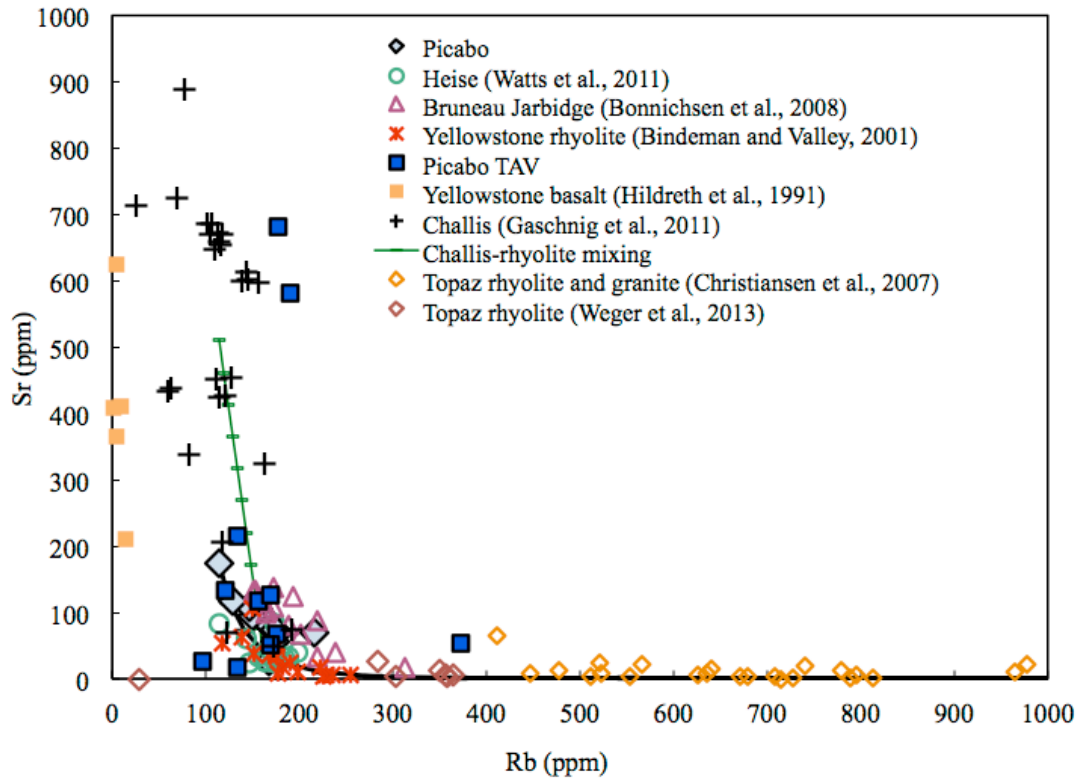


Fig. F3. k. Sr versus Rb for Picabo rhyolites in comparison to surrounding SRP volcanic centers, topaz rhyolites and granites, Yellowstone basalt, and Challis volcanics and intrusives.

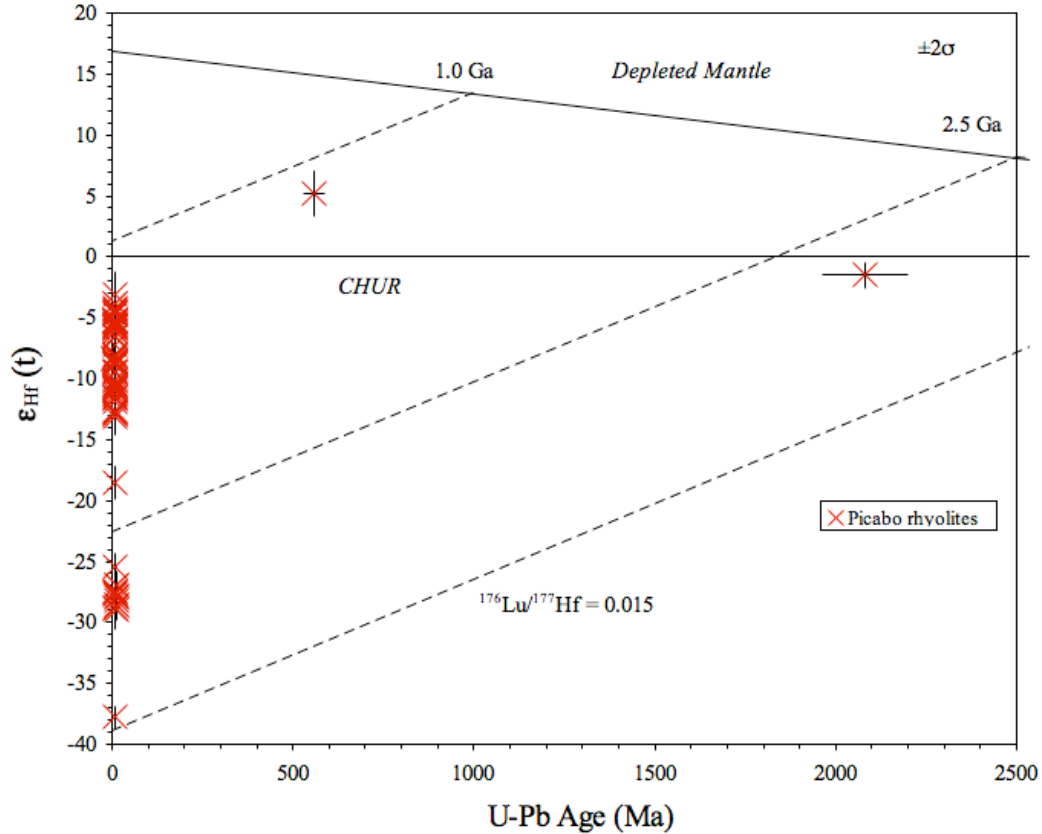


Fig. F4. $\epsilon_{\text{Hf}}(t)$ versus U-Pb age for Picabo zircons, in comparison to depleted mantle, CHUR and continental crust, highlighting the presence of xenocrysts.

Trace element analysis

Fractional crystallization

Rhyolites can be produced through two end-member scenarios: pure fractional crystallization of basalt (Quaternary SRP volcanism) or melting of the Archean upper crust (TAV). However, in the SRP relatively restricted Sr and Nd isotopes in rhyolites and their coeval variations with respect to SRP basalt (McCurry and Rodgers, Nash et al., 2006) prohibit pure crustal melting and suggest partial melting of mafic crust, therefore we consider all three mechanisms and the role they play in generating Picabo rhyolites.

In assessing the geochemical characteristics of the Picabo related rhyolites the lack of a suite of compositions precluded extensive modeling of fractional crystallization paths however, other magmatics erupted in and surrounding the SRP pre-dating and post-dating hotspot related volcanism provide a basis for comparison. In the eastern Snake

River Plain there are a series of Quaternary cryptodomes, domes, and flows of a compositional suite including high-silica rhyolite that post-date hotspot volcanism. These volcanics are unique in that they demonstrate systematic compositional trends, and have been estimated to undergo ~77% fractional crystallization from a basaltic trachyandesite parent (McCurry et al., 2008) with very limited (< 7%) assimilation of Archean crust based on Sr and Nd isotopes ($^{87}\text{Sr}/^{86}\text{Sr}_i=0.7080-0.7102$; McCurry et al., 2008). These rhyolites derived from Big Southern Butte and East Butte were used as an end-member example of rhyolite formation through pure fractional crystallization in comparison to pure crustal melts. Trace element variations in Ba, Rb Sr, Zr, La, Th, Nd, and U demonstrate that overall OIB and average continental crust display similar patterns, with OIB concentrations slightly elevated in incompatible elements, while rhyolites produced by pure fractional crystallization demonstrate severe depletions in Sr, Sc and La as a result of plagioclase, pyroxene, and magnetite fractionation. The variations between Big Southern Butte and East Butte and various Picabo rhyolites demonstrate that many of the trace element trends can be attributed to different mineral abundances and the degree of fractional crystallization.

Considering that during fractional crystallization uranium remains completely incompatible, 95% fractional crystallization of basalt would be required, further emphasizing the importance of crustal melting in producing the evolved compositions observed. The large variation in $^{87}\text{Sr}/^{86}\text{Sr}_i$ also demonstrates the large degree of heterogeneity in the assimilated craton. Increases in FeO_T and $^{143}\text{Nd}/^{144}\text{Nd}$ throughout the eruptive sequence demonstrate that basaltic contributions were greater in the waning stages of volcanism, similar to Bruneau-Jarbidge tuffs (Leeman et al., 2008; Ellis et al., 2010). The crust was primed through interaction with basaltic magma and/or the magma reservoir became reactivated due to primitive basalt injection and only involved minimal crustal melting. Although a steady rate of magma injection is assumed, the basalt may become more thermally available throughout the life of the Picabo eruptive center due to increases in ambient temperature of the country rock and less energy required for remelting glassy high silica rhyolite (~200 kJ/kg, see Simakin and Bindeman, 2012 for a more detailed treatment). Therefore in subsequent eruptions it is more energetically favorable to remelt volcanic remnants instead of incorporating large degrees of

continental crust. Christiansen and McCurry (2008) also demonstrated that partial melting of gabbro rather than upper crustal rocks or lower crustal granulite can better reproduce trace element signatures (Rb, Th, U and Pb) of SRP rhyolites.

Uranium and thorium concentrations in zircon can range from 100 to tens of thousands of ppm, and relate to the connection between volcanic products and plutons. In Yellowstone zircons, the most elevated concentrations (39,000 ppm U and 15,000 ppm Th) were found in post-caldera low- $\delta^{18}\text{O}$ tuffs and in the Lava Creek Tuff (Bindeman et al., 2008). These high concentrations are indicative of equilibrium crystallization in an incompatible element rich melt in the waning stages of the volcanic fields life, and therefore these zircons were likely inherited from an unerupted plutonic root (Bindeman et al., 2008). Since the partition coefficient of U in zircon is approximately 300 (Mahood and Hildreth, 1983), 50% fraction crystallization would be required to generate a melt with 10 ppm U and zircons with 3000 ppm U (Bindeman et al., 2008). The plutonic zircons found in the Yellowstone rhyolites further corroborate an intertwined history of plutons and erupted volcanics. In many volcanic systems plutons represent a prolonged history of magma evolution while the volcanic products provide snapshots of magmatic conditions through time. Concentrations of U in individual zircons ranges from 50 to 8000 ppm. Bindeman et al., 2008 argues that the U and Th rich zones of zircon crystallized from the last portions of incompatible element rich melts and therefore may have been inherited from the unerupted subvolcanic equivalents of surface units. (the higher the U the more fractional crystallization.

Trace element trends

The trace and major element concentrations of rhyolites of the Picabo volcanic were compared to other centers of the SRP (Heise, Bruneau Jarbidge, Twin Falls, and Yellowstone), Jim Sage and Cotterel Mountain volcanics, Topaz rhyolites, Challis volcanics and intrusives, Great Basin volcanics, Hawkins Basin volcanics, Magic Reservoir, and Quaternary SRP volcanics. Since the Tuff of Arbon Valley is both compositionally zoned and distinct, comparison of the TAV to other volcanics derived from other sources were used to shed light on the source of the TAV. The TAV has a

poorly welded base (samples PC-12 and to some extent PC-08), and the chemical composition of this sample is likely affected by post depositional alteration. More specifically PC-12 has low Ba and Sr, suggesting leaching of fluid mobile trace elements.

Although the TAV shows similarities to the Topaz rhyolites in F and Cl contents of glassy melt inclusions the whole rock trace element ratios shows greater similarities to the Challis and Snake River Plain volcanics. More specifically the Topaz rhyolites demonstrate enrichments in LILE and low concentrations of HFSEs.

The Challis volcanics, derived from a subduction related source, show the lowest concentrations of U and Th, with Topaz rhyolites showing the greatest concentration. This demonstrates that genesis of the topaz rhyolites involved the greatest amount of fractional crystallization or enrichment of incompatible elements. Clear distinctions between the topaz rhyolites, SRP rhyolites, and Challis volcanics are shown in Rb/Zr versus Ba/Sr, Y/Nb versus Ce/Nb.

APPENDIX G

MIXING CALCULATION

For the binary mixing calculation of $^{87}\text{Sr}/^{86}\text{Sr}_i$ and $^{143}\text{Nd}/^{144}\text{Nd}$, I used an average crustal composition of SRP xenolith samples (Leeman et al., 1985). The average is similar to xenolith sample DM-103, which has been deemed to be most representative xenolith sample (Watts et al., 2010; Leeman et al., 1985). The Sr and Nd data of Yellowstone basalts (Hildreth et al., 1991) was averaged to represent the primitive SRP end-member. The TAV samples provide the unique opportunity to fit the mixing curve at a more crustal-like composition, confirming that the crustal end-member chosen was representative.

The binary mixing line is based on the equation:

$$R_{\text{mix}} = [R_A C_A F_A + R_B C_B (1 - F_A)] / [C_A F_A + C_B (1 - F_A)];$$

R=isotope ratio of element, F=mass fraction, C=concentration of element

I chose to use a binary mixing curve because in such a large rhyolite systems where there is wall rock and roof rock erosion with massive amounts of crustal incorporation, mixing is more representative than coupled assimilation and fractional crystallization. Since reincorporation of previous materials occurs throughout the eruptive sequence the Sr and Nd isotopic signatures of late stage Picabo rhyolites can be influenced and therefore this only applies to the initial TAV eruption.

Literature compilation for basalt field:

- Steens basalt (Camp and Hanan, 2008)
- INEL borehole, and surface basalt samples (Hughes et al., 2002)
- Newberry, High Lava Plains, and Owyhee Plateau (Graham et al., 2009)
- The Yellowstone basalts (Hildreth et al., 1991) represent the average of basalt samples and therefore were chosen as a conservative mantle end-member for modeling.

Summary of mixing end-members:

Sr vs. Nd:

Crust:

Sr: 0.73199±0.01091, 347.16

Nd: 0.51079±0.000113, 18.22

Mantle:

Sr: 0.7063, 300 ppm

Nd: 0.5124, 23 ppm

The Challis and Idaho batholith $^{87}\text{Sr}/^{86}\text{Sr}$ was corrected to an age of 9 Ma to more accurately reflect ratios at the time of Picabo volcanism. This created a negligible difference between the xenolith data and therefore was only calculated for Challis and Idaho batholith.

Hf vs. O:

Crust:

Hf: An average composition of Archean crust was used (Vervoort and Patchett, 1996); $\epsilon_{\text{Hf}} = -44$, Hf = 9 ppm.

O: 48.83 wt. % (Watts et al., 2010; Leeman, unpublished); $\delta^{18}\text{O} = 7.4\text{‰}$ (Watts et al., 2010).

Challis:

Hf: 9 ppm Hf; $\epsilon_{\text{Hf}} = -12.5$ (Gaschnig et al., 2011)

O: 49 wt. % (approximated from rhyolite compositions used by Watts et al., 2010); $\delta^{18}\text{O} = -3.6\text{‰}$; The range of $\delta^{18}\text{O}$ in low $\delta^{18}\text{O}$ rhyolites found associated with Challis volcanics are from -4.5 to -20.5‰ (Criss et al., 1991), therefore an average of -3.6‰ was used.

Mantle:

Hf: We used 3.6 ppm Hf, an average Yellowstone basalt composition (Hildreth et al., 1991). For ϵ_{Hf} we used 15, Columbia River basalts and SRP basalts range from -8.3 to 11.3 (Stefano, 2010: thesis).

O: 43.53 wt. %; $\delta^{18}\text{O} = 5.6\text{‰}$ (Graham et al., 2010; Watts et al., 2010).

APPENDIX H

ADDITIONAL MELT INCLUSION BACKGROUND INFORMATION

Magma degassing

Volatiles are a critical component of volcanic eruptions, governing eruption style and explosivity, however volatiles are released both before and during eruptions making volcanic volatile budgets a difficult parameter to quantify. With increased analytical innovation it is now possible to measure melt inclusions volatile and chemical composition preserved in phenocrysts, which were quenched during eruption. Natural systems contain a variety of volatiles including H₂O, CO₂, S, Cl, F, noble gases etc., and these volatiles can exist as a dissolved species of the melt and as a separate exsolved vapor phase, with H₂O and CO₂ being the most abundant. These volatiles can greatly impact magma fractionation, crystallizing assemblage, liquidus temperature as well as magma rheology, density, and viscosity. Quantifying H₂O and CO₂ in melt inclusions also provides one of the most accurate pressure estimates, which can be used to quantify storage in the crust (Putirka, 2008). The solubility of CO₂ is approximately 30x lower than H₂O, and both CO₂ and H₂O are more soluble in rhyolite melts than basalt melts.

Introduction to quartz-hosted melt inclusions

Melt inclusions, are trapped pockets of silicate melt preserved in phenocrysts that record the composition of the pre-eruptive melt as well as the dissolved volatiles present in the melt. Melt inclusions are trapped in crystals due to a variety of processes related to the formation of irregular surfaces of a grain during crystallization and/or rapid skeletal crystal growth (Frezzotti, 2001). Reconstructing the chemical composition of the melt relies on the critical assumption that the inclusions have remained as closed systems after entrapment and have not experienced subsequent changes as the magma continued to evolve and ascend towards the surface. Rapidly quenched melt inclusions are therefore targeted because the inclusion will not devitrify or become crystalline. Although melt inclusions trap minerals and contain bubbles, they should be free of quench crystals

(Frezzotti, 2001). Due to the importance of melt inclusion quality, doubly polished thin sections are required to observe the size, shape, distribution and presence of cracks, in a target melt inclusion. Quartz is an abundant phase in the majority of rhyolite magmas and quartz-hosted melt inclusions can provide a snapshot of the pre-eruptive melt and volatile composition in rapidly quenched samples (typically pumice) of silicic systems.

H₂O and CO₂ concentrations vary in melt inclusions as a function of the following three parameters: 1) degassing path of the magma prior to melt inclusion entrapment; 2) magma evolution and differentiation; and 3) variations at the source (Metrich and Wallace, 2008). Under open-system degassing conditions gas exsolves and is constantly separated from the melt. Under these conditions the CO₂ concentration of the melt decreases and the H₂O does not decrease significantly until the melt reaches the vapor saturation pressure for H₂O. However, for closed-system degassing when gas that exsolves remains entrained in the melt in a state of equilibrium, H₂O exsolution is more significant and can even induce crystallization (Metrich and Wallace, 2008). Since crystallization continues through magma ascent and degassing, melt inclusions can be trapped at various stages of evolution and thus melt inclusions from a given sample have large variations in H₂O and CO₂. Assuming vapor saturation and that the total vapor pressure is equivalent to the CO₂ and H₂O partial pressures, the CO₂ and H₂O concentrations can be used to calculate entrapment pressure and corresponding depth (using programs such as VolatileCalc).

Although melt inclusions are a robust tool and one of the few ways to preserve melt compositions there are a variety of complicating factors. For example, since these melt inclusions are trapped along the surface there are chemical boundary layer phenomena that can affect the composition of the inclusion as a function of diffusion. However, analyzing inclusions larger than 50 microns has been shown to make this effect negligible (Metrich and Wallace, 2008). Post entrapment volatile loss of H₂ is also likely a problem but to what extent is unknown.

The role of fluorine

Fluorite (CaF₂) stability is a function of the activities of CaO and F₂O in the melt, as well as the melt aluminosity (Dolkes and Baker, 2006). Experiments on peraluminous, subaluminous, and peralkaline haplogranites by Doljes and Baker (2006) demonstrated that the high concentrations of CaO needed to crystallize fluorite in F-rich peraluminous melts are not observed in nature therefore the crystallization of fluorite in peraluminous (topaz-bearing) systems is suppressed. In CaO-rich melts fluorite has a low solubility. In peraluminous topaz granites fluorite is only stable within 25 to 40°C of the solidus, outside this envelope fluorite will melt completely (Weidner and Martin, 1987; Xiong et al., 2002). The general instability of fluorite promotes F enrichment and if present it forms late and as a secondary phase.

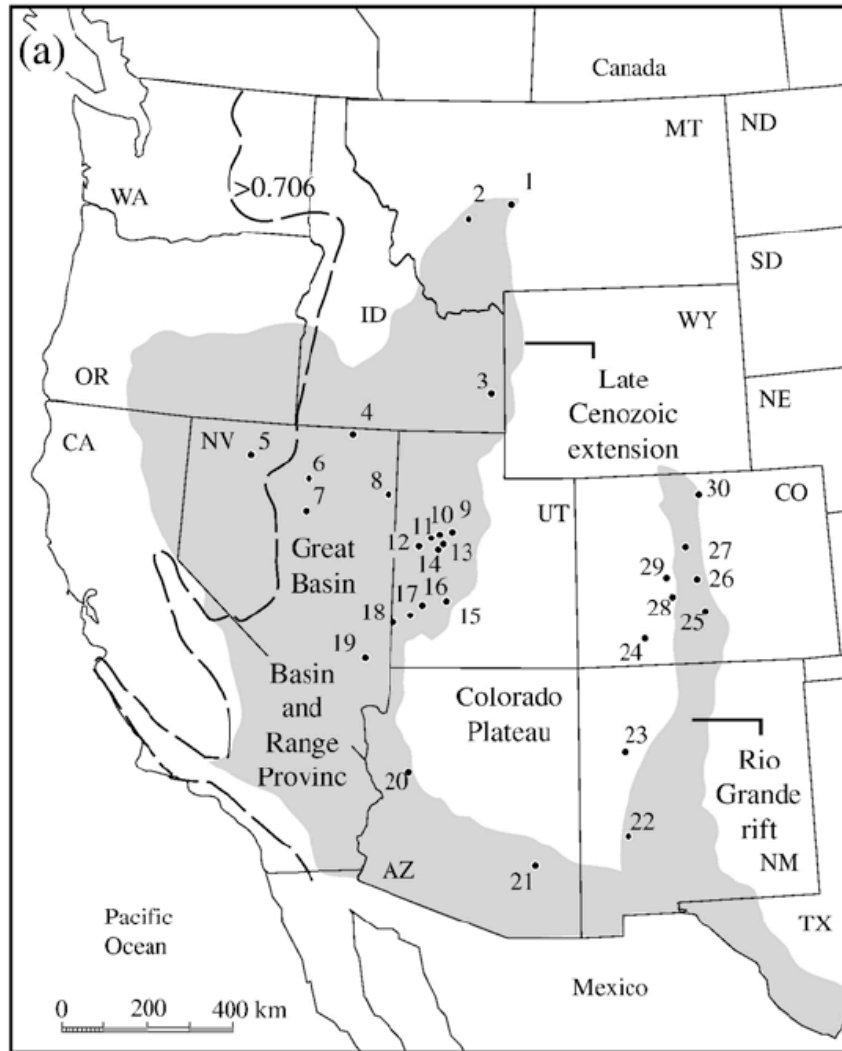
Gravitational settling of crystals in magma chamber is governed by Stoke's Law

$$V = [2gr^2(\rho_s - \rho_l)] / 9\eta$$

Where V is the settling velocity (cm/s), g is acceleration due to gravity (980 cm/s²), r is the radius of spherical particle (cm), ρ_s is the density of the particle (g/cm³), ρ_l is the density of the liquid (g/cm³), and η is the viscosity of the liquid (poise or g/cm s).

Therefore considering a basic rhyolitic melt crystallizing plagioclase (radius of 0.1 cm) and a 0.03 g/cm³ density decrease and an order of magnitude viscosity decrease due the presence of fluorine the settling velocity would increase from 2.75 cm/yr to 3 cm/yr.

Therefore the changes in density and viscosity induced by the presence of fluorine can affect magma fractionation. However, Anderson et al. (2000) report settling rates of ~8 cm/yr for 1 mm quartz phenocrysts in the Bishop Tuff magma body, highlighting that it is possible for settling rates to be even faster than I calculated. Therefore, it would take at least 40 ky for quartz to sink 3.6 km.



Topaz rhyolites in the western United States

- | | | |
|-------------------------|--------------------------|------------------------|
| 1 Little Belt Mountains | 11 Spor Mountain | 21 Saddle Mountain |
| 2 Elkhorn Mountains | 12 Honeycomb Hills | 22 Black Range |
| 3 Blackfoot lava field | 13 Smelter Knolls | 23 Grants Ridge |
| 4 Jarbidge | 14 Little Drum Mountains | 24 Lake City |
| 5 Buff Peak | 15 Mineral Mountains | 25 Silver Cliff-Rosita |
| 6 Sheep Creek Range | 16 Wah Wah Mountains | 26 Nathrop |
| 7 Cortez Mountains | 17 Mountain Home Range | 27 Chalk Mountain |
| 8 Toano Range | 18 White Rock Mountains | 28 Tomichi Dome |
| 9 Keg Mountain | 19 Kane Spring Wash | 29 Boston Peak |
| 10 Thomas Range | 20 Burro Creek | 30 Specimen Mountain |

Fig. H1. Distribution of topaz rhyolites in the western U.S. (Christiansen et al., 2007).

Major fluorite and fluorspar deposits exist in Idaho, many of which are observed in association with Challis volcanics. Fluorite and fluorspar mineralization is largely found along faults and fractures, and in veins likely due to dilute hydrothermal waters (Van Alstine, 1976). Fluorspar deposits are formed at low temperatures (below 200°C) and pressures. Although these deposits are north of the Snake River Plain they suggest a local source of fluorine. Snyder (1978) proposes that the source is Cambrian and Ordovician sediments, quartz-porphyry intrusives, or Eocene volcanism. The most common trace element enrichments associated with Tertiary fluorspar deposits are Be, Fe, Mn, Mo, Pb, REEs, U, V, W, Sn, and Zn. The regions of erupted topaz rhyolite and fluorspar deposits show striking similarities, demonstrating that the source of fluorine in the TAV is likely connected.

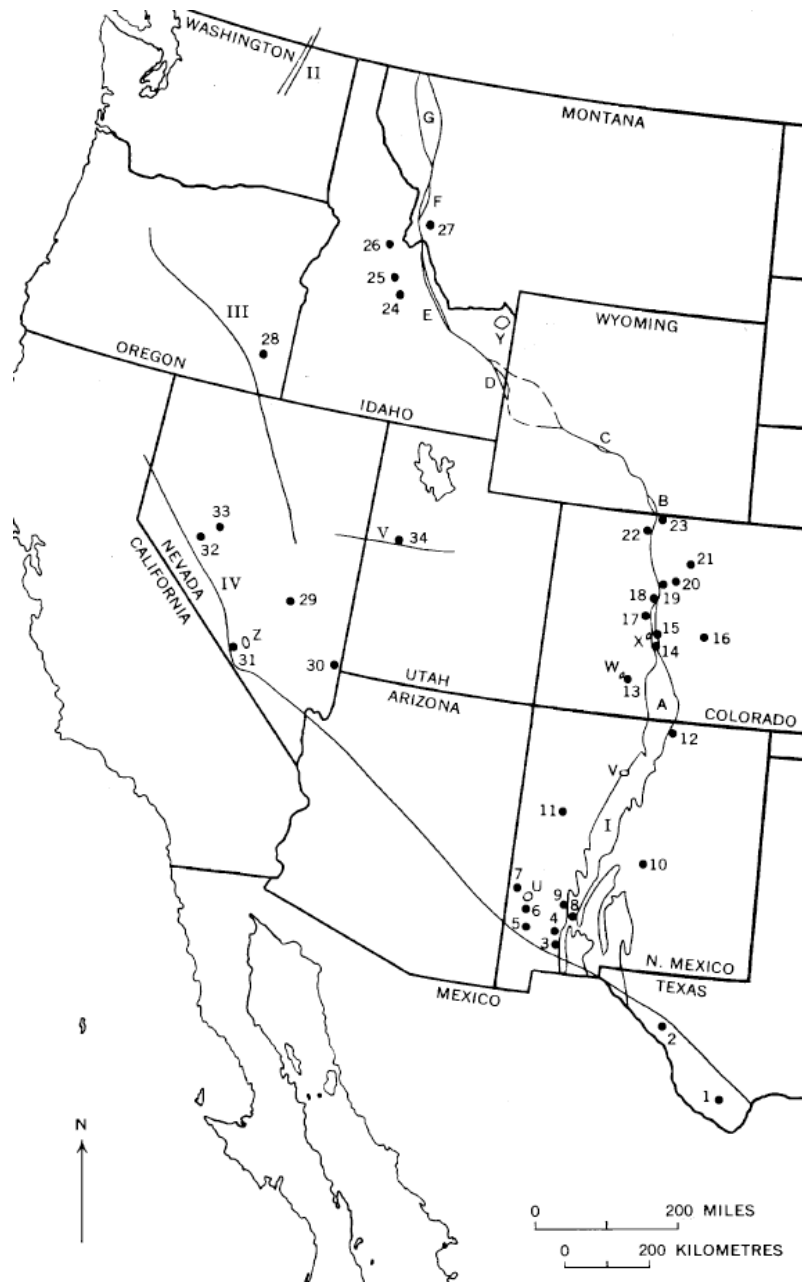


Fig. H2. Distribution of fluorspar deposits in the western U.S. (Van Alstine, 1976).

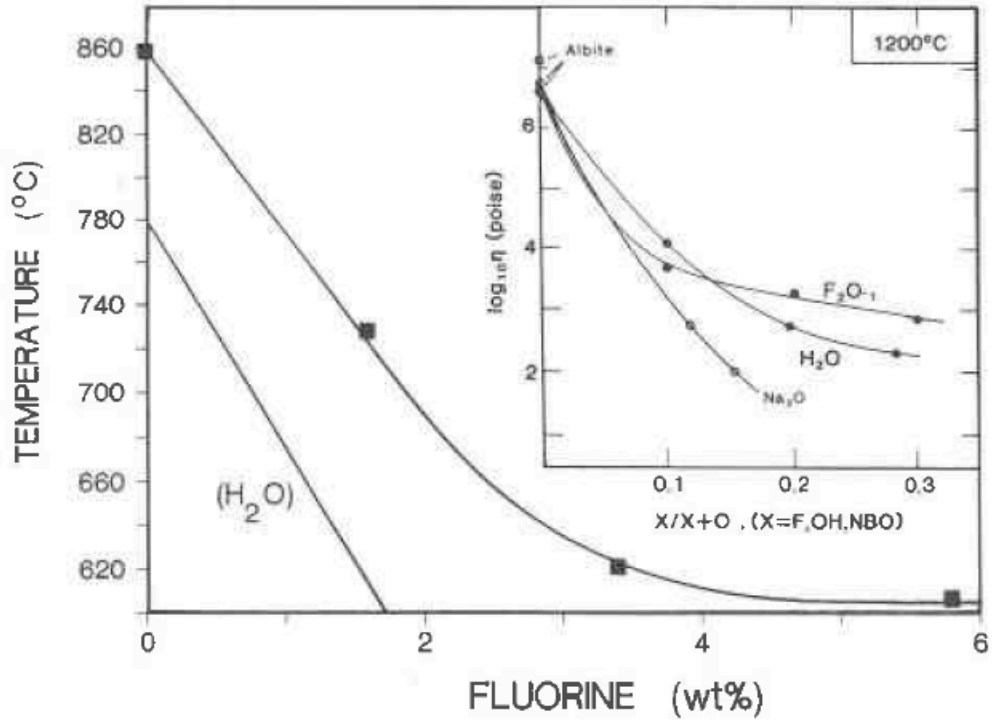


Fig. H3. The effects of fluorine on the glass transition temperature for rhyolite (line labeled H₂O) and albite (Dingwell and Webb, 1992).

APPENDIX I
DETAILED METHODS, RAW FTIR MEASUREMENTS, AND
PHOTOMICROGRAPHS

Volatile contents of quartz-hosted melt inclusions

Pumice clasts were collected from the rapidly-quenched airfall of the TAV and gently crushed, keeping each pumice clast isolated. These pumice fragments are considered to be quenched vesiculated rhyolitic magma. Quartz crystals were handpicked under a binocular microscope and glassy melt inclusions 50 microns or larger that were round were targeted during sample preparation. Individual quartz phenocrysts were mounted on one inch glass rounds with crystal bond and polished to make a thin wafer with the melt inclusion polished on both sides. Melt inclusions were doubly polished using fine sandpaper, and 6 and 0.25 micron diamond paste in order to expose the melt inclusion on each side of the 20 to 75 micron quartz wafer. Pictures were taken of the melt inclusions and measurements of the melt inclusion and host crystal size were made before flipping the wafers to polish the second side, since large portions of the crystals were lost during preparation of the doubly polished wafer. Each individual inclusion was analyzed by Fourier Transform Infrared Spectroscopy (FTIR) for H₂O and CO₂, and at least three spectra were measured for each inclusion. The 32X lens and condenser was used for all inclusions and during analyses a plastic protective cap on the lens was used to isolate the sample to avoid CO₂ interferences. The OH (3570 cm⁻¹) and CO₂ absorbance peaks were measured using transmitted IR light and 256 scans. The background was measured on the salt plate. However when the water content exceeded the capacity, of the FTIR the near IR water peaks, bound hydroxyl (4520 cm⁻¹) and molecular H₂O (5230 cm⁻¹), were used. For each absorbance intensity peak measurement, the background was individually characterized and subtracted from the analysis. For 3570 cm⁻¹ absorbance peak IR light was used and for the near IR peaks white light was used to reduce the background. To measure the thickness of each inclusion with the reflectance method on the FTIR, the reflectance was measured during 120 scans using white light. The background was measured on the gold plate.

The Beer Lambert Law was used to calculate molecular H₂O and CO₂ concentrations from the measured absorbance peaks.

Beer Lambert Law: (Molecular mass x absorbance)/(density of glass x thickness x molar absorbance of grains). An initial density and absorbance of 5230 and 80 respectively, was used to calculate concentrations. Then in a series of iterations the calculated water concentration was used to correct the density and absorbance because the density of each inclusion is dependent on the total water content (Silver et al., 1990).

The thickness of each quartz wafer was measured using the micrometer and the reflectance method on the FTIR. For melt inclusions that were not intersected on each side, the thickness was corrected with the technique of Nichols and Wysoczanski (2007). For the near IR peaks the revised algorithm of Beer's Law by Zhang et al. (1997) was used to calculate total H₂O.

$$C(1-C) = a_0\bar{A}_{523} + (b_0 + b_1\bar{A}_{523} + b_2\bar{A}_{452})\bar{A}_{452}$$

$$a_0 = 0.04217 \pm 0.0013 \text{ mm}$$

$$b_0 = 0.04012 \pm 0.0023 \text{ mm}$$

$$b_1 = -0.02011 \pm 0.0051 \text{ mm}^2$$

$$b_2 = 0.0522 \pm 0.0051 \text{ mm}^2$$

Ti concentrations and cathodoluminescence imaging of quartz

Ti in quartz measurements were made during two analytical sessions. During the first session two quartz mounts were made of a series of Picabo samples: one with 21 quartz grains (1-3 mm in size) from two samples with quartz grains one to three millimeters in size and the other mount with 76 grains (less than 1 mm) from eight samples and two standards. Grains were mounted on tape, filled with epoxy, backfilled with epoxy, ground to expose the cores, polished and carbon coated. Using the FEI Quanta 200 ESEM Microscope, I conducted cathode luminescence imaging to analyze zoning patterns in the quartz grains. The images were produced with the blue bandwidth filter, averaging over frames produced at a speed of 512. The quartz phenocrysts were analyzed on the Cameca SX100 electron microprobe at the University of Oregon

MicroAnalytical Facility at a beam energy of 15 keV, a beam diameter of 10 microns and a beam current of 100 nanoamps. The count rates for Ti in quartz were 80 seconds for unknowns and 20 seconds for standards. Two glass standards, NBS-K412 mineral glass and SiO₂ synthetic, and a synthetic TiO₂ standard were analyzed with the unknowns. Ti was measured on three different spectrometers with the LIF, large PET and regular PET crystals, and unknown concentrations were blank corrected and aggregated (Donovan et al., 2011). The SiO₂ synthetic standard contains a negligible concentration of Ti of 1.42 ppm and therefore was used as a blank corrected. The Ti standard quartz detection limit for each spectrometer was 20, 30 and 90 ppm demonstrating that the LIF (lower intensity crystal) was less optimal for the Ti measurement. However these measurements were within the standard deviation and could be considered 0 and were still sufficiently accurate for measurement of the unknowns.

During the second analytical session the quartz wafers containing double polished melt inclusions were mounted in epoxy and analyzed for Ti, Fe, K, Na, and Al. These grains were first imaged on the FEI Quanta 200 ESEM with cathode luminescence imaging to investigate zoning patterns and then observed zones were targeted for trace element measurements on the Cameca SX100. For this session a beam energy of 15 keV, a beam diameter of 10 microns, and a count time of 100 seconds was used for each unknown. The LLIF crystal was used for Fe, LPET for Ti, PET for K, and TAP for Al and Na. The SiO₂ synthetic standard was analyzed as an unknown and used for a blank correction.

Table II.

FTIR measurements of the OH⁻, H₂O_{total}, molecular H₂O and bound OH⁻ absorbance peaks, and micrometer and reflectance thicknesses of melt inclusion wafers.

Melt inclusion	Run	Micrometer Average Thickness	Reflectance Average Thickness	Used/corrected thickness	OH abs 3570	H ₂ O _m abs 1630	Molecular CO ₂ 2350	Bound Hydroxyl 4520	Molecular H ₂ O 5230
PC-P2.6									
IR	Run 1	44.67	44.05	44.05	1.465	1.21	0.079	0.01	0.05
IR	Run 2	44.67	44.05	44.05	1.505	1.203	0.078	0.005	0.048
IR	Run 3	44.67	44.05	44.05	1.412	1.125	0.07	-	-
	Average	44.67	44.05	44.05	1.46	1.18	0.08	0.0075	0.049
	S.D.	-	-	-	0.047	0.047	0.005	0.004	0.001
PC-P4.1									
IR	Run 1	35.00	26.41	14.31	0.368	0.5	0.01	-	-
IR	Run 2	35.00	26.41	17.87	0.606	0.516	0.017	-	-
IR	Run 3	35.00	26.41	17.79	0.593	0.477	0.026	-	-
	Average	35.00	26.41	16.66	0.52	0.50	0.02	-	-
	S.D.	-	-	-	0.134	0.020	0.008	-	-
PC-P3.2									
IR	Run 1	35.00	32.77	18.87	0.982	0.732	0.045	-	-
IR	Run 2	35.00	32.77	17.27	0.797	0.69	0.048	-	-
IR	Run 3	35.00	32.77	10.23	0.433	0.574	0.043	-	-
	Average	35.00	32.77	15.45	0.74	0.67	0.05	-	-
	S.D.	-	-	4.59	0.279	0.082	0.003	-	-
PC-P3.3									
IR	Run 1	71.00	66.32	45.84	0.954	1.129	0.035	-	-
IR	Run 2	71.00	66.32	47.22	1.185	1.539	0.029	-	-
IR	Run 3	71.00	66.32	40.19	0.968	1.498	0.031	0.019	0.051
	Average	71.00	66.32	44.42	1.04	1.39	0.03	0.02	0.05
	S.D.	-	-	-	0.130	0.226	0.004	-	-
PC-P3.4									
IR	Run 1	35.00	34.41	21.57	0.382	0.486	0.02	-	-
IR	Run 2	35.00	34.41	24.20	0.559	0.571	0.028	-	-
IR	Run 3	35.00	34.41	22.72	0.315	0.475	0.016	-	-
	Average	35.00	34.41	22.83	0.42	0.51	0.02	-	-

	S.D.	-	-	-	0.126	0.053	0.006	-	-	
PC-P2.2										
MI 1										
IR	Run 1	33.7	31.69	24.942	0.809	0.666	0.017	-	-	
IR	Run 2	33.7	31.69	23.592	0.639	0.522	0.020	-	-	
IR	Run 3	33.7	31.69	22.384	0.514	0.497	0.021	-	-	
	Average	33.7	31.69	23.64	0.65	0.56	0.02	-	-	
	S.D.	-	-	-	0.148	0.091	0.002	-	-	
PC-P2.2										
MI 2										
IR	Run 4	33.7	31.69	15.07	0.606	0.509	-	-	-	
IR	Run 5	33.7	31.69	17.97	1.162	0.688	0.015	-	-	
IR	Run 6	33.7	31.69	13.51	0.958	0.609	0.01	-	-	
	Average	33.7	31.69	15.52	0.91	0.60	0.01	-	-	
	S.D.	-	-	-	0.281	0.090	0.004	-	-	
PC-P6.1										
IR	Run 1	67.0	65.89	65.89	-	-	0.017	0.003	0.062	
IR	Run 2	67.0	65.89	65.89	-	-	0.012	-	-	
IR	Run 3	67.0	65.89	65.89	-	-	0.013	-	0.06	
White	Run 5	67.0	65.89	65.89	1.137	-	0.017	0.022	0.076	
White	Run 6	67.0	65.89	65.89	1.958	-	0.014	-	-	
White	Run 7	67.0	65.89	65.89	0.861	-	-	0.0192	0.0526	
	Average	67.0	65.89	65.89	1.32	-	0.01	-	-	
	S.D.	-	-	-	0.571	-	0.002	-	-	
PC-P1.3										
IR	Run 1	51.00	51.37	51.00	-	1.791	0.073	0.007	0.054	
IR	Run 2	51.00	51.37	51.00	-	1.935	0.072	-	-	
IR	Run 3	51.00	51.37	51.00	-	1.495	0.0748	0.014	0.05	
White	Run 4	51.00	51.37	51.00	-	-	-	0.019	0.18	
White	Run 5	51.00	51.37	51.00	-	0.327	0.08	0.0114	0.059	
White	Run 6	51.00	51.37	51.00	-	1.508	0.073	0.011	0.062	
	Average	51.00	51.37	51.00	-	0.92	0.08	0.0125	0.081	
	S.D.	-	-	-	-	0.835	0.005	0.0044	0.0555	
PC-P4.2B										
IR	Run 1	62.30	62.30	7.39	0.487	0.93	-	0.009	0.047	
IR	Run 2	62.30	62.30	42.93	1.076	0.871	0.0087	0.007	0.061	

IR	Run 3	62.30	62.30	34.64	0.784	0.819	0.005	0.001	0.061
	Average	62.30	62.30	28.32	0.78	0.87	0.01	0.01	0.06
	S.D.	-	-	-	0.295	0.056	0.003	0.004	0.008
<hr/>									
PC-P3.1									
MI 1									
IR	Run 1	50.00	50.30	50.00	-	1.302	0.027	0.0157	0.047
White	Run 2	50.00	50.30	50.00	-	0.81	0.033	0.011	0.046
White	Run 3	50.00	50.30	50.00	-	0.847	0.035	0.014	0.042
White	Run 4	50.00	50.30	50.00	-	-	0.029	0.011	0.037
	Average	50.00	50.30	50.00	-	0.99	0.03	0.012925	0.043
	S.D.	-	-	-	-	0.274	0.004	0.002	0.005
<hr/>									
PC-P3.1									
MI 2									
White	Run 5	50.00	50.30	50.00	-	-	0.046	0.014	0.062
White	Run 6	50.00	50.30	50.00	-	-	0.043	0.0115	0.059
White	Run 7	50.00	50.30	50.00	-	-	0.046	0.018	0.062
	Average	50.00	50.30	50.00	-	-	0.05	0.01	0.06
	S.D.	-	-	-	-	-	0.002	0.003	0.002
<hr/>									
PC-P6.3									
MI 1									
IR	Run 1-	53.67	54.321	53.67	1.665	0.896	0.030	0.010	0.039
IR	Run 2	53.67	54.321	53.67	-	1.081	0.037	-	0.038
IR	Run 3	53.67	54.321	53.67	-	1.225	0.035	0.013	0.040
White	Run 4	53.67	54.321	53.67	-	-	0.034	0.01	0.04
White	Run 5	53.67	54.321	53.67	-	0.975	0.031	0.01	0.038
White	Run 6	53.67	54.321	53.67	-	-	0.033	0.012	0.035
	Average	53.67	54.32	53.67	-	1.04	0.03	0.01	0.04
	S.D.	-	-	-	-	0.142	0.003	0.002	0.001
<hr/>									
PC-P6.3									
MI 2									
IR	Run 1	53.670	54.321	53.670	-	1.295	0.027	0.011	0.045
White	Run 2	53.670	54.321	53.670	-	-	0.026	0.011	0.049
White	Run 3	53.670	54.321	53.670	1.413	-	-	0.014	0.050
White	Run 4	53.670	54.321	53.670	-	-	0.027	0.012	0.047
	Average	53.67	54.32	53.67	1.413	1.295	0.03	0.012	0.048
	S.D.	-	-	-	-	-	0.001	0.001	0.002

PC-P6										
IR	Run 1	33.00	32.42	32.42	1.206	0.643	0.019	-	-	-
IR	Run 2	33.00	32.42	32.42	1.286	0.737	0.024	-	-	-
IR	Run 3	33.00	32.42	32.42	1.275	0.679	0.0213	-	-	-
	Average	33.00	32.42	32.42	1.26	0.69	0.02	-	-	-
	S.D.	-	-	-	0.043	0.047	0.003	-	-	-
PC-P12										
IR	Run 1	39.00	37.79	26.65	1.071	0.722	-	-	-	-
IR	Run 2	39.00	37.79	31.19	1.568	0.905	-	-	-	-
IR	Run 3	39.00	37.79	29.92	1.35	0.865	0.0068	0.008	0.037	0.037
	Average	39.00	37.79	29.25	1.33	0.83	0.0068	0.008	0.037	0.037
	S.D.	-	-	-	0.249	0.096	-	-	-	-
PC-P1.2										
MI 1										
White	Run 2	64.00	62.614	62.614	1.82	-	0.037	0.0113	0.0716	0.0716
White	Run 3	64.00	62.614	62.614	1.786	-	0.036	0.009	0.066	0.066
White	Run 4	64.00	62.614	62.614	1.953	-	0.04	0.012	0.049	0.049
	Average	64.00	62.61	62.61	1.85	-	0.04	0.01	0.06	0.06
	S.D.	-	-	-	0.088	-	0.002	0.002	0.012	0.012
PC-P1.2										
MI 2										
White	Run 5	64.00	62.614	62.614	-	-	0.081	0.011	0.059	0.059
White	Run 6	64.00	62.614	62.614	-	-	0.083	-	-	-
White	Run 7	64.00	62.614	62.614	-	-	0.073	0.009	0.067	0.067
	Average	64.00	62.614	62.61	-	-	0.079	0.010	0.063	0.063
	S.D.	-	-	-	-	-	0.005	0.001	0.006	0.006
PC-P5.1										
MI 1										
IR	Run 1	44.00	44.12	44.00	1.991	1.125	0.112	0.0089	0.0394	0.0394
IR	Run 2	44.00	44.12	44.00	1.885	1.057	0.108	0.0089	0.0417	0.0417
IR	Run 3	44.00	44.12	44.00	2.032	1.139	0.11	0.0087	0.0392	0.0392
	Average	44.00	44.12	44.00	1.97	1.11	0.11	0.01	0.04	0.04
	S.D.	-	-	-	0.076	0.044	0.002	0.000	0.001	0.001
PC-P5.1										
MI 2										
IR	Run 4	44.00	44.12	44.00	1.682	1.012	0.115	0.002	0.043	0.043

IR	Run 5	44.00	44.12	44.00	1.232	0.856	0.113	0.007	0.036
IR	Run 6	44.00	44.12	44.00	1.031	0.789	0.109	-	-
	Average	44.00	44.12	44.00	1.32	0.89	0.11	0.005	0.040
	S.D.	-	-	-	0.333	0.114	0.003	0.004	0.005
<hr/>									
PC-P1.4									
IR	Run 1	77.00	77.00	77.00	-	-	0.086	0.0153	0.0749
White	Run 2	77.00	77.00	77.00	-	-	0.083	0.012	0.072
White	Run 3	77.00	77.00	77.00	-	-	0.088	0.011	0.075
White	Run 4	77.00	77.00	77.00	-	-	0.09	0.013	0.073
	Average	77.00	77.00	77.00	-	-	0.087	0.013	0.074
	S.D.	-	-	-	-	-	0.003	0.002	0.001
<hr/>									

Table I2.

Ratios of total water to hydroxyl and molecular water to hydroxyl for individual FTIR analyses.

	Total water/hydroxyl	Molecular water/bound hydroxyl
PC-P2.6		
IR	0.83	0.20
IR	0.80	0.10
IR	0.80	0.00
PC-P4.1		
IR	1.36	-
IR	0.85	-
IR	0.80	-
PC-P3.2		
IR	0.75	-
IR	0.87	-
IR	1.33	-
PC-P3.3		
IR	1.18	0.22
IR	1.30	0.10
IR	1.55	0.37
PC-P3.4		
IR	1.27	-
IR	1.02	-
IR	1.51	-
PC-P2.2 MI 1		
IR	0.82	-
IR	0.82	-
IR	0.97	-
PC-P2.2 MI 2		
IR	0.84	-
IR	0.59	-
IR	0.64	-
PC-P6.1		
IR	-	0.05
IR	-	0.00
IR	-	0.00
White	-	0.29
White	-	0.18
White	-	0.37
PC-P1.3		
IR	-	0.13

IR	-	
IR	-	0.28
White	-	0.11
White	-	0.19
White	-	0.18
<hr/>		
PC-P4.2B		
IR	1.91	0.19
IR	0.81	0.11
IR	1.04	0.02
<hr/>		
PC-P3.1 MI 1		
White	-	0.23
White	-	0.19
White	-	0.29
<hr/>		
PC-P6.3 MI 1		
IR	0.54	0.26
IR	-	
IR	-	0.33
White	-	0.25
White	-	0.26
White	-	0.34
<hr/>		
PC-P6.3 MI 2		
IR	-	0.24
White	-	0.22
White	-	0.28
White	-	0.26
<hr/>		
PC-P6		
IR	0.53	-
IR	0.57	-
IR	0.53	-
<hr/>		
PC-P12		
IR	0.67	-
IR	0.58	-
IR	0.64	0.22
<hr/>		
PC-P1.2 MI 1		
IR	0.78	0.46
White	-	0.16
White	-	0.14
White	-	0.24
<hr/>		
PC-P1.2 MI 2		
White	-	0.19
White	-	0.00
White	-	0.13
<hr/>		

PC-P5.1 MI 1		
IR	0.57	0.23
IR	0.56	0.21
IR	0.56	0.22
PC-P5.1 MI 2		
IR	0.60	0.05
IR	0.69	0.19
IR	0.77	-
PC-P1.4		
IR	-	0.20
White	-	0.17
White	-	0.15
White	-	0.18

Table I3.

Normalized major elements and unnormalized total of rhyolitic TAV quartz-hosted melt inclusions. An italics *0* is present where any negative measurements were made and n refers to the number of measurements averaged for each inclusion.

Sample	n	SiO ₂	TiO ₂	Al ₂ O ₃	FeO	MgO	CaO	Na ₂ O	K ₂ O	P ₂ O ₅	S	Cl	F	Total
PC-P1.2 MI 1	1	75.54	0.007	12.71	0.77	0.005	0.453	1.43	9.08	<i>0</i>	<i>0</i>	0.072	1.21	94.67
PC-P1.2 MI 2	2	78.06	0.030	12.73	0.68	0.001	0.437	3.00	5.06	<i>0</i>	0.0022	0.079	1.36	92.35
PC-P1.4	2	75.98	0.032	13.07	0.72	0.007	0.464	1.29	8.44	<i>0</i>	0.0005	0.079	1.11	94.55
PC-P12 MI 2	1	78.52	-0.007	12.93	0.67	<i>0</i>	0.452	2.74	4.70	<i>0</i>	<i>0</i>	0.078	1.45	92.43
PC-P2.2 MI 2	1	77.08	0.053	12.90	0.64	<i>0</i>	0.332	4.57	4.43	<i>0</i>	0.0023	0.066	0.89	91.82
PC-P2.6	2	77.73	0.061	12.58	0.72	0.004	0.462	3.84	4.52	0.09	0.0112	0.089	1.37	91.66
PC-P3.1 MI 1	1	75.38	0.014	12.96	0.73	0.002	0.458	1.32	9.13	<i>0</i>	<i>0</i>	0.080	1.20	94.29
PC-P3.2	2	78.04	0.038	13.10	0.75	0.001	0.466	2.73	4.89	<i>0</i>	0.0015	0.076	1.36	92.14
PC-P3.3	2	77.96	0.000	12.68	0.69	0.004	0.448	3.82	4.41	<i>0</i>	<i>0</i>	0.074	1.14	93.11
PC-P3.4	2	78.80	0.037	12.83	0.73	0.005	0.460	2.33	4.81	<i>0</i>	0.0045	0.082	1.47	91.83
PC-P4.1	2	77.33	0.021	12.81	0.65	0.000	0.372	4.33	4.48	<i>0</i>	0.0015	0.064	0.96	92.57
PC-P4.2B	2	78.34	0.045	12.74	0.70	0.008	0.455	2.76	4.95	<i>0</i>	0.0032	0.077	1.16	93.19
PC-P5.1 MI 1	2	77.16	0.063	12.50	1.06	0.026	0.469	3.28	5.44	<i>0</i>	0.0018	0.121	0.22	94.68
PC-P5.1 MI 2	2	77.13	0.044	12.50	1.02	0.029	0.452	3.32	5.50	<i>0</i>	0.0018	0.120	0.22	94.86
PC-P6	2	76.87	0.040	12.44	0.69	0.002	0.435	1.16	8.36	<i>0</i>	0.0019	0.073	0.54	94.02
PC-P6.1	2	77.81	0.034	12.53	0.70	0.008	0.442	3.26	5.22	<i>0</i>	0.0008	0.075	0.49	93.48
PC-P6.3 MI 1	2	76.01	0.017	12.97	0.70	0.001	0.452	1.32	8.53	<i>0</i>	0.0005	0.079	0.43	94.30
PC-P6.3 MI 2	2	77.60	0.021	12.77	0.68	0.003	0.430	3.32	5.17	<i>0</i>	0.0011	0.079	0.53	94.82

Table I4.

Trace element concentrations (in ppm) of quartz-hosted rhyolitic melt inclusions of the TAV. Concentrations were corrected according to the individual SiO₂ content of each inclusion.

ppm	PC-P3.3	PC-P2.2-2	PC-P2.6	PC-P3.1-2	PC-P3.1-1	PC-P6.3-1	PC-P5.1-1	PC-P5.1-2	PC-P1.4	PC-P1.2-2	PC-P1.2-1
Li	150.68	132.33	144.44	134.50	4.13	51.92	39.26	41.40	0.64	129.96	17.38
B	101.54	87.14	95.13	93.43	79.12	90.52	32.37	39.39	90.39	97.57	89.71
Si	364435.3	360321.6	363360.1	352374.7	352374.7	355319.8	360695.6	360555.4	355179.5	364902.8	353122.7
P	45.58	58.65	53.90	55.68	5.73	101.68	69.20	66.03	42.46	60.02	58.49
Ca	3080.76	2394.79	3021.86	2929.50	2801.65	2699.28	3165.40	2696.45	2324.73	2957.81	2833.47
Ti	143.74	135.45	147.83	138.62	138.15	127.18	377.28	321.49	143.49	136.49	177.91
Rb	577.70	527.95	551.22	533.33	521.99	514.18	286.93	275.91	604.20	573.75	564.93
Sr	0.17	0.06	No_Data	0.03	0.12	0.11	0.56	0.39	0.03	No Data	0.16
Y	152.65	144.72	144.38	137.86	134.72	129.24	97.96	101.65	133.16	150.62	138.01
Zr	94.81	90.72	84.53	83.33	81.33	79.64	99.88	82.69	75.34	87.31	80.97
Nb	60.26	63.66	57.05	52.79	57.16	48.94	112.07	112.82	54.57	52.41	60.95
Sn	12.33	12.44	11.29	11.38	11.87	11.19	4.01	4.30	11.27	11.83	11.86
Ba	0.07	0.09	0.24	0.14	0.07	0.12	2.68	1.21	0.14	0.09	0.23
La	8.38	6.77	7.04	7.47	6.67	6.14	21.30	15.63	6.70	7.25	8.14
Ce	25.62	22.20	22.62	22.44	21.32	19.63	59.66	45.28	21.38	21.83	26.24
Pr	3.74	3.50	3.39	3.05	3.12	2.84	7.08	5.45	2.85	3.11	3.50
Nd	16.56	14.65	15.53	14.81	15.15	15.00	31.58	24.90	14.93	14.94	16.68
Sm	8.21	7.61	8.31	7.84	6.97	7.06	10.98	10.92	7.53	8.24	8.24
Eu	No Data	No Data	No Data	No Data	No Data	No Data	0.05	No Data	No Data	No Data	No Data
Gd	12.29	11.53	12.01	12.61	11.01	10.75	14.63	12.36	12.27	13.10	12.45
Dy	19.07	18.42	19.27	18.60	16.41	16.74	20.04	19.96	17.70	19.91	19.19
Er	14.37	14.20	14.15	12.49	14.03	12.43	12.45	12.55	13.52	14.12	13.40
Yb	16.88	15.82	17.22	15.82	13.48	16.62	10.48	11.51	15.10	17.00	16.31
Hf	7.38	6.44	6.86	6.64	5.82	5.81	4.93	3.90	5.25	7.48	6.55
Ta	11.03	11.41	11.24	9.71	9.61	9.76	4.52	4.87	10.93	10.30	10.49
Pb	78.31	68.26	72.45	76.28	68.25	73.20	58.79	55.52	77.86	70.46	78.03
Th	32.66	29.60	31.04	30.56	26.89	27.38	40.32	41.13	27.80	30.19	30.88
U	19.23	20.11	18.00	18.20	16.39	17.45	15.38	16.38	17.24	17.42	18.68

Table I4 continued

ppm	PC-P4.2-1	PC-P1.3
Li	97.59	138.95
B	89.58	99.38
Si	366211.7	361350.0
P	50.30	66.04
Ca	2969.02	2400.78
Ti	123.66	132.19
Rb	546.64	560.01
Sr	0.10	No Data
Y	129.58	143.79
Zr	77.57	83.88
Nb	51.95	53.40
Sn	11.94	12.36
Ba	0.11	0.03
La	6.62	6.66
Ce	21.89	22.67
Pr	3.07	3.20
Nd	13.30	14.36
Sm	7.29	8.95
Eu	No Data	No Data
Gd	11.33	11.66
Dy	15.53	17.15
Er	12.03	13.57
Yb	14.75	14.10
Hf	5.73	7.12
Ta	8.91	9.61
Pb	74.28	78.27
Th	27.93	28.41
U	18.04	18.53

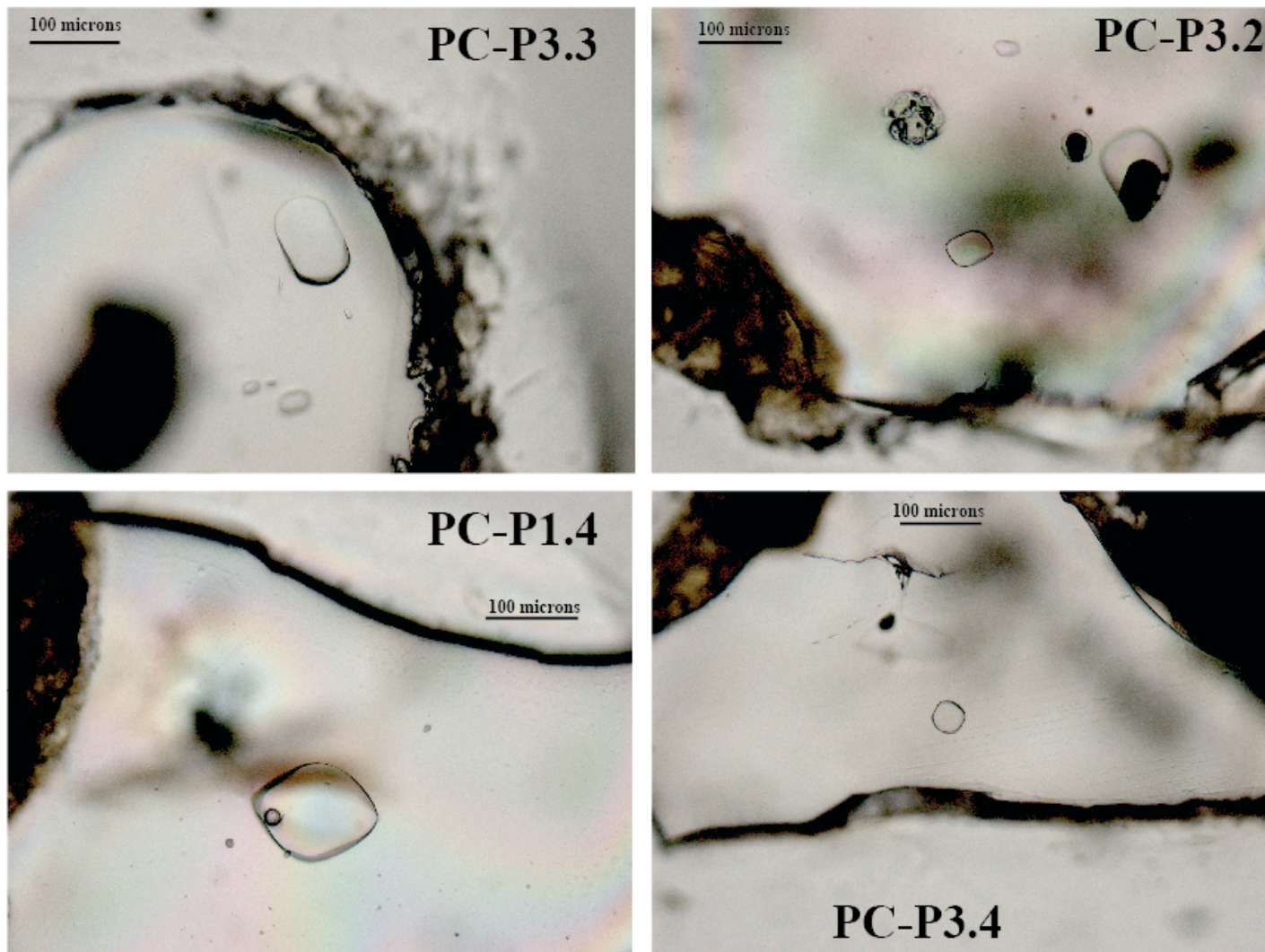


Fig. 11. a. Compilation of photomicrographs of singly polished melt inclusions taken with transmitted light at 10X.

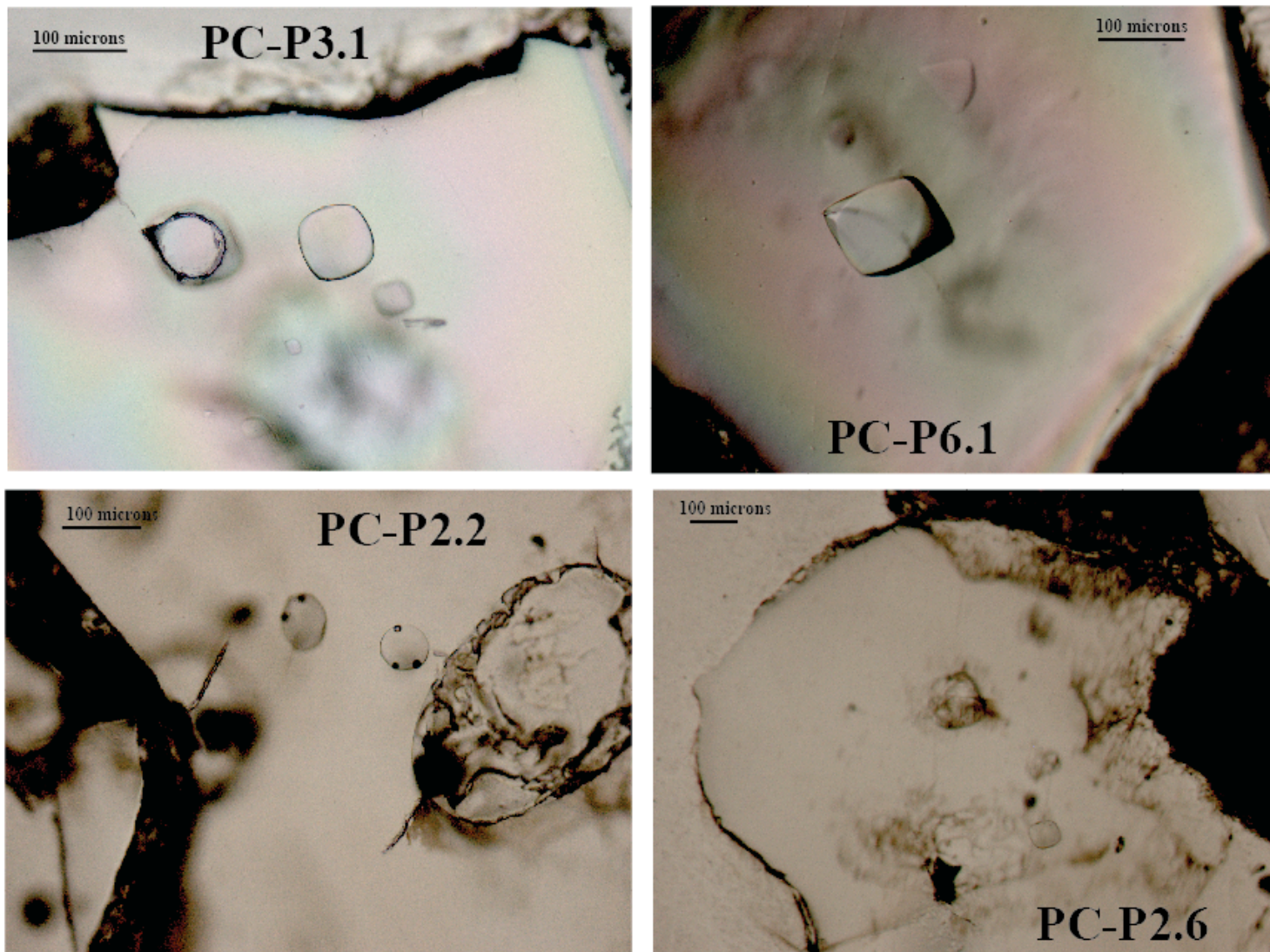


Fig. 11. b. Compilation of photomicrographs of singly polished melt inclusions taken with transmitted light at 10X.

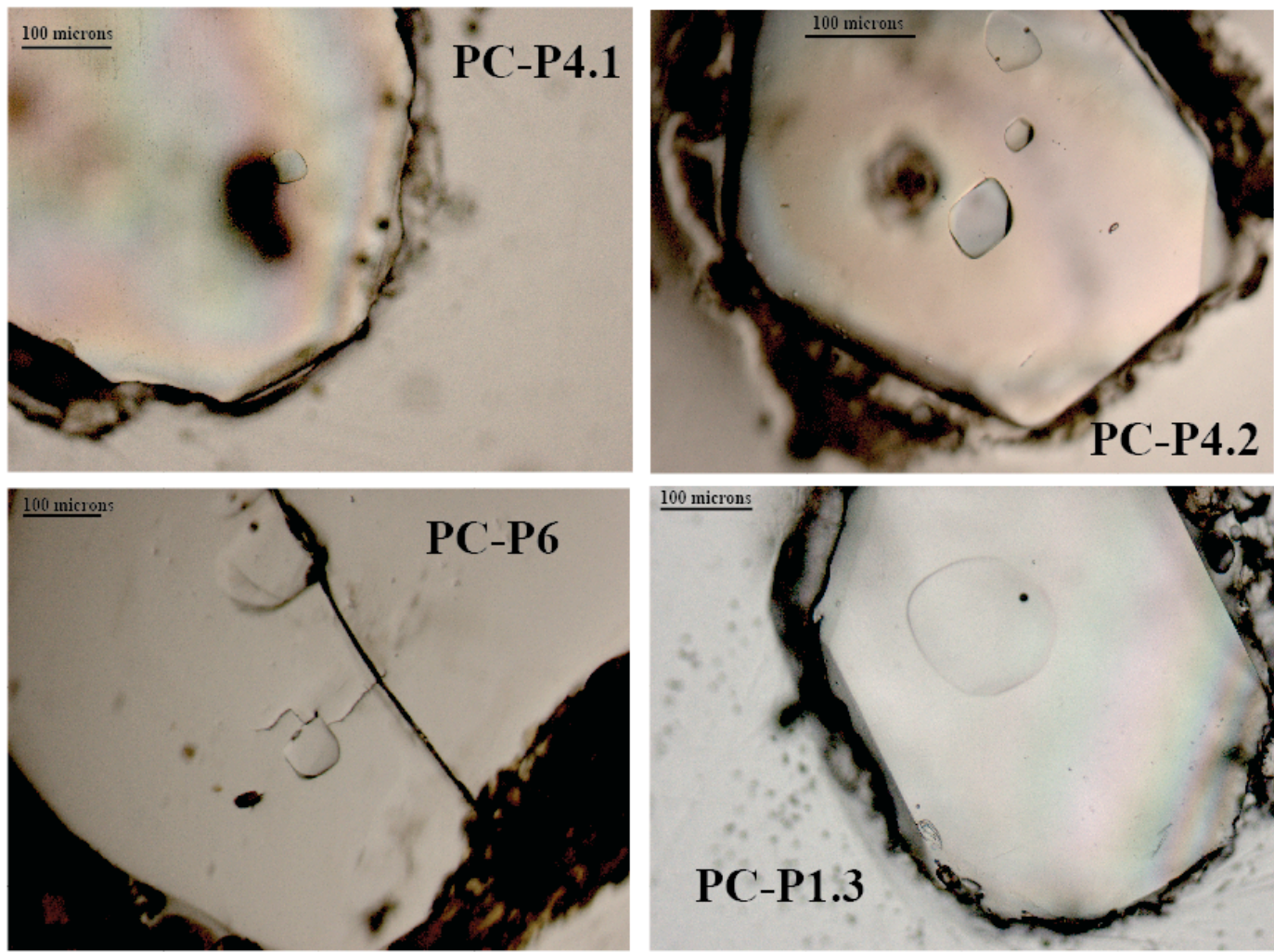


Fig. 11. c. Compilation of photomicrographs of singly polished melt inclusions taken with transmitted light at 10X.

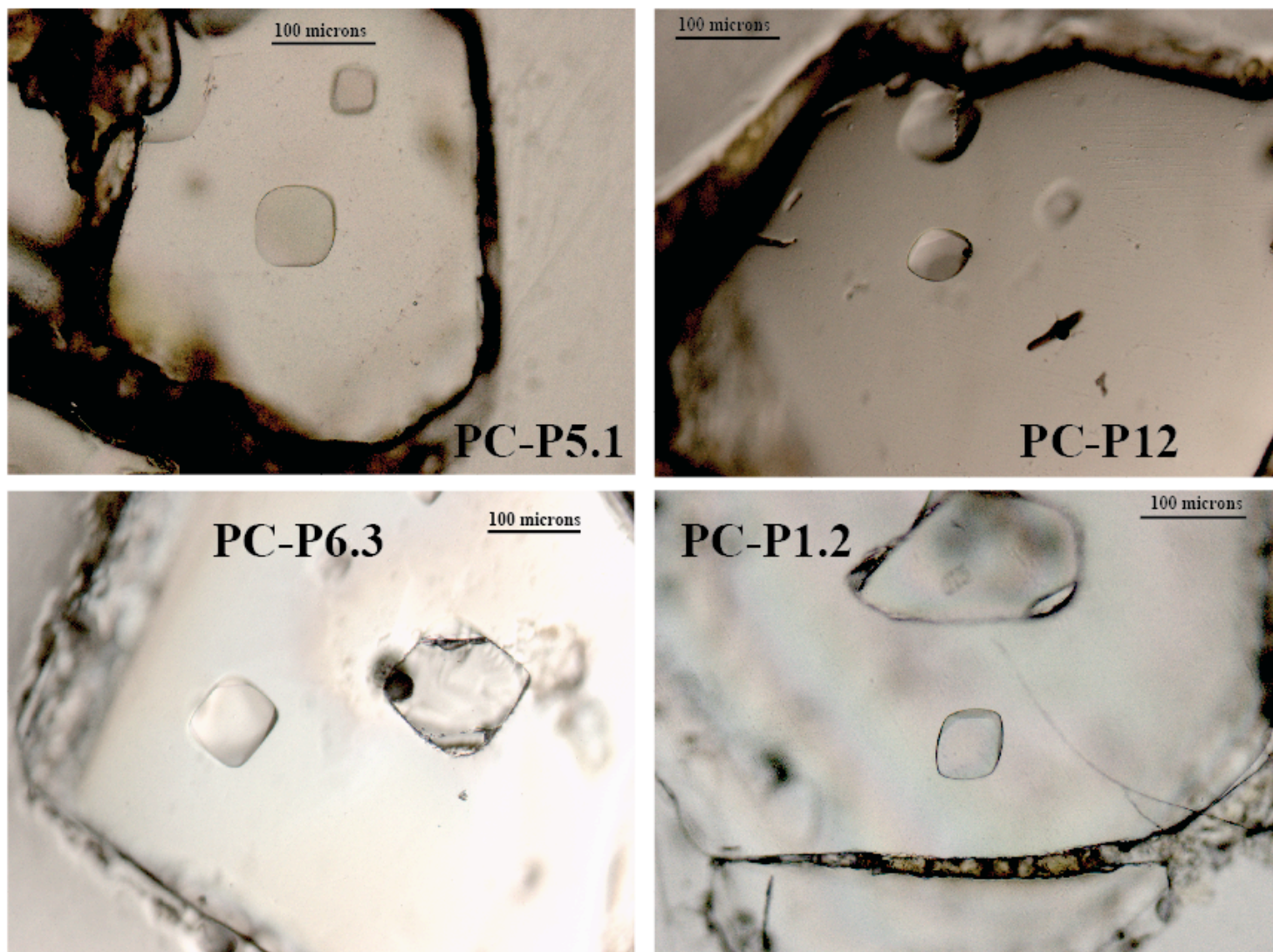


Fig. 11. d. Compilation of photomicrographs of singly polished melt inclusions taken with transmitted light at 10X.

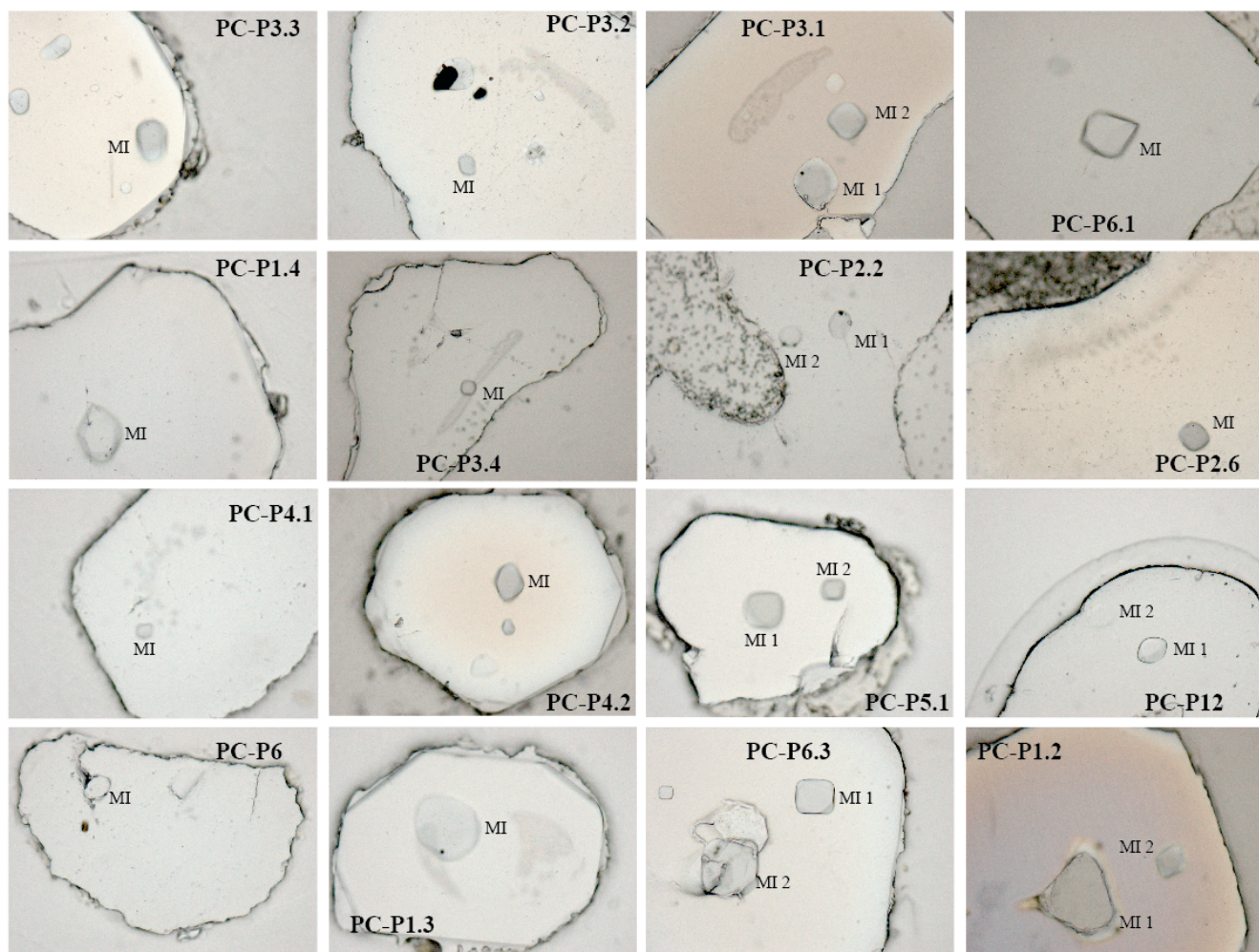


Fig. 12. Compilation of photomicrographs of doubly polished melt inclusions taken with transmitted light at 10X.

APPENDIX J

CATHODOLUMINESCENCE IMAGES

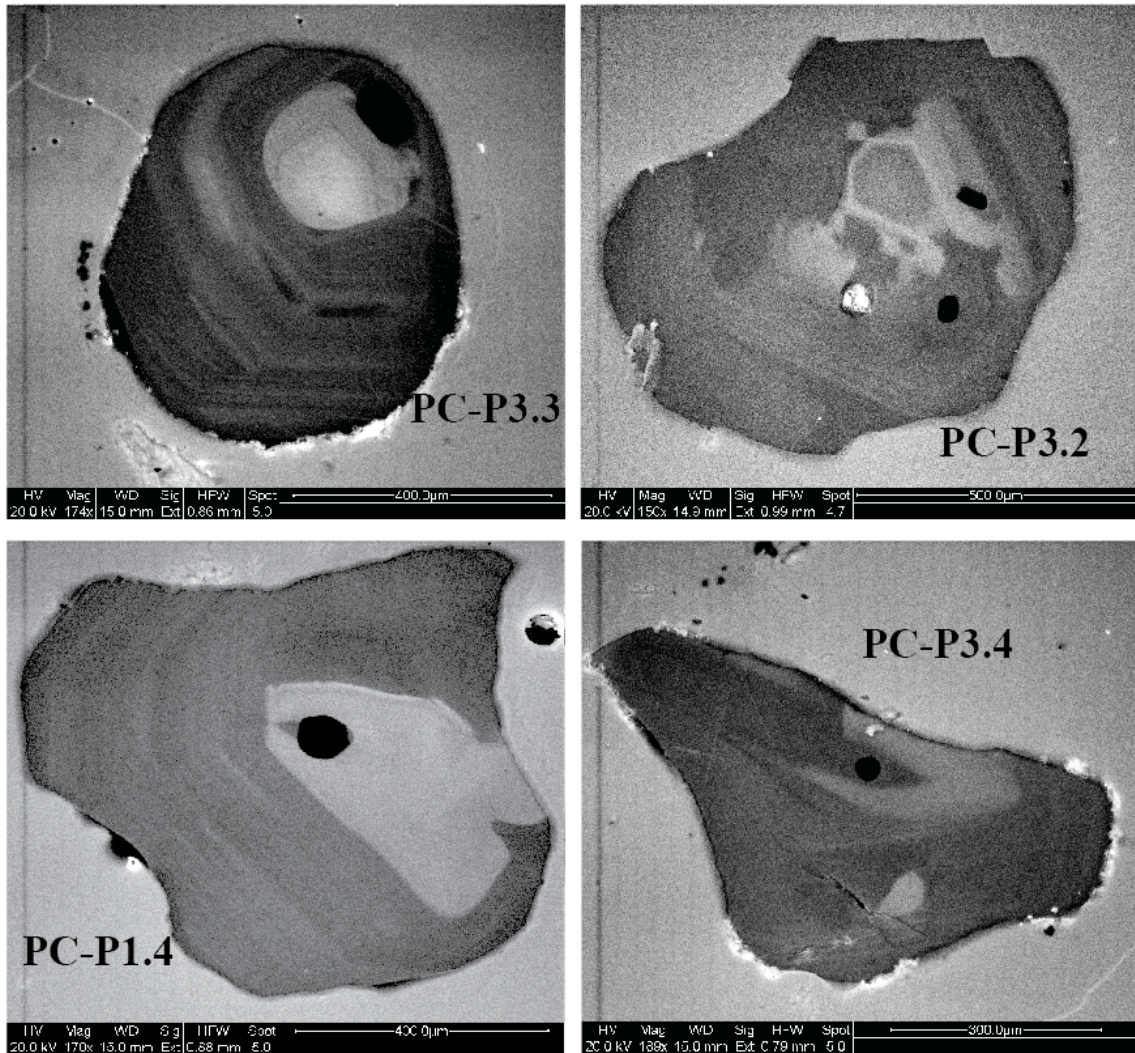


Fig. J1. a. CL images taken on the scanning electron microscope (SEM) of melt inclusion host quartz phenocrysts.

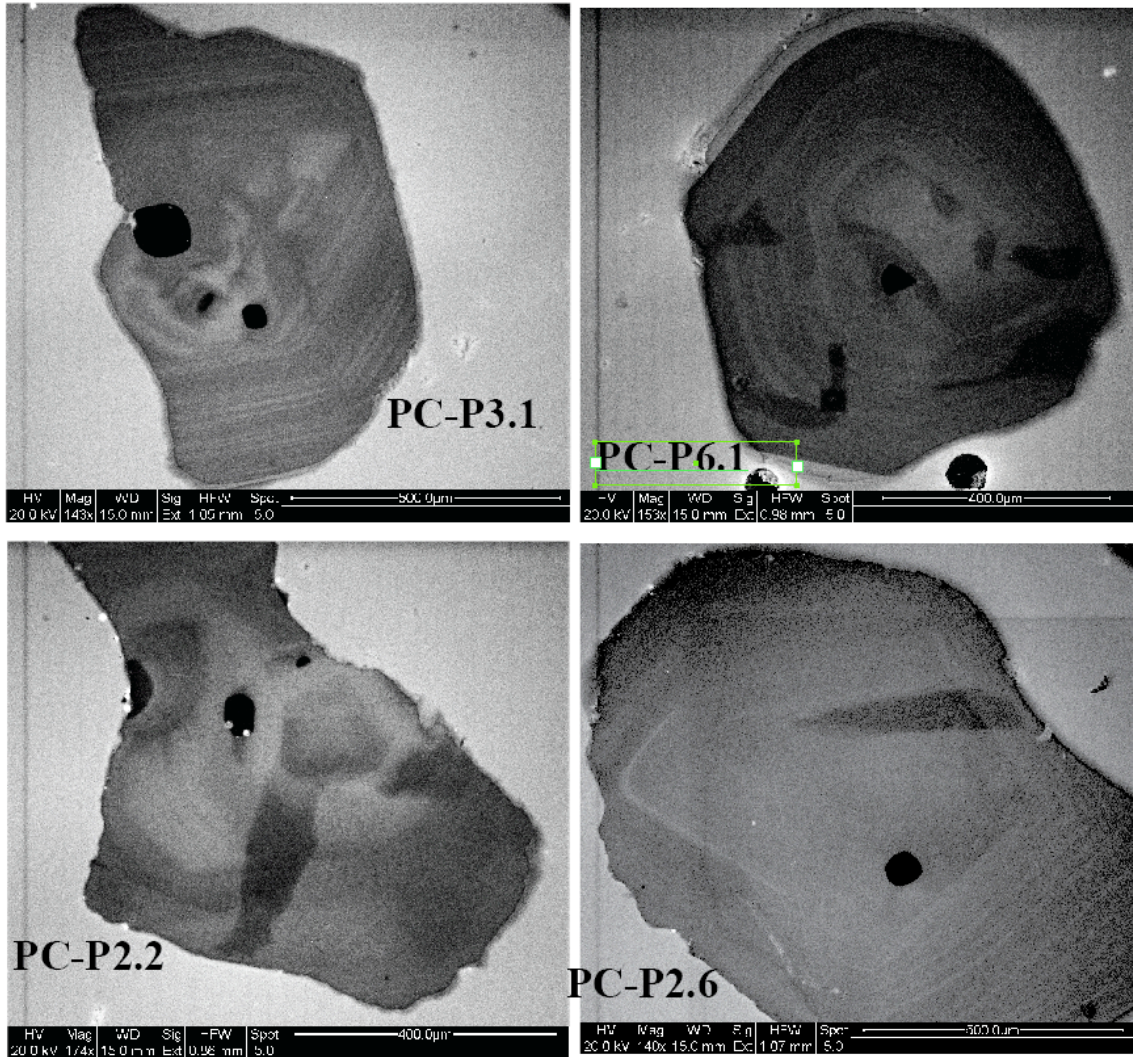


Fig. J1. b. CL images taken on the scanning electron microscope (SEM).

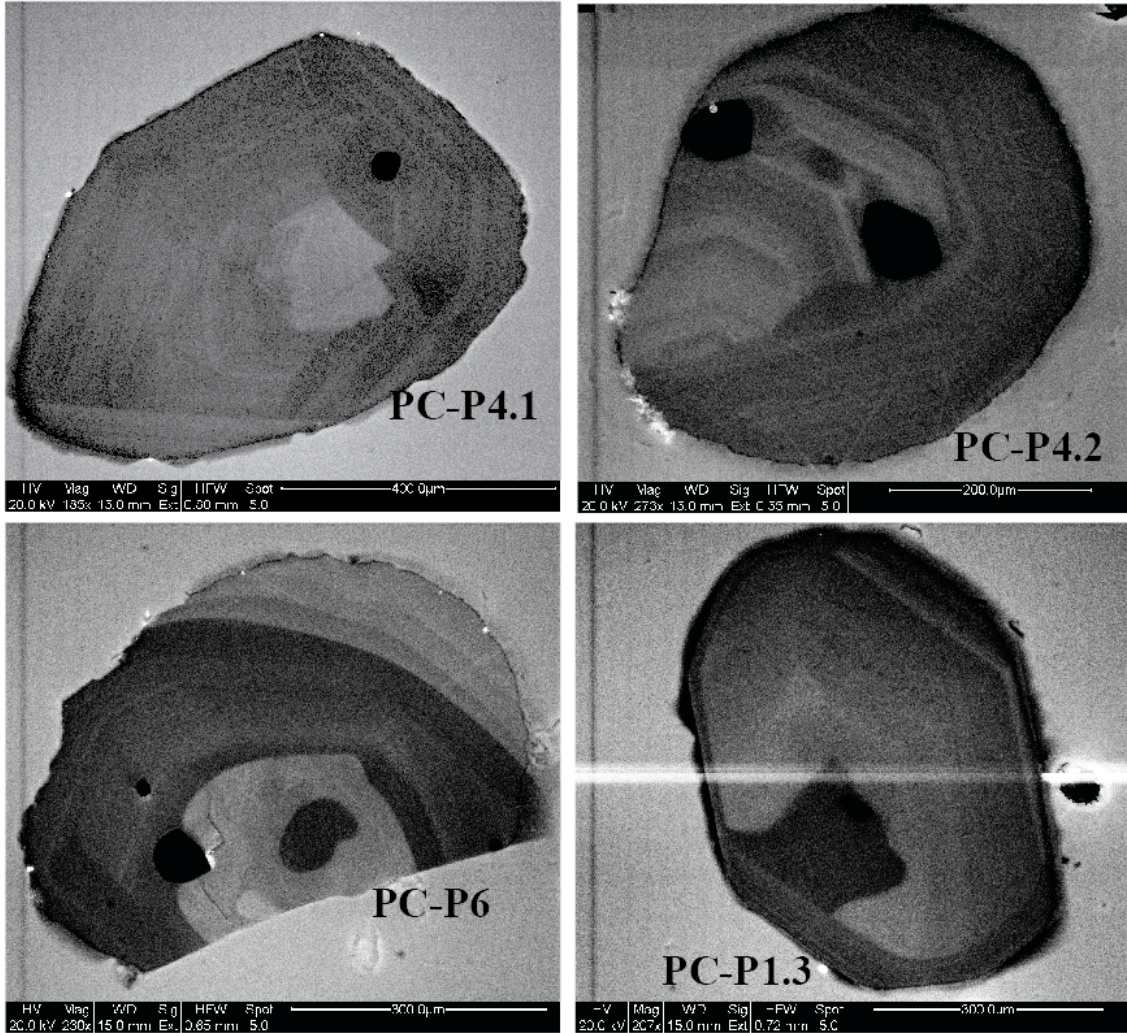


Fig. J1. c. CL images taken on the scanning electron microscope (SEM).

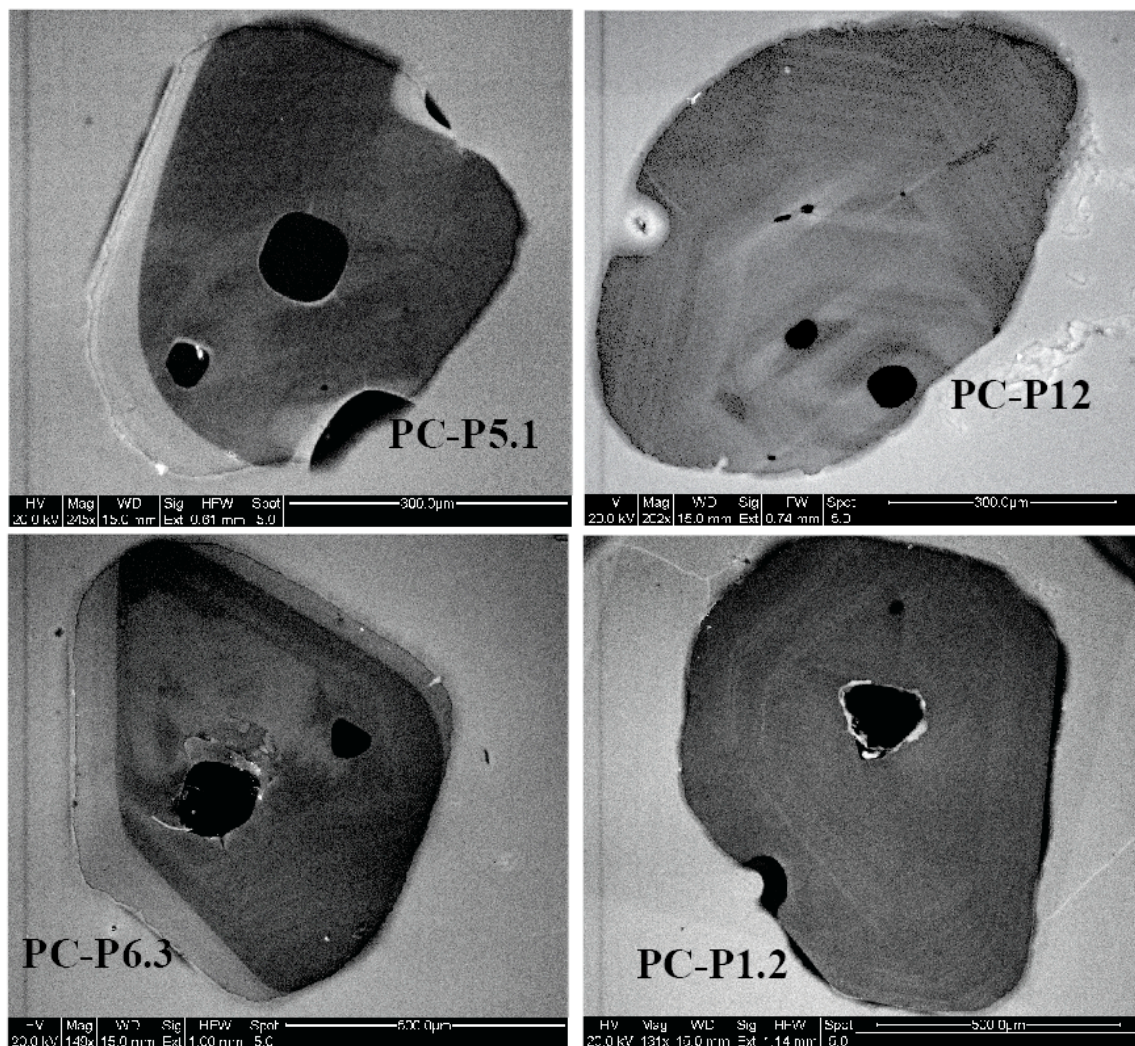


Fig. J1. d. CL images taken on the scanning electron microscope (SEM).

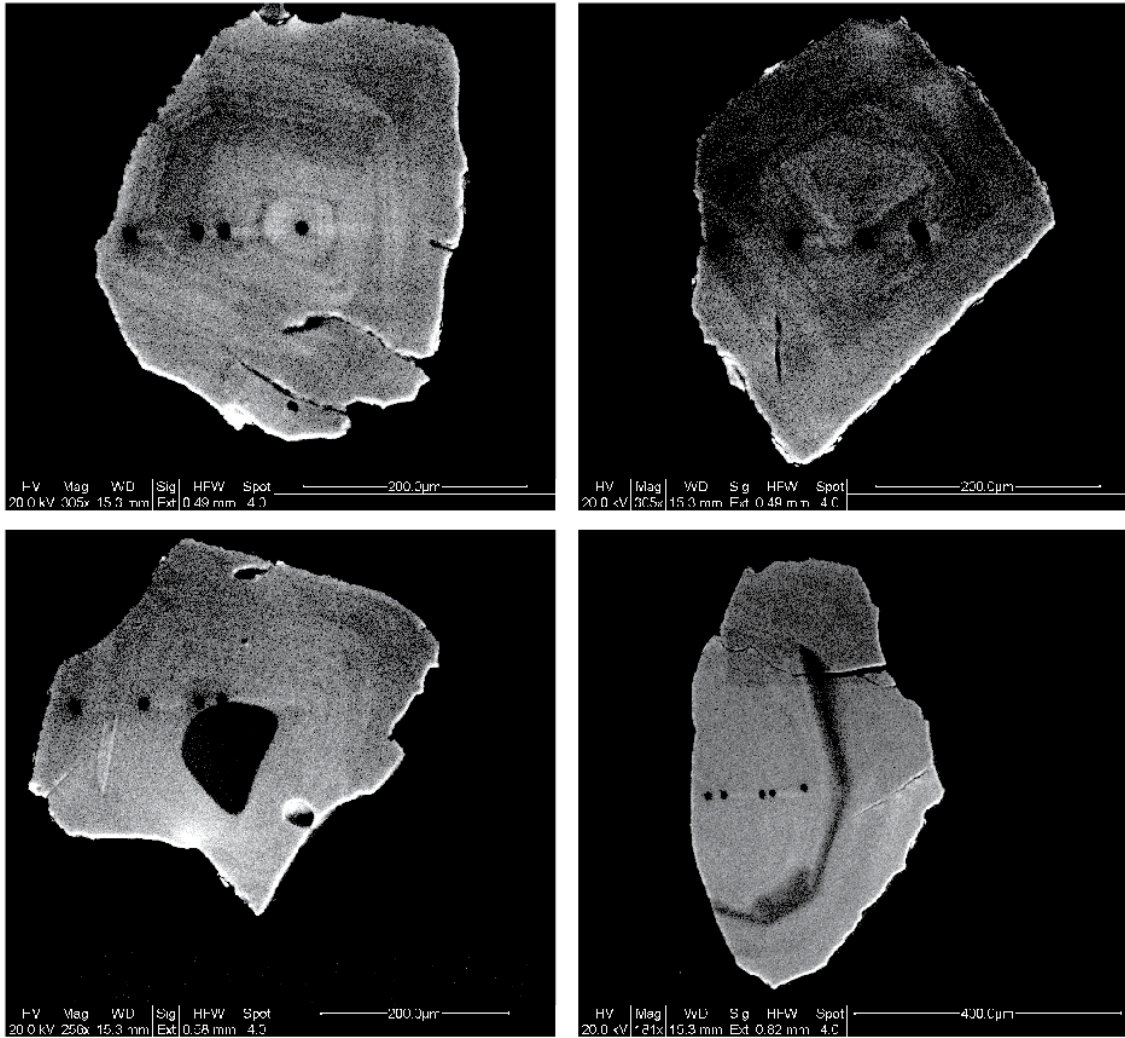


Fig. J2. Cathodoluminescence images of quartz phenocrysts from the West Pocatello rhyolite (PC-01). (top row (left to right): PC-1.3, PC-1.5; bottom row: PC-1.2, PC-1.1).

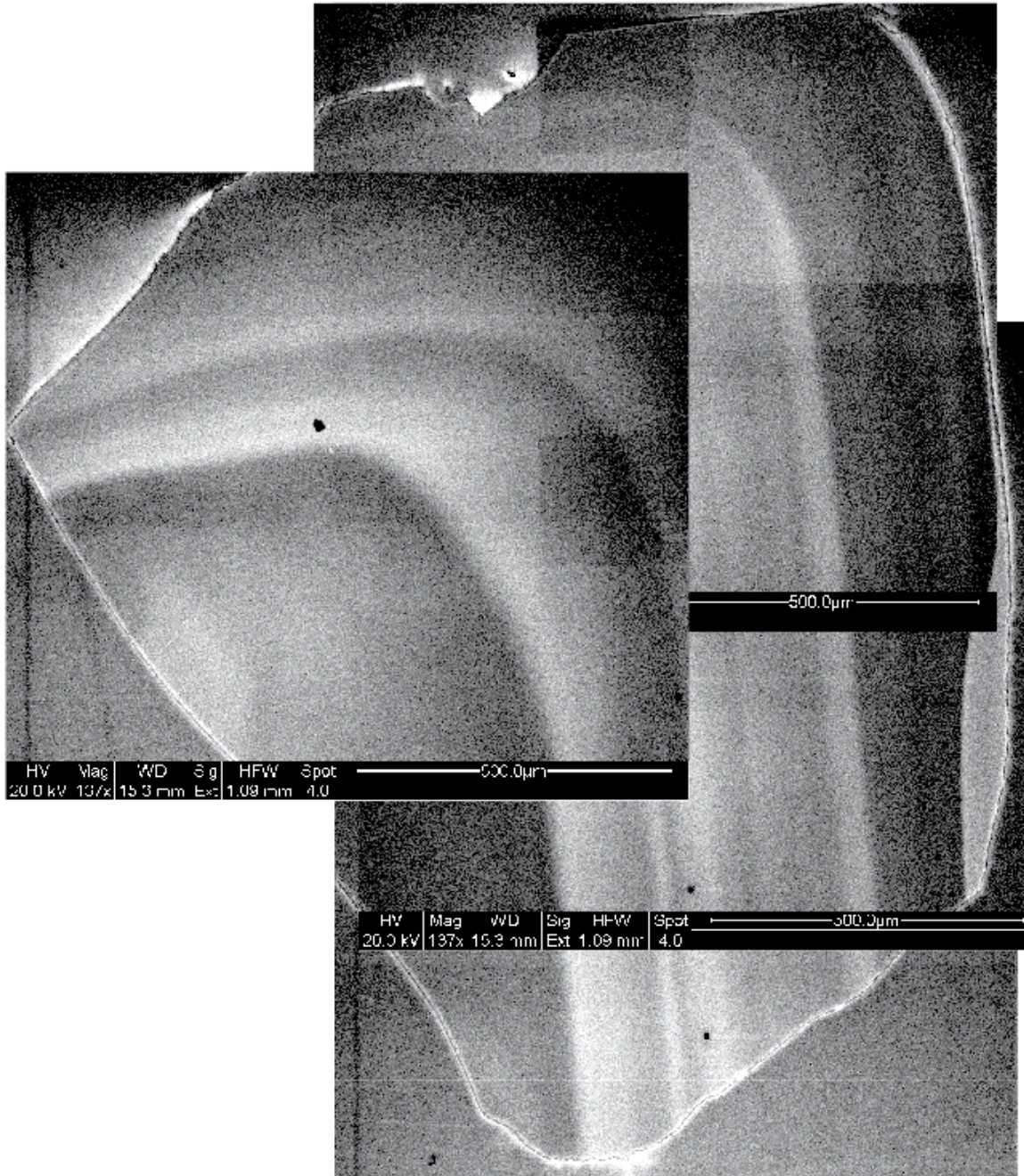


Fig. J3. a. Cathodoluminescence image compilation of a quartz phenocryst PC-14.1 from the upper TAV (PC-14).

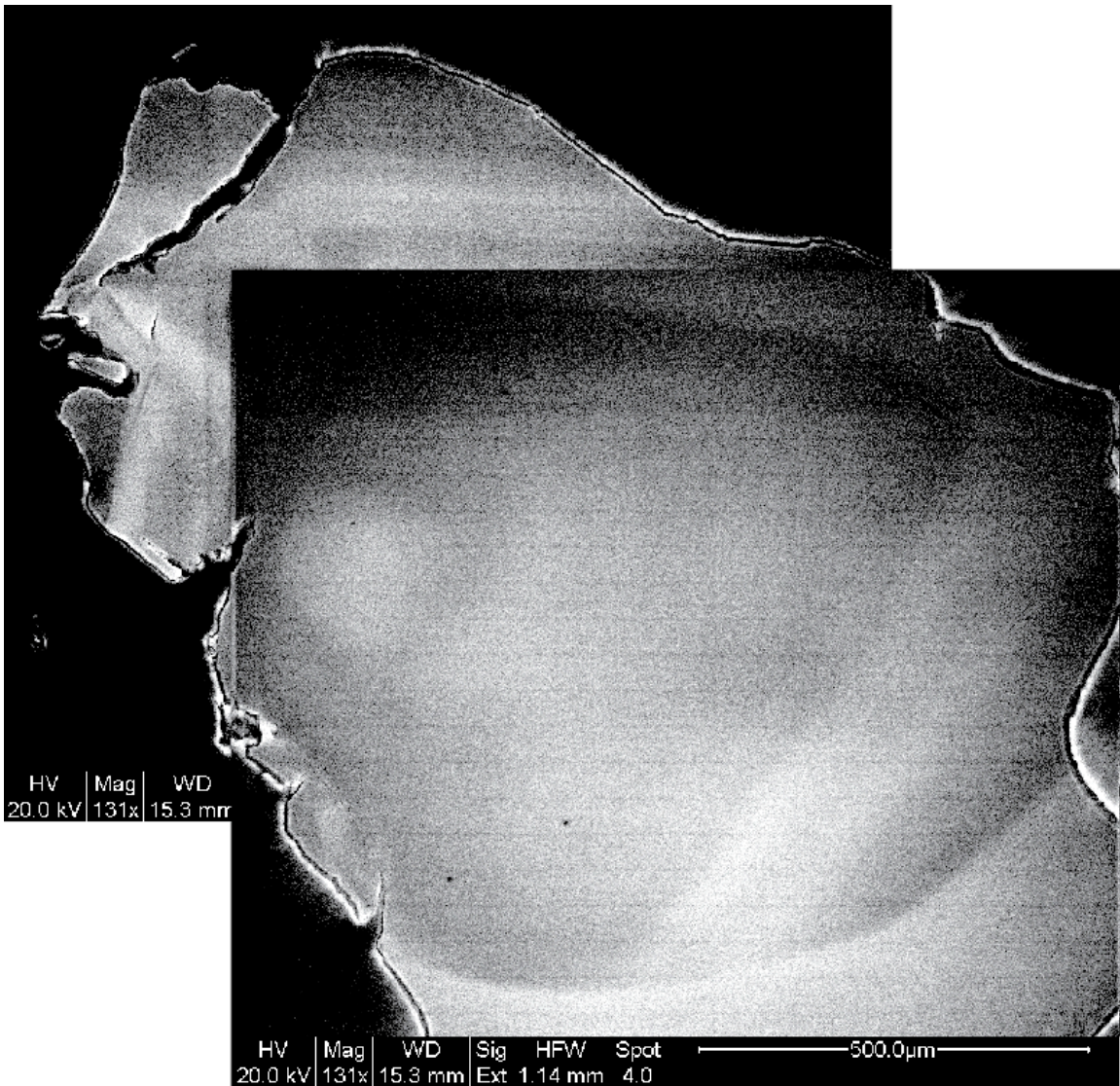


Fig. J3. b. Annotated cathodoluminescence image of a quartz phenocryst PC-14.7 from the upper TAV (PC-14).

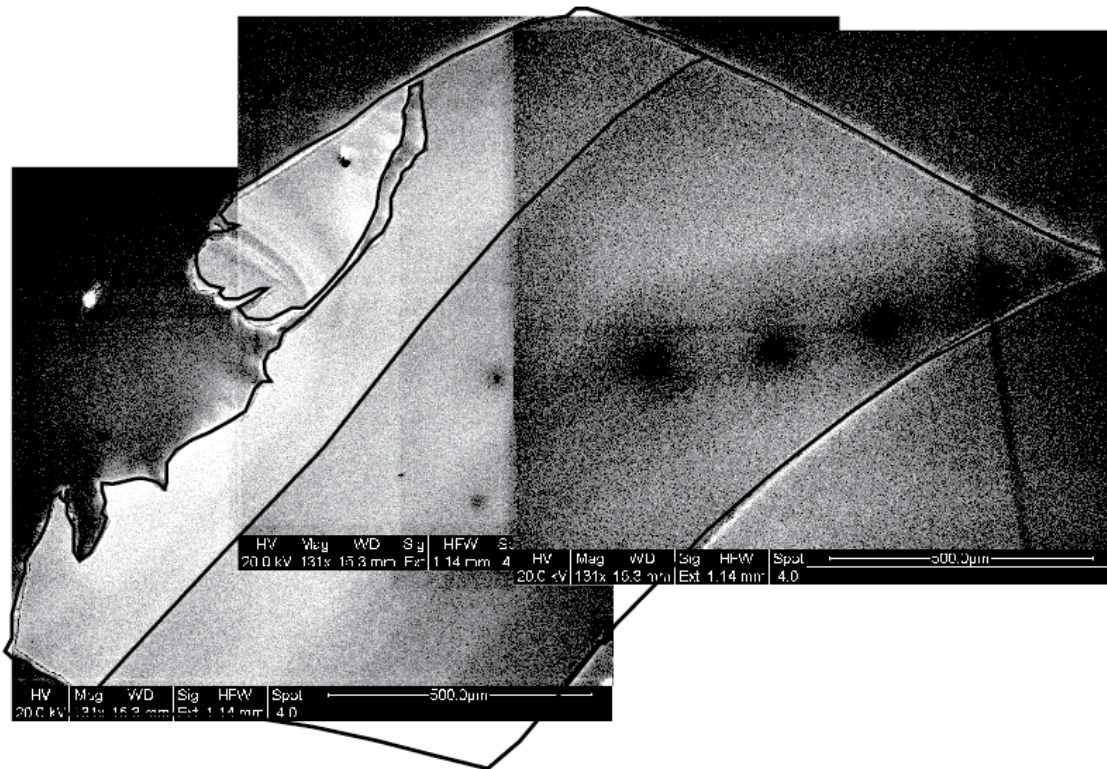


Fig. J3. c. Annotated compilation of cathodoluminescence images of a quartz phenocryst PC-14.5 from the upper TAV (PC-14).

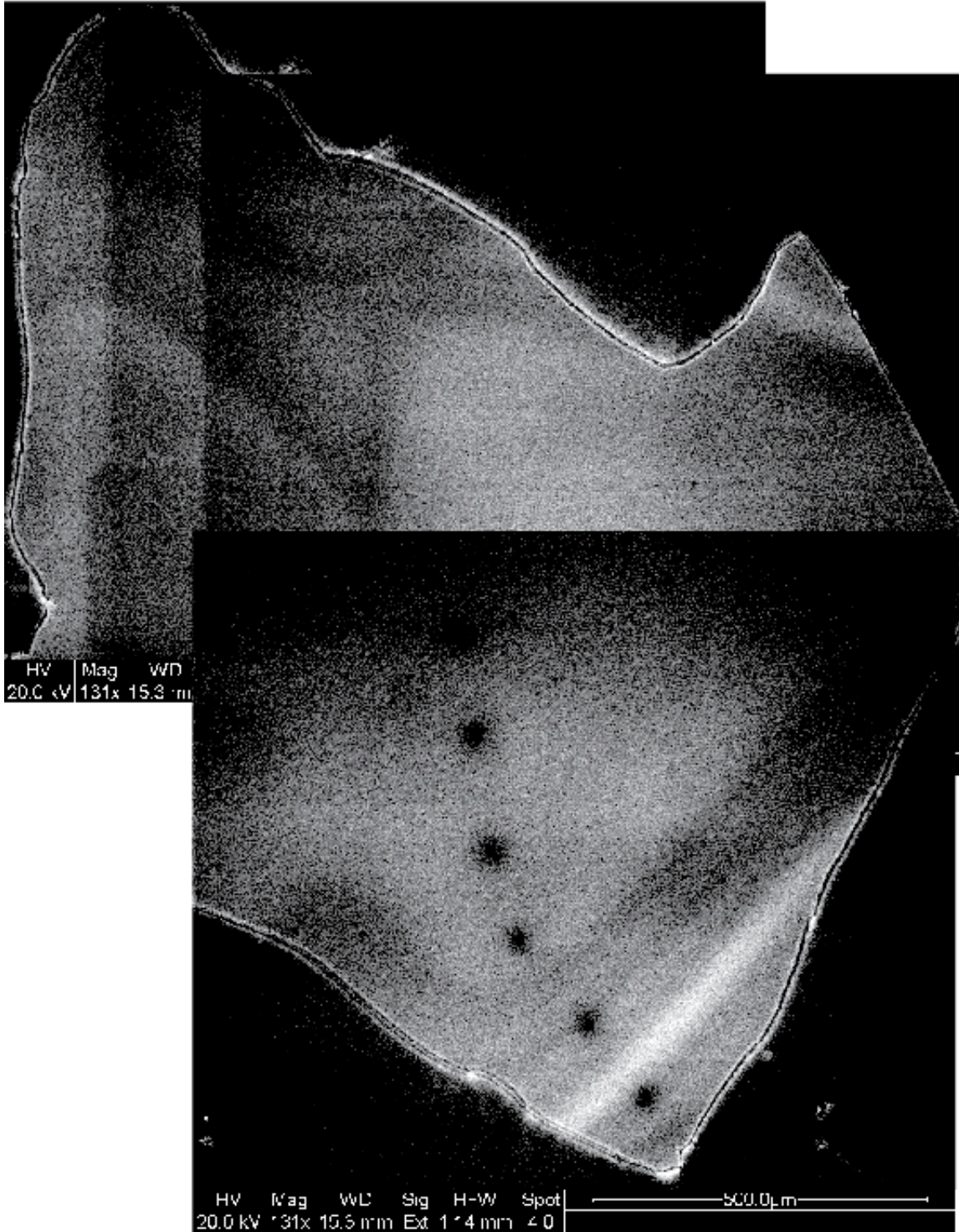


Fig. J3. d. Compilation of cathodoluminescence images of a quartz phenocryst PC-14.2 from the upper TAV (PC-14).

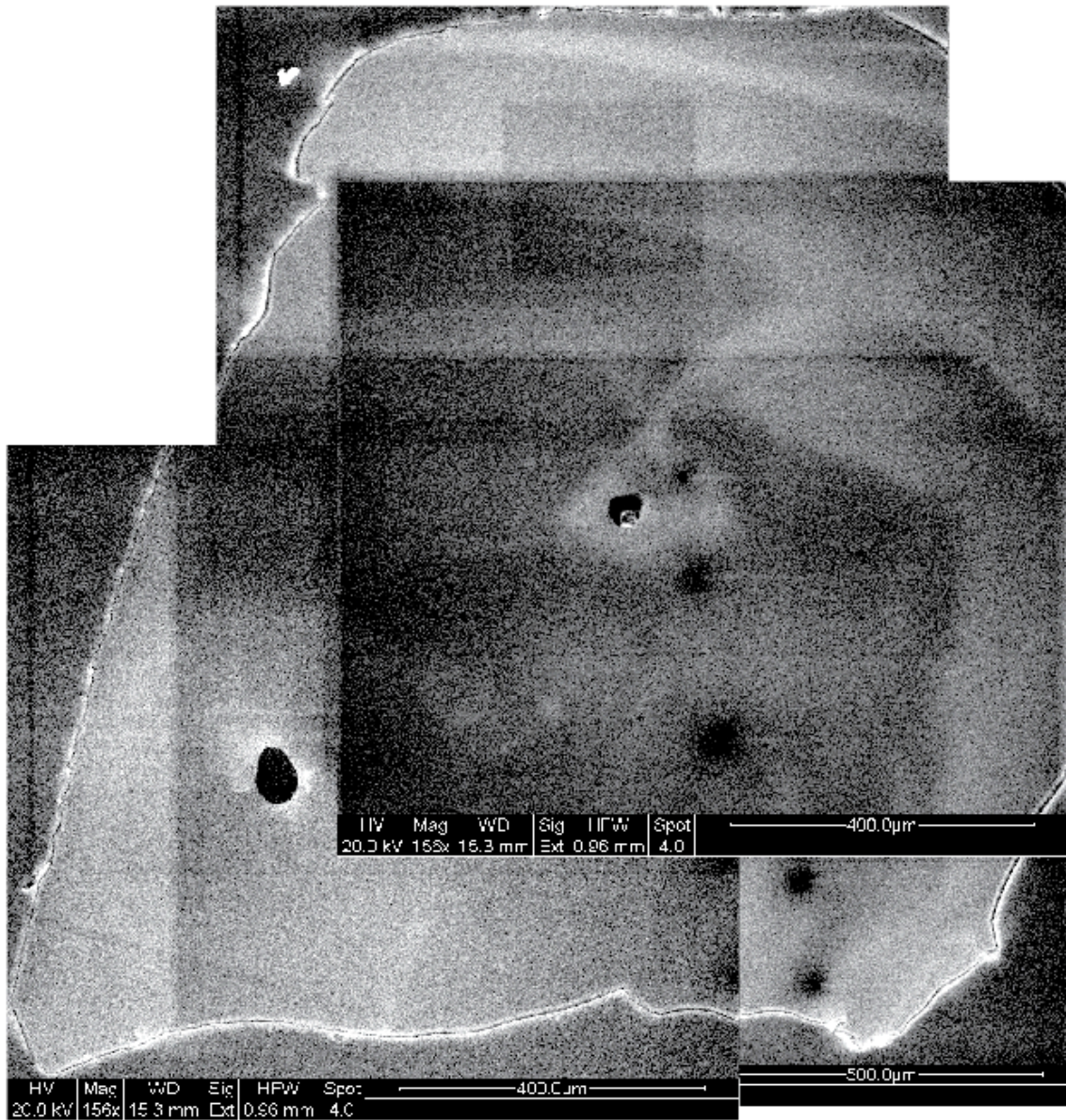


Fig. J3. e. Compilation of cathodoluminescence image of a quartz phenocryst from the upper TAV (PC-14).

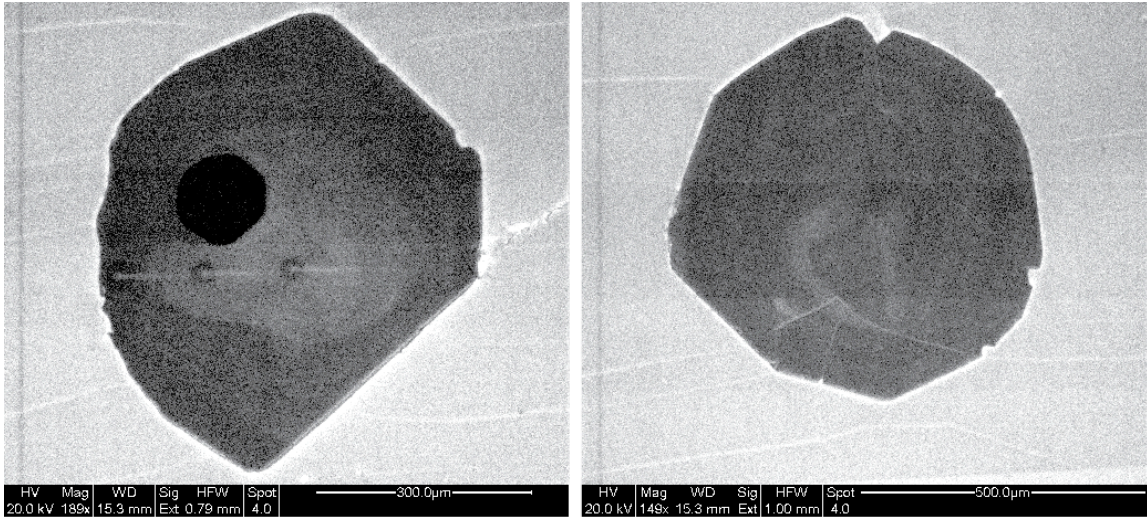


Fig. J4. a. Cathodoluminescence image of a quartz phenocryst from the lower TAV (PC-12). Samples (left to right) include PC-12.2 and PC-12.6.

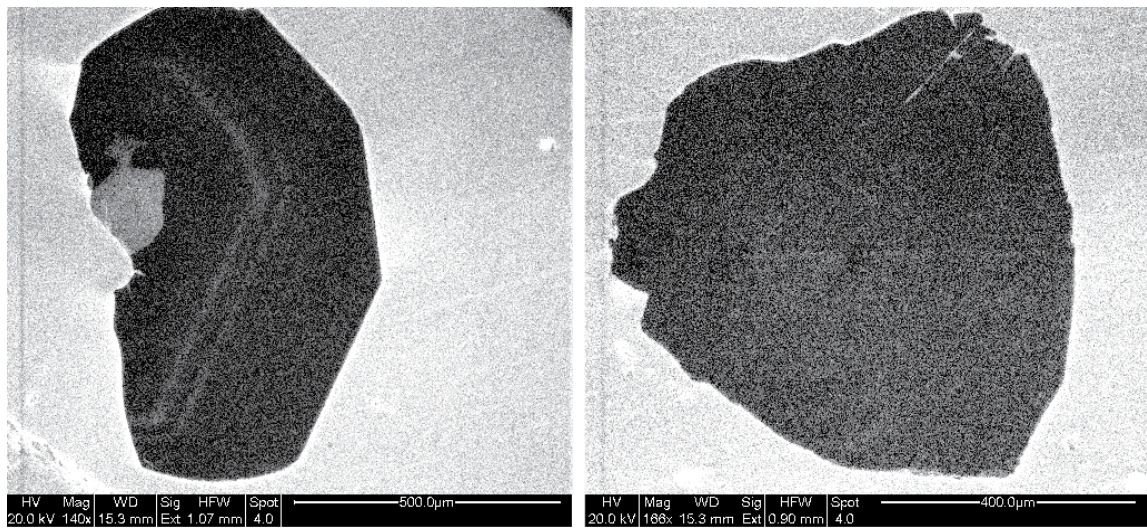


Fig. J4. b. Cathodoluminescence image of a quartz phenocryst from the lower TAV (PC-12). Samples (left to right) include PC-12.7 and PC-12.3.

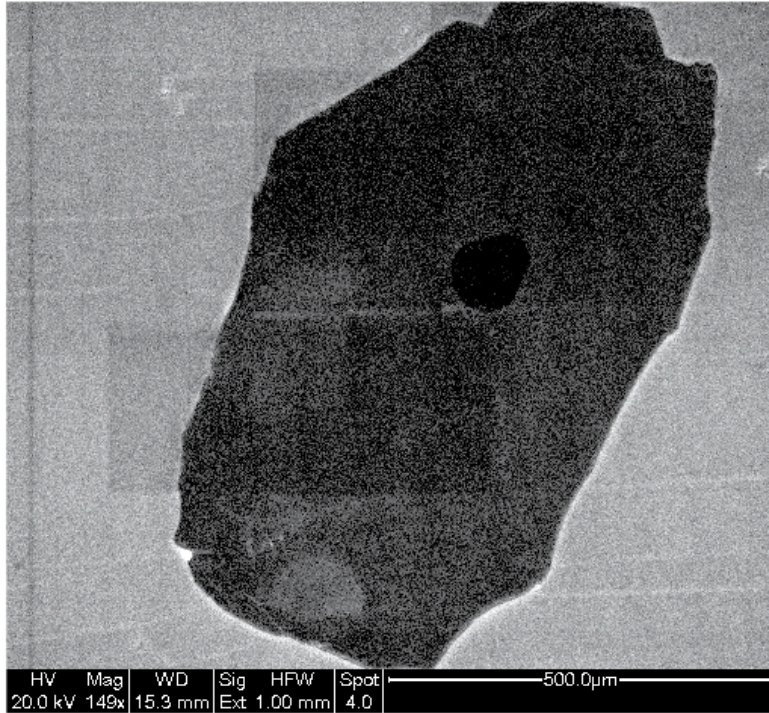


Fig. J4. c. Cathodoluminescence image of a quartz phenocryst (PC-12.1) from the lower TAV (PC-12).

APPENDIX K

TI IN QUARTZ MEASUREMENTS, BACKSCATTER IMAGES OF SPOT LOCATIONS OF TI IN QUARTZ MEASUREMENTS

Table K1.

Blank corrected trace element Ti, Fe, and Al concentrations (in ppm) of quartz samples analyzed for melt inclusions. The sampling spot number refers to labeled backscatter images. Italics zeroes are measured negative concentrations that were assumed to be zero.

PC-P3.3			
Spot	Ti	Fe	Al
18	39	54	157
19	47	42	157
20	71	19	156
21	78	17	164
22	22	4	130
23	14	30	133
24	7	26	151

PC-P2.2			
Spot	Ti	Fe	Al
25	35	20	147
26	48	38	435
27	24	-7	157
28	17	-2	136
29	21	18	126

PC-P4.1			
Spot	Ti	Fe	Al
30	14	24	134
31	38	15	143
32	41	16	141
33	5	21	131
34	25	14	142
35	30	9	127

PC-P3.2			
Spot	Ti	Fe	Al
36	44	14	130
37	23	111	157
38	27	439	166
39	19	51	170
40	27	1	150

PC-P2.6			
Spot	Ti	Fe	Al
41	14	50	130
42	28	32	126
43	17	13	118

44	30	17	131
----	----	----	-----

PC-P4.2

Spot	Ti	Fe	Al
45	25	63	154
46	49	48	130
47	36	-11	169
48	25	6	145
49	35	68	153

PC-P1.3

Spot	Ti	Fe	Al
50	42	41	152
51	32	23	128
52	19	41	119
53	17	30	167
54	25	27	137
55	14	22	142
56	0	19	178
57	25	26	175

PC-P6.1

Spot	Ti	Fe	Al
58	29	54	141
59	45	31	145
60	55	48	147
61	22	10	110
62	26	17	127
63	55	13	152

PC-P3.4

Spot	Ti	Fe	Al
64	35	50	202
65	19	23	121
66	15	17	143
67	26	13	134
68	20	22	161
69	41	21	161

PC-P3.1

Spot	Ti	Fe	Al
70	39	43	132
71	33	32	183
72	42	15	161
73	41	21	121

PC-P6.3

Spot	Ti	Fe	Al
74	63	34	173
75	40	32	145
76	49	8	136

77	16	0	120
78	28	34	134
79	9	7	161
80	26	64	142

PC-P6

Spot	Ti	Fe	Al
81	54	32	157
82	18	53	141
83	31	65	206
84	42	2	139
85	31	17	132
86	26	26	131
87	62	4	148
88	276	18	155

PC-12

Spot	Ti	Fe	Al
89	24	43	144
90	32	89	333
91	31	22	154
92	29	3	140

PC-1.2

Spot	Ti	Fe	Al
93	22	29	133
94	28	38	134
95	17	29	134

PC-1.4

Spot	Ti	Fe	Al
96	32	268	3066
97	64	74	150
98	64	10	147
99	20	31	123
100	6	18	127
101	32	15	137

PC-5.1

Spot	Ti	Fe	Al
102	82	27	149
103	63	20	147
104	5	66	160
105	43	50	147
107	24	19	138

Table K2.

Blank and aggregate corrected Ti and Al trace element concentrations (in ppm) in quartz samples. The spot numbers refer to the back scatter image. Italics zeroes are measured negative concentrations that were inferred to be zero.

PC-25.1		
Spot	Al	Ti
170	92	189
171	108	179
172	116	182
173	142	157
174	149	153
175	170	170

PC-01.1		
Spot	Al	Ti
176	106	266
177	118	259
178	149	268
179	126	266
180	157	247

PC-01.2		
Spot	Al	Ti
181	107	230
182	147	263
183	135	274
184	193	228

PC-01.3		
Spot	Al	Ti
185	134	289
186	117	249
187	139	251
188	151	230

PC-01.4		
Spot	Al	Ti
189	124475	189
190	123463	188
191	123031	582

PC-01.5		
Spot	Al	Ti
192	138	240
193	127	244
194	181	218

PC-12.1		
Spot	Al	Ti
195	67	13
196	90	9
197	77	26

PC-12.2		
Spot	Al	Ti
198	61	8
199	82	26
200	89	6

PC-12.3		
----------------	--	--

Spot	Al	Ti
201	55	0
202	229	8
203	104	0

PC-12.4

Spot	Al	Ti
204	66	23
205	39	10
206	86	6

PC-12.5

Spot	Al	Ti
207	96	0
208	112	0
209	72	15

PC-20.1

Spot	Al	Ti
210	162	134
211	167	117
212	152	89

PC-20.2

Spot	Al	Ti
213	159	112
214	155	128
215	252	118

PC-20.3

Spot	Al	Ti
216	158	115
217	171	120
218	159	137
219	164	137

PC-20.4

Spot	Al	Ti
220	165	116
221	133	89
222	172	123
223	247	95

PC-14.1

Spot	Al	Ti
224	109	112
225	111	89
226	123	112
227	118	118

PC-14.2

Spot	Al	Ti
228	127	146
229	138	149
230	144	159
231	118	147
232	149	168
233	146	158

PC-14.3

Spot	Al	Ti
234	170	184

235	174	186
236	157	196
237	123	151
238	127	121
239	104	117

PC-14.4

Spot	Al	Ti
240	145	180
241	157	176
242	138	152
243	129	98
244	117	125

PC-14.5

Spot	Al	Ti
245	92	100
246	80	51
247	92	23
248	88	29
249	96	58
250	130	64

PC-14.6

Spot	Al	Ti
251	82	87
252	145	65
253	80	48
254	78	64
255	83	67

PC-34.1

Spot	Al	Ti
288	67	48
289	74	37
290	77	49
291	82	26

PC-34.2

Spot	Al	Ti
292	95	98
293	81	58
294	107	70
295	101	67

PC-34.3

Spot	Al	Ti
296	116	41
297	77	48
298	105	49
299	115	62

PC-34.4

Spot	Al	Ti
300	99	68
301	119	71
302	104	79
303	127	104

PC-34.5

Spot	Al	Ti
------	----	----

304	85	63
305	105	57
306	99	61
307	152	71

PC-25.2

Spot	Al	Ti
308	133	207
309	116	196
310	125	172
311	203	178

PC-25.3

Spot	Al	Ti
312	102	188
313	139	180
314	145	172

PC-25.4

Spot	Al	Ti
315	126	153
316	82	168
317	165	177
318	229	159

PC-25.5

Spot	Al	Ti
319	135	166
320	133	162
321	132	183
322	151	179

APPENDIX L

ADDITIONAL GEOCHEMICAL FIGURES AND TABLES

Table L1.

Maximum, average, and the detection limit Ti concentrations (ppm) in quartz and corresponding temperatures at various activities and a pressure of 2 kbars (calibration of Huang and Audetat, 2012).

Ti (ppm)	activity of TiO ₂		
	0.9	0.6	0.2
max: 82	713	762	925
detection limit: 30	609	648	775
average: 32	615	654	783

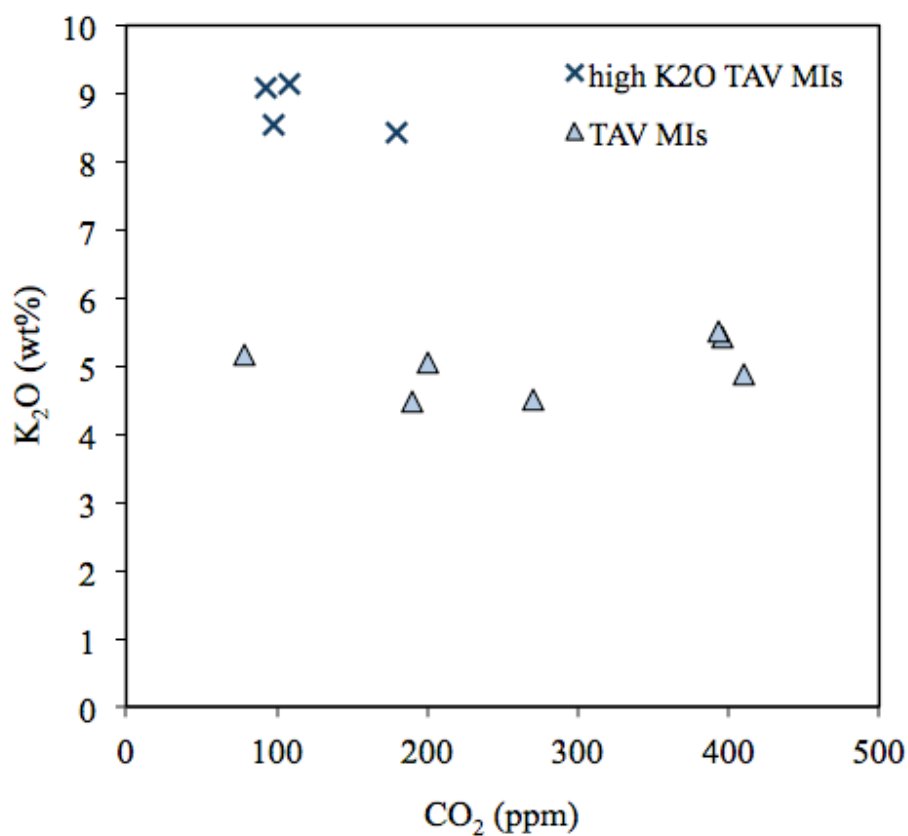


Fig. L1. a. K₂O variations with CO₂ of TAV melt inclusions.

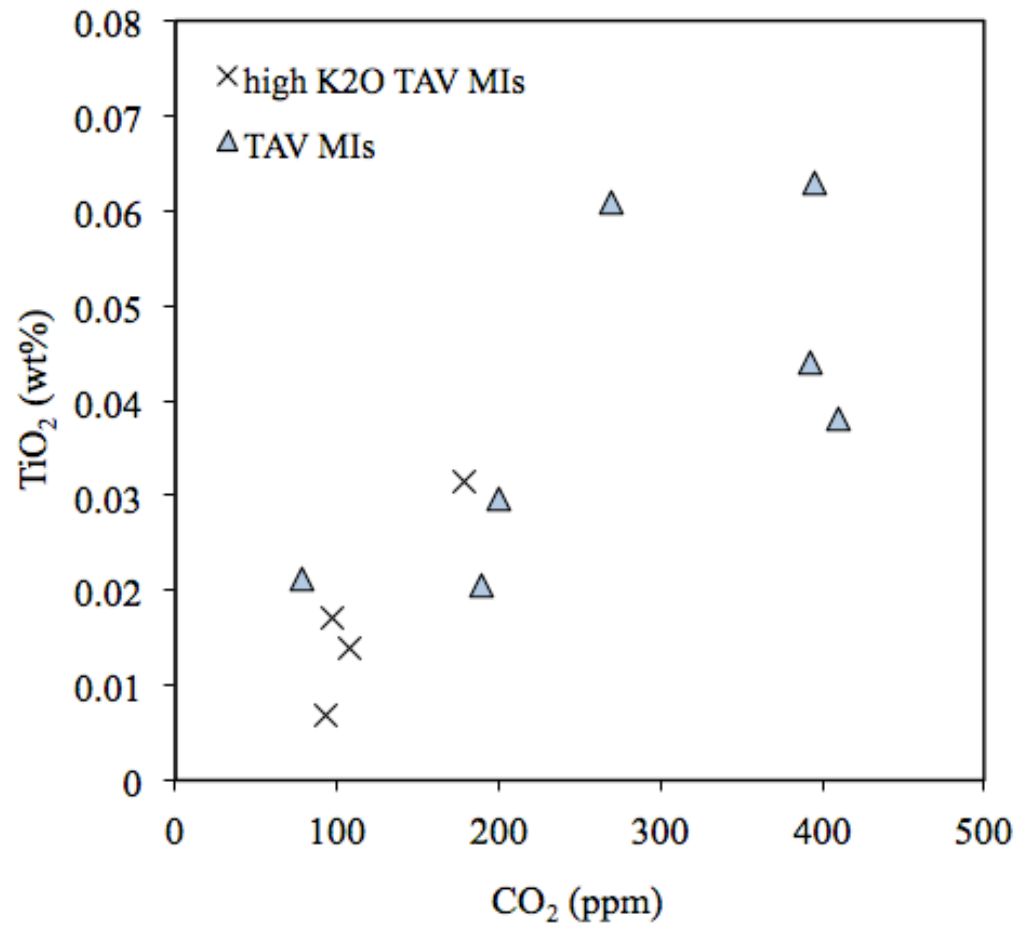


Fig. L1. b. TiO₂ variations with CO₂ of TAV melt inclusions.

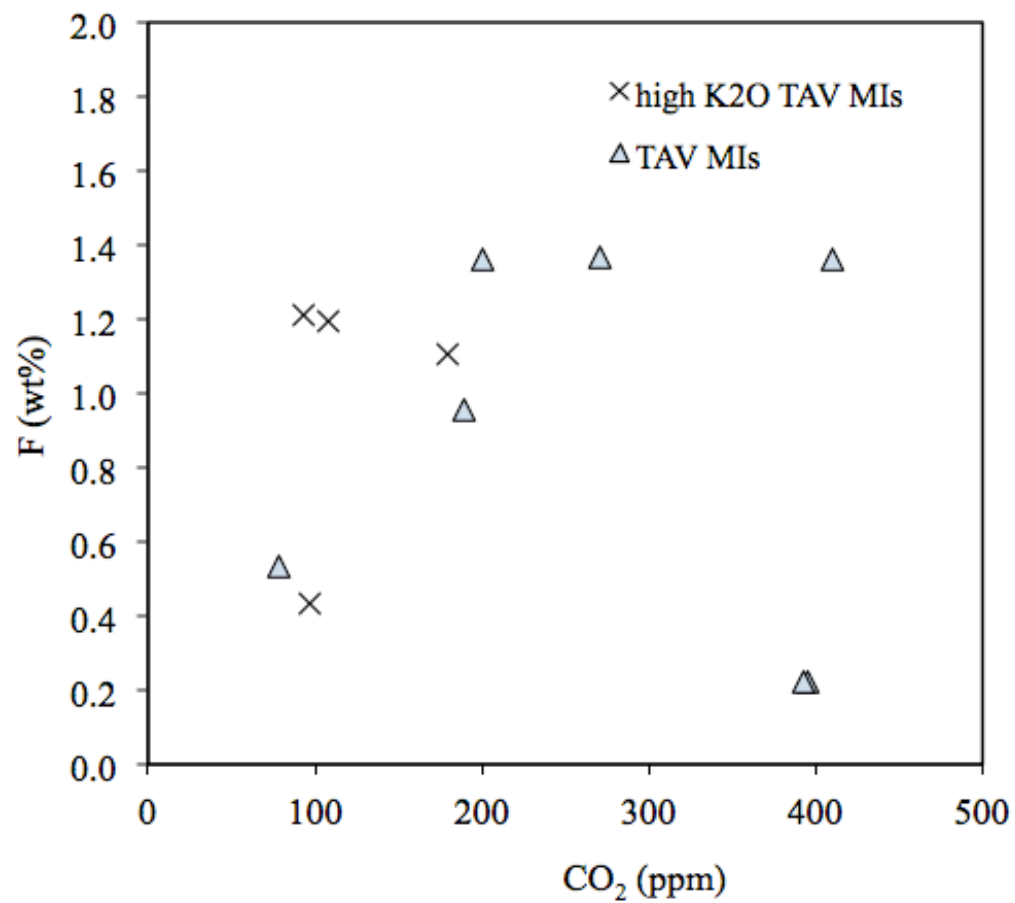


Fig. L1. c. F variations with CO₂ of TAV melt inclusions.

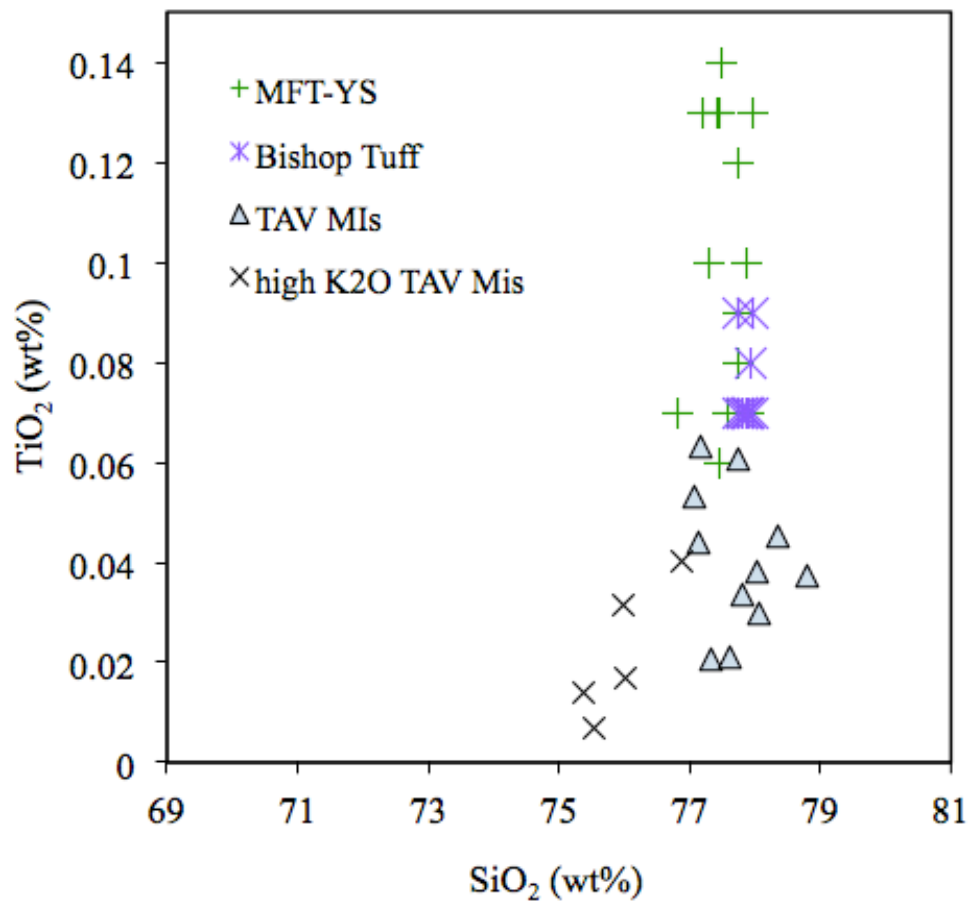


Fig. L1. d. TiO₂ variations with SiO₂ of TAV melt inclusions in comparison to quartz hosted melt inclusions from the Bishop Tuff (Wallace et al., 1999) and Yellowstone Mesa Falls Tuff (Gansecki, 1998).

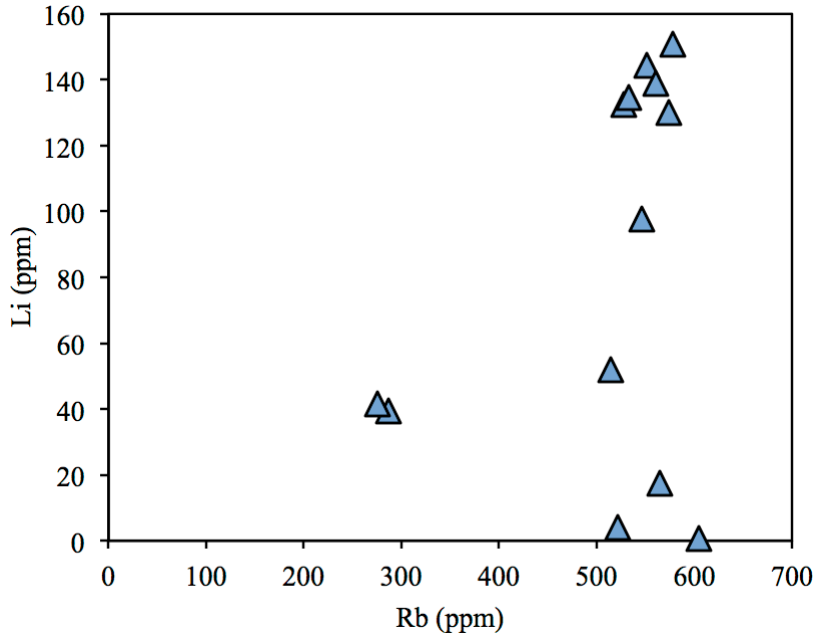


Fig. L2. a. Li (fast-diffusing element) variations with Rb (slow-diffusing element) of TAV melt inclusions.

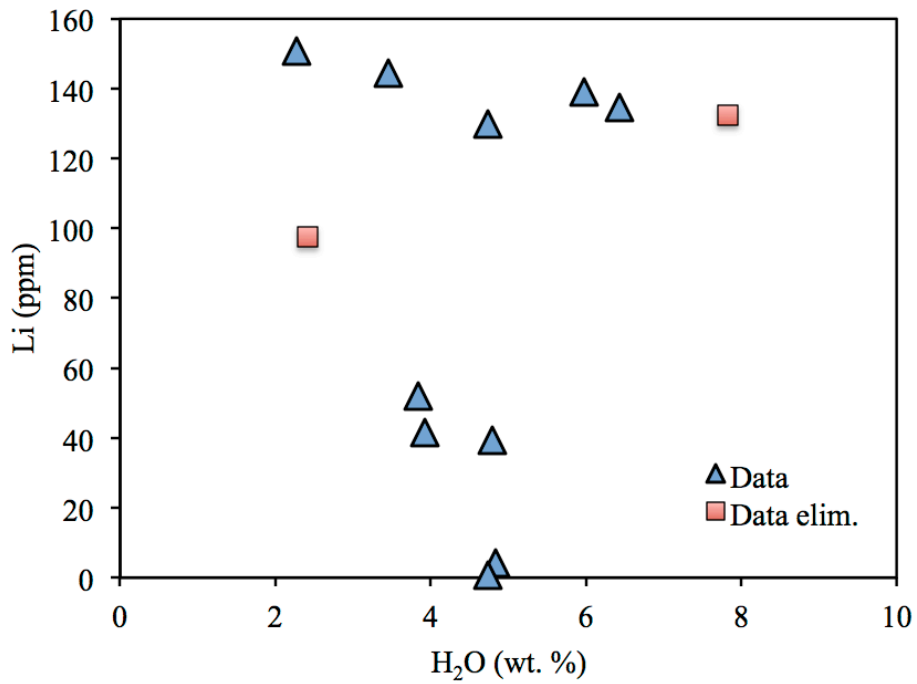


Fig. L2. b. Li (fast-diffusing element) variations with H₂O (fast-diffusing) of TAV melt inclusions.

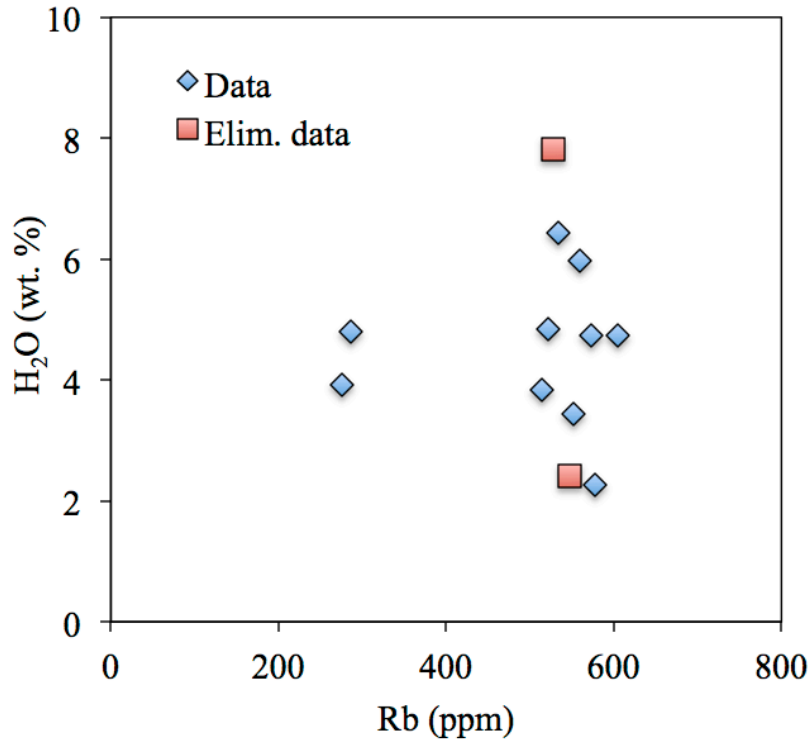


Fig. L2. c. H₂O (fast-diffusing) variations with Rb (slow-diffusing element) of TAV melt inclusions.

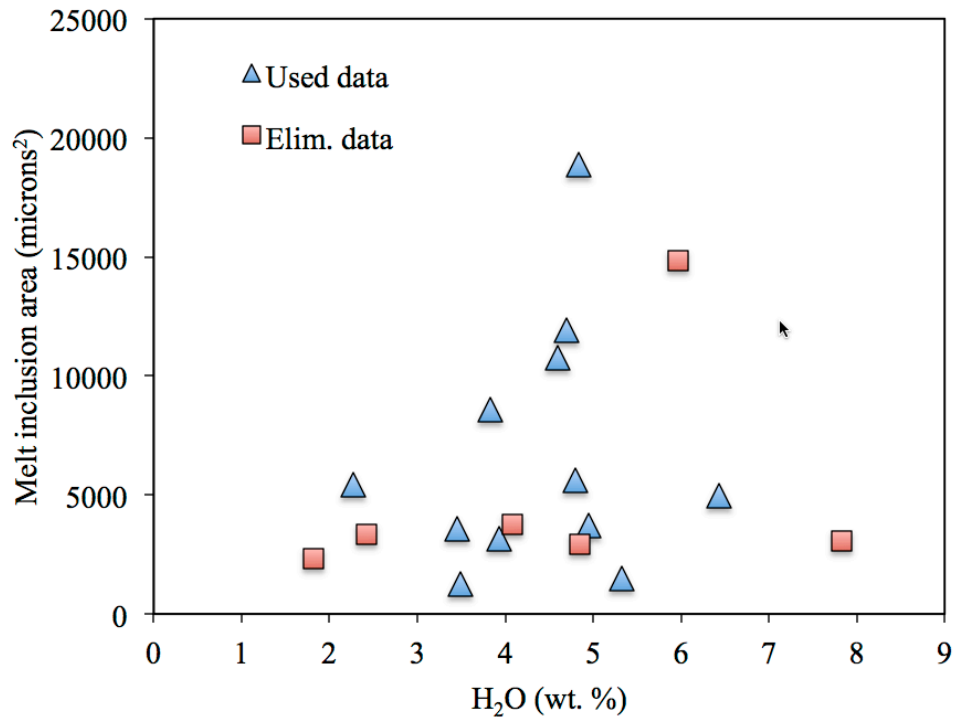


Fig. L2. d. Melt inclusion area (estimated from the ellipse formula) with variations in H₂O of TAV melt inclusions.

REFERENCES CITED

- Agangi, A., Kamenetsky, V.S., McPhie, J., 2012. Evolution and emplacement of high fluorine rhyolites in the Mesoproterozoic Gawler silicic large igneous province, South Australia. *Precam. Res.* 208-211, 124-144.
- Almeev, R., Bolte, T., Nash, B., Holtz, F., Erdmann, M., Cathey, H., 2012. High-temperature, low-H₂O Silicic Magmas of the Yellowstone Hotspot; an Experimental Study of Rhyolite from the Bruneau-Jarbidge Eruptive Center, Central Snake River Plain, USA. *J. Petrol.* 53(9), 1837-1866.
- Anders, M.H., Saltzman, J., Hackett, W.R., 1997. Borehole WO-2, the Rosetta stone (core) of the Heise volcanics of east central Idaho: implications for the track of the Yellowstone hotspot. *Geol. Soc. Am.* 29 (6), A-365 Abstracts with Programs.
- Anders, M., Saltzman, J., Hemming, S., 2009. Neogene tephra correlations in eastern Idaho and Wyoming; Implications for Yellowstone hotspot-related volcanism and tectonic activity. *Geol. Soc. Am. Bull.* 121(5-6), 837-856.
- Anderson, A.T., Davis, A.M., Fangqiong, L., 2000. Evolution of Bishop Tuff rhyolitic magma based on melt and magnetite inclusions and zoned phenocrysts. *J. Petrol.* 41(3), 449-473.
- Armstrong, R.L., Ward, P.L., 1991. Evolving geographic patterns of Cenozoic magmatism in the North American Cordillera: The temporal and spatial association of magmatism and metamorphic core complexes. *J. Geophys. Res.* 96(B8), 13201-13224.
- Armstrong, R.L., 1978. Cenozoic igneous history of the U.S. Cordillera from latitude 42° N to 49° N. *Geol. Soc. Am. Mem.* 152, 265-282.
- Armstrong, R.K., Taubenech, W.H., Hales, P.O., 1977. Rb-Sr and K-Ar geochronometry of Mesozoic granitic rocks and their Sr isotopic composition, Oregon, Washington and Idaho. *Geol. Soc. Am. Bull.* 88, 397-411.
- Bacon, C.R., Newman, S., Stolper, E., 1992. Water, CO₂, Cl, and F in melt inclusions in phenocrysts from three Holocene explosive eruptions, Crater Lake, Oregon. *Am. Mineral.* 77, 1021-1030.
- Bachmann, O., Bergantz, G.W., 2008. Rhyolites and their source mushes across tectonic settings. *J. Petrol.* 49(12), 2277-2285.
- Best, M.G., Christiansen, E.H., 1991. Limited extension during peak Tertiary volcanism, Great Basin of Nevada and Utah. *J. Geophys. Res.* 96(B8), 13509-13528.

- Best, M.G., Christiansen, E.H., Deino, A.L., Grommr, C.S., McKee, E.H., Noble, D.C., 1989. Eocene through Miocene volcanism in the Great Basin of the western United States. *N.M. Bur. Mines Miner. Resour.* 47, 91-133.
- Beyer, C., Klemme, S., Wiedenbeck, A., Stracke, A., Vollmer, C., 2012. Fluorine in nominally fluorine-free mantle minerals: Experimental partitioning of F between olivine, orthopyroxene and silicate melts with implications for magmatic processes. *Earth Planet. Sci. Letters* 337-338, 1-9.
- Bickford, M.E., Chase, R.B., Nelson, B.K., Schuster, R.D., Arruda, E.C., 1981. U–Pb studies of zircon cores and overgrowths and monazite: implications for age and petrogenesis of the northeastern Idaho batholith. *J. Geology* 89, 433– 457.
- Bindeman, I.N., 2008. Oxygen isotopes in mantle and crustal magmas as revealed by single crystal analysis. In: Putirka, K. D. & Tepley, F. J., III (eds) *Minerals, Inclusions and Volcanic Processes. Mineralogical Society of America and Geochemical Society, Reviews in Mineralogy and Geochemistry* 69, 445-478.
- Bindeman, I.N., Valley, J., 2001. Low-¹⁸O Rhyolites from Yellowstone: Magmatic Evolution Based on Analyses of Zircons and Individual Phenocrysts *42*(8), 1491-1517.
- Bindeman, I.N., Valley, J.W., Wooden, J.L. Persing, H.M., 2001. Post-caldera volcanism: in situ measurement of U-Pb age and oxygen isotope ratio in Pleistocene zircons from Yellowstone caldera. *Earth and Planet. Sci. Lett.* 189, 197-206.
- Bindeman, I.N., Watts, K.E., Schmitt, A.K., Morgan, L.A., Shanks, P.W.C., 2007. Voluminous low- $\delta^{18}\text{O}$ magmas in the late Miocene Heise volcanic field, Idaho: Implications for the fate of Yellowstone hotspot calderas. *Geology* 35(11), 1019.
- Bindeman, I.N., Valley, J.W., 2003. Rapid generation of both high- and low- $\delta^{18}\text{O}$, large-volume silicic magmas at the Timber Mountain/Oasis Valley caldera complex, Nevada. *Geol. Soc. Am. Bull.* 115(5), 581-595.
- Bindeman, I.N., Fu, B., Kita, N.T., Valley, J.W., 2008. Origin and Evolution of Silicic Magmatism at Yellowstone Based on Ion Microprobe Analysis of Isotopically Zoned Zircons. *J. Petrol.* 49(1), 163-193.
- Bindeman, I.N., 2005. Fragmentation phenomena in populations of magmatic crystals. *Am. Mineral.* 90, 1801-1815.
- Bonnichsen, B., Leeman, W.P., Honjo, N., McIntosh, W.C., Godchaux, M.M., 2008. Miocene silicic volcanism in southwestern Idaho: geochronology, geochemistry, and evolution of the central Snake River Plain. *Bull. Volcanol.* 70(3), 315-342.

- Blundy, J., Cashman, K., 2001. Ascent-driven crystallization of dacite magmas at Mount St Helens, 1980-1986. *Contrib. Mineral. Petrol.* 140, 631-650.
- Boroughs, S. B., Wolff, J., Bonnicksen, B., Godchaux, M., Larson, P., 2005. Large volume, low- $\delta^{18}\text{O}$ rhyolites of the central Snake River Plain, Idaho, USA. *Geology* 33, 821-824.
- Boroughs, S., Wolff, J.A., Ellis, B.S., Bonnicksen, B., Larson, P., 2012. Evaluation of models for the origin of Miocene low- $\delta^{18}\text{O}$ rhyolites of the Yellowstone/Columbia River Large Igneous Province. *Earth Planet. Sci. Lett.* 313-314, 45-55.
- Branney, M. J., Bonnicksen, B., Andrews, G. D. M., Ellis, B., Barry, T. L., & McCurry, M., 2008. "Snake River (SR)-type" volcanism at the Yellowstone hotspot track: distinctive products from unusual, high-temperature silicic super-eruptions. *Bull. Volcanol.* 70(3), 293-314.
- Breitsprecher, K., Thorkelson, D.J., Groome, W.G., Dostal, J., 2003. Geochemical confirmation of the Kula-Farallon slab window beneath the Pacific northwest in Eocene time. *Geology* 31, 351-354.
- Brugger, C.R., Johnston, D.A., Cashman, K.V., 2003. Phase relations in silicic systems at one-atmosphere pressure. *Contrib. Mineral. Petrol.* 146, 356-369.
- Bruseke, M., Hart, W., Heizler, M., 2008. Diverse mid-Miocene silicic volcanism associated with the Yellowstone-Newberry thermal anomaly. *Bull. Volcanol.* 70, 343-360.
- Burt, D.M., Sheridan, M.F., Bikun, J.V., Christiansen, E.H., 1982. Topaz Rhyolites-Distribution, Origin, and Significance for Exploration. *Econ. Geol.* 77, 1818-1836.
- Calliccoat, J., Brueseke, M.E., 2009. Mid-Miocene volcanism in northeast Nevada: Spatial, chemical and chronologic significance of the Jarbidge Rhyolite. GSA Meeting abstract, 106-12.
- Camp, V.E., Hanan, B.B., 2008. A plume-triggered delamination origin for the Columbia River Basalt Group. *Geosphere* 4(3), 480-495.
- Camp, V.E., Ross, M.E., 2004. Mantle dynamics and genesis of mafic magmatism in the intermontane Pacific Northwest. *J. Geophys. Res.* 109 (B08204) 14 pp.
- Carlson, R.W., Hart, W.K., 1988. Flood basalt volcanism in the northwestern United States. In: MacDougall, J.D. (Ed.), *Continental Flood Basalts*, 35-61.

- Cathey, H.E., Nash, B.P., 2004. The Cougar Point Tuff: implications for thermochemical zonation and longevity of high-temperature, large-volume silicic magmas of the Miocene Yellowstone hotspot. *J. Petrol.* 45(1), 27-58.
- Cathey, H.E., Nash, B.P., 2009. Pyroxene thermometry of rhyolite lavas of the Bruneau-Jarbidge eruptive center, Central Snake River Plain. *J. Volcanol. Geotherm. Res.* 188, 173-185.
- Cathey, H.E., Nash, B.P., Allen, C.M., Campbell, I.H., Valley, J.W., Kita, N., 2008. U-Pb zircon geochronology and Ti-in-zircon thermometry of large-volume low- $\delta^{18}\text{O}$ magmas of the Miocene Yellowstone hotspot. *Geochem. Cosmochim.* 72, A143.
- Chang, Z., Meinert, L.D., 2008. The Empire Cu-Zn Mine, Idaho: Exploration Implications of Unusual Skarn Features Related to High Fluorine Activity. *Econ. Geol.* 103, 909-938.
- Chase, R.B., Bickford, M.E., Tripp, S.E., 1978. Rb-Sr and U-Pb isotopic studies of the northeastern Idaho batholith and border zone. *Geol. Soc. Am. Bull.* 89, 1325-1334.
- Cherniak, D.J., Hanchar, J.M., Watson, E.B., 1997. Diffusion of tetravalent cations in zircon. *Contrib. Mineral. Petrol.* 127, 383-390.
- Cherniak, D., Watson, E., 2003. Diffusion in zircon. *Revs. Mineral. Geochem.* 53, 113-143.
- Christiansen, R.L., 2001. *The Quaternary and Pliocene Yellowstone Plateau Volcanic Field of Wyoming, Idaho, and Montana. US Geological Survey, Professional Papers* 729-G.
- Christiansen, E., McCurry, M., 2008. Contrasting origins of Cenozoic silicic volcanic rocks from the western Cordillera of the United States. *Bull. Volcanol.* 70(3), 251-267.
- Christiansen, E., Burt, D., Sheridan, M., Wilson, R., 1983. The Petrogenesis of Topaz Rhyolites from the Western United States. *Contrib. Mineral. and Petrol.* 83(1-2), 16-30.
- Christiansen, E.H., Keith, J.D., Thompson, T.J., 1996. Origin of gem red beryl in the Wah Wah Mountains, Utah. *Mining Engineering* 49, 37-41.
- Christiansen, R.L., Yeats, R.S., 1992. Post-Laramide geology of the U.S. Cordilleran region, *in* Burchfiel, B.C., et al., eds., *The Cordilleran orogen: Conterminous U.S.*: Boulder, Colorado, Geol. Soc. Am G-3, 261-406.

- Christiansen, E.H., Haapala, I., Hart, G.L., 2007. Are Cenozoic topaz rhyolites the erupted equivalents of Proterozoic rapakivi granite? Examples from the western United States and Finland. *Lithos* 97, 219-246.
- Christiansen, R.L., Foulger, G.R., Evans, J.R., 2002. Upper-mantle origin of the Yellowstone hotspot. *Geol. Soc. Am. Bull.* 114, 1245–1256.
- Coble, M., Mahood, G., 2012. Initial impingement of the Yellowstone plume locate by widespread silicic volcanism contemporaneous with Columbia River flood basalts. *Geology* 40(7), 655-658.
- Colgan, J.P., Henry, C.D., 2009, Rapid middle Miocene collapse of the Mesozoic orogenic plateau in north-central Nevada. *International Geology Review* 51, 920–
- Coney, P.J., 1980. Cordilleran metamorphic core complexes: An overview. *Mem. Geol. Soc. Am.* 153, 7-31.
- Congdon, R.D., Nash, W.P., 1988. High-fluorine rhyolite: An eruptive pegmatite magma at the Honeycomb Hills, Utah. *Geology* 16, 1018-1021.
- Covington, H.R., 1983. Structural evolution of the Raft River Basin, Idaho; Tectonic and stratigraphic studies in the eastern Great Basin, in Miller, D.M., et al., eds., *Tectonic and stratigraphic studies in the eastern Great Basin*. *Geol. Soc. Am. Mem.* 157, 229–237.
- Criss, R.E., Fleck, R.J., 1987. Petrogenesis, geochronology, and hydrothermal systems in the northern Idaho batholith and adjacent areas based on $^{18}\text{O}/^{16}\text{O}$, D/H, $^{87}\text{Sr}/^{86}\text{Sr}$, K-Ar, and $^{40}\text{Ar}/^{39}\text{Ar}$ studies. *U.S. Geological Survey Professional Paper* 1436, 95-137.
- Criss, R.E., Taylor, H.P., 1986. Meteoric-hydrothermal systems. *Rev. Mineral.* 16, 373-424.
- Criss, R., Fleck, R., Taylor, H., 1991. Tertiary Meteoric Hydrothermal Systems and their relation to Ore Deposition, Northwestern United States and Southern British Columbia. *J. Geophys. Res.* 96(B8), 13,3335-113,356.
- Dingwell, D.B., Knoche, R., Webb, S.L., 1993. The effect of F on the density of haplogranite melt. *Am. Mineral.* 78, 325-330.
- Dingwell, D.B., Webb, S.L., 1992. The fluxing effect of fluorine at magmatic temperatures (600-800 °C): A scanning calorimetric study. *Am. Mineral.* 77, 30-33.

- Dingwell, D.B., Scarfe, C.M., Cronin, D.J., 1985. The effect of fluorine on viscosities of melts in the system NaO-AlO₂-SiO₂: Implications for phonolites, trachytes and rhyolites. *Am. Mineral.* 70, 80-87.
- Doherty, D., McBroome, L., Kuntz, M., 1979. Preliminary geological interpretation and lithologic log of the exploratory geothermal test well (INEL-1), Idaho National Engineering Laboratory, eastern Snake River Plain, Idaho. *Open-File Report - U.S. Geological Survey*.
- Doljes, D., Baker, D.R., 2006. Fluorite solubility in hydrous haplogranite melts at 100 MPa. *Chem. Geol.* 225, 40-60.
- Donovan, J.J., Lowers, H.A., Rusk, B.G., 2011. Improved electron probe microanalysis of trace elements in quartz. *Am. Mineral.* 96(2-3), 274-282.
- Drew, D.L., Bindeman, I.N., Watts, K.E., Schmitt, A.K., Fu, B., McCurry, M., 2013. Crustal-scale recycling in caldera complexes and rift zones along the Yellowstone hotspot track: O and Hf isotopic evidence in diverse zircons from voluminous rhyolites of the Picabo volcanic field, Idaho. *Earth Planet. Sci. Letters* 381, 63-77.
- Ebadi, A., Johannes, W., 1991. Beginning of melting and composition of first melts in the system Qz-Ab-Or-H₂O-CO₂. *Contrib. Mineral. Petrol.* 106, 286-295.
- Eggins, S.M., Grün, R., McCulloch, M.T., Pike, A.W.G., Chappell, J., Kinsley, L., Mortimer, G., Shelley, M., Murray-Wallace, C.V., Spötle, C., Taylor, L., 2005. In situ U-series dating by laser-ablation multi-collector ICPMS: new prospects for Quaternary geochronology. *Quat. Sci. Rev.* 24, 2523-2538.
- Ellis, B.S., Barry, T., Branney, M.J., Wolff, J.A., Bindeman, I., Wilson, R., Bonnicksen, B., 2010. Petrologic constraints on the development of a large-volume, high temperature, silicic magma system: The Twin Falls eruptive centre, central Snake River Plain. *Lithos* 120(3-4), 475-489.
- Farmer, G.L., Depaolo, D.J., 1983. Origin of Mesozoic and Tertiary granite in the western United States and implications for Mesozoic crustal structure: 1. Nd and Sr isotopic studies in the geocline of the northern Great Basin. *J. Geophys. Res.* 88, 3379-3401.
- Fleck, R.J., Criss, R.E., 1985. Strontium and oxygen isotopic variations in Mesozoic and Tertiary plutons of central Idaho. *Contrib. Mineral. Petrol.* 90, 291-308.
- Foster, D.A., Fanning, C.M., 1997. Geochronology of the northern Idaho Batholith and the Bitterroot metamorphic core complex; magmatism preceding and contemporaneous with extension. *Geol. Soc. Am. Bull.* 109, 379-394.

- Foster, D.A., Doughty P.T., Kalakay, T.J., Fanning, C.M., Coyner, S., Grice Jr., W.C., Vogl, J.J., 2007. Kinematics and timing of exhumation of Eocene metamorphic core complexes along the Lewis and Clark fault zone, northern Rocky Mountains, USA, in *Exhumation along Major Continental Strike-Slip Systems*. Spec. Pap. Geol. Soc. Am. 434, 205–229.
- Foster, D.A., Raza, A., 2002. Low-temperature thermochronological record of exhumation of the Bitterroot metamorphic core complex, northern Cordilleran Orogen. *Tectonophys.* 249, 23-36.
- Foster, D.A., Grice Jr., W.C., Kalakay, T.J., 2010. Extension of the Anaconda metamorphic core complex: $^{40}\text{Ar}/^{39}\text{Ar}$ thermochronology and implications for Eocene tectonics of the northern Rocky Mountains and the Boulder batholith. *Lithosphere* 2, 232–246.
- Foster, D.A., Schafer, C., Fanning, M.C., Hyndman, D.W., 2001. Relationships between crustal partial melting, plutonism, orogeny, and exhumation: Idaho–Bitterroot batholith: *Tectonophysics* 342, 313–350.
- Fournier, R.O., 1989. Geochemistry and dynamics of the Yellowstone National Park hydrothermal system. *Ann. Rev. Earth Planet. Sci. Lett.* 17, 13-53.
- Frezzotti, M., 2001. Silicate-melt inclusions in magmatic rocks: applications to petrology. *Lithos* 55, 273-299.
- Friedmann, S.J., Burbank, D.W., 1995. Rift basins and supradetachment basins: intracontinental extension end-members. *Basin Research* 7, 109-127.
- Friedman, I., Lipman, P.W., Obradovich, J.D., Gleason, J.D., Christiansen, R.L., 1974. Meteoric Water in Magmas. *Science* 184(4141), 1069-1072.
- Fritschle, T., Prelevic, D., Foley, S.F., Jacob, D.E., 2013. Petrological characterization of the mantle source of Mediterranean lamprolites: Indications from major and trace elements of phlogopite. *Chem. Geol.* 353, 267-279.
- Gansecki, C.A., 1998. $^{40}\text{Ar}/^{39}\text{Ar}$ geochronology and pre-eruptive geochemistry of the Yellowstone Plateau volcanic field rhyolites. Stanford University Ph.D. thesis.
- Gans, P.B., 1987. An open-system, two-layer crustal stretching model for the eastern Great Basin. *Tectonics* 6, 1–12.
- Gaschnig, R., Vervoort, J., Lewis, R., Tikoff, B., 2011. Isotopic Evolution of the Idaho Batholith and Challis Intrusive Province, Northern US Cordillera. *J. Petrol.* 52(12), 2397-2429.

- Gilliam, C.E., Valley, J.W., 1997. Low $\delta^{18}\text{O}$ magma, Isle of Skye, Scotland: Evidence from zircons. *Geochim. Coschim. Acta.* 61(23), 4975-4981.
- Giordano, D., Romano, C., Dingwell, D.B., Poe, B., Behrens, H., 2004. The combined effects of water and fluorine on the viscosity of silicic magmas. *Geochim. Cosmochim. Acta.* 68(24), 5159-5168.
- Glazner, A.F., Coleman, D.S., Bartley, J.M., 2008. The tenuous connection between high-silica rhyolites and granodiorite plutons. *Geology* 36(2), 182-186.
- Graham, D.W., Reid, M.R., Jordan, B.T., Grunder, A.L., Leeman, W.P., Lupton, J.E., 2009. Mantle source provinces beneath the Northwestern USA delimited by helium isotopes in young basalts. *J. Volcanol. and Geothermal Res.* 188(1-3), 128-140.
- Hanchar, J., Watson, E., 2003. Zircon saturation thermometry. *Rev. in Mineral. and Geochem.* 53, 89-112.
- Haapala, I., 1977. Petrography and geochemistry of the Eurajoki stock a rapakivi-granite complex with greisen-type mineralization in southwestern Finland. *Geol. Surv. of Finland Bull.* 286, 1-128.
- Hamilton, W., 1978. Mesozoic tectonics of the Western United States. In: Howell, D.G., McDougall, K.A. (Eds.), *Mesozoic Paleogeography of the Western United States*. Society of Economic Paleontologists and Mineralogists, Pacific Section, Pacific Coast Paleogeography Symposium 2, 33– 70.
- Henshaw, N.D., 2002. *Temperature of silicic magmas from the Yellowstone hotspot*. University of Utah.
- Hildreth, W., Halliday, A. N., Christiansen, R. L., 1991. Isotopic and chemical evidence concerning the genesis and contamination of basaltic and rhyolitic magmas beneath the Yellowstone Plateau Volcanic Field. *J. Petrol.* 32, 63-138.
- Hildreth, W., Christiansen, R.L., O'Neill, J.R., 1984. Catastrophic Isotopic Modification of Rhyolitic Magma at Times of Caldera Subsidence, Yellowstone Plateau Volcanic Field. *J. Geophys. Res.* 89(B10), 8339-8369.
- Hildreth, W., Wilson, C.J.N., 2007. Compositional zoning of the Bishop Tuff. *J. Petrol.* 28(5), 951-999.
- Hoskin, P.W.O., Schaltegger, U., 2003. The composition of zircon and igneous and metamorphic petrogenesis. in: *Zircon* (J.M. Hanchar and P.W.O. Hoskin, editors). *Rev. Mineral. Geochem.* 53, 27-62.

- House, M.A., Isachsen, C.E., Hodges, K.A., Bowring, S.A., 1993. Geochronologic evidence for a complex, post-extensional thermal structure in the Bitterroot dome metamorphic core complex, MT. Geological Society of America Abstracts with Programs 25, A-411.
- Huang, R., Audetat, A., 2012. The titanium-in-quartz (TitaniQ) thermobarometer: A critical examination and re-calibration. *Geochim. Cosmochim. Acta.* 84, 75-89.
- Huber, C., Bachman, O., Vigneresse, J., Dufek, J., Parmigiani, A., 2012. A physical model for metal extraction and transport in shallow magmatic systems. *Geochem. Geophys. Geosys.* 13(8), 1525-2027.
- Hughes, S., McCurry, M., 2004. Bulk major and trace element evidence for a time-space evolution of Snake River Plain rhyolites, Idaho. In: Bonnichsen, B., White, C.M., McCurry, M. (Eds), *Tectonic and Magmatic Evolution of the Snake River Plain Volcanic Province. Idaho Geol. Surv. Bull.* 20, 157-176.
- Hughes, S.S., McCurry, M., Geist, D.J., 2002. Geochemical correlations and implications for the magmatic evolution of basalt flow groups at the Idaho National Engineering and Environmental Laboratory. *Geol. Soc. Am. Special Paper* 353, 151-173.
- Hyndman, D.W., 1980. Bitterroot dome–Sapphire tectonic block, an example of a plutonic core– gneiss–dome complex with its detached suprastructure. In: Crittenden, M.D., Coney, P.J., Davis, G.H. (Eds.), *Cordilleran Metamorphic Core Complexes. Geol. Soc. Am. Mem.* 153, 427– 443.
- Hyndman, D.W., 1981. Controls on source and depth of emplacement of granitic magma. *Geology* 9, 244–249.
- Hyndman, D.W., 1983. The Idaho batholith and associated plutons, Idaho and Western Montana. In: Roddick, J.A. (Ed.), *Circum-Pacific Plutonic Terranes. Geol. Soc. Am. Mem.* 159, 213–240.
- Hyndman, D.W., Foster, D.A., 1988. The role of tonalites and mafic dikes in the generation of the Idaho batholith. *J. Geology* 96, 31– 46.
- Hyndman, D.W., Myers, S.A., 1988. The transition from amphibolite-facies mylonite to chloritic breccia and role of the mylonite in formation of Eocene epizonal plutons, Bitterroot dome, Montana. *Geologische Rundschau* 77, 211 – 226.
- John, D.A., Wallace, A.R., Ponce, D.A., Fleck, R.B., Conrad, J.E., 2000. New perspectives on the geology and origin of the northern Nevada Rift. In: Cluer, J.K., Price, J.G., Struhsacker, E.M., Hardyman, R.F., Morris, C.L. (Eds.), *Geology and Ore Deposits 2000: the Great Basin and Beyond: Geological Society of Nevada Symposium Proceedings, May 15–18,* 127–154.

- John, T., Scambelluri, M., Frische, M., Barnes, J.D., Wolfgang, B., 2011. Dehydration of subducting serpentinite: Implications for halogen mobility in subduction zones and the deep halogen cycle. *Earth Planet. Sci. Lett.* 308, 65-76.
- Jones, M.T., Sparks, R.S.J., Valdes, P.J., 2007. The climatic impact of supervolcanic ash blankets. *Clim. Dyn.* 29, 553-546.
- Kellogg, K.S., Harlan, S.S., Mehnert, H.H., Snee, L.W., Pierce, K.L., Hackett, W.R., & Rodgers, D.W., 1994. Major 10.2 Ma Rhyolitic Volcanism in the Eastern Snake River Plain, Idaho-Isotopic Age and Stratigraphic Setting of the Arbon Valley Tuff Member of the Starlight Formation. *U.S. Geol. Surv. Bull.* 2091, 1-18.
- Kellogg, K.S., Marvin, R.F., 1988. New Potassium-Argon Ages, Geochemistry, and Tectonic Setting of Upper Cenozoic Volcanic Rocks Near Blackfoot, Idaho. *U.S. Geol. Surv. Bull.* 1806, 1-19.
- Kharaka, Y.K., Mariner, R.H., 2005. Geothermal Systems.
- King, E., Valley, J., 2001. The source, magmatic contamination, and alteration of the Idaho batholith. *Contrib. Mineral. Petrol.* 142(1), 72-88.
- Kinny, P. D., Roland, M., 2003. Lu-Hf and Sm-Nd Isotope Systematics in Zircon. *GeoScience World* 53, 327-41.
- Konstantinou, A., Strickland, A., Miller, E., Wooden, J., 2012. Multistage Cenozoic extension of the Albion-Raft River-Grouse Creek metamorphic core complex; geochronologic and stratigraphic constraints. *Geosphere Pre-Issue* 8(6), 1429-1466.
- Konstantinou, A., 2011. Off-axis Snake River Plain magmatism along an active extensional detachment: An example from the Jim Sage volcanic suite, southern I D. *Geol. Soc. Am.* 43(5), 106.
- Kortemeier, W.T., Burt, D.M., 1988. Ongonite and topazite dikes in the Flying W Ranch area, Tonto Basin, Arizona. *Am. Mineral.* 73, 507-523.
- Kuntz, M.A., Covington, H.R., Schorr, L.J., 1992. An overview of basaltic volcanism of the eastern Snake River Plain, Idaho. In: Link, P.K., Kuntz, M.A., Platt, L.P. (Eds.), *Regional Geology of Eastern Idaho and Western Wyoming. Geol. Soc. Am. Mem.* 179, 227-267.
- Leeman, W.P., Menzies, M.A., Matty, D.J., Embree, G.F., 1985. Strontium, neodymium and lead isotopic compositions of deep crustal xenoliths from the Snake River Plain: Evidence for Archean basement. *Earth Planet. Sci. Lett.* 75, 354-368.

- Leeman, W., Annen, C., Dufek, J., 2008. Snake River Plain-Yellowstone silicic volcanism; implications for magma genesis and magma fluxes. *Geol. Soc. Special Publications* 304, 235-259.
- Link, P.K., Fanning, C.M., Bernek, L.P., 2005. Reliability and longitudinal change of detrital-zircon age spectra in the Snake River system, Idaho and Wyoming: An example of reproducing the bumpy barcode. *Sed. Geology* 182, 101-142.
- Liu, L., Stegman, D.R., 2011. Origin of Columbia River flood basalt controlled by propagating rapture of the Farallon slab. *Nature Letter* 482, 386-390.
- Lukkari, S., Thomas, R., Haapala, I., 2009. Crystallization of the Kymi Topaz Granite Stock within the Wiborg Rapakivi Granite Batholith, Finland: Evidence from melt inclusions. *Canadian Mineral.* 47, 1359-1374.
- Luth, W.C., Jahns, R.H., Tuttle, O.F., 1964. The granite system at pressures of 4 to 10 kilobars. *J. Geophys. Res.* 69, 759-773.
- Manning, C., 1983. The role of fluorine and boron in the generation of granitic melts. In: *Migmatites and metamorphism; proceedings of the Geochemical Group of the Mineralogical Society*, 94-109.
- McBroome, L.A., 1981. Stratigraphy and origin of Neogene ash-flow tuffs on the northcentral margin of the eastern Snake River Plain, Idaho. MS Thesis, University of Colorado, Boulder, 74 pp.
- McCurry, Michael, 2009. The Arbon Valley Tuff: A new look at a highly anomalous ignimbrite from the Yellowstone-Snake River Plain volcanic track. *Geological Society of American Abstracts with Programs* 41.6, 43.
- McCurry, M., Hayden, K. P., Morse, L. H., Mertzman, S., 2007. Genesis of post-hotspot, A-type rhyolite of the Eastern Snake River Plain volcanic field by extreme fractional crystallization of olivine tholeite. *Bull. Volcanol.* 70(3), 361-383.
- McCurry, M., Rodgers, D.W., 2009. Mass transfer along the Yellowstone hotspot track I: Petrologic constraints on the volume of mantle-derived magma. *J. Volcanol. Geotherm. Res.* 188(1-3), 86-98.
- McDonough, W.F., Sun, S.S., 1995. The composition of the Earth. *Chem. Geol.* 120, 223-253.
- Metrich, N., Wallace, P.J., 2008. Volatile Abundances in Basaltic Magmas and Their Degassing Paths Tracked by Melt Inclusions. *Rev. Mineral. Geochem.* 69, 363-402.

- Miller, E.L., Dumitru, T.A., Brown, R.W., Gans, P.B., 1999. Rapid Miocene slip on the Snake Range–Deep Creek Range fault system, east-central Nevada. *Geol. Soc. Am. Bull.* 111, 886–905.
- Miller, C., Meschter McDowell, S., Mapes, R., 2003. Hot and cold granites? Implications of zircon saturation temperatures and preservation of inheritance. *Geology*, 31(6), 529-532.
- Morgan, L.A., McIntosh, W.C., 2005. Timing and development of the Heise volcanic field, Snake River Plain, Idaho, western USA. *Geol. Soc. Am. Bull.* 117(3), 288.
- Morgan, L., Doherty, D., Leeman, W., 1984. Ignimbrites of the eastern Snake River Plain: Evidence for major caldera-forming eruptions. *J. Geophys. Res.* 89(B10), 8665-8678.
- Morgan, W.J., 1972, Plate motions and deep-mantle convection: *Geol. Soc. Am. Mem.* 132, 7–22.
- Nash, B., Perkins, M., Christensen, J., Lee, D., Halliday, A., 2006. The Yellowstone hotspot in space and time: Nd and Hf isotopes in silicic magmas. *Earth and Planet. Sci. Lett.* 247(1-2), 143-156.
- Nash, B.P., Perkins, M.E., 2012. Neogene fallout tuffs from the Yellowstone hotspot in the Columbia Plateau region, Oregon, Washington and Idaho, USA. *Plos* 7(10), 1-13.
- Newman, S., Lowenstern, J.B., 2002. VolatileCalc: a silicate melt-H₂O-CO₂ solution model written in Visual Basic for excel. *Computers and Geosciences* 28, 597-604.
- Nichols, A.R.L., Wysoczanski, R.J., 2007. Using micro-FTIR spectroscopy to measure volatile contents in small and unexposed inclusions hosted in olivine crystals. *Chem. Geol.* 242, 371-384.
- Norman, M.D., Mertzman, S.A., 1991. Petrogenesis of Challis volcanics from central and southwestern Idaho: Trace element and Pb isotopic evidence. *J. Geophys. Res.* 96 (B8), 13279-13293.
- Orr, W. N., Orr, E. L., 1996. Central Idaho and Snake River Plain and Owyhee Uplands. In *Geology of the Pacific Northwest*, 160-211.
- Paces, J.B., Miller, J.D., 1993. Precise U-Pb ages of Duluth Complex and related mafic intrusions, northeastern Minnesota: Geochronological insights to physical, petrogenetic, paleomagnetic, and tectonomagmatic processes associated with the 1.1 Ga mid-continent rift system. *J. Geophys. Res.* 98, 13997-14013.

- Patchett, J.P., Kouvo, O., Hedge, C.E., Tatsumoto, M., 1981. Evolution of Continental Crust and Mantle Heterogeneity: Evidence from Hf Isotopes. *Contrib. Mineral. Petrol.* 78.3, 279-97.
- Paton, C., Hellstrom, J., Paul, B., Woodhead, J., Hergt, J., 2011. Iolite: Freeware for the visualization and processing of mass spectrometric data. *J. Anal. At. Spectrom.* 26, 2508-2518.
- Peck, W.H., Valley, J.W., Graham, C.M., 2003. Slow oxygen diffusion rates in igneous zircons from metamorphic rocks. *Am. Mineral.* 88, 1003-1014.
- Peppard, B.T., Steele, I.M., Davis, A.M., Wallace, P.J., Anderson, A.T., 2001. Zoned quartz phenocrysts from the rhyolitic Bishop Tuff. *Am. Mineral.* 86, 1034-1052.
- Peytcheva, I., Von Quadt, A., Georgiev, N., Ivanov, Z., Heinrich, C.A., Frank, M., 2008. Combining Trace-element Compositions, U–Pb Geochronology and Hf Isotopes in Zircons to Unravel Complex Calcalkaline Magma Chambers in the Upper Cretaceous Srednogorie Zone (Bulgaria). *Lithos* 104.1-4, 405-27.
- Peterson, J.W., Chacko, T., Kuehner, S.M., 1991. The effects of fluorine on the vapor-absent melting of phlogopite + quartz: Implications for deep-crustal processes. *Am. Mineral.* 76, 470-476.
- Pierce, K., Morgan, L., 1992. The track of the Yellowstone hot spot: Volcanism, faulting, and uplift. *Geological Society of America Memoir*, 179, 1-53.
- Pierce, K.L., Morgan, L.A., 2009. Is the track of the Yellowstone hotspot drive by a deep mantle plume? – Review of volcanism, faulting, and uplift in light of new data. *J. Volcanol. Geotherm. Res.* 188, 1-25.
- Pierce, K.L., Covington, H.R., Williams, P.L., McIntyre, D.H., 1983. Geologic map of the Cotterel Mountains and the northern Raft River valley, Cassia County, Idaho. U.S. Geol. Surv. Miscellaneous Investigations I-1450.
- Pope, A. D., 2002. *Geology of the Wakley Peak, Idaho, 7.5' Quadrangle: Multiple Phases of Late Miocene to Pliocene Extension, and Relations to the Southern Hawkins Basin Volcanic Center.* Idaho State University.
- Putirka K. D., Tepley F. J. (Eds), 2008. Minerals, inclusions and volcanic processes. *Rev Mineral* 69, 674.
- Rodgers, D., McCurry, M., 2009. Mass transfer along the Yellowstone hotspot track II: Kinematic constraints on the volume of mantle-derived magma. *J. Volcanol. Geotherm. Res.* 188(1-3), 99-107.

- Putirka, K., Jean, M., Cousens, B., Sharma, R., Torrez, G., Carlson, C., 2012. Cenozoic volcanism in the Sierra Nevada and Walker lane, California, and a new model for lithosphere degradation. *Geosphere* 8, 265–291.
- Putirka, K.D., 2008. Thermometers and Barometers for Volcanic Systems. *Reviews in Mineralogy and Geochemistry* 69, 61-120.
- Roberge, J., Wallace, P.J., Kent, A.R.J., 2013. Magmatic processes in the Bishop Tuff rhyolitic magma based on trace elements in melt inclusions and pumice matrix glass. *Contrib. Mineral. Petrol.* 165, 237-257.
- Robock, A., 2010. Volcanic eruptions and climate. *Rev. Geophys.* 38(2), 191-219.
- Rudnick, R.L., Gao, S., 2003. Composition of the Continental Crust. In *The Crust* (ed. R.L. Rudnick) Vol. 3, *Treatise on Geochemistry*. (eds. H.D. Holland and K.K. Turekian).
- Schmandt, B., Dueker, K., Humphreys, E., Hansen, S., 2012. Hot mantle upwelling across the 600 beneath Yellowstone. *Earth Planet. Sci. Lett.* 331-332, 224-236.
- Schmitt, A.K., Grove, M., Harrison, T.M., Lovera, O., Hulen, J., Walters, M., 2003. The Geysers – Cobb Mountain Magma System, California (Part 1): U-Pb zircon ages of volcanic rocks, conditions of zircon crystallization and magma residence times: *Geochim. Cosmochim. Acta.* 67, 3423-3442.
- Seligman, A.N., 2012. Generation of low- $\delta^{18}\text{O}$ silicic magmas, Bruneau Jarbidge volcanic center, Yellowstone hotspot: Evidence from zircons, including oxygen isotopes, U-Th-Pb dating, and melt inclusions. M.S. Thesis, The University of Utah.
- Shervais, J.W., Vetter, S.K., Hanan, B.B., 2006. Layered mafic sill complex beneath the eastern Snake River Plain: evidence from cyclic geochemical variations in basalt. *Geology* 34 (5), 365–368.
- Silver, L.A., Ihinger, P.D., Stolper, E., 1990. The influence of bulk composition on the speciation of water in silicate-glass. *Contrib. Mineral. Petrol.* 104(2), 142–162.
- Simakin, A.G., Bindeman, I.N., 2012. Remelting in caldera and rift environments and the genesis of hot, “recycled” rhyolites. *Earth Planet. Sci. Lett.* 337-338, 224-235.
- Skjerlie, K.P., Johnston, D.A., 1992. Vapor-absent melting at 10 kbar of a biotite- and amphibole-bearing tonalitic gneiss: Implications for the generation of A-type granites. *Geology* 20, 263-266.

- Slama, J., Kosler, J., Condon, D.J., Crowley, J.L., Gerdes, A., Hanchar, J.M., Horstwood, M.S.A., Morris, G.A., Nasdala, L., Norberg, N., Schaltegger, U., Schoene, B., Tubrett, M.N., Whitehouse, M.J., 2008. Plesovice zircon: a new natural reference material for U–Pb and Hf isotopic microanalysis. *Chem. Geol.*, 249, 1–35.
- Smith, R.B., Siegel, L.J., 2000. *Windows into the Earth; the geologic story of Yellowstone and Grand Teton National Parks*. Oxford University Press, Oxford, United Kingdom, 242.
- Snyder, K.D., 1978. Geology of the Bayhourse Fluorite Deposit, Custer Country, Idaho. *Econ. Geol.* 73, 207-214.
- Stefano, C.J., Mukasa, S.B., Andronikov, A., Leeman, W.P., 2011. Water and other volatile systematics of olivine-hosted melt inclusions from the Yellowstone hotspot track. *Contrib. Mineral. Petrol.* 161, 615-633.
- Stewart, J.H., Walker, G.W., Kleinhampl, F.J., 1975. Oregon–Nevada lineament. *Geology* 3, 265–268.
- Stockli, D.F., 1999, Regional timing and spatial distribution of Miocene extension in the northern Basin and Range Province. Stanford University Ph.D. thesis, 239 p.
- Straub, S.M., Layne, G.D., 2003. The systematics of chlorine, fluorine, and water in Izu arc front volcanic rocks: Implications for volatile recycling in subduction zones. *Geochim. Cosmochim.* 67(21), 4179-4203.
- Sun, S.S., McDonough, W.F., 1989. Chemical and isotopic systematics of oceanic basalts; implications for mantle composition and processes, in Saunders, A.D., and Norry, M.J., eds., *Magmatism in the ocean basins*: Geol. Soc. [London] Special Publication 42, 313–345.
- Suneson, N.H., Lucchitta, I., 1983. Origin of bimodal volcanism, southern Basin and Range province, west-central Arizona. *Geol. Soc. Am. Bull.* 94, 1005–1019.
- Taylor, S.R., McLennan, S.M., 1985. *The Continental Crust: its Composition and Evolution*. Oxford: Blackwell.
- Taylor, H. P., Jr., 1986. Igneous rocks: II. Isotopic case studies of circumpacific magmatism. In: Valley, J. W., Taylor, H. P., Jr & O’Neil, J. R. (eds) *Stable Isotopes in High Temperature Geological Processes*. *Rev. Mineral.* 16, 273–316.
- Thomas, J.B., Watson, E.B., Spear, F.S., Shemella, P.T., Nayak, S.K., Lanzirotti, A., 2010. TitaniQ under pressure: the effect of pressure and temperature on the solubility of Ti in quartz. *Contrib. Mineral. Petrol.* 160, 743–759.

- Tolan, T.L., Reidel, S.P., Beeson, M.H., Anderson, J.L., Fecht, K.R., Swanson, D.A., 1989. Revisions of the extent and volume of the Columbia River Basalt Group. In: Reidel, S.P., Hooper, P.R. (Eds.), *Volcanism and Tectonism in the Columbia River Flood-Basalt Province*. Geol. Soc. Am. Special Paper 239, 1–20.
- Toth, M.I., 1987. Petrology and origin of the Bitterroot lobe of the Idaho batholith. In: Vallier, T.L., Brooks, H.C. (Eds.), *Geology of the Blue Mountains Region of Oregon, Idaho, and Washington*. U.S. Geo. Surv. Professional Paper 1436, 9– 35.
- Trail, D., Mojzsis, S.J., Harrison, T.M., Schmitt, A.K., Watson, E.B., Young, E.D., 2007. Constraints on Hadean zircon protoliths from oxygen isotopes, Ti-thermometry, and rare earth elements: *Geochemistry Geophysics Geosystems*, 8(1), 1-22.
- Trimble, D.E., Carr, W.J., 1976. *Geology of the Rockland and Arbon Quadrangles, Power County, Idaho*. Geol. Surv. Bull. 1399, 1-115.
- Tuttle, O.F., Bowen, N.L., 1958. Origin of granite in the light of experimental studies in the system $\text{NaAlSi}_3\text{O}_8\text{-KAlSi}_3\text{O}_8\text{-SiO}_2\text{-H}_2\text{O}$. Geol. Soc. Am. Mem. 74.
- Valley, J.W., 2003, Oxygen isotopes in zircon: In: Hanchar, J.M., Hoskin, P.W.O (eds) *Zircon*. Rev. Mineral. Geochem. 53, 343-385.
- Valley, J.W., Bindeman, I.N., Peck, W.H., 2003. Empirical calibration of oxygen isotope fractionation in zircon. *Geochim. Cosmochim. Acta.* 67(17), 3257-3266.
- Valley, P.M., Fisher, C.M., Hanchar, J.M., Lam, R., Tubrett, M., 2010. Hafnium Isotopes in Zircon: A Tracer of Fluid-rock Interaction during Magnetite-apatite ("Kiruna-type") Mineralization. *Chem. Geol.* 275, 208-20.
- Valley, J.W., Chiarenzelli, J.R., McLelland, J.M., 1994. Oxygen isotope geochemistry of zircon. *Earth and Planet. Sci. Lett.* 126, 187–206.
- Van Alstine, R.E., 1976. Continental Rifts and Lineaments Associated with Major Fluorspar Districts. *Bull. of the Soc. of Econ. Geologists* 71, 997-987.
- Vazquez, J.A., Manning, C.E., Reid, M.R., 2004. Experimental Determination of Allantite Stability in High-Silica Rhyolite. *American Geophysical Union abstracts* V41C-1407.
- Vazquez J.A., Reid M.R., 2002. Time scales of magma storage and differentiation of voluminous high-silica rhyolites at Yellowstone caldera, Wyoming. *Contrib. Mineral. Petrol.* 144, 274–285
- Waite, G.P., Smith, R.L., Allen, R.L., 2006. VP and VS structure of the Yellowstone Hotspot from teleseismic tomography: evidence for an upper mantle plume. *J. Geophys. Res.* 111 (B04303). 21 pp.

- Wallace, P.J., Anderson, A.T., Davis, A.M., 1999. Gradients in H₂O, CO₂, and exsolved gas in a large-volume silicic magma system: Interpreting the record preserved in melt inclusions from the Bishop Tuff. *J. Geophys. Res.* 104 (B9), 20,097-20,122.
- Wark, D., Watson, E., 2006. TitaniQ; a titanium-in-quartz geothermometer. *Contrib. Mineral. Petrol.* 152(6), 743-754.
- Watts, K.E., Bindeman, I.N., Schmitt, A.K., 2012. Crystal scale anatomy of a dying supervolcano: an isotope and geochronology study of individual phenocrysts from voluminous rhyolites of the Yellowstone caldera. *Contrib. Mineral. Petrol.*
- Watts, K.E., Bindeman, I.N., Schmitt, A.K., 2011. Large-volume Rhyolite Genesis in Caldera Complexes of the Snake River Plain: Insights from the Kilgore Tuff of the Heise Volcanic Field, Idaho, with Comparison to Yellowstone and Bruneau-Jarbidge Rhyolites. *J. Petrol.* 52(5), 857-890.
- Watts K.E., Leeman W.P., Bindeman I. N., Larson P.B., 2010. Supereruptions of the Snake River Plain: Two-stage derivation of low- $\delta^{18}\text{O}$ rhyolites from normal- $\delta^{18}\text{O}$ crust as constrained by Archean xenoliths. *Geology* 38, 503–506.
- Wark, D.A., Hildreth, W., Spear, F.S., Cherniak, D.J., Watson, E.B., 2007. Pre-eruption recharge of the Bishop magma system. *Geology* 35, 235–238
- Wark, D., Watson, E., 2006. Titaniq; a titanium-in-quartz geothermometer. *Contrib. Mineral. Petrol.* 152(6), 743-754.
- Watson, B.E., 1996. Dissolution, growth and survival of zircons during crustal fusion: kinetic principles, geological models and implications for isotopic inheritance. *Geol. Soc. Am. Special Papers* 315, 43-56.
- Watson, E.B., Cherniak, D.J., 1997. Oxygen diffusion in zircon. *Earth and Planet. Sci. Lett.* 148, 527-544.
- Wegert, D., Parker, D., Ren, M., 2013. The Nathrop Domes, Colorado: Geochemistry and petrogenesis of a topaz rhyolite. *Rocky Mountain Geology* 48(1), 1-14.
- Weidner, J.R., Martin, R.F., 1987. Phase equilibria of a fluorine-rich leucogranite from the St. Austell pluton, Cornwall. *Geochim. Cosmochim. Acta.* 51, 1591– 1597.
- Wells, M.L., Snee, L.W., Blythe, A.E., 2000. Dating of major normal fault systems using thermochronology: An example from the Raft River detachment, Basin and Range, western United States. *J. Geophys. Res.* 105, 16,303-16,327.

- Werner, C., Brantley, S.L., Boomer, K., 2000. CO₂ emissions related to the Yellowstone volcanic system; 2. Statistical sampling, total degassing, and transport mechanisms. *J. Geophys. Res.* 105,10831-10846.
- Wernicke, B., 1992. Cenozoic extensional tectonics of the U.S. Cordillera. In: Buchfiel, B.C., Lipman, P.W., Zoback, M.L. (Eds.), *The Cordilleran Orogen; conterminous U.S. The Geology of North America Geological Society of America G-3*, 553–581.
- Whitaker, M.L., Nekvasil, H., Lindsley, D.H., Difrancesco, N.J., 2007. The role of pressure in producing compositional diversity in intraplate basaltic magmas. *J. Petrol.* 48(2), 365-393.
- Whitehead, R.L., 1992. Geohydrologic framework of the Snake River Plain aquifer system, Idaho and Eastern Oregon. *U. S. Geological Survey Professional Paper 1408-B*.
- Wiedenbeck, M., Alle, P., Corfu, F., Griffin, W.L., Meier, M., Oberli, F., Von Quadt, A., Roddick, J.C., Spiegel, W., 1995. Three natural zircon standards for U-Th-Pb, Lu-Hf, trace element and REE analyses. *Geostand. Newslett.* 19, 1–23.
- Wilson, C.J.N., Seward, T.M., Allan, A.S.R., Charlier, B.L.A., Bello, L., 2012. A comment on: ‘TitaniQ under pressure: the effect of pressure and temperature on the solubility of Ti in quartz’, by Jay B. Thomas, E. Bruce Watson, Frank S. Spear, Philip T. Shemella, Saroj K. Nayak and Antonio Lazirotti. *Contrib. Mineral. Petrol.* 164, 359-368.
- Wolff, D.E., Leeman, W.P., and Vervoort, J.D., 2005. U-Pb zircon geochronology of crustal xenoliths confirms presence of Archean basement beneath the central and eastern Snake River Plain: Geological Society of America Abstracts with Programs, 37(7), 60.
- Wolff, J.A., Ellis, B.S., Ramos, F.C., 2011. Strontium isotopes and magma dynamics: Insights from high-temperature rhyolites. *Geology* 39(10), 931-934.
- Woodhead, J.D., Hergt, J.M., 2005: A preliminary appraisal of seven natural zircon reference materials for in situ Hf isotope determination. *Geost. Geoanal. Res.*, 29, 183–195.
- Woodhead, J., Hergt, J., Shelley, M., Eggins, S., Kemp, R., 2004. Zircon Hf-isotope analysis with an excimer laser, depth profiling, ablation of complex geometries, and concomitant age estimation. *Chem. Geol.* 209, 121–135.

- Xiong, X.L., Rao, B., Chen, F.R., Zhu, J.C., Zhao, Z.H., 2002. Crystallization and melting experiments of a fluorine-rich leucogranite from the Xianghualing Pluton, South China, at 150 MPa and H₂O-saturated conditions. *J. Asian Earth Sci.* 21, 175–188.
- Yuan, H., Dueker, K., Stachnik, J., 2010. Crustal structure and thickness along the Yellowstone hot spot track: Evidence for lower crustal outflow-from beneath the eastern Snake River Plain. *Geochem. Geophys. Geosyst.* 11(3), 1-14.
- Yuan, H., Dueker, K., 2005. Teleseismic P-wave tomogram of the Yellowstone plume. *Geophys. Res. Lett.* 32 (L07304).
- Zhang, Y., Belcher, R., Ihinger, P.D., Wang, L., Xu, Z., Newman, S., 1997. New calibration of infrared measurement of dissolved water in rhyolitic glasses. *Geochim. Cosmochim. Acta.* 61(15), 3089-3100.
- Zoback, M.L., Thompson, G.A., 1978. Basin and Range rifting in northern Nevada—clues from a mid-Miocene rift and its subsequent offsets. *Geology* 6, 111–116.
- Zoback, M.L., Anderson, R.E., Thompson, G.A., 1981. Cenozoic evolution of the state of stress and style of tectonism of the Basin and Range province of the western United States. *Philosophical Transactions of the Royal Society of London, Series A: Mathematical and Physical Sciences* 300, 407–434.